

AN INVESTIGATION OF SPIN-VALVES AND RELATED FILMS BY TEM

by Jason Peters King

**Submitted for the degree of Ph.D. at the Department of Physics and Astronomy,
University of Glasgow**

December 1999

© Jason P. King 1999

ProQuest Number: 13834096

All rights reserved

INFORMATION TO ALL USERS

The quality of this reproduction is dependent upon the quality of the copy submitted.

In the unlikely event that the author did not send a complete manuscript and there are missing pages, these will be noted. Also, if material had to be removed, a note will indicate the deletion.



ProQuest 13834096

Published by ProQuest LLC (2019). Copyright of the Dissertation is held by the Author.

All rights reserved.

This work is protected against unauthorized copying under Title 17, United States Code
Microform Edition © ProQuest LLC.

ProQuest LLC.
789 East Eisenhower Parkway
P.O. Box 1346
Ann Arbor, MI 48106 – 1346

GLASGOW
UNIVERSITY
LIBRARY

11766 (copy 1)

SUMMARY

The work presented in this thesis is a study of the reversal mechanisms of the magnetic layers within spin-valve materials and related films. Spin-valves display the phenomenon of giant magnetoresistance (GMR) and are now being utilised as magnetoresistive read heads in commercial applications.

A spin-valve typically consists of two ferromagnetic layers separated by a thin spacer layer (eg Cu in the range 2-10nm). One of the ferromagnetic layers is “pinned” or fixed in direction by exchange coupling to an antiferromagnetic layer such as FeMn or IrMn. This shifts the hysteresis loop by a few hundred Oersted (Oe), and so only the other “free” ferromagnetic layer can reverse under the influence of the comparatively small magnetic field from a passing tape or disk. This reversal corresponds to a change between a parallel ‘low’ resistance state to an antiparallel ‘high’ resistance state under the application of a magnetic field of $\approx 10-15\text{Oe}$.

The reversal mechanisms that take place in the “free” and “pinned” magnetic layers in a range of spin-valve materials have been studied using Lorentz modes of transmission electron microscopy. These results form the bulk of this thesis. The effect of Molybdenum impurity on the magnetoresistance of $\text{Ni}_{80}\text{Fe}_{20}$ is considered as a secondary topic, and only chapter 6 is given over to these results.

The first chapter introduces the basic concepts of ferromagnetism, magnetoresistance, and its application in magnetic storage technology. Particular emphasis is given to the various energy contributions that are present in thin magnetic films. This leads to the concept of domains and domain walls. Anisotropic magnetoresistance (AMR) and giant magnetoresistance (GMR) are introduced. These phenomena have enabled the production of many thin film sensors for applications including magnetic storage technology. Spin-valves are then discussed, reference being given to their application as a sensor in magnetic read-head assemblies. The possible commercial benefits of using GMR based devices for magnetic storage applications are highlighted.

Transmission electron microscopy was the primary tool used to investigate the materials discussed in this thesis. Thus chapter 2 is devoted to discussion of the instrumentation and techniques employed. An overview of the important parts of a TEM is introduced,

including the electron gun and microscope column. The aberrations which limit the resolution of the microscope are mentioned before the techniques used to image structural properties are presented. Particular attention is then paid to the Fresnel, Foucault and Low angle diffraction (LAD) imaging modes of Lorentz electron microscopy which are used to investigate the magnetic structures in thin films. Finally, the methods used to apply magnetic fields in-situ are discussed.

Chapter 3 begins with a review of spin-valves detailing parameters such as the magnetic layer configuration, anisotropy arrangement, free layer reversal and deposition technique used for the samples investigated in this thesis.

Structural properties such as the average grain size of the spin-valves are investigated by bright and dark field imaging. Diffraction studies allow some compositional data and the level of texture to be evaluated.

The main body of results in this chapter concentrates on the magnetisation reversal mechanism of the free layer in a range of FeMn-biased spin-valves with parallel anisotropy. The thickness of the copper spacer layer (and hence the strength of the interlayer coupling strength), is varied in the range 2-10nm, as is the angle of applied field, θ , with respect to the biasing direction. Fresnel imaging and LAD studies reveal there to be 3 modes of reversal that are possible in the free layer depending on the interlayer coupling strength and field orientation. Two of the observed modes involve a combination of magnetisation rotation and domain assisted processes while the third involves coherent rotation of magnetisation alone. The boundary between the modes of reversal was shown to be indistinct, and involved a free layer reversal that proceeded by an increasing amount of magnetisation rotation as θ was decreased. This was accompanied by the formation of an increasing density of low angle, low mobility domain walls.

The observed modes of reversal are presented on a phase diagram and shown to be in many ways consistent with a coherent rotation model by Labrune. The main discrepancy between the model and observed modes of reversal is that domains are forbidden in the model. The chapter concludes with a brief study of a spin valve in a crossed anisotropy arrangement.

Magnetic modelling of the free layer reversal of FeMn-biased spin-valves is presented in Chapter 4. This uses the modified Stoner-Wohlfarth coherent rotation model

of Labrune. The model makes 3 assumptions, namely that i) the presence of domains and domain processes are forbidden; ii) there can be no twist of the magnetisation vector within a ferromagnetic layer; iii) the biased layer magnetisation remains fixed.

Using this model, the spin-valve free layer energy is modelled as a function of magnetisation for several of the samples studied experimentally in chapter 3. It is found that for all cases, except that for which coherent rotation of magnetisation alone is observed, an energy barrier is overcome at the switching field.

The form of the energy curves allows for a quantitative description of the observed domain processes to be made. For reversals that are seen to take place by a low number of domain walls rapidly sweeping through the free layer, the energy curves reveals that a large energy barrier with a deep minimum is overcome at the switching field. On the other hand, for cases where the magnetisation reversal proceeds by a higher density of low angle, low mobility domain walls, the energy curves display small energy barriers and shallow minima. For the case of coherent rotation of magnetisation alone, a single energy minimum is present throughout the reversal process.

For successful operation of a spin-valve, one of the magnetic layers must remain fixed while the other reverses under the influence of an external magnetic field. One way of achieving this is by exchange biasing one of the ferromagnetic layers with an antiferromagnetic pinning layer such as FeMn or IrMn. Chapter 5 investigates both the structural and magnetic properties of such an arrangement, emphasizing the influence of temperature on the exchange biasing mechanism. This is of interest because spin-valves incorporated into commercial devices often have to operate at elevated temperatures.

Reversals of the pinned ferromagnetic layer in the range -150°C to 300°C are conducted on samples of $\text{Ni}_{80}\text{Fe}_{20}$ biased by $\text{Fe}_{50}\text{Mn}_{50}$ and $\text{Ir}_{20}\text{Mn}_{80}$. Initially, at room temperature (where good alignment between the direction of applied field and the biasing direction is achieved), the reversal is observed to take place by complex domain assisted process and involved large numbers of 360° wall structures which are stable to high values of applied field strength. The reversal is markedly different from that observed for free layer spin-valve reversals. Exchange biasing densities of 0.098mJ/m^2 and 0.115mJ/m^2 are obtained for FeMn and IrMn at room temperature respectively. A linear decrease in the strength of the exchange biasing occurs as the temperature is increased, and the amount of magnetisation rotation gradually increases as the temperature is raised. This is partly due to

a slight misalignment between the biasing direction and applied field direction in the variable temperature rods, but is also due to the decreasing strength of the exchange biasing at elevated temperatures.

When the temperature is increased above the blocking temperature of the antiferromagnetic pinning layers, the reversal mechanism takes place at low applied field strengths, and an increase in the magnetisation ripple followed by a single domain wall sweeping rapidly through the ferromagnetic layer is observed. This corresponds to the exchange biasing effect disappearing as all magnetic order is lost in the antiferromagnetic layer above its blocking temperature ($\approx 140-150^\circ\text{C}$ for FeMn and $\approx 285^\circ-300^\circ$ for IrMn). The pinned layer then behaves like an isolated ferromagnetic layer. After cooling back to room temperature in the presence of a magnetic field along the biasing direction back to room temperature, the exchange biasing effect returns. However its strength is diminished when compared to the initial room temperature measurement.

The effect of Molybdenum impurity on $\text{Ni}_{80}\text{Fe}_{20}$ is investigated in chapter 6. Magnetic heads exploiting the AMR effect which were produced in Philips manufacturing displayed a reduced AMR ratio than was achievable in research. This was thought to be due to the diffusion of Mo into the permalloy during the manufacturing process. Annealing experiments carried out on samples of $\text{Ni}_{80}\text{Fe}_{20}$ with a Mo layer deposited on top are carried out. It is found that for annealing temperatures $\leq 275^\circ\text{C}$ that a slight improvement in the AMR could be achieved. This is thought to be due to grain growth which reduced the sheet resistance of the samples. For annealing at 300°C and above a decrease in the AMR ratio is observed. Rutherford Backscattering Spectrometry (RBS) revealed that Mo diffusion into the $\text{Ni}_{80}\text{Fe}_{20}$ layer is taking place. The amount of diffusion was low ($\approx 1\%$), and did not increase with temperature. It is likely that the Mo which diffused into the $\text{Ni}_{80}\text{Fe}_{20}$ did so by diffusing down the grain boundaries as opposed to an interdiffusion process between the two layers.

ACKNOWLEDGEMENTS

There are many people who over the past 3 years have helped make the completion of this thesis possible. Primarily I must thank Prof. John Chapman who has proved to be an excellent supervisor. I am also indebted to Dr Murray Gillies and Dr Jacques Kools, who not only supplied the samples, but also contributed invaluable feedback and knowledge. Thanks are also extended to my backup supervisor Prof. Bob Ferrier for his continual encouragement.

I am grateful to Dr Pat Nicholson, Dr Stephen McVitie and Dr Sam McFadyen for helping to teach me how to operate the various microscopes in the Solid State Physics Group and for keeping them in excellent working order. For the maintenance of the JEOL microscopes and provision of photographic film I would like to thank Mr Colin How and Mr William Smith.

I am deeply indebted to various people at the Philips Research Laboratories in Eindhoven. Particular thanks are extended to Ton Kuiper who supervised me during my stay. I would also like to thank Mr Wouter Oepts and Miss Jaqueline Van Driel who helped make my stay extremely enjoyable and beneficial.

Special thanks are extended to Prof. Alan Craven, Dr Peter Aitchison, and Dr Maureen McKenzie for providing continual encouragement and always being willing to discuss results and bounce ideas off. Special thanks to Dr Katherine Kirk for provision of patterned samples, and many useful discussions.

There are many other people whom during the tenure of this PhD who should not go unacknowledged. In particular Mr Alan Howie played an important role in the provision of computer facilities and whose computer know-how has been of immense benefit. Also, Dr John Rose has been extremely supportive and his friendship over the last 3 years helped me stay sane. Thanks to Miss Beverley Lynn for assisting in the organisation of many arrangements and nights out. Finally it remains for me to thank my friends and family for their continual support and companionship.

DECLARATION

This thesis is a record of the experiments which have been carried out by myself in the Department of Physics and Astronomy at the University of Glasgow during 1995-98. The work described herein is my own, apart from the preparation of samples which were prepared by Dr J.C.S Kools, Dr M Gillies, and Dr Ton Kuiper. Some of the work given in this thesis can be found in the following papers:

- (1) Magnetisation reversal mechanisms of FeMn-biased spin-valves as a function of interlayer coupling strength and field orientation.

J P King, J N Chapman, and J C S Kools, *J. Magn, Magn, Mat.*, **177** (1998) 896.

- (2) On the free layer reversal mechanism of FeMn-biased spin-valves with parallel anisotropy.

J P King, J N Chapman, J C S Kools, and M F Gillies, *J. Phys D: Appl Phys.* **32** (1999) 1087.

SUMMARY	i
ACKNOWLEDGEMENTS	v
DECLARATION	vi
CONTENTS	vii
CHAPTER 1: MAGNETISM OF THIN FERROMAGNETIC FILMS	1-26
1.1 INTRODUCTION	1
1.2 FERROMAGNETISM	1
1.3 MAGNETIC ENERGY CONTRIBUTIONS	3
1.3.1 EXCHANGE ENERGY	4
1.3.2 ANISOTROPY ENERGY	4
1.3.3 MAGNETOSTATIC ENERGY	6
1.3.4 ZEEMAN ENERGY	8
1.3.5 MAGNETIC DOMAINS	8
1.3.6 DOMAIN WALLS	9
1.3.7 TOTAL ENERGY	11
1.4 HYSTERESIS	11
1.5 MAGNETORESISTANCE	12
1.5.1 ANISOTROPIC MAGNETORESISTANCE (AMR)	12
1.5.2 GIANT MAGNETORESISTANCE (GMR)	14
1.6 SPIN-VALVES	16
1.7 MAGNETIC RECORDING AND SENSORS	19
1.7.1 INTRODUCTION	19
1.7.2 MAGNETORESISTIVE HEADS (MRH's)	21
1.7.3 GIANT MAGNETORESISTIVE HEADS (GMRH's)	23
CHAPTER 1 REFERENCES	25

CHAPTER 2: INSTRUMENTATION AND TECHNIQUES	27-43
2.1 INTRODUCTION	27
2.2 ELECTRON MICROSCOPY	28
2.2.1 THE ELECTRON GUN	30
2.2.2 THE MICROSCOPE COLUMN	30
2.2.3 IMAGE ACQUISITION	33
2.2.4 ABBERATIONS IN A CTEM	33
2.3 IMAGING OF STRUCTURAL PROPERTIES IN THE CTEM	35
2.3.1 DIFFRACTION PATTERNS	35
2.3.2 BRIGHT AND DARK FIELD IMAGING	36
2.4 ELECTRON SPECIMEN INTERACTIONS	37
2.5 FRESNEL IMAGING	39
2.6 FOUCAULT IMAGING	40
2.7 LOW ANGLE DIFFRACTION	41
2.8 THE APPLICATION OF MAGNETIC FIELDS IN-SITU	42
CHAPTER 2 REFERENCES	43

**CHAPTER 3: STUDY OF THE FREE LAYER REVERSAL MECHANISM 44-85
OF FeMn-BIASED SPIN-VALVES.**

3.1 INTRODUCTION	44
3.2 REVIEW OF SPIN VALVES	44
3.3 PREVIOUS TEM INVESTIGATIONS	47
3.4 SPUTTER DEPOSITION OF SPIN-VALVE MULTILAYERS	48
3.5 STRUCTURAL PROPERTIES	49
3.6 MAGNETIC PROPERTIES	52
3.6.1 INTRODUCTION	52
3.6.2 EASY AXIS REVERSALS AND h_j .	53

3.7 INVESTIGATIONS AS A FUNCTION OF APPLIED FIELD DIRECTION	56
3.7.1 SPIN-VALVES WITH $h_j < 1$.	56
3.7.2 SPIN-VALVES WITH $h_j > 1$.	70
3.8 INTERPRETATION AND PHASE DIAGRAM	77
3.9 CROSSED GEOMETRY	78
3.9.1 INTRODUCTION	78
3.9.2: CROSSED ANISOTROPY SPIN-VALVES WITH $h_j < 1$	79
3.10 DISCUSSIONS AND SUMMARY	82
CHAPTER 3 REFERENCES	85
CHAPTER 4: MAGNETIC MODELLING OF THE FREE LAYER REVERSAL OF FeMn BIASED SPIN-VALVES.	86-104
4.1 INTRODUCTION	86
4.2 MODELLING OF THE FREE LAYER REVERSAL PROCESS	86
4.3 MODELLING OF THE FREE LAYER EASY AXIS REVERSAL	88
4.4 MODELLING OF MODES OF REVERSAL	91
4.5 DOMAINS AND DOMAIN WALL CONSIDERATIONS	98
4.5.1 CASE 1	98
4.5.2 CASE 2	101
4.5.3 CASE 3	102
4.6 DISCUSSIONS AND SUMMARY	104
CHAPTER 4 REFERENCES	104

CHAPTER 5: EXCHANGE BIASING OF Ni₈₀Fe₂₀ BY FeMn AND IrMn	105-133
ANTIFERROMAGNETIC LAYERS	
5.1 INTRODUCTION	105
5.2 Ni ₈₀ Fe ₂₀ LAYERS BIASED BY Fe ₅₀ Mn ₅₀ and Ir ₂₀ Mn ₈₀	109
5.2.1 STRUCTURAL PROPERTIES	109
5.2.2 MAGNETIC PROPERTIES	113
5.3 TEMPERATURE DEPENDENCE OF BIASING	117
5.3.1 EFFECT OF COOLING ON MAGNETIC MICROSTRUCTURE	120
5.3.2 EFFECT OF HEATING ON MAGNETIC MICROSTRUCTURE	125
5.3.3 COOLING FROM ABOVE THE BLOCKING TEMPERATURE	129
5.4 DISCUSSIONS AND SUMMARY	131
CHAPTER 5 REFERENCES	133
CHAPTER 6: THE EFFECT OF MOLYBDENUM IMPURITY ON	134-144
PERMALLOY	
6.1 INTRODUCTION	134
6.2 EXPERIMENTAL CONDITIONS	135
6.3 ELECTRICAL AND MAGNETORESISTIVE PROPERTIES	136
6.3.1 INITIAL EXPERIMENTS	136
6.3.2 ANNEALING EXPERIMENTS	137
6.4 RUTHERFORD BACKSCATTERING SPECTOMETRY	141
6.5 DISCUSSIONS AND SUMMARY	143
CHAPTER 6 REFERENCES	144

CHAPTER 7: CONCLUSIONS AND FUTURE WORK	145-155
7.1 INTRODUCTION	145
7.2 CONCLUSIONS	145
7.3 FUTURE WORK ON CONTINUOUS FILMS	148
7.3.1 ALTERNATE ANISOTROPY ARRANGEMENTS	148
7.3.2 INFLUENCE OF TEMPERATURE ON SPIN-VALVE SAMPLES	149
7.3.3 INFLUENCE OF COOLING	149
7.4 PATTERNED SAMPLES	150
7.4.1 INTRODUCTION	150
7.4.2 'L-SHAPED' SAMPLES	150
7.4.3 OTHER SHAPES AND SIZES OF ELEMENTS	153

CHAPTER 1: MAGNETISM OF THIN FERROMAGNETIC FILMS

1.1 INTRODUCTION

This chapter introduces the basic concepts of ferromagnetism and antiferromagnetism and discusses the various magnetic energy contributions that affect the properties and characteristics of ferromagnetic films. This is followed by an introduction to magnetic hysteresis. The subject of magnetoresistance, particularly giant magnetoresistance (GMR), is discussed and spin-valve multilayers, which exhibit GMR, are introduced. Finally the chapter concludes with a discussion of the important applications of spin-valves for example in magnetic recording, sensors, and magnetic memories.

1.2 FERROMAGNETISM

A material is said to be ferromagnetic if, in the absence of an applied field, it possesses a spontaneous non-zero magnetic moment. Ferromagnetism is exhibited mostly by transition metals, alloys, rare earths and also some oxides such as CrO_2 . There are two possible origins of magnetic moments in magnetic substances: an orbital magnetic moment due to orbital angular momentum, and a spin magnetic moment due to electron spin. The magnetic moments of the important ferromagnetic elements Fe, Co and Ni are caused mostly by the spin component of angular momentum from unpaired electrons in the 3d electron shell. In these cases, it is said that the orbital angular momentum is 'quenched' (classically it is said that the orbits are fixed in space, or locked in to the 'crystal fields'). This subject is discussed in more detail in references [1,2]. In the case of rare earth metals at room temperature the atomic magnetic moment is due to both orbital and spin components of angular momentum from the 4f electrons. The crystal fields are significant for many properties of the rare earth atoms, but they are not significantly strong to quench the orbital momentum. Below a critical temperature known as the Curie temperature, T_c , the spins are aligned almost perfectly parallel to one another as a result of a strong positive interaction between neighbouring electron spins. This was first described by Weiss^[3] who postulated that each magnetic moment is assumed to be acted on by a molecular field which is proportional to the magnetisation of its environment. If a parallel alignment of

moments should appear locally at any place in the lattice a molecular field will be produced which, in turn will promote further alignment of the magnetic moments. However, as the temperature increases, the arrangement of the spins is disturbed by thermal agitation resulting in a loss of the magnetic order at T_c . At this point the magnetic moments become randomly oriented in zero field and the material is said to have become paramagnetic, figure 1.1a. In this case only a weak positive interaction of the magnetic moments is observed in the presence of an applied field.

It was Heisenberg^[4] who accounted for the molecular field by proposing a quantum mechanical interaction, known as the exchange interaction acting between pairs of electrons. The Pauli exclusion principle^[5] states that the total wave function must be antisymmetric or, alternatively expressed, that the two electrons cannot have exactly the same quantum numbers. Recalling that the electron wave function can be thought of as the product of spatial and spin parts, it follows that the electron distributions are different for parallel and anti-parallel spins, and the electrostatic (Coulomb) energy will therefore be different in the two cases. The exchange interaction thus results in an alignment of the electron spins in order to lower the electrostatic energy.

It should be noted that in the above discussion, the electrons are assumed to be localised at their respective atoms. This 'localised' model works well in the case of rare earth metals and ferromagnetic oxides where the unpaired electrons responsible for magnetism are in the inner 4f shells of individual atoms. In the case of transition metals such as Fe, Co and Ni, the 3d electrons are more exposed, and their wave functions overlap with those of neighbouring atoms. In this case, the 3d electrons can be thought to be spread into a sea of electrons (the energy levels of 3d electrons are perturbed and spread to form an energy band). This concept leads to the 'itinerant' or 'band' theory of ferromagnetism^[6] which includes the ability to explain non-integral values of atomic magnetic moments and to predict some aspects of the magnetic behaviour of the 3d metals and alloys. It should be noted that it is extremely difficult to make fundamental calculations based on the itinerant model, and in many cases interpretations of magnetic properties are still more often made on the basis of the localised electron model.

The exchange interaction results in an alignment of the electron spins in order to lower the electrostatic energy.

$$E_{ex} = -J(r_{ij}) \underline{s}_i \cdot \underline{s}_j \quad 1.1$$

Here E_{ex} is the exchange energy for two interacting electron spins s_i and s_j separated by a distance r_{ij} and $J(r_{ij})$ is the exchange integral. For cases where $J > 0$, this leads to the phenomenon of ferromagnetism, whereas for $J < 0$ antiferromagnetism results. A schematic of the spin-arrangement in a ferromagnetic substance is shown in figure 1.1b.

Below a temperature known as the Néel temperature certain substances exhibit antiparallel alignment of magnetic moments in adjacent atom planes, figure 1.1c. This is known as antiferromagnetism, and the net magnetic moment is 0. Examples of such materials are Cr, Mn, MnO, and NiO.

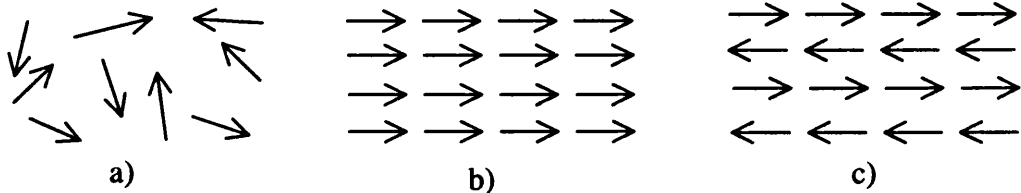


Figure 1.1: Schematic representation of magnetic moments in a) paramagnetic, b) ferromagnetic and c) antiferromagnetic materials.

1.3 MAGNETIC ENERGY CONTRIBUTIONS

The magnetisation \underline{M} is the magnetic moment per unit volume of a magnetic solid and is described by a vector field

$$\underline{M} = \frac{1}{V} \sum_v \underline{\mu}_i \quad 1.2$$

where $\underline{\mu}_i$ is the magnetic moment on each atom i , summed over the volume V . The magnetic configuration of a solid corresponds to a minimum in the potential energy with various magnetic energies contributing to the overall potential energy of the system. In the

following sections we discuss the various contributions to the magnetic potential energy which must then be minimised in a macroscopic magnetic solid.

1.3.1 EXCHANGE ENERGY

When considering a finite volume of magnetic material it is normally necessary to consider only nearest neighbour electron spin interactions. This simplifies the calculation of the exchange energy significantly. Integrating over the volume V of magnetic material gives:

$$E_{ex} = A \int_V [(\nabla\alpha)^2 + (\nabla\beta)^2 + (\nabla\gamma)^2] dV \quad 1.3$$

where α , β , and γ are the direction cosines of the magnetic vector and A is the exchange constant of the material. It relates approximately to J by

$$A = \frac{kJS^2}{a} \quad 1.4$$

k is a constant depending on the crystallite structure (1 for simple cubic, 2 for body-centred cubic, and 4 for face-centred cubic structures), a is the lattice parameter, and S is the spin magnetic moment of an atom.

1.3.2 ANISOTROPY ENERGY

There is an energy in ferromagnetic crystals called the magnetocrystalline anisotropy energy which is a minimum along certain crystallographic axes called “easy axes”. Deviations of the magnetisation from an easy axis leads to an increase in the anisotropy energy, which has its maximum along a “hard axis”.

For hexagonal or uniaxial crystals such as Co, the hexagonal axis (c-axis) is the easy direction, and the anisotropy energy is described by

$$E_a = \int_V [K_1(1 - \gamma^2) + K_2(1 - \gamma^2)^2] dV \quad 1.5$$

where K_1 and K_2 are the first two anisotropy constants of the material, and γ is the direction cosine of the magnetisation from the hexagonal, or c axis.

For cubic crystals such as Fe the [100] directions are the directions of easy magnetisation. The anisotropy energy is well represented by

$$E_a = \int_V [K_1(\alpha^2\beta^2 + \alpha^2\gamma^2 + \beta^2\gamma^2) + K_2\alpha^2\beta^2\gamma^2] dV \quad 1.6$$

For most transition metals $K_1 \gg K_2$ and the anisotropy energy can usually be simplified to a single term. An exception is Co where this is not true over the field temperature range up to T_c .

In the case of micro-polycrystalline magnetic materials the anisotropy direction varies locally from crystallite to crystallite which results in a random contribution to the local easy direction. This causes fluctuations in the local magnetisation direction from the average easy direction, a phenomenon which is known as magnetisation ripple^[7].

For polycrystalline random alloys such as permalloy ($\text{Ni}_{80}\text{Fe}_{20}$) there is near zero anisotropy energy. This means that the material is isotropic having no preferred easy (or hard) axes. In these cases it is possible to cause an induced anisotropy either by deposition of the film in the presence of a magnetic field or by annealing after deposition in a magnetic field. The magnitude of the field has only to be sufficient to saturate the film along the field direction. The induced anisotropy is caused by “preferential pair ordering” of magnetic atoms in an otherwise disordered alloy^[8]. It is related to the fact that an atom pair can have different energies as its orientation is changed with respect to the lattice in which it is situated. Therefore atom pairs occupy the lattice preferentially during deposition in the presence of a magnetic field, or similarly a fraction of reordering takes place during a magnetic annealing. The atom pairs are then “frozen” in upon cooling resulting in an induced anisotropy.

Magnetostriction is a phenomenon in which the material changes its size depending on its state of magnetisation. This is a manifestation of the spin-orbit interaction, in which the greater the change in spin-orbit energy with changes in atom to atom spacing, the greater the magnetostriction. A material has a positive magneto-strictive coefficient, λ_p , if along some dimension p it increases in length from l to $l+\Delta l$ upon being magnetised from $M=0$ to

$M=M_s$, the saturation magnetisation. If the material were to shrink under these conditions then λ_p would be negative. It is also possible to change the magnetic state of a magnetostrictive material by the application of external mechanical stress. For example a material with negative λ_p will become partially demagnetised by the application of tensile stress. The magnetostriction is usually large when the magnetocrystalline anisotropy is large. Thus for the case of permalloy which has near zero magnetocrystalline anisotropy the magnetic properties are relatively unaffected by stress and $\lambda \approx 0$.

1.3.3 MAGNETOSTATIC ENERGY

In a magnetic system there is a magnetostatic energy which is due to the presence of magnetic charges either within the body of the material or on its surfaces if there is a divergent component of magnetisation. These charges give rise to an external stray field, and an internal field termed the demagnetising field, H_d , which is in the opposite sense to the magnetisation. Figure 1.2 shows both the internal demagnetising field and external stray field for the simple case of a bar uniformly magnetised from left to right as indicated.

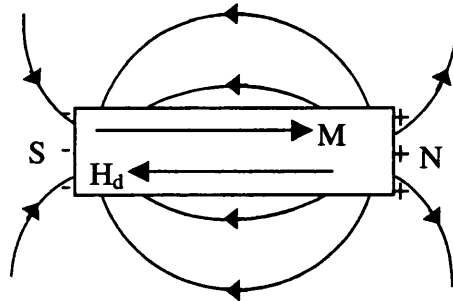


Figure 1.2: Uniformly magnetised bar, with magnetic charges giving rise to external stray field and internal demagnetising field H_d opposite to the direction of magnetisation M .

H_d can be calculated using Gauss theorem, in terms of an integral over the volume and surface enclosing the source of the free poles:

$$\underline{H}_d(\underline{R}) = \frac{1}{4\pi} \int_V \frac{-\nabla \cdot \underline{M}}{R^2} dV + \frac{1}{4\pi} \int_S \frac{\underline{M} \cdot \underline{n}}{R^2} dS \quad 1.7$$

Here \underline{R} is the position vector for the point in space where the field from the charge is evaluated and \underline{n} is the outward pointing unit vector normal to the surface. The term $\nabla \cdot \underline{M}$ is equivalent to the magnetic volume charge and $\underline{M} \cdot \underline{n}$ is the magnetic surface charge. This integral is only simple to evaluate for the simple case of a uniformly magnetised ellipsoid, and in general cases it has no simple analytical form.

For regularly shaped specimens one may write

$$H_d = NM \quad 1.8$$

where N is the demagnetising factor which is a function of the shape of the specimen and M is the magnetisation. In this case H_d depends on the direction of magnetisation. For a flat ellipsoid whose two long axes are a and b are very large compared to the short axis c ($a > b \gg c$) the demagnetising factors of the a and b axes are approximately given by

$$N_a = \frac{\pi c}{4 a} \left[1 - \frac{1}{4} \left(\frac{a-b}{a} \right) - \frac{3}{16} \left(\frac{a-b}{a} \right)^2 \right] \quad 1.9$$

$$N_b = \frac{\pi c}{4 a} \left[1 + \frac{5}{4} \left(\frac{a-b}{a} \right) + \frac{21}{16} \left(\frac{a-b}{a} \right)^2 \right] \quad 1.10$$

$$\text{Also, } N_a + N_b + N_c = 1 \quad 1.11$$

So for a flat plate, which is regarded as an ellipsoid with $a=b=\infty$, $N_a=N_b=0$, $N_c \rightarrow 1$.

The magnetostatic energy contribution from the interaction of the magnetic charges takes the form

$$E_m = -\frac{1}{2} \mu_0 \int_V \underline{M} \cdot \underline{H}_d dV \quad 1.12$$

where μ_0 is the permeability of free space.

1.3.4 ZEEMAN ENERGY

If an external field is applied to the specimen then the Zeeman energy takes the form

$$E_z = -\mu_0 \int_V \underline{M} \cdot \underline{H} dV \quad 1.13$$

where \underline{H} is the applied field. When the external field is applied then the magnetic moments of the specimen attempt to align towards the applied field in the minimum energy state.

1.3.5 MAGNETIC DOMAINS

In many cases the magnetisation of a ferromagnetic material is less than the total saturation magnetisation M_s and can take any value between $-M_s$ and $+M_s$ depending on the magnetic history of the sample. This was accounted for by the concept of magnetic domains^[9], in which there are many different areas of the specimen called domains in which the magnetic moments are locally aligned. Each domain has a local magnetisation M_s along the direction of aligned magnetisation. However, the orientation of the magnetic moments in adjacent domains may be random (in a fully demagnetised state) or possibly partially aligned (depending on the history of the sample). This leads to a lowering of the total magnetisation of the sample. The individual domains are separated by domain walls across which the magnetisation rotates between the directions of magnetisation in adjacent domains.

It was shown^[10] that domain structure was a natural consequence of the various contributions to the energy. For example domain formation is favoured if there is an energy saving by going from a saturated state with high magnetic energy to a domain configuration with a lower total energy. This concept is better understood by considering figure 1.3 in which 3 possible domain structures are shown for a small element of magnetic material. Figure 1.3a shows the element in a single domain state, in which there is a high magnetostatic contribution to the energy due to the large number of charges formed on the top and bottom surfaces. The magnetostatic energy can be reduced by splitting into domains such as in figure 1.3b.

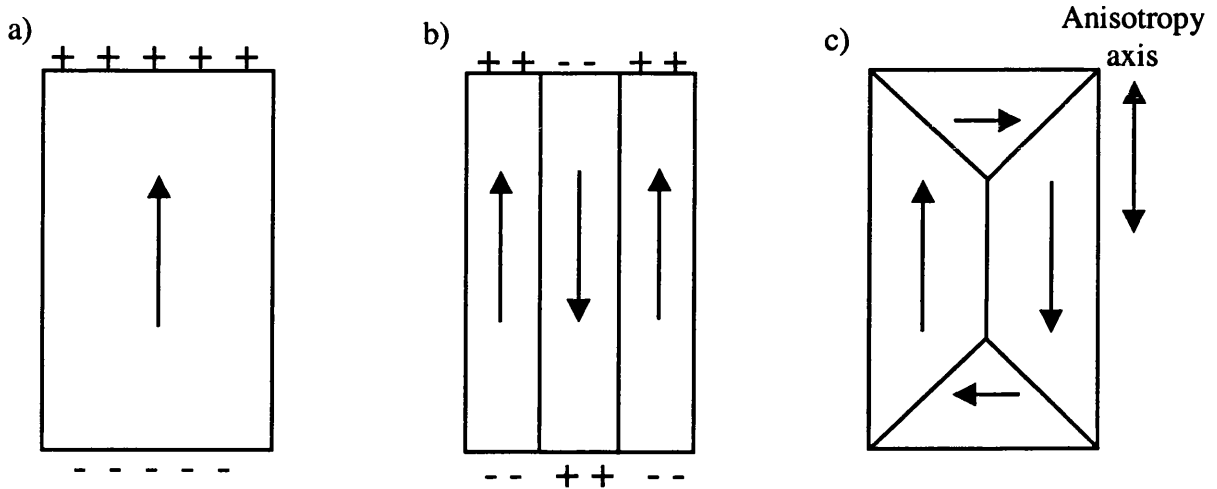


Figure 1.3: Small magnetic element showing 3 possible domain configurations.

In cases such as this, the magnetostatic energy is reduced to $\approx 1/N$ of that of case a) where N is the number of domains. This is due to the reduced spatial extent of the field outside the element. Figure 1.3c shows a domain structure in which “closure domains” are formed. This has the consequence of reducing the magnetostatic energy to zero because there are no longer any surface charges. However, in magnetic materials that have a unidirectional anisotropy, this structure increases the anisotropy energy due to the magnetisation oriented along the “hard axis” of the material.

In most cases the actual magnetic structure is much more complicated than in the simple cases outlined above and the observed domain structure is highly dependent on the exchange, anisotropy, and magnetostatic energies.

1.3.6 DOMAIN WALLS

Domain walls separate individual domains, and the magnetisation rotates coherently across the transition region. Three types of domain wall are discussed: Néel^[11], Bloch^[12], and Cross-Tie walls^[13]. In a Néel wall the magnetisation rotates in the plane of the sample as shown in figure 1.4(a). In the case of a Bloch wall the magnetisation rotates out of the plane of the sample, as in figure 1.4(b). In certain thicknesses of film, an intermediate type of domain structure can form, called a cross-tie wall which contains both Néel-like and Bloch-like regions. The structure^[13] is shown schematically in figure 1.5.

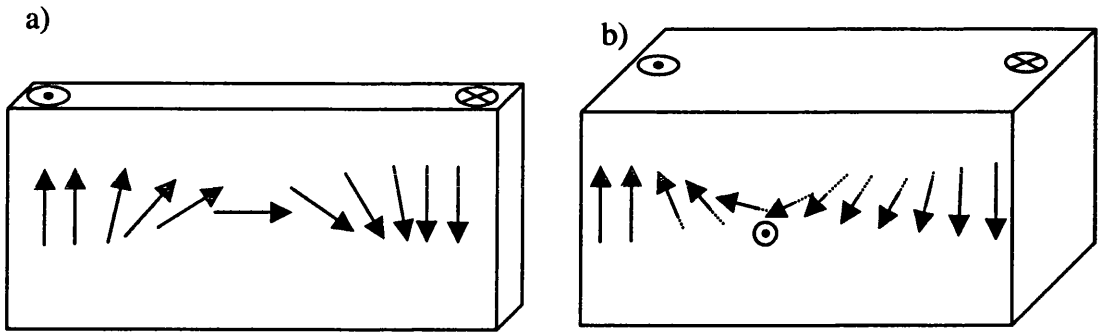


Figure 1.4: Schematic representation of (a) the Néel wall and (b) the Bloch wall.

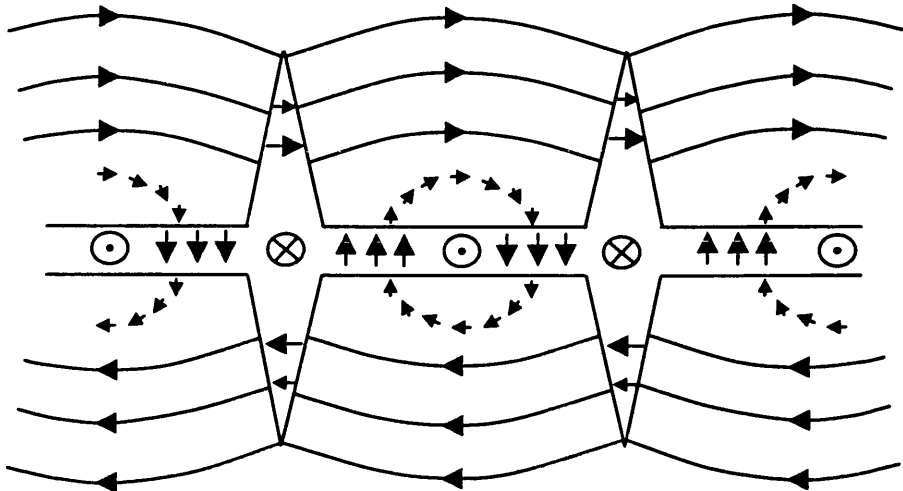


Figure 1.5: Schematic representation of a cross-tie wall.

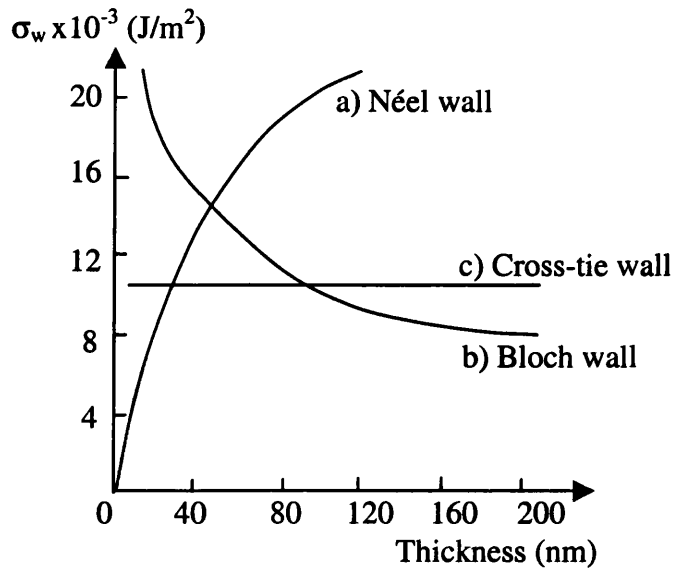


Figure 1.6: Comparison between the energy densities of Néel (a), Bloch (b), and Cross-tie walls (c) as a function of permalloy film thickness^[14].

The type of domain walls observed in ferromagnetic materials is highly dependent on the thickness of the film. A graph of the expected wall type as a function of thickness is shown in figure 1.6 for permalloy. It can be seen from this figure that Néel type walls are favourable for films with thicknesses $\leq 40\text{nm}$. Although the energy of domain walls is related to the previously discussed exchange, anisotropy and magnetostatic energies it is often possible to ascribe a domain wall energy E_w to the presence of domain walls in ferromagnetic films.

1.3.7 TOTAL ENERGY

The various energy terms all contribute to the total potential energy of a magnetic system, with there being a complex interplay between these in any magnetic material.

$$E_{TOT} = E_{ex} + E_a + E_m + E_z \quad 1.14$$

An observed magnetic configuration of a magnetic sample corresponds to a minimum in the potential energy, however this is often only a local energy minimum. In this way the magnetic state depends on the history of the sample which leads to the concept of hysteresis.

1.4 HYSTERESIS

Figure 1.7 shows an example of a hysteresis loop for a ferromagnet, that is, how the overall magnetisation of the sample M varies as a function of applied field H . If the specimen is in a completely demagnetised state at zero H the individual magnetic domains are randomly oriented, figure 1.7 (A) and the sample has 0 net magnetisation. Upon application of a magnetic field the magnetisation follows the initial magnetisation curve (A→B). As H is then increased further the magnetisation of the sample approaches saturation (M_s) as indicated (C). During magnetisation along A-C the randomly oriented magnetic vectors align towards the applied field direction either by magnetisation rotation or by motion of domain walls through the sample until saturation is approached and perfect alignment of M along H is achieved. Now, if the applied field strength is decreased, the magnetisation does not decrease along C→B→A but follows the solid curve along D→E→F. D is the

magnetisation M_R which is present at $H=0$. At this point there is still partial alignment of magnetisation along the applied field direction. As H becomes negative the magnetisation decreases to 0 at the coercive field H_c (E). As H becomes increasingly negative, the magnetisation approaches saturation in the opposite sense at point F. Increasing H once more results in M tracing along the curve $G \rightarrow C \dots$

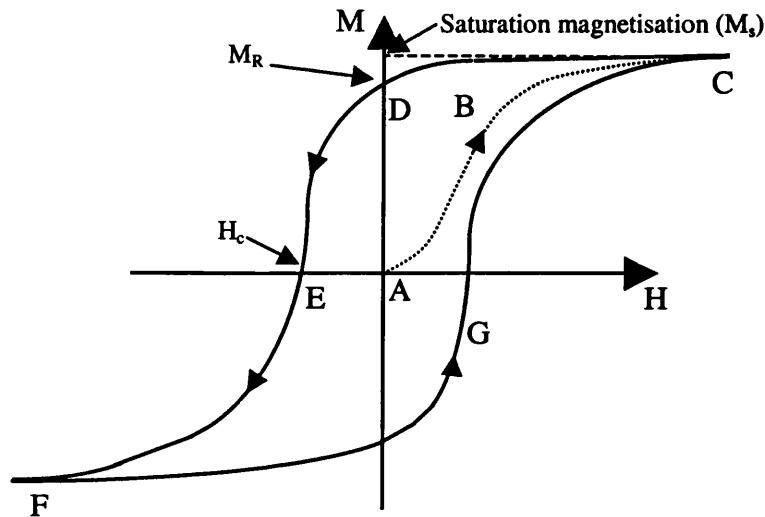


Figure 1.7: Hysteresis loop showing initial magnetisation curve and points of M_s , M_R and H_c .

The saturation magnetisation M_s is an intrinsic property of the ferromagnetic material under consideration, while M_R and H_c are extrinsic in that they can be varied by different deposition methods and processing such as annealing. All 3 are important parameters in magnetic materials as they define the form of the hysteresis loop and therefore they must all be considered for the application in mind.

1.5 MAGNETORESISTANCE

1.5.1 ANISOTROPIC MAGNETORESISTANCE (AMR)

Upon application of an external magnetic field to ferromagnetic materials a change in resistance is observed which depends on the magnitude and direction of the applied field H . This is known as anisotropic magnetoresistance (AMR) and was discovered in 1857 by W Thompson^[15] who later became Lord Kelvin. The phenomenon of AMR is reviewed in

detail in reference^[16]. It is due to two distinct physical effects which occur when an external field is applied. The first effect, which was originally referred to as the 'ordinary effect' is an isotropic effect which was explained by Mott's theory of resistivity^[17], and has to do with the scattering of conduction electrons into exchange-split d bands. The second physical effect which was known as the 'extraordinary effect' or the 'ferromagnetic resistivity effect', is dependent upon the relative orientation of the sample magnetisation with respect to the current direction. It is caused by spin orbit coupling between hybridised sd bands^[16]. The maximum in resistance is generally observed when the average magnetisation direction is parallel to the current direction. This is because in most cases the sd scattering probability is greatest for electrons traveling parallel to the magnetisation direction. This results in a \cos^2 dependence for the AMR amplitude for applied fields orthogonal to I as shown schematically in figure 1.8 where the angle between the magnetisation, M, and the current direction, I, is θ .

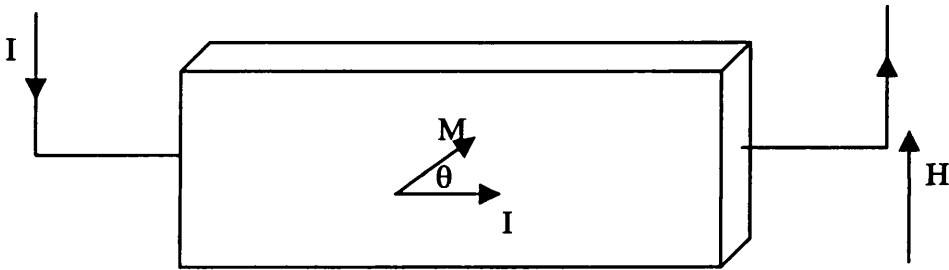


Figure 1.8: The AMR effect in a single domain thin-film strip.

The electrical resistance can be written as

$$R = R_0 + \Delta R \cos^2 \theta \quad 1.15$$

where R_0 and ΔR are the field independent and field dependent parts of the resistance respectively. The AMR ratio is almost always quoted as $\Delta R/R_{av}$ where ΔR is the maximum change in the resistance and R_{av} is the average resistance observed during the change. An important point is that as a ferromagnetic film becomes thinner the film resistance R_{av} increases due to additional surface scattering of the conduction electrons. This becomes important for all thin ferromagnetic films and lowers the AMR ratio, especially below 10 nm thickness and is referred to as the size effect^[16].

1.5.2 GIANT MAGNETORESISTANCE (GMR)

Giant magnetoresistance (GMR) was first observed in antiferromagnetically coupled Fe/Cr multilayers by Baibich et al^[18]. They reported a decrease in resistivity of a factor of 2 at 4.2K in MBE grown Fe/Cr multilayers upon application of a magnetic field of 20kOe. The physical origin of the effect was correctly suggested by these authors to be due to spin-dependent scattering of the conduction electrons predominantly at the interfaces between the adjacent Fe and Cr layers. Many other multilayer systems based on the magnetic transition metals and their alloys have now been discovered exhibiting the GMR effect. One such case is in sputtered multilayers^[19]; for example, a change in resistance in a sputtered Co/Cu multilayer system of greater than 100% was observed with the current in the plane of the layers, but required a 13kOe field to achieve the change^[20]. For the successful utilisation of the GMR effect in microelectronic devices such as read heads a sensor with high sensitivity in the low field range is required. The sensitivity is normally quoted as

$$s = \frac{1}{H} \left(\frac{\Delta R}{R_p} \right) \quad 1.16$$

where ΔR is the maximum change in the resistance and R_p is the low resistance state of the multilayer (see below). Other properties which are advantageous for sensor application are a linear response with a good signal to noise ratio. Also low magnetostriction (deformation of the sample under the influence of a magnetic field) and good thermal stability are required. Note that in all these systems that the GMR is associated with different scattering rates of the conduction electrons at the interfaces and in the magnetic layers brought about by changes in the relative orientation of the magnetisation in successive ferromagnetic layers.

The GMR ratio is quoted as $\Delta R/R_p$ (%). The resistance can be measured with the current either perpendicular to the plane of the layers (CPP geometry) which leads to a higher change in the resistance because the current is directed across the interfaces but an extremely low overall resistance is obtained (typically $10^{-8}\Omega/\text{mm}^2$ for a 100nm thick multilayer). Thus the contact leads have a much higher resistance than the sensitive layer which currently prevents CPP geometry in practical applications. The other method is to apply the current in the plane of the magnetic layers (CIP geometry). In this case a lower

change in the resistance is obtained because the electron motion is a diffusive process through the multilayer. This results in a higher overall resistance which gives good matching with the contact leads. It is the CIP geometry which is likely to be used in the practical application of GMR devices.

The GMR effect is due to the different scattering rates of spin-up and spin-down electrons in the two ferromagnetic layers and at their interfaces. Often the latter is dominant. When an electron traverses an interface it has a probability of being scattered. An electron whose spin is antiparallel to the magnetisation at the interface (spin-down) will be strongly scattered. For spin-up electrons whose spin is parallel to the magnetisation at the interface the scattering probability is significantly less. Thus when successive magnetic layers lie antiparallel to each other both the spin-up and spin-down electrons will scatter strongly at one of the interface types and weakly at the other. When the magnetic layers are parallel one of the electron types (the spin-down electrons, say) are strongly scattered whilst the spin-up electrons are weakly scattered. Scattering of the electrons gives rise to resistance, so it is clear that the resistance of the system depends on the relative orientation of the magnetisations in successive ferromagnetic layers. The parallel state is the low resistance state due to shunting of the electron current in the weakly scattered low resistance spin-up electron channel. The antiparallel state is the high resistance state. Application of an external magnetic field can result in a change in the relative orientation of the ferromagnets and this is what leads to the large change in resistance which is known as GMR.

Using such a two current model,^[24] the change in the resistance of the low resistance (parallel alignment) state is given by

$$R_P = \frac{R \uparrow R \downarrow}{(R \uparrow + R \downarrow)} \quad 1.17$$

where $R \uparrow$ and $R \downarrow$ are the resistances of the spin \uparrow and spin \downarrow electrons respectively. The high resistance (antiparallel) state is given by

$$R_{AP} = \frac{(R \uparrow + R \downarrow)}{4} \quad 1.18$$

and the GMR amplitude is then given by

$$\frac{\Delta R}{R_p} = \frac{(R \uparrow - R \downarrow)^2}{4R \uparrow R \downarrow} = \frac{(1 - \alpha)^2}{4\alpha} \quad \text{with} \quad \alpha = \frac{R \downarrow}{R \uparrow} \quad 1.19$$

1.6 SPIN-VALVES

One such example of a magnetic multilayer exhibiting GMR is the so called spin-valve multilayer. These have received much attention in recent years as they exhibit a large change in resistance at room temperature in a relatively low applied field range (<20Oe). The structure of a basic spin-valve is shown schematically in figure 1.9.

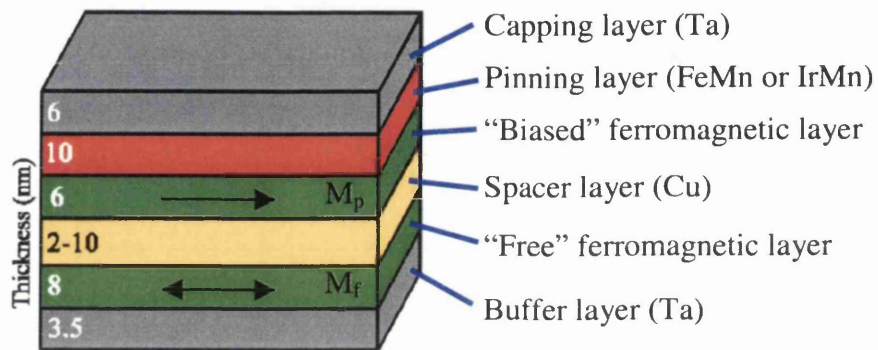


Figure 1.9: Schematic diagram of standard spin-valve structure with typical layer thicknesses indicated (nm).

The structure is grown upon a Ta buffer or seed layer which enhances <111> growth and minimises the crystalline anisotropy of the subsequent ferromagnetic layers. There are then two ferromagnetic layers which are separated by a non magnetic copper spacer. The upper ferromagnetic layer which is known as the ‘biased’ or ‘pinned’ layer is in contact with an antiferromagnetic (AF) layer which fixes its magnetisation by exchange coupling. Although there are several different materials which can be used as the biasing material only FeMn and IrMn have been studied in this thesis (FeMn being the standard AF used). The material used as the ferromagnetic material in this case is either permalloy ($\text{Ni}_{80}\text{Fe}_{20}$) or $\text{Ni}_{66}\text{Fe}_{16}\text{Co}_{18}$. The latter composition is chosen as the presence of Co enhances the amount of spin dependent scattering and it lies close to the zero magnetostriction line of the NiFeCo ternary phase diagram^[21-23]. The copper spacer layer’s thickness is chosen in the range 2-10 nm so that the two ferromagnetic layers are magnetically decoupled and a weak ferromagnetic coupling exists between them. As a result of this the lower

ferromagnetic layer can be reversed under the influence of a weak external magnetic field, and is therefore known as the “free” layer. It is the reversal mechanism of this layer which determines aspects of the performance of devices based upon spin-valves for example linear operating field range and noise characteristics. The main subject of study in this thesis is the free layer reversal mechanism of such spin-valves whose magnetic properties are discussed in detail in section 3.1.

A typical MR loop for a spin-valve such as described above is shown below, figure 1.10,

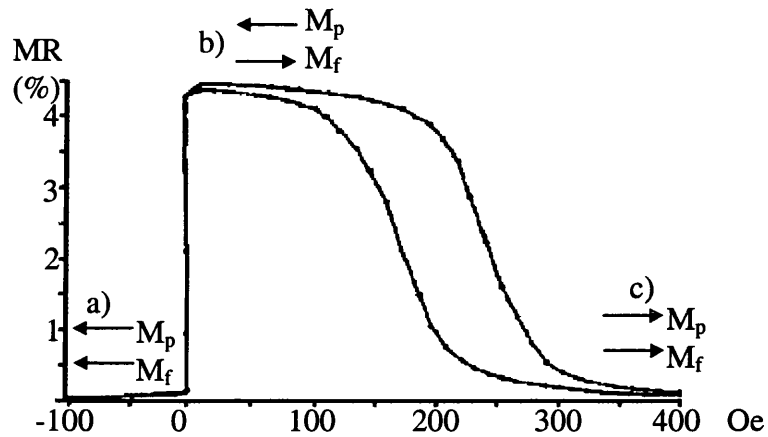


Figure 1.10: Typical room temperature MR loop for a spin-valve biased by FeMn with relative orientations of pinned and free layer magnetisation indicated.

It can be seen from figure 1.10 that the spin-valve MR response can be divided into 3 areas; (a) in the field range $-\infty \rightarrow \sim 15$ Oe where there is low resistance and corresponding to parallel alignment between the two ferromagnetic layers M_p and M_f . (b) a high resistance plateau in the range $\sim 15 \rightarrow \sim 250$ Oe where there is antiparallel alignment between the two ferromagnetic layers. Finally (c) there is another low resistance regime where the biasing between the upper ferromagnet M_p and the antiferromagnet is overcome and parallel alignment between the ferromagnetic layers is once again achieved.

When optimising a spin-valve for device applications it is desirable to achieve maximum MR amplitude. For example the thickness of the Cu spacer should be sufficient to decouple the two ferromagnetic layers. If this layer is insufficiently thick, exchange coupling will exist between the layers which is highly detrimental to device performance. In the limit of a thick copper layer additional shunting of the current takes place, an effect which lowers the overall MR response as less spin dependent scattering is contributing to

the overall resistance. Similarly the thickness of the ferromagnetic layers plays a role in the overall MR amplitude of a spin-valve. Ideally their thickness should be of the order of the mean free path of the conduction electron in the material. Figure 1.11 shows the MR response for a spin-valve as a function of permalloy layer thickness^[25] in which it can be seen that there is a maximum around 8 nm. The decrease below this value is due to insufficient scattering of the spin \downarrow electrons when the thickness becomes less than the mean free path of the spin \downarrow electrons^[26]. Above 8 nm the decrease is due to shunting of the sense current and insufficient mixing of the electrons between the two permalloy layers.

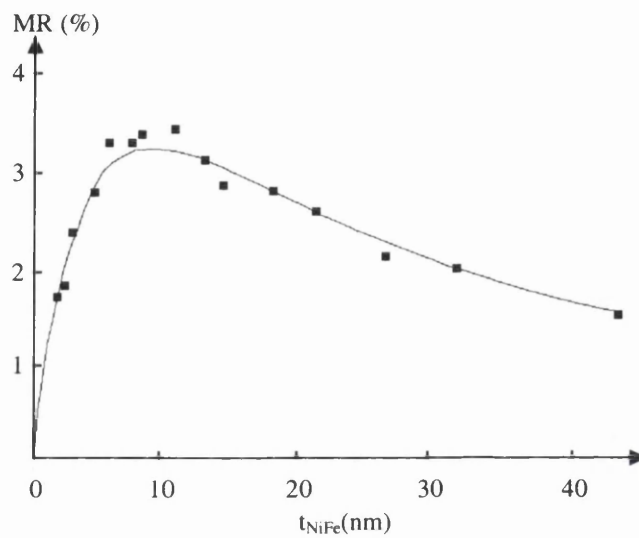


Figure 1.11: MR amplitude as a function of permalloy layer thickness^[25].

There have been several other ways to increase the overall MR of the spin-valve device. Two such examples are to modify the layer configuration in the spin-valve as shown schematically in figure 1.12:

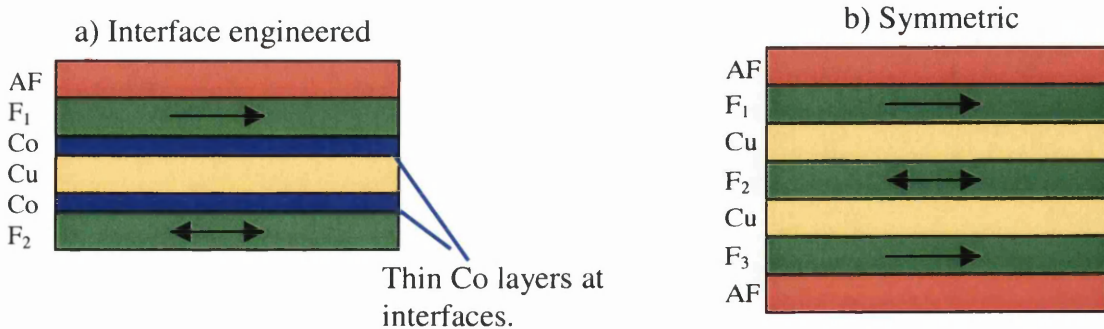


Figure 1.12: Schematic representation of a) interface engineered and b) symmetric spin-valve structures.

Figure 1.12 (a) shows what is called an interface engineered spin-valve. It was found^[27] that by depositing very thin layers (a few monolayers) of Co at the F/Cu interfaces (where F is a ferromagnetic layer) that the MR response increased from $\approx 5\%$ to 8% , although a decrease in the sensitivity of the spin-valve was observed as Co has a higher anisotropy than permalloy. Figure 1.12 (b) shows a symmetric spin-valve which consists of a spin-valve with an additional biased layer. If the thicknesses are chosen carefully the electrons may pass four interfaces instead of two, thus increasing the MR ratio. Note however that as the free layer is between two pinned layers it is influenced by twice the coupling strength. For this type of structure it was possible to attain a GMR ratio of 23.4% at room temperature^[28], however the free layer reversal did show considerable hysteresis ($H_c=50$ Oe). The symmetric spin-valve is a combination of the standard and “inverted”^[29] spin-valves in which the position of the AF layer with respect to the rest of the structure determines its name.

1.7 MAGNETIC RECORDING AND SENSORS

1.7.1 INTRODUCTION

The ability to store information for later retrieval or manipulation has been utilised for decades and a particularly relevant area has been in the storage of data in digital form. This section introduces the basic concepts behind such storage exploiting magnetic materials and technology.

Any information to be stored firstly has to be recorded into a magnetic recording media. This is achieved by using an inductive write-head or “ring” head, shown schematically in figure 1.13. When a current is passed through the coil it induces a flux in the magnetic “core” of the head. In turn this flux fringes out of the head gap and locally magnetises the recording media as indicated. If the write current is then turned off, the fringing field reduces to 0. However the locally magnetised media retains its direction of magnetisation (and hence the information) due to its hysteresis, section 1.4. If the current in the coil is alternately oscillated then the polarity of the fringing field at the head gap alternates in unison. Thus as the media passes the writing head, information can be stored as alternately magnetised “bits” in the recording medium. NiZn or MnZn ferrite are often

used in ring heads. They are electrical insulators and can be operated at high frequencies (>10MHz).

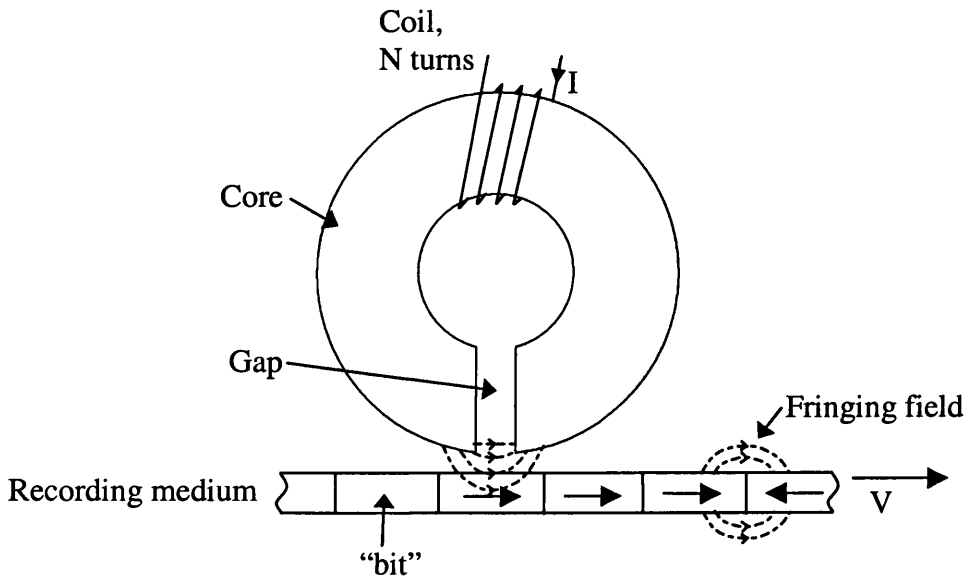


Figure 1.13: Schematic showing idealised inductive head and the magnetic recording process.

In order to retrieve the information at a later time the changes in magnetisation of the media must be sensed and an electrical signal obtained. This is achieved by sensing the transition between successive magnetic bits in which two oppositely magnetised regions have a fringing field which emanates above and below the plane of the media, figure 1.13. An inductive head can also be used to read the information, in essence the writing process in reverse. Here the core acts as a flux closure path for the fringing flux which induces a magnetic field in the core material. This in turn produces a current in the coil by Faraday's induction law

$$V = -N \frac{d\phi}{dt} \quad 1.20$$

Which states that the e.m.f. induced in a circuit is equal to the rate of change of flux linking the circuit. Here V is the induced e.m.f., N is the number of turns in the coil and ϕ the magnetic flux.

Thin film technology allowed the head structure to be deposited layer by layer. The core is usually referred to as the "yoke" in thin-film heads and is made of thin layers

of NiFe or AlFeSi alloys. This enabled smaller pole tips on the head and subsequently a higher fringing flux emanating from the gap. Another advantage is that a higher permeability is obtained in thin film heads which allows high frequency operation. As the bit density increases a media with higher coercivity is required to constrain the magnetisation in the recorded bit. The higher fringing flux from the thin film head was required to magnetise the media and record the necessary information. A problem does however arise in reading higher bit densities with inductive heads, which will be returned to in section 1.7.2.

The recording media is usually in the form of a magnetic tape or a spinning disk and inductive heads can actually be used to record either analogue or digital signals. The advantage of digital recording is that a greater bit density can be achieved allowing more information to be stored in a given amount of media as well as a higher signal to noise ratio. Original recording media was particulate in nature, for example metal particle ferrite granules. Today disk applications favouring small bit sizes mainly employ continuous films based on CoCr alloys.

1.7.2 MAGNETORESISTIVE HEADS (MRH's)

As the bit size decreases for a given magnetic media the stray field emanating from the bit transition also decreases. Eventually the inductive head is insufficiently sensitive to read the weak stray fields.

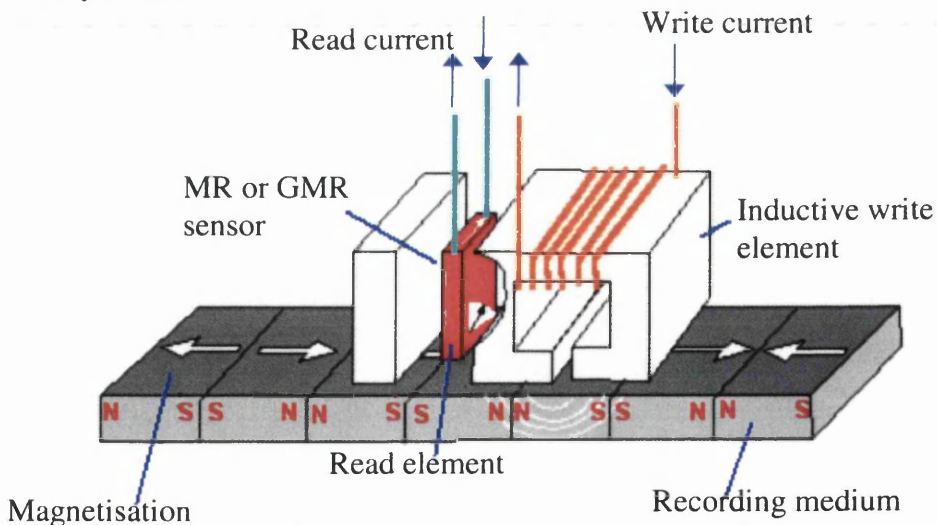


Figure 1.14: Schematic showing composite head assembly commonly used for applications using magnetoresistive read-head technology.

While working for the Ampex Corporation it was Robert Hunt who overcame this problem by inventing the magnetoresistive head (MRH)^[30] which exploited the AMR effect and had a higher sensitivity than the inductive read-head. Although it is possible to have a separate write-head along side the MR read-head it is more common to have the two incorporated into a single composite structure such as shown in figure 1.14.

A simple AMR read element can be made from a thin-film of permalloy which can be single domain and demagnetising fields cause the magnetisation to remain virtually parallel to the plane of the film.

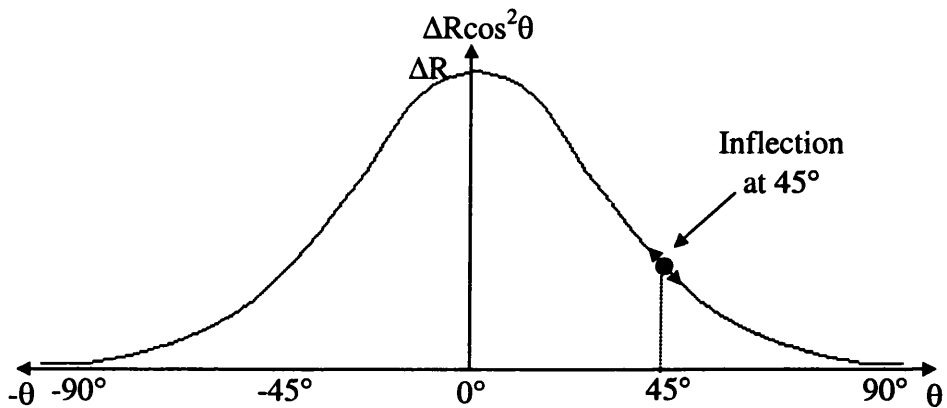


Figure 1.15: The MR change in resistance versus magnetisation angle.

Figure 1.15 shows the resistance change for an AMR material as a function of the angle of magnetisation. It is highly desirable for the resistance change to be as large as possible in a small field range and linear. In order for this to be achieved one must operate an AMR sensor with the current direction at 45° to the average direction of magnetisation. This problem has been a fertile area for invention in recent years, and the mechanism utilised for achieving linear operation in the Philips DCC compact cassette system is called “barber poling”^[31]. This consists of depositing thin strips of Cu or Au on top of the continuous layer of permalloy. These are at 45° to the length of the sensor and cause the sense current to channel across the strips. Thus when the sense current then passes through the permalloy it is at 45° to the magnetisation and the sensor is correctly biased. Several other mechanisms for biasing AMR sensors now exist, and it was the successful implementation of optimum biasing which led to large scale production of MRH’s.

Thus AMR based sensors provided an improved sensitivity (typically 0.5%/Oe) and signal to noise ratio over inductive heads. However the digital revolution has caused an

unrelenting pressure for increased data storage capacity. Along with the need for reliable and fast data access organisations demand low cost hardware. This has led to a steady decrease in the cost per megabyte over the years as well as an increase in the overall data storage density over several orders of magnitude. Because of the increasing bit density and need for rapid data access it is anticipated that simple AMR based sensors will have insufficient sensitivity and signal to noise ratio to detect the rapidly varying weak stray fields in future magnetic recording applications.

1.7.3 GIANT MAGNETORESISTIVE HEADS (GMRH's)

It has only been 10 years since the discovery of the GMR effect and already several research groups have prototype heads utilising the GMR effect^[32-34]. In fact, IBM have recently (1998) launched a portable computer hard disk drive incorporating GMR heads^[35].

The advantages of using GMR over AMR based devices is that an improved low field sensitivity is achieved (up to 1.5%/Oe has been reported^[36] which is 3 times higher than for comparable AMR heads). In a fully optimised spin-valve a sensor with a high sensitivity, a fully linear dynamic range (as long as the sensitive layer is not saturated), a response that is free of hysteresis and Barkhausen noise can be obtained. The optimisation process is complex and discussed in more detail in section 3.2.

Depending on the application in mind different head designs are used. For example in hard disk recording a sensor-in-gap (SIG) head is preferred^[37]. The MR stripe is situated in between two soft magnetic flux guides (shields) and embedded above and below by two non magnetic gap layers, for example see figure 1.16a. This type of head is preferred for hard disk applications because the sensor is close to the medium which offers the largest output.

For tape applications where the head assembly comes into contact with the medium yoke-type heads are often used^[37]. This is because contact between the MR element and the medium results in an extra thermally induced contribution to the noise which favours the use of yoke-type heads where the MR element is recessed. In these type of heads the soft magnetic flux guides are separated by one nonmagnetic gap and the flux guides form a closed path inside the head, guiding the flux from the head surface to the MR element, as in figure 1.16b. For a yoke type GMR head an output gain of a factor of 10 has been obtained compared to a barber-pole biased AMR head^[33].

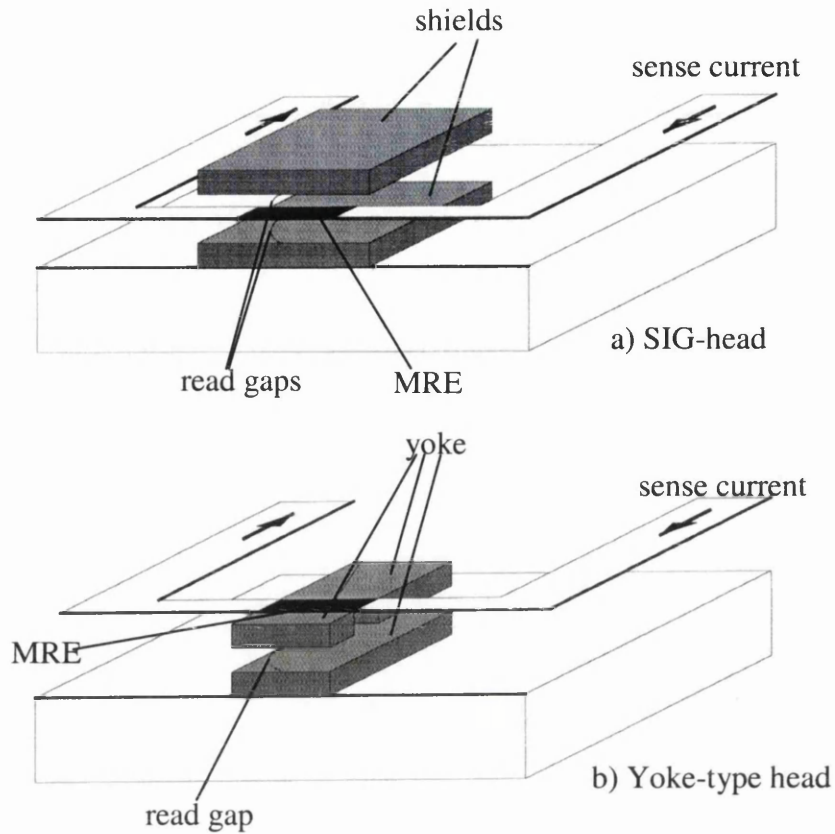


Figure 1.16: Schematic showing **a)** SIG-type head, and **b)** yoke-type head structures.

Due to the sensitive and highly linear response that can be obtained with spin-valves, applications also include rotation-speed, position sensors, encoders, compasses and current sensors. Another application that exploits a rectangular hysteretic response of certain spin-valves is in magnetic memories, namely Magnetic Random Access Memory (MRAM)^[38,39].

REFERENCES

- [1] Morrish A. H. (1965) *The physical principals of magnetism*, Wiley, New York.
- [2] Kittell C. (1986) *Introduction to Solid State Physics*, 6th Edⁿ, Wiley, New York.
- [3] Weiss P, (1907) *J. de Phys.* **6**, 661.
- [4] Heisenberg W, (1928) *Z. Phys.* **49**, 619.
- [5] Pauli W, (1925) *Z Phys.* **31**, 765.
- [6] Stoner E. C (1933) *Phil. Mag.* **15**, 1080.
- [7] Fuller H M, Hale M E, (1960) *J. Appl Phys.*, **31**, 238.
- [8] Chikazumi S, (1950) *J. Phys. Soc. Japan*, **5**, 327. ??Right??
- [9] Becker R, (1930) *Z. Physik*, **62**, 253.
- [10] Landau L, Lifshitz E, (1935) *Phys. Z. Sowjetunion*, **8**, 153.
- [11] Hubert A, (1970) *Phys. Solidi* **38**, 699.
- [12] Bloch F, (1932) *Z. Physik*, **74**, 295.
- [13] Huber E E, Smith D O, Goodenough J B, (1958) *J. Appl. Phys* **29**, 294.
- [14] Prutton M, (1964) *Thin ferromagnetic films* (Butterworths).
- [15] Thompson W, (1857) *Proc. Roy. Soc.* **8**, 546.
- [16] McGuire T R, Potter R I, (1975) *IEEE Trans. Magn.* **MAG-11(4)**, 1018.
- [17] Mott N F, Wills H H, (1936) *Proc. Roc. Soc.* **A156**, 368.
- [18] Baibich M N et al, (1988) *Phys. Rev. Lett.* **61**, 2472.
- [19] Parkin S S P et al, (1990) *Phys. Rev. Lett.* **64**, 2304.
- [20] Parkin S S P et al (1991) *Phys. Rev. B*, **66**, 2152.
- [21] Wilts C H, Humphrey F B, (1968) *J. Appl. Phys.*, **39** 1191.
- [22] Kitade Y et al (1995) *IEEE Trans. Magn.*, **31**, 2600.
- [23] Miyazaki T et al (1994) *J. Magn. Magn. Mat.*, **129**, L135.
- [24] Fert A, Bruno P, (1992) *Ultrathin Magnetic Structures* eds. Heinrich B, Bland A, Springer-Verlang, Berlin.
- [25] Dieny B et al (1991) *J. Appl. Phys.*, **69**, 4774.
- [26] Dieny B, (1994) *J. Magn. Magn. Mat.*, **136**, 335.
- [27] Parkin S S P (1993) *Phys. Rev. Lett.*, **71**, 1641.
- [28] Egelhoff W F et al (1995) *J Appl. Phys.*, **78**, 273.
- [29] Lenssen K –M H et al (1997) *J. Appl. Phys.*, **81**, 4915.
- [30] Hunt R P (1970) *IEEE Trans. Mag.*, **11**, 4.

- [31] Kuijk K E et al (1975) *IEEE Trans. Mag.*, **11**, 1215.
- [32] Heim D E et al (1994) *IEEE Trans. Mag.*, **30**, 316.
- [33] Folkerts W et al (1995) *IEEE Trans. Mag.*, **31**, 2591.
- [34] Fujikata J et al (1995) *IEEE Trans. Mag.*, **31**, 3936.
- [35] *Data Storage Magazine*, April 1998, page 12.
- [36] Rijks Th. G S M et al (1994) **65**, 916.
- [37] Lenssen K –M H et al (1997) *Sensors and Actuators A-physical*, **60**, 90.
- [38] Pohm V A et al (1994) *IEEE Trans. Mag.*, **30**, 4650.
- [39] Tang D D et al (1995) *IEEE Trans. Mag.*, **31**, 3206.

CHAPTER 2: INSTRUMENTATION AND TECHNIQUES

2.1 INTRODUCTION

The purpose of this chapter is to introduce the instrumental requirements of a transmission electron microscope (TEM) for imaging the structural and micromagnetic properties of thin films. Lorentz electron microscopy in particular is described as this is the main magnetic imaging technique used to collect the majority of results presented in this thesis.

The first technique that was used to image magnetic domains was the decoration method of Bitter^[1]. This involved coating the surface of the ferromagnet with a colloidal suspension of small magnetic particles. These tend to congregate around regions of high magnetic stray field, for example domain walls that are intersecting the sample surface. This method therefore reveals the positions of domain walls at the sample surfaces. However, the technique only provides information of the surface domain structures, and furthermore reveals no information upon the directionality of magnetisation within the domains. The resolution is limited by the wavelength of the light used, which was originally optical light. A significant improvement can be made by utilising the scanning electron microscope (SEM) which is operated at smaller wavelengths.

Other optical techniques that have been developed exploit the rotation of polarised light when reflected from the surface of an opaque specimen (the Kerr effect) or when transmitted through a thin transparent specimen (the Faraday effect). The Kerr effect is once again limited to the investigation of surface domain structures whilst the Faraday effect provides information on the domain structure throughout the thickness of a thin sample. A distinct advantage of these two techniques is that they are relatively simple to implement and can be used in dynamic experiments.

Another technique called magnetic force microscopy (MFM) images the stray magnetic field above the sample surface. This is a non-contact method and involves scanning a magnetic tip mounted on a cantilever across the surface. A detector mounted on the back side of the cantilever detects the interaction between the sample and tip, and a reconstruction of the sample stray field is then generated by computer. Different grey or colour values are assigned to the varying interaction strengths forming a microscopic

image of the interaction on the sample surface. Using an etched nickel wire as a tip, details of 10nm size have been resolved on a rapidly quenched FeNdB sample^[2].

Electron microscopy can also be used to observe the domain structure in magnetic specimens, and this was first achieved over 35 years ago^[3]. In this case with the specimen located in field free space a defocused image revealed the positions of domain walls as either bright or dark bands on a uniform background. This contrast arose because of the small deflections that the electrons suffered as they passed through the specimen. This was due to the action of the Lorentz force upon the electron trajectories, and since then has led to several imaging techniques collectively known as Lorentz electron microscopy. It is the purpose of this chapter to review some of the techniques of electron microscopy required to image both the structural and magnetic properties of thin-film samples. This includes the various modes of Lorentz microscopy and the electron microscopes on which they are implemented.

2.2: ELECTRON MICROSCOPY

Electron microscopy is a large and diverse field with applications ranging from high resolution materials work to studies of biological materials. Correspondingly there are many variants of microscope optimised for the application in mind. In the following discussions there is therefore an emphasis on aspects which are of particular relevance to the study of magnetic materials and Lorentz imaging. The majority of results presented in this thesis have been performed on the Philips CM20 FEG and JEOL 2000 FX transmission electron microscopes (TEMs) at the University of Glasgow.

2.2.1 THE ELECTRON GUN

The source of electrons in an electron microscope is the electron gun which can produce an electron beam with energies ranging from ~40 to ~3000keV. For the majority of studies 200keV is adequate and is standard in most Conventional Transmission Electron Microscopes (CTEMs).

Two basic types of electron gun can be distinguished: the *thermionic* gun and the *field emission* gun. The JEOL 2000 microscope is fitted with such a thermionic gun which has a tungsten hairpin filament as the source of electrons. This is usually held at a high

negative potential and operates at high temperature (2700K) resulting in a large beam current from a few to $\approx 20\text{mA}$ with an energy spread of 3-4eV. A thermionic gun also comprises a Wehnelt which is held at a more negative potential than the filament. This controls the emission from the tip and forms the first crossover of the electron beam. The anode is then positioned below the Wehnelt and accelerates the electron beam. Thermionic tips offer a high brightness (defined as the current density per unit steradian), defined as $1\text{A cm}^{-2}\text{srad}^{-1}$ for a tungsten tip. A LaB_6 tip can also be used, this provides a slightly higher brightness (≈ 20) at the expense of the beam current.

The Philips CM20 electron microscope is fitted with a thermal Field Emission Gun (FEG) which is a Schottky emitter. This comprises a sharp tungsten needle which has an oxide coating, frequently zirconia (ZrO_2). The coating enhances electron emission by lowering the work function of the tungsten and makes possible the use of a broader tip. Although the FEG requires a different gun design than for thermionic guns the advantages are a smaller energy spread of the electrons (0.6-1.2eV), a much smaller source size (6nm virtual source size), vastly improved brightness (≥ 1000 times that of a tungsten filament) and a higher degree of coherence. These improvements are important factors for Lorentz imaging where it is important that the source is not only small and bright but also that the angle subtended by it is sufficiently less than the Lorentz deflection angle. Also applications such as coherent Foucault imaging^[4] and electron holography^[5,6] require a high level of coherence.

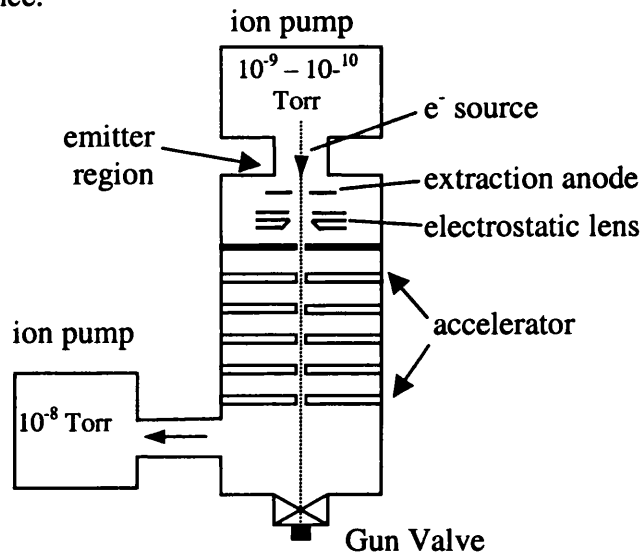


Figure 2.1: A schematic of the gun design used in the Philips CM20 FEG.

The gun design used in the Philips CM20 is shown schematically in figure 2.1. The emitter region is pumped by an ion-getter pump which achieves a vacuum of 10^{-9} to 10^{-10} Torr. The gun, which is optimised for high beam current and stability, contains the field emitter source, an extraction anode and an electrostatic gun lens. The extraction anode provides the extraction voltage in the range 1.0 to ≈ 6.0 keV that controls electron emission from the tip from a few μA to $\sim 250\mu\text{A}$. However to maintain tip lifetime, the extraction voltage is normally set to provide electron emission of $\approx 100\mu\text{A}$. The 3-stage electrostatic gun lens focusses the electron beam to its initial crossover and provides an initial acceleration of the beam to around 40 keV. Several accelerator anodes then increase the electron energies up to 200 keV in the CM20 electron microscope. The accelerator region is separately pumped from the emitter region by another ion pump which achieves a vacuum of $\sim 10^{-8}$ Torr in the accelerator. This separation of source and accelerator prevents small bursts of gas disturbing the electron emission. This type of gun configuration^[7] provides very low chromatic aberration (see later) and produces a very coherent beam of electrons with high brightness from a small virtual source size.

2.2.2 THE MICROSCOPE COLUMN

The microscope column encapsulates the electron beam from the gun to the viewing screen as shown in figure 2.2 for the Philips CM20 electron microscope. All of the lenses in the electron microscopes are electromagnetic (with the exception of the electrostatic gun lens) and they act to either converge or diverge the electron beam. Their operation is, however, markedly different to light lenses but the principles of light optics can be applied.

The condenser lenses are the first to affect the electron beam once it has exited the gun assembly and in most modern CTEM's there are two condenser lenses. The first acts to demagnify the electron source, i.e. it determines the electron spot size at the specimen. The second condenser lens determines how strongly the electron beam is projected onto the specimen, thus it changes the angular convergence of the beam. Next is the beam defining condenser aperture which also controls the beam convergence. Since it is at the top of the column its alignment is crucial to the quality of electron probe formed. Several aperture sizes are available in the range 30 to $200\mu\text{m}$ with a smaller aperture producing an electron beam with higher coherence and smaller convergence angle.

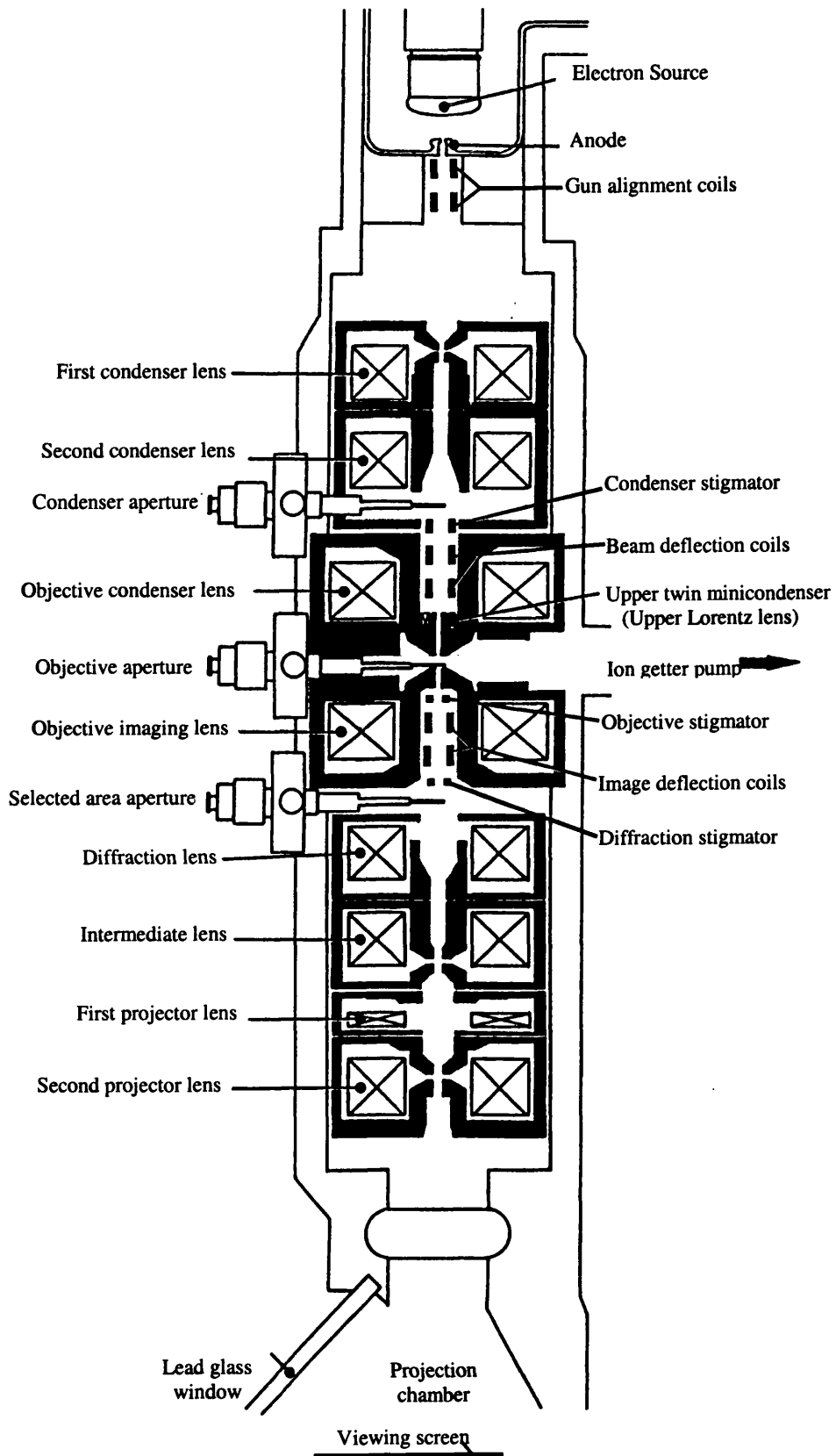


Figure 2.2: Diagram of the electron microscope column the Philips CM20 FEG.

The main imaging lens in most microscopes is the objective lens and thus it determines the overall resolution and performance of the instrument. For these reasons aberrations in the objective lens are of critical importance. The specimen is normally positioned at the centre of the objective lens and a magnified image (~20 to 50x) is produced. In the case of magnetic lenses a large magnetic field (0.5 to 1.5T) exists in this region in order to focus the electron beam. When imaging magnetic materials this field severely perturbs or destroys any magnetic information which is to be studied. To overcome this problem highly modified objective lenses have been used. In the JEOL 2000 FX electron microscope a split pole-piece lens^[8] is fitted which creates a field free region around the specimen. In the case of the Philips CM20 electron microscope a split condenser-objective lens incorporating additional minicondenser lenses^[9,10] is used. This is shown schematically in figure 2.3. When magnetic materials are to be studied the main objective lens can be switched off and the imaging role of the objective lens is replicated by minicondenser lenses (known as upper and lower Lorentz lenses). These enable the specimen to be imaged in nearly field free space. This lens design has several advantages namely that the objective lens can be weakly excited at the control of the operator and controllable amounts of magnetic field induced in the plane of the sample by simply tilting the specimen rod. The gap in between the objective lens pole-pieces has also been widened to 20mm in this microscope which allows for a micromagnetic “laboratory” around the specimen, allowing a magnetising stage or specialised specimen rods to be used (for example heating, cooling or x-ray investigations may be undertaken). The Lorentz lenses achieve field free magnetic imaging with a point resolution of 2.1nm, or a line resolution of 1.3nm. The objective aperture is located just above the lower objective lens pole-piece. Its role is to produce diffraction contrast or to enable the Foucault imaging mode (see section 2.6).

The remainder of the lenses in the microscope (diffraction, intermediate and projector lenses) are normally used to produce further magnification of the image or to project it onto the various detectors. Note that the diffraction lens can play other roles, for example in the case of low magnification mode it is the principal imaging lens or it can be used to produce diffraction patterns, see section 2.3.1. Finally the selected area aperture which is located just above the diffraction lens is used to generate diffraction patterns from selected areas of the sample. Under normal microscope operation the entire column (excluding the lens coils) is held at a pressure of around 10^{-7} Torr by an ion getter pump.

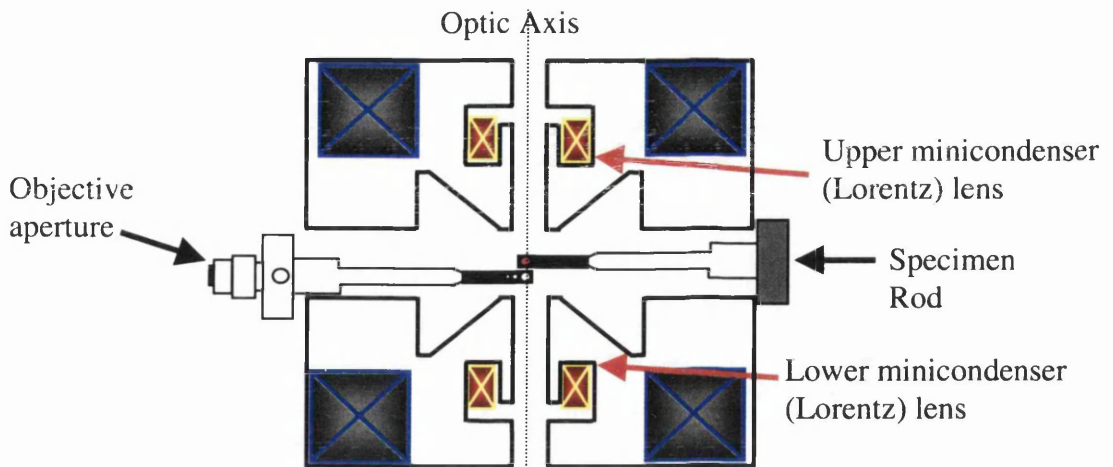


Figure 2.3: Schematic of modified objective lens system in the Philips CM20. Additional “Lorentz” lenses are highlighted.

2.2.3 IMAGE ACQUISITION

Images can be collected from the microscope in a number of ways. In this project either photographic film or a CCD camera have been used. The photographic plates are CEA Reflex-15 and while they offer a high resolution they are both time consuming to prepare and develop. The Philips CM20 electron microscope is fitted with a Gatan 690 high performance, slow scan CCD camera which has a high sensitivity, and produces high resolution images. The main advantage of using the CCD camera is that it is possible to capture high quality images that are immediately available for viewing with on-line computer processing and analysis.

2.2.4 ABBERATIONS IN A CTEM

There are aberrations in a CTEM which limit the attainable resolution of the microscope in various ways. The aberrations of the objective lens are by far the most important^[11] as this is usually the most powerful imaging lens. Although eight third order aberrations have been listed for a magnetic lens^[12] we will only be concerned with spherical aberrations, astigmatism and chromatic aberration.

Spherical aberration is the principal defect in the objective lens and at present there is no convenient way of correcting it. Figure 2.4 shows how electrons leaving a point P on

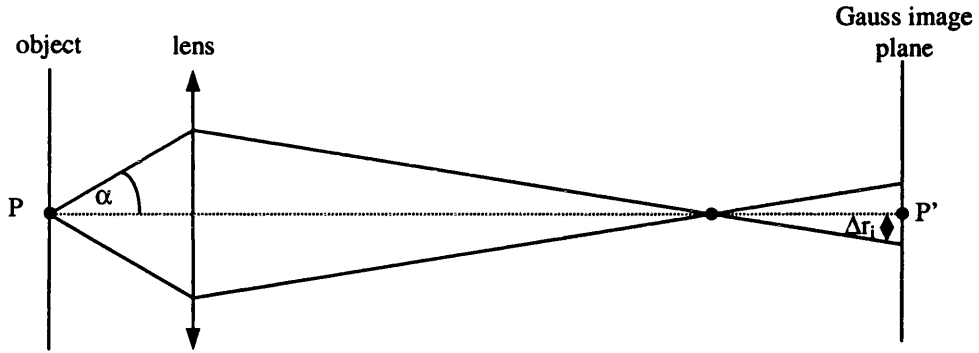


Figure 2.4: Illustration of spherical aberration.

the object at an angle α to the axis arrive at the Gaussian image plane at a distance $\Delta r_i = MC_s \alpha^3$ away from the Gauss image point P' . A pencil of semi-angle α thus gives rise to a disk of confusion of radius Δr_i in the image plane. The off axis ray is always bent more than it should be and marginal rays are always brought to a focus closer to the lens than axial rays. Referred back to the object, the corresponding disk of least confusion is of radius

$$\Delta r_s = \frac{1}{4} C_s \alpha^3 \quad 2.1$$

where C_s is the spherical aberration coefficient of the lens (always >0 for a round magnetic lens) and $\approx 6.5\text{mm}$ for the CM20 objective lens with 20mm gap.

Astigmatism is caused by defects in the pole piece of the lens which result in an asymmetrical lens field. This effectively leads to different focal lengths for paraxial rays but can be corrected for by the use of a stigmator. This device, which can be either an electrostatic or magnetic slug type, works by introducing astigmatism which is equal and opposite to that created by the magnetic lens. This can result in near cancellation of the lens astigmatism and allows a higher resolution to be obtained. The CM20 has various stigmators for its various lenses, figure 2.2.

Chromatic aberration is a consequence of the focal length of a magnetic lens being dependent on the energy of the electrons. Any spread in the energy, caused by either instabilities in the beam voltage or from the specimen itself results in a blurring of the image. Effectively electrons which have lost energy are bent more by the magnetic lens field. This also results in a disc of confusion, which is given by,

$$\Delta r_c = C_c \alpha \frac{\Delta E}{E}$$

2.2

where ΔE is the energy spread and C_c is the chromatic aberration constant.

2.3 IMAGING OF STRUCTURAL PROPERTIES IN THE CTEM

This section outlines some of the normal operational modes of the CTEM which can be used to investigate the microstructural properties of thin films.

2.3.1 DIFFRACTION PATTERNS

When the electron beam strikes the specimen a number of complex scattering processes can occur including Bragg scattering from crystallographic planes. Many of the scattered electrons which pass through the object then enter the objective lens and are subsequently focussed by its magnetic field. The ray diagram of figure 2.5 pertains to a crystalline specimen and shows coherent Bragg diffracted beams leaving the sample.

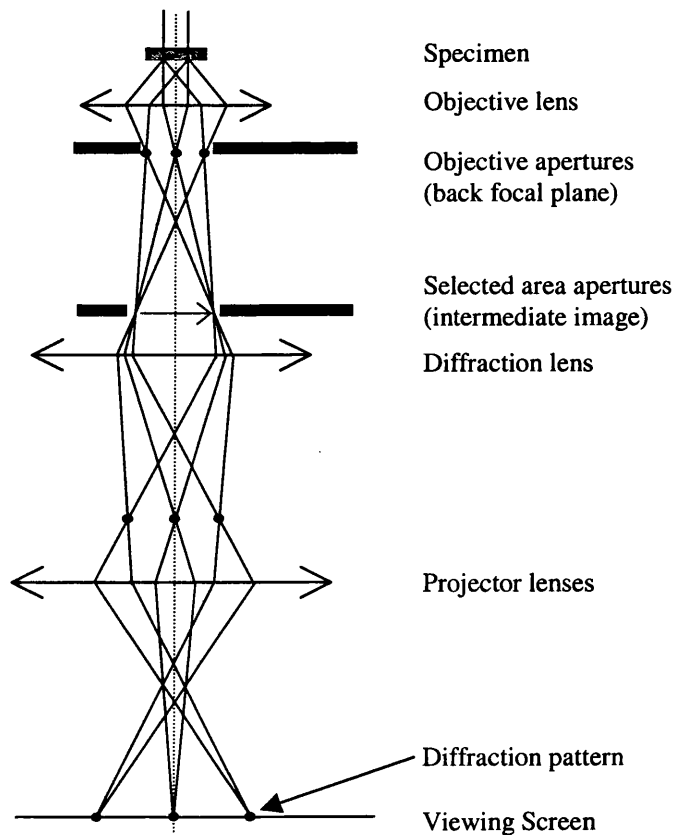


Figure 2.5: Schematic ray diagram showing conditions for imaging diffraction patterns

If the incident beam is parallel then the diffracted beams are brought to a focus in the back focal plane of the objective lens and this is where the diffraction pattern is first formed. In order to image the diffraction pattern the back focal plane of the objective lens must be imaged onto the viewing screen. This is achieved by running the diffraction lens at a reduced excitation with the intermediate and projector lenses providing necessary magnification. It is also possible to generate diffraction patterns from selected areas of the specimen, a technique which is known as selected area diffraction (SA diffraction). This is achieved by inserting an SA aperture just above the diffraction lens which is the position of the intermediate image formed by the objective lens. The aperture restricts the area observed and allows diffraction features on a fine scale (down to $\sim 1\mu\text{m}$) to be observed.

2.3.2 BRIGHT AND DARK FIELD IMAGING

A series of interchangeable objective apertures varying in size from $50\mu\text{m}$ to $200\mu\text{m}$ are placed close to the back focal plane of the objective lens and play an important role when imaging structural contrast. The ray diagram of figure 2.6a shows an objective aperture placed to intercept all the diffracted beams and allows only the direct or undeviated beam to pass through. This is a mode of deficiency contrast known as bright field imaging in which contrast in the image is produced by differences in the intensities of electrons scattered coherently from various parts of the specimen. Note that the insertion of the aperture also reduces spherical aberration.

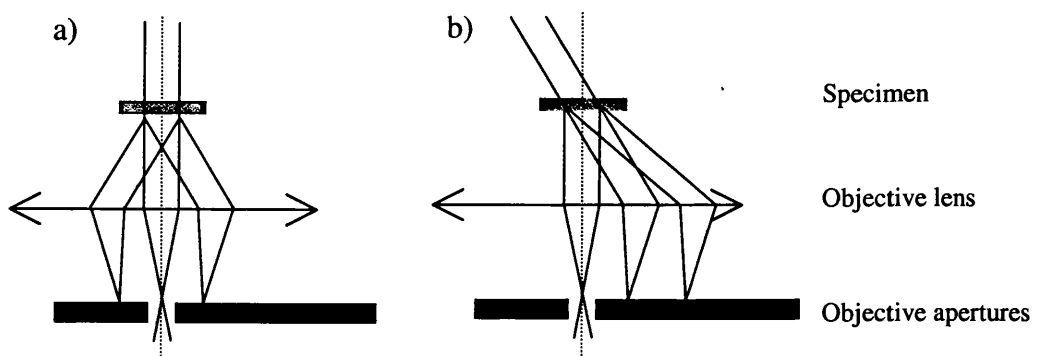


Figure 2.6: a) Schematic diagram for bright field imaging and b) dark field imaging.

It is also possible to isolate a single chosen diffracted beam rather than the undeviated beam - a technique which is known as dark field imaging. This can be done by displacing the objective aperture to intercept the desired beam, but this introduces astigmatism into

Consider figure 2.7a which shows a cross sectional schematic of a thin ferromagnetic film containing 3 domains separated by two domain walls. The directions of magnetisation are in the plane of the specimen as indicated. A parallel electron beam, incident perpendicular to the plane of the film along the z-axis, experiences a Lorentz deflection in the x-direction through an angle β_L , given by

$$\beta_L(x) = \frac{e\lambda}{h} \int_{-\infty}^{\infty} B_y(x,z) dz \quad 2.3$$

where $B_y(x,z)$ is the y-component of magnetic induction at point (x,z) , e is the electronic charge, λ the electron wavelength and h is Planck's constant. Assuming that the film is of a uniform thickness t , and that there is no stray field emanating from the film, then equation 2.3 becomes,

$$\beta_L = \frac{eB_0\lambda t}{h} \quad 2.4$$

where B_0 is the saturation induction ($B_0 = \mu_0 M_s$). For example, for 200kV electrons with $\lambda = 2.508 \text{ pm}$ passing through a 8nm thick film with saturation induction of 1.08T gives $\beta \approx 5 \times 10^{-6}$ rad. This is much smaller than a typical Bragg angle of $\sim 5 \times 10^{-3}$ rad.

A quantum mechanical description of the electron specimen interaction has also been provided^[14]. This is necessary where quantitative analysis is required or when interference effects must be considered. This showed that the effect of the magnetic induction is to introduce a phase shift between two electron rays originating from the original point which rejoin after travelling different equidistant paths. The phase shift generated by two electrons enclosing a magnetic flux N is given by

$$\varphi = \frac{2\pi eN}{h} \quad 2.5$$

where all other symbols are as before. In the case of a plane wave incident on a specimen such as in figure 2.7 the phase shift between any two points x_1 and x_2 along the x-axis is given by

$$\Delta\varphi(x) = \frac{2\pi e t}{h} \int_{x_1}^{x_2} B_y(x) dx \quad 2.6$$

Thus ferromagnetic specimens act as pure phase objects to the electron beam and Lorentz microscopy is a branch of phase contrast electron microscopy.

2.5 FRESNEL IMAGING

The Fresnel mode of Lorentz electron microscopy involves defocusing the imaging lens to produce magnetic contrast. This reveals domain walls as either bright or dark bands on a uniform background. Considering figure 2.7a again, it can be seen that the two domains with magnetisation out of the plane of the page deflect the electron beam to the right by equal amounts β_L . On the other hand the domain whose magnetisation lies into the plane of the page deflects the electron beam in the opposite direction to the left by β_L . If the imaging lens is slightly defocused by amount $\pm\Delta z$ then the imaging plane is no longer coincident with the specimen plane and the effect of the magnetisation is to produce either a convergent or divergent electron wave in the region around the domain wall. The domain walls are then imaged as either narrow bright or dark bands whose contrast is highly dependent on the value of defocus. The magnetic contrast produced by the domain configuration in figure 2.7a by an over-focused imaging lens is shown schematically in figure 2.7b. If the imaging lens were to be under-focused by $+\Delta z$ then the magnetic contrast would be inverted. If the electron source is sufficiently coherent then interference fringes may be observed due to the interference effects of the convergent electron wavefront. Magnetisation ripple can also be observed in Fresnel imaging mode, and assuming that the direction of the magnetisation ripple is orthogonal to the local magnetisation direction allows a qualitative investigation of the domain structures to be made.

The advantages of the Fresnel mode are the ease with which it can be implemented and the high contrast which arises from domain walls. However, the fact that the imaging lens must be defocused results in a poor resolution and non-linearity makes it difficult to

deduce quantitative information. It is also difficult to relate magnetic information directly to topographic features. Figure 2.8 shows an example of a Fresnel image in which areas with oppositely oriented magnetisation are separated by domain walls that are shown as either bright or dark bands. Magnetisation ripple can also be seen.

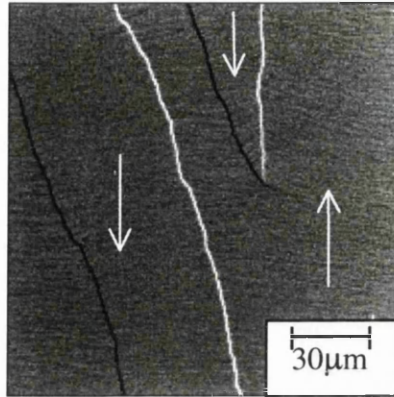


Figure 2.8: Fresnel image showing domain wall contrast and approximate directions of magnetisation.

2.6 FOUCAULT IMAGING

Foucault imaging is also a standard Lorentz imaging mode and often used to complement Fresnel imaging. It was not however, used to collect images during the experimental chapters of this thesis but is described at this point. Foucault imaging is an in-focus technique and magnetic contrast is generated by inserting an opaque aperture close to the back focal plane of the objective lens as shown in figure 2.9a. As it is at this position that the diffraction pattern is first formed, all electrons deflected by a given magnetisation direction come to a focus at a point in this plane. The aperture therefore removes electrons, deflected by the Lorentz force, from a certain range of magnetisation orientations. This produces contrast relating to the direction of magnetisation in different domains. The position of the aperture can be manipulated in order to “map” in different directions and it is normal practice to collect two images with orthogonal mapping directions. This technique is also relatively simple to implement and it provides higher resolution than Fresnel imaging. However, variations in the contrast that arise from small movements in the objective aperture make it ill suited for quantitative studies.

2.7 LOW ANGLE DIFFRACTION

As noted in the previous section relating to Foucault imaging, all electrons deflected by a given magnetisation direction are brought to a focus at the same position close to the back focal plane of the imaging lens. In Low Angle Diffraction mode (LAD) the configuration of the post specimen lenses are changed so that this plane is projected onto the viewing screen (similar to viewing a diffraction pattern, section 2.3.1). This is of interest for magnetic studies when the central spot which is unscattered by Bragg deflections is considered.

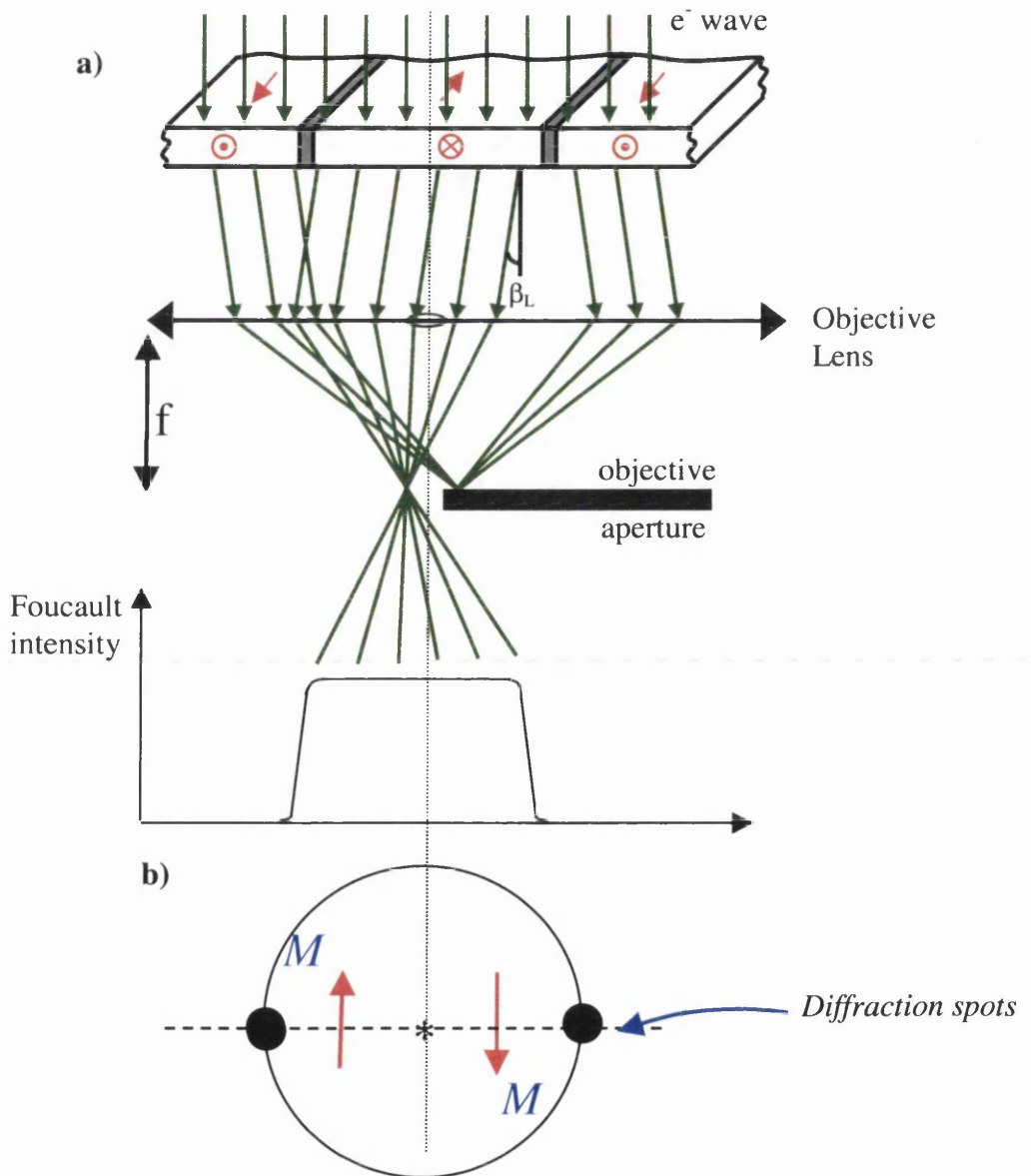


Figure 2.9: a) Schematic diagram of Foucault mode and b) corresponding LAD pattern that would be formed with the objective aperture removed.

When the specimen is in a multi-domain state the central spot is split into several sub-spots with each spot corresponding to a different direction of magnetisation in the sample. The intensity of the individual spots is indicative of the relative fraction of the illuminated area of sample with the given magnetisation orientation. Figure 2.9b shows the corresponding low angle diffraction pattern for the domain configuration shown in figure 2.9a with the objective aperture removed and at a high camera length. In a multi-domain state the diffraction spot is split; lines from the centre to the spot representing a vector that is perpendicular to the magnetisation giving rise to the deflection. The centre of the circle represents the position which the electron beam would occupy in a specimen with no magnetic layer present. However, the magnetisation within a given domain deflects the electron beam by the Lorentz force; the locus of possible end points is a circle. The deflection angle is determined by the saturation magnetisation of the free layer and its thickness. The size of the circle is determined by the camera length used to magnify the diffraction pattern.

2.8 THE APPLICATION OF MAGNETIC FIELDS IN-SITU

In order to investigate the magnetic properties of thin film magnetic materials it is desirable to apply variable magnetic fields to a range of samples of interest whilst imaging the specimen. In the JEOL 2000 FX electron microscope this has been achieved by the use of a specialised magnetisation stage as shown in figure 2.10. The sample is mounted onto a stub between the two coils and can be rotated so that the fields are applied at variable angles^[15]. The magnetic field is generated by passing a DC current through the coils with the resultant fields in the range -120Oe to $+120\text{Oe}$ in the plane of the specimen.

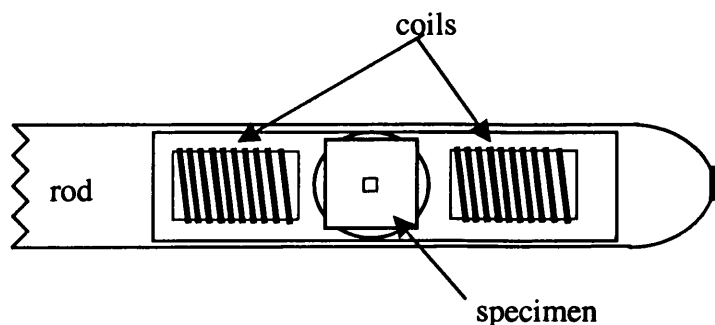


Figure 2.10: Schematic of magnetising stage in the JEOL 2000 FX TEM

The field introduces a DC tilt of the electron beam which must be corrected for by using the electrical beam tilts within the microscope.

In the Philips CM20 electron microscope the application of magnetic fields is achieved by using the objective lens of the microscope. As already discussed, the Lorentz lenses can be used as the imaging lenses, with the objective lens switched off. However, it is also possible to weakly excite the objective lens and provide a vertical field in the specimen region. Tilting of the sample rod then results in a controllable component of this field in the plane of the specimen. This technique has advantages in that no DC deflection of the electron beam is produced as the sample is tilted and also that higher fields may be applied (up to 6.3kOe vertical field) than in the magnetising stage^[15,16].

REFERENCES

- [1] Bitter F, (1931) *Phys. Rev.*, **38**, 1903.
- [2] Grutter P et al, (1998), *J. Vac. Sci. Technol. A* **6(2)**, 279.
- [3] Hale M E et al, (1959) *J. Appl. Phys.*, **30**, 789.
- [4] Chapman J N et al, (1994) *IEEE Trans. Mag.*, **30**, No. 6.
- [5] Tonomura A, (1987), *Rev. Mod. Phys.*, **59**, No.3.
- [6] Cowley J M, (1992) *Ultramicroscopy*, **41**, 335.
- [7] Mull P M et al, (1990) *ICEM* **12**, 100.
- [8] Tsuno K et al, (1983) *J. Appl. Phys.*, **22**, 1047.
- [9] Mast K et al, (1980) *Electron Microscopy (The Hague)*, **1**, 72.
- [10] Hagemann P et al, (1987), *Philips Electronic Instruments, Mahwah, New Jersey*, 33.
- [11] Hirsch et al, (1965), "Electron microscopy of thin crystals", pubs. Butterworths.
- [12] Hall C E, (1953), "Introduction to electron microscopy", McGraw-Hill.
- [13] Chapman J N, (1984), *J. Phys. D, Appl. Phys.*, **17**, 623.
- [14] Hefferman S J et al, (1991), *J. Mag. Mag. Mat.*, **95**, 76.
- [15] Chapman J N et al, (1995), *Proceedings of the 2nd International symposium on advanced materials*.
- [16] McVitie S et al, (1995), *Mag. Mag. Mat.*, **148**,

CHAPTER 3: STUDY OF THE FREE LAYER REVERSAL MECHANISM OF FeMn-BIASED SPIN-VALVES.

3.1 INTRODUCTION

In this chapter the magnetic properties of the “free” layer in a range of FeMn-biased spin-valves with various anisotropy arrangements are presented. Free layer reversals have been studied as a function of applied field strength and orientation on samples that have a range of interlayer coupling strengths h_j . The samples were deposited by dc magnetron sputtering onto substrates that allowed direct observation by transmission electron microscopy. This allows the structural properties of the spin-valves to be investigated. Bright and dark field images as well as diffraction patterns are recorded and examples are presented in this chapter. Domain observations are made using the Fresnel imaging mode, whilst low angle diffraction (LAD) has been used to provide a description of the level of dispersion present during the reversals. The principal motivation for this study is to understand in detail the range of reversal mechanisms which can occur in the free layer of spin-valves. This is interesting from a fundamental point of view but is also necessary as the free layer reversal mechanism plays a role in the overall performance and noise characteristics of devices based upon spin valves.

3.2 REVIEW OF SPIN VALVES

Although spin-valves were discussed in section 1.6 it is worth reviewing a few more fundamental points before presenting the main body of the experimental results. The configuration of a typical standard spin-valve is shown schematically in figure 1.9, and basically consists of two ferromagnetic layers (usually permalloy) separated by a copper spacer. The thickness of the copper is chosen such that a weak ferromagnetic coupling exists between the two ferromagnets^[1]; this causes parallel alignment between the two layers in zero applied field. If the copper layer is insufficiently thick (<2-3nm) then direct exchange coupling results and the “free” layer becomes strongly coupled to the pinned layer. On the other hand, if the Cu layer is too thick then the strength of the interlayer

coupling decreases and the GMR ratio of the spin-valve also depreciates due to additional shunting of the sense current through the conducting Cu layer. It is possible to define a preferred orientation of the magnetisation at zero applied field by depositing (or annealing) the spin-valve in the presence of an applied field sufficient to saturate the ferromagnetic layers (<150 Oe). This is known as an uniaxial induced anisotropy, and in the absence of other anisotropy effects such as magnetocrystalline or magnetostriction-induced anisotropy is coincident with the easy axis. It is caused by preferential pair ordering of the magnetic spins in an otherwise unordered alloy during the deposition or an anneal^[2]. If both ferromagnetic layers have the same directions of easy magnetisation then the spin-valve is said to be in a parallel anisotropy arrangement. The presence of the magnetic field also has the effect of defining the biasing direction which is the direction of magnetisation brought about by exchange coupling between the biasing layer and adjacent “pinned” ferromagnetic layer. Alternatively a “crossed” anisotropy configuration of the magnetic layers can be obtained by either i) rotating the magnetic field before deposition of the second magnetic layer or ii) raising the antiferromagnetic pinning layer through its Néel temperature (≈ 150 - 160° for FeMn) and subsequently cooling in the presence of a magnetic field. A “crossed” anisotropy arrangement is obtained when the free and pinned magnetic easy directions are 90° misaligned.

For sensor applications the free layer is ideally magnetically soft, and can typically be reversed by the application of a field of around 5-15Oe. When the applied field is along the easy axis of a spin-valve this corresponds to the reversal between parallel (low resistance) and antiparallel (high resistance) states, which corresponds to the transition between ‘a’ and ‘b’ in figure 1.10.

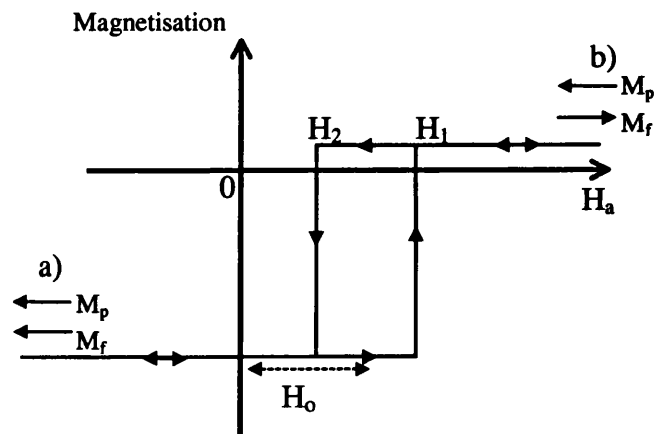


Figure 3.1: Schematic magnetisation loop of a spin-valve free layer easy axis reversal.

This transition is shown in more detail in the schematic magnetisation loop, figure 3.1, in which a free layer easy axis reversal of a spin-valve with parallel anisotropy is depicted. With the biasing direction and thus the weak ferromagnetic coupling along the –ve x-axis, parallel alignment of the free and pinned layer magnetisation is observed at 0 applied field H_a . As H_a is increased the magnetisation in the two ferromagnetic layers remains parallel until the weak coupling is overcome at H_1 , resulting in antiparallel alignment between the two layers. Upon decrease of H_a , antiparallel alignment is observed until the field is decreased to H_2 where a transition to parallel alignment is once again achieved. This is the field at which H_a is no longer sufficient to overcome the weak ferromagnetic coupling. The average of the two switching fields H_1 and H_2 results in an offset field H_0 of the free layer magnetisation loop along the +ve x-axis as indicated.

For spin-valves to operate efficiently in a magnetoresistive read-head or sensor it is undesirable to have a free layer characteristic such as is described above. The response characteristic is non-linear and free layer reversals for the above configuration have been seen to be facilitated by the sweeping of domain walls through the free layer which is also known to be a source of Barkhausen noise^[3,4]. For reliable device applications one wishes to operate the spin-valve such that the response is linear and anhysteretic, and one may wish to employ an alternative anisotropy arrangement or applied field direction.

The purpose of this chapter is to investigate possible free layer reversal mechanisms as a function of the angle of applied field θ with respect to the biasing direction H_b in a range of spin-valves. The in-plane magnetisation vectors are shown schematically in figure 3.2, where application of H_a at an angle θ to the H_b results in the free layer magnetisation, m , lying at some equilibrium direction ϕ to H_b .

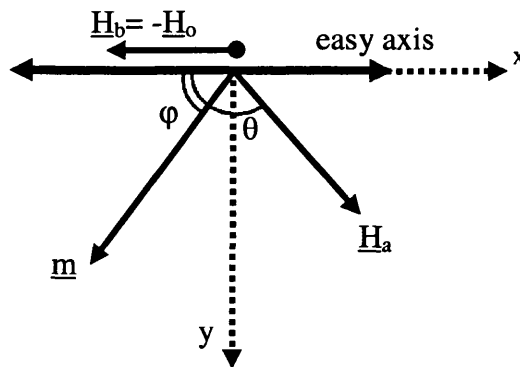


Figure 3.2: Orientation of in-plane magnetisation vectors.

The value of the free layer offset H_0 can be varied in a number of ways. One way is to change the thickness of the Cu spacer, which changes the strength of the weak ferromagnetic coupling. Another method is to use magnetic layers with different anisotropies. In this thesis both methods are used.

3.3 PREVIOUS TEM INVESTIGATIONS

This section briefly introduces some of the previous work on TEM investigations of the magnetic properties of unpatterned spin-valves. Of particular interest is the work by M Gillies et al^[3,5,6]. Magnetisation ripple was observed to be present in both the free and biased layers of FeMn-biased spin-valves, although it was substantially reduced in the case of the biased layer. Easy axis reversals of the free layer in spin-valves were studied, and compared with the reversal of isolated permalloy layers. The most significant result was the large number of 360°walls that formed during the reversal of spin-valve layers. The applied fields required to reverse the free layer were increased when compared to that of isolated layers. This was due to the effect of the interlayer coupling from the spin-valve pinned layer. The pinning mechanism of the biased layer in FeMn and TbCo spin-valves has also been studied. In the case of FeMn, the reversal of the pinned layer proceeds by the nucleation of erratic domain structures which exist on a scale of typically a few microns. In the case of uniaxial TbCo the reversal was observed to be quite different and the phenomenon of magnetisation creep was prominent during the reversal process. The reversals in this case were dominated by domain wall motion and the accompanying domain wall density was low. Continuous crossed anisotropy spin-valves with $h_J > 1$ were studied. The main result was that coherent rotation of the free layer magnetisation could be achieved by off-setting the applied field with the biasing direction by a small angle ($< 4^\circ$). Perfect alignment caused the rotation of adjacent regions of the free layer magnetisation in clockwise and anti-clockwise senses with the formation of 360degree walls between the boundaries.

3.4 SPUTTER DEPOSITION OF SPIN-VALVE MULTILAYERS

The films under investigation were prepared by dc-magnetron sputtering. This is a physical vapour deposition (PVD) technique that is suitable for deposition of almost all metals. It involves the removal of source atoms from a target through bombardment by energetic ions from a dc plasma. The target atoms are ionised and are then attracted towards suitable substrates where the multilayer system is grown. The sputtering gas is Ar^+ with a pressure of around 5mTorr. Concentrating magnets confine the plasma to a small area which results in an intensified bombardment of the target by the Ar^+ atoms. The deposition rate can be controlled by varying the input power to the plasma and the gas pressure affects the surface morphology and microstructural characteristics of the deposited layers. The target to substrate distance is 110mm, and film thicknesses were controlled by computer-controlled shutters in front of the targets. A deposition rate of approximately 0.2nm s^{-1} was used with several cylindrical substrate holders rotating to improve the lateral homogeneity of the sample being grown. By exposing the substrates to different sources in turn it is possible to subsequently deposit different layered thin-films such as spin-valves. Permanent magnets with a magnetic field of $\approx 150\text{Oe}$ were mounted onto the substrate holders so that the samples were exposed to a magnetic field during deposition, this induced a uniaxial anisotropy in the ferromagnetic layers and was also used to define the exchange anisotropy direction in the exchange-biased layers (the biasing direction). Note also that the background pressure of the entire system was 10^{-8} to 10^{-9} Torr, and is such that there is very little contamination of the films by residual gas atoms (e.g. N, O, and H).

The samples which are studied in this thesis have been deposited onto supported Si_3N_4 membranes that can be used in the transmission electron microscope^[7]. Cross-sectional and planar views of such substrates are shown in figure 3.3(a,b) respectively. The substrates are made by first depositing a Si_3N_4 layer (variable thicknesses which can be chosen to be in the range 10-100nm) onto a Si substrate. Then, by using a lithographically defined mask, etching is done in the $\langle 111 \rangle$ direction at sites which are $\approx 2000\mu\text{m}$ apart. This gives a matrix of pyramidal holes over the substrate which are still covered by Si_3N_4 . The films can then be deposited on top of this and the substrate can be broken into single windows which are immediately suitable for investigation in the transmission electron microscope.

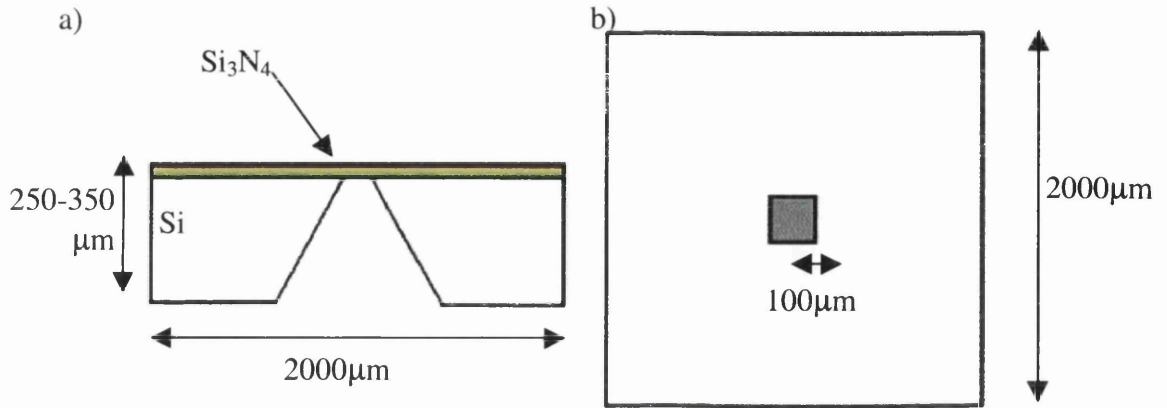


Figure 3.3: Schematic diagram of a) cross-section and b) planar view of TEM substrate.

3.5 STRUCTURAL PROPERTIES

Before the magnetic properties of the spin-valves are presented, it is worth investigating the structural properties. The structural properties of a reference layer of 3.5nm Ta / 8.0nm Ni₈₀Fe₂₀ / 1.5nm Cu / 3.5nm Ta and 3 spin-valves with configurations: 3.5nm Ta / 8.0nm Ni₈₀Fe₂₀ / t_{Cu} / 6.0nm Ni₈₀Fe₂₀ / 10.0nm Fe₅₀Mn₅₀ / 3.5nm Ta are presented.

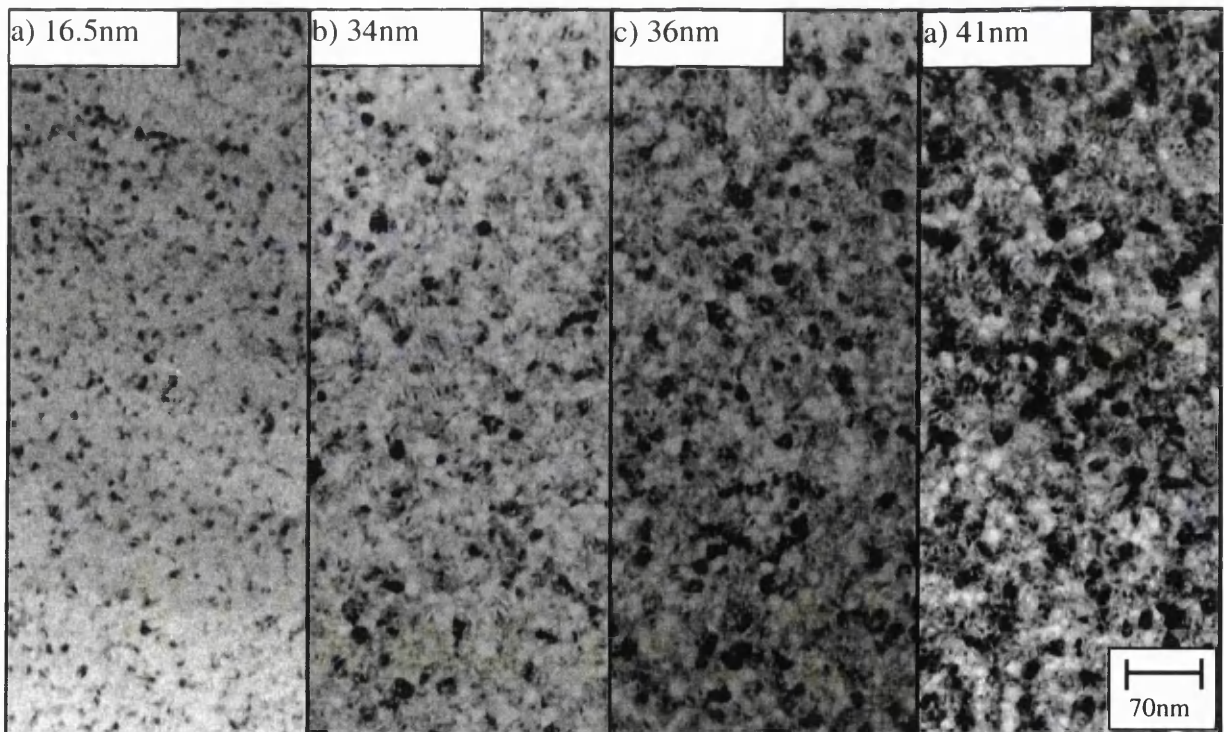


Figure 3.4: Images of crystallites in a) a single Ni₈₀Fe₂₀ layer and (b-d) Ni₈₀Fe₂₀ spin-valves with increasing Cu thickness. The total sample thicknesses are indicated.

These were taken in the JEOL 2000FX TEM. The thickness of copper is given by t_{Cu} which is in the range 2-10nm, the reason for which is discussed in more detail in section 3.6.

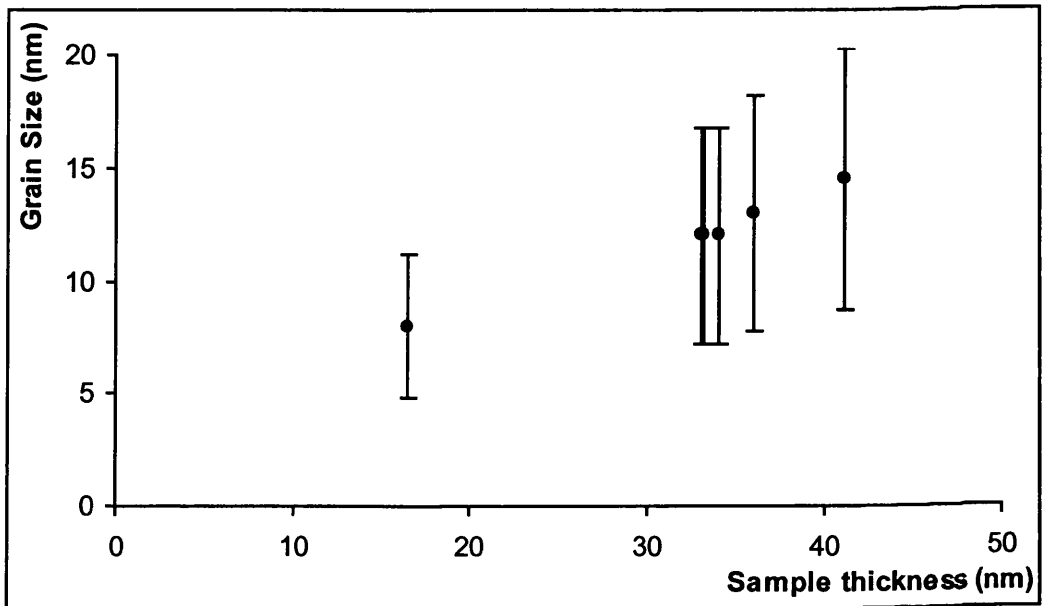


Figure 3.5: Variation in grain size with increasing sample thickness.

These Cu thicknesses result in total sample thicknesses in the range 33-41nm for the spin-valves. Bright field images of the crystallites are shown in figure 3.4(a-d). The grain size is estimated by randomly measuring a large number of grains (>40) from the electron micrographs and calculating the average and standard deviation for each sample. The smallest grains that are observed are of the order of 3 ± 1 nm in size, and one can usually observe some of these in all films. As the thickness of the films increases, the average size and spread in the grain size increases, see figures 3.4 & 3.5. In the cases of the thickest samples some comparatively large grains can be observed (≈ 25 nm diameter). Closer inspection reveals that these often tend to comprise several smaller grains of $\approx 10-12$ nm in diameter closely clustered together, see figure 3.4(d). It is likely that the largest grains observed are due to several smaller grains that have coalesced into one during deposition of the thicker samples. From the samples studied here, it is estimated that this upper limit to the grain size is < 20 nm, and likely to be in the range 10-15nm.

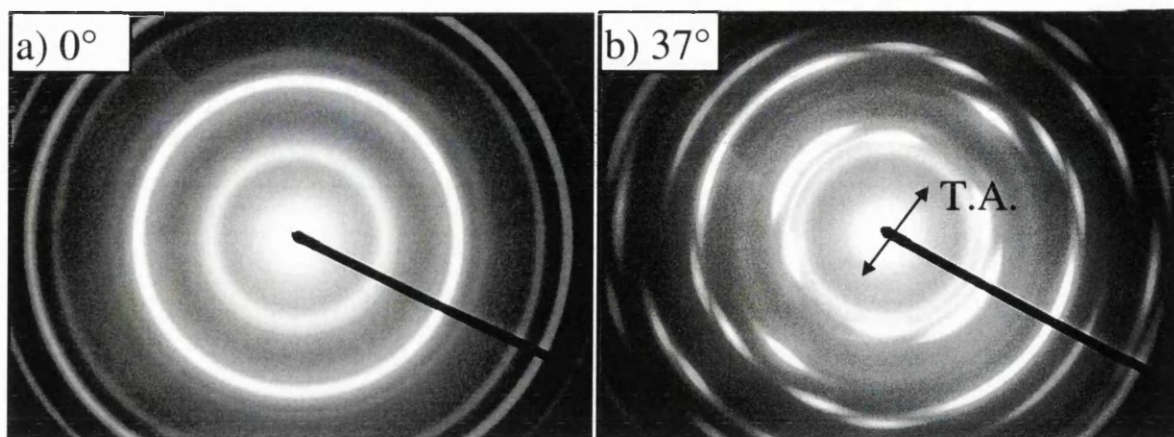


Figure 3.6: Electron diffraction patterns from a $\text{Ni}_{80}\text{Fe}_{20}$ spin-valve with $t_{\text{Cu}} = 5.0$ nm. (a) 0° tilt, (b) 37° tilt, with tilt axis (T.A.) shown.

In order that the crystalline film properties and level of texture could be evaluated, electron diffraction patterns were also recorded. Figure 3.6(a) shows a typical diffraction pattern with the sample at 0° tilt, in which the rings are homogeneous. Figure 3.6(b) shows the tilted specimen diffraction pattern in which additional reflections and considerable texturing can be seen. Indexing of the tilted specimen diffraction pattern, figure 3.7, showed that the Ta ($a=0.330\text{nm}$) buffer and capping layers have a body-centred cubic structure (bcc) and the ferromagnetic layers ($a=0.352\text{nm}$) have face-centred cubic structure (fcc). Further, it can be seen from figures 3.6 and 3.7 that the tantalum was very poorly crystalline and contributed diffuse untextured rings, and that the $\text{Ni}_{80}\text{Fe}_{20}$ layers were highly textured. (The Cu and FeMn rings were unresolved in the pattern but are almost coincident with the $\text{Ni}_{80}\text{Fe}_{20}$ rings.). Upon tilting of the sample it can be seen the (220) ring lies on the tilt axis (T.A.), which is consistent with a $\langle 111 \rangle$ zone axis, figure 3.6(b). This is expected as the Ta seed layer promotes $\langle 111 \rangle$ growth^[8]. The structural results presented here are typical for all of the investigated spin-valves.

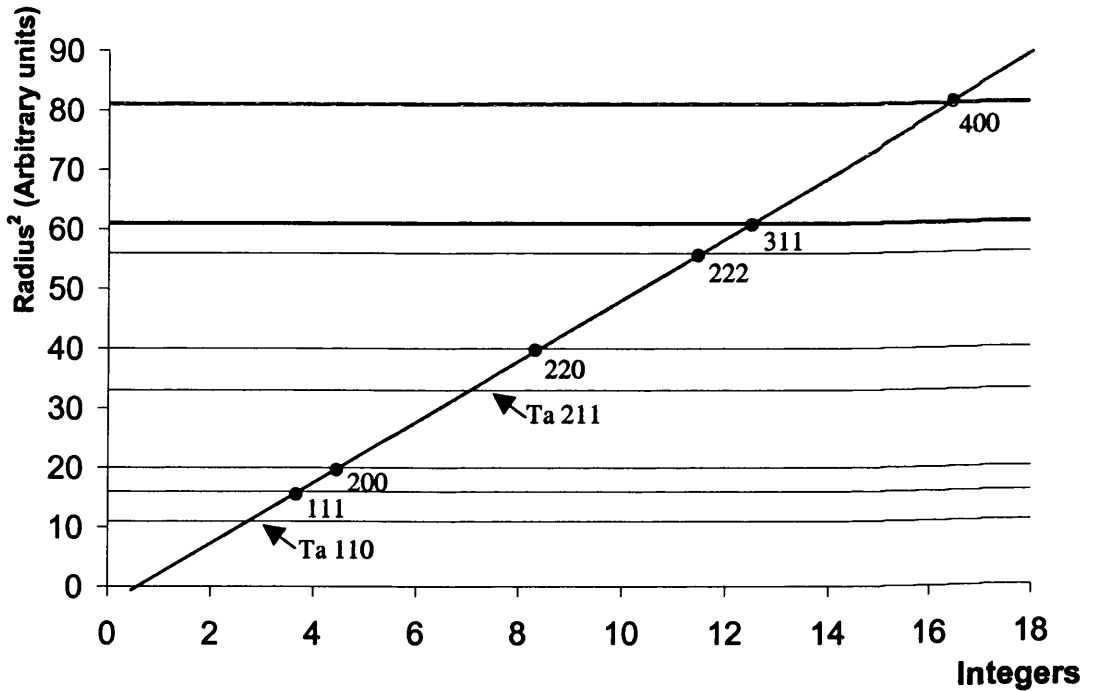


Figure 3.7: Indexed diffraction pattern from a $Ni_{80}Fe_{20}$ spin-valve with $t_{Cu} = 5.0$ nm.

3.6 MAGNETIC PROPERTIES

3.6.1 INTRODUCTION

In this section the magnetic properties of the free layer reversal mechanism in a range of spin-valves is presented. The spin-valves which are studied all have FeMn as the antiferromagnetic biasing material, however the ferromagnetic layers are either $Ni_{80}Fe_{20}$ or $Ni_{66}Fe_{16}Co_{18}$, the latter material is chosen as it lies close to the zero magnetostriction line on the NiFeCo ternary phase diagram^[8-11]. The copper spacer layers have thicknesses, t_{Cu} , in the range 2-10nm which results in interlayer coupling strengths $h_j = H_0/H_k$ in the range 0.15-1.13 (in reduced units). H_0 is the easy axis offset of the free layer hysteresis loop and is determined by taking the average of the two experimental free layer switching fields, H_1 and H_2 , when the applied field is along the easy direction in parallel anisotropy spin-valves, see figure 3.1 and the following section. The interlayer coupling strength h_j is then obtained by normalising by the anisotropy field H_k . ($H_k(Ni_{80}Fe_{20}) \approx 4.6Oe$, $H_k(Ni_{66}Fe_{16}Co_{18}) \approx 19.4Oe$)^[11]. Magnetic fields are applied to these samples at variable angles θ to the biasing direction H_b and the free layer reversals are observed via Lorentz

imaging. Both the JEOL 2000 and Philips CM20 electron microscopes have been used to collect results in this chapter. The CM20 has been used in cases where it was desired to collect both Fresnel images and low angle diffraction (LAD) data.

3.6.2 EASY AXIS REVERSALS AND h_J .

In order to fully understand the free layer reversal mechanisms it is first necessary to observe easy axis reversals. This primarily enables the interlayer coupling, h_J , to be determined but also provides standard initial experimental conditions for the different spin-valves from which comparisons can be made. Figure 3.8(a-e) shows an easy axis reversal ($\theta=180^\circ$) for a $\text{Ni}_{80}\text{Fe}_{20}$ spin-valve with $t_{\text{Cu}}=3.0\text{nm}$. In the zero field state the free layer magnetisation is coincident with H_b and two 360° loops can be seen to be present in the free layer, figure 3.8(a). Apart from these, the remainder of viewable area remains single domain. A faint ripple contrast can be seen in the Fresnel images which arises from local fluctuations in the magnetisation direction. It is orthogonal to the average direction of magnetisation within a domain and enables directions of magnetisation to be deduced throughout the reversal process. As the applied field H_a is increased a slight increase in the magnetisation ripple contrast is observed before domains are formed at $H_a=H_1=7.1\text{Oe}$, figure 3.8(b). The domain walls that are observed rapidly sweep through the free layer facilitating the growth of domains whose magnetisation is coincident with H_a . Once the domain walls have swept across the area of view the majority of the free layer magnetisation is coincident with H_a , and few changes in the magnetic structure are observed as H_a is increased beyond that necessary to reverse the majority of the free layer. This process corresponds to the reversal from parallel to antiparallel alignment of the free and pinned layer magnetisations. Upon decrease of H_a broadly similar processes are observed. An initial increase in the magnetisation ripple is observed before domains are formed whose walls sweep rapidly through the free layer at $H_a=H_2=3.4\text{Oe}$, figure 3.8(d).

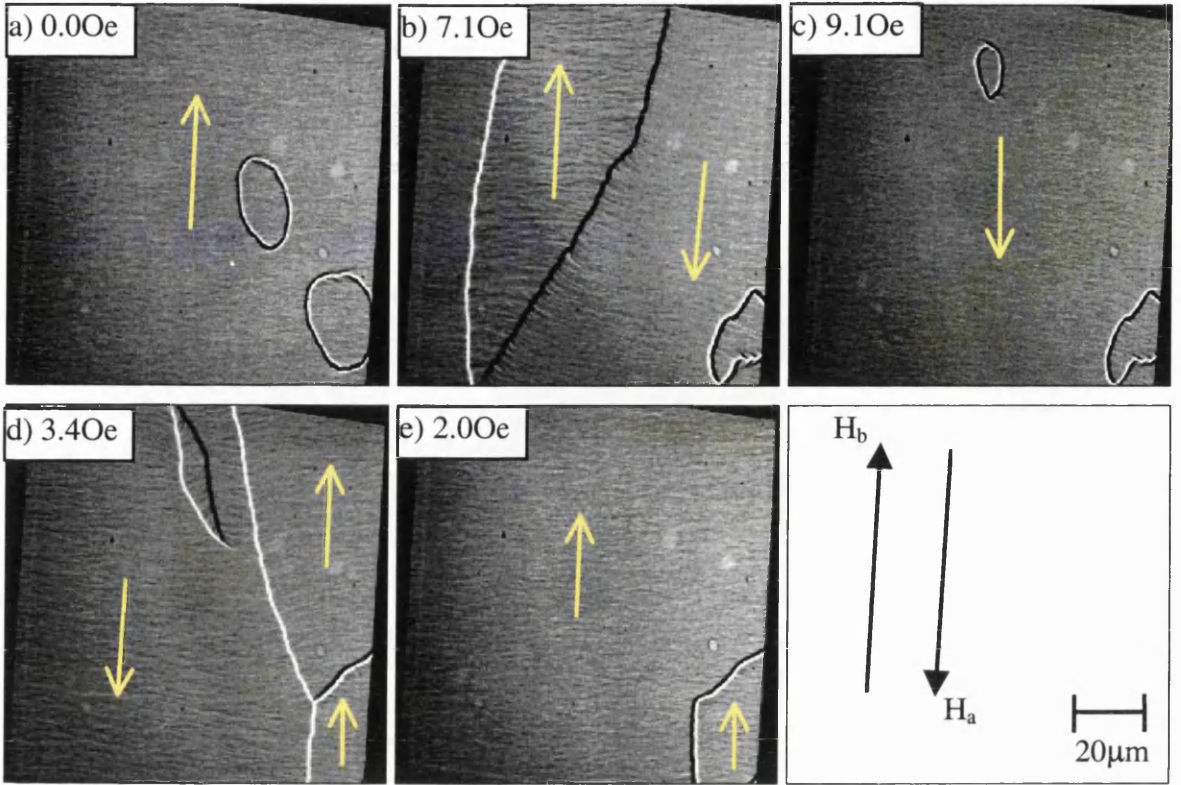


Figure 3.8(a-e): Free layer reversal mechanism for a $\text{Ni}_{80}\text{Fe}_{20}$ spin-valve with $t_{\text{Cu}}=3.0\text{nm}$.

The applied field direction is along the easy axis ($\theta=180^\circ$) and $H_0=5.25\text{Oe}$, $h_J=1.13$.

The magnetisation in the “switched” domains has returned to its initial direction along H_b , figure 3.8(e). The free layer offset $H_0=5.25\text{Oe}$ is calculated from the average of H_1 and H_2 , and corresponds to an interlayer coupling strength of $h_J=1.13$ (in reduced units).

Easy axis reversals for 3 other spin-valves with various t_{Cu} were also recorded, another example is shown in figure 3.9 for a spin-valve with $t_{\text{Cu}}=10.0\text{nm}$. It was found that the above magnetic reversal mechanism is typical for H_a oriented along the easy axis ($\theta=180^\circ$) for parallel anisotropy spin-valves. For a given ferromagnetic alloy, thicker t_{Cu} generally results in spin-valves with lower h_J . The results are summarised in table 3.1.

Alloy	t_{Cu} (nm)	H_k (Oe)	H_0 (Oe)	h_J (reduced units)
$\text{Ni}_{80}\text{Fe}_{20}$	3.0	4.65	5.25	1.13
$\text{Ni}_{80}\text{Fe}_{20}$	5.0	4.65	1.78	0.38
$\text{Ni}_{80}\text{Fe}_{20}$	10.0	4.65	0.70	0.15
$\text{Ni}_{66}\text{Fe}_{16}\text{Co}_{18}$	2.0	19.4	9.55	0.49

Table 3.1: Summary of sample properties and magnetic parameters.

A sample with $t_{Cu}=2.0\text{nm}$ and $\text{Ni}_{66}\text{Fe}_{16}\text{Co}_{18}$ as the ferromagnetic layers is also studied in this thesis. This alloy has a higher anisotropy than $\text{Ni}_{80}\text{Fe}_{20}$ (due to the presence of Co). It was observed that the free layer reversal for $\theta=180^\circ$ also proceeded by the same mechanism as for $\text{Ni}_{80}\text{Fe}_{20}$ spin-valves, but reversal occurred at higher applied fields. This resulted in $H_0=9.55\text{Oe}$ and a corresponding $h_J=0.49$, see table 3.1.

Note that the 360° loops that are observed often form in the free layers when observing an easy axis reversal. These have been described in much more detail elsewhere^[3]. However I pause to mention that they are stable structures which require a much higher field to annihilate them than is required to reverse the majority of the free layer. They are commonly observed when H_a is applied close to $\theta=180^\circ$ for all of the studied spin-valves.

Figure 3.9(a-f) shows the free layer reversal of a spin-valve with $t_{Cu}=10.0\text{nm}$ at $\theta=180^\circ$. It can be seen from the images that the reversal process is broadly similar to that shown in figure 3.8 for the spin-valve with $t_{Cu}=3.0\text{nm}$. The important point to note in this case is that $H_2 = -1.0\text{Oe}$ (i.e $H_a < 0$).

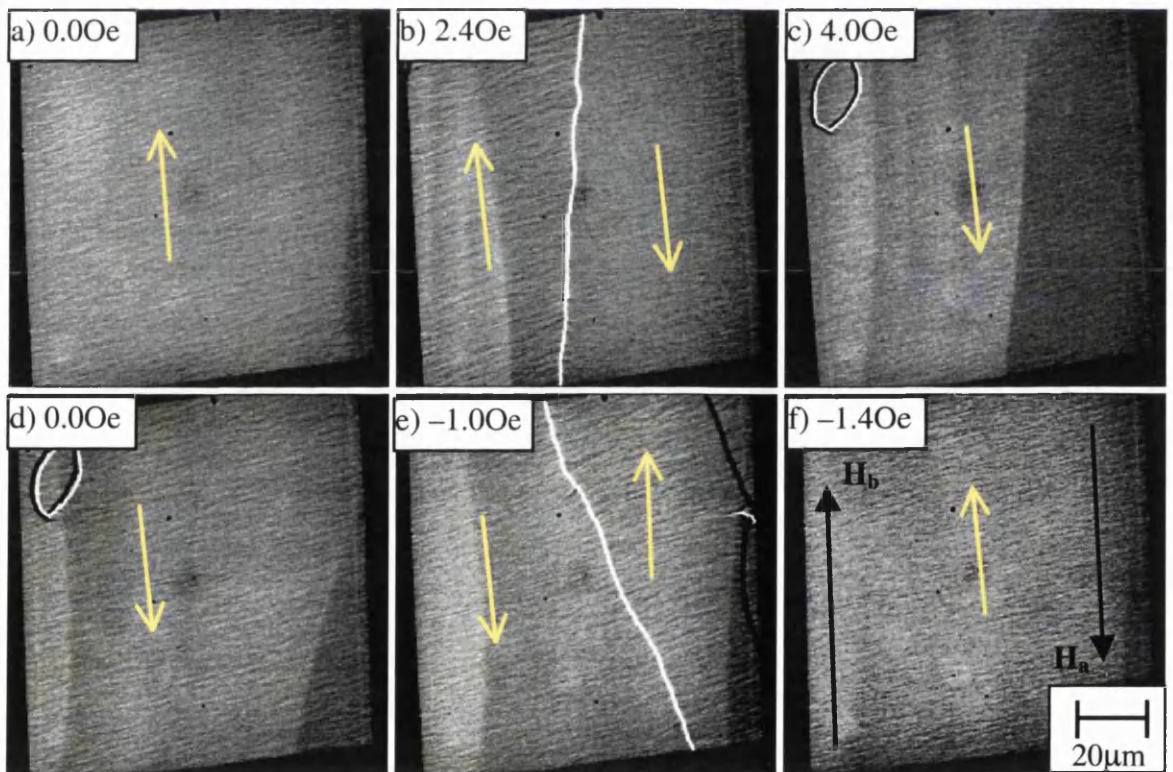


Figure 3.9(a-f): Free layer reversal mechanism for a $\text{Ni}_{80}\text{Fe}_{20}$ spin-valve with $t_{Cu}=10.0\text{nm}$.

The applied field direction is along the easy axis ($\theta=180^\circ$) and $H_0=0.7\text{Oe}$, $h_J=0.15$.

This corresponds to the case where the interlayer coupling strength is insufficiently strong to overcome the anisotropy field H_k at $H_a=0\text{Oe}$. For the “free” layer to return to parallel alignment with the “pinned” layer, H_a must be applied along the direction of biasing to aid the reversal to parallel alignment, as shown in figure 3.9(e). This is required to overcome the anisotropy of the free layer. This results in $H_0=0.7\text{Oe}$ which corresponds to $h_J=0.15$.

3.7 INVESTIGATIONS AS A FUNCTION OF APPLIED FIELD DIRECTION, θ .

For a given spin-valve with reduced interlayer coupling strength h_J the applied field H_a was initially aligned with the easy axis of the spin-valve ($\theta=180^\circ$). The angle of applied field θ was then decreased from antiparallel to the biasing direction in the interval $90^\circ<\theta<180^\circ$ and the free layer reversal mechanism observed for various values of θ . Three distinct modes have been observed; examples of these and the trends in the magnetic properties between modes are presented below. For several of the examples low angle diffraction data is included and is discussed where appropriate.

3.7.1 SPIN-VALVES WITH $h_J<1$.

This section describes free layer reversals observed for the spin-valves with $h_J<1$ described in table 3.1. Figure 3.10 shows a free layer reversal for the spin-valve with $h_J=0.15$ with the angle of H_a reduced to $\theta=163^\circ$. At $H_a=0.0\text{Oe}$ the direction of free layer magnetisation is along the easy direction (coincident with H_b), figure 3.10(a). As H_a is increased in strength, the magnetisation in the free layer rotates to the *left*, towards the applied field direction in an anti-clockwise sense. The rotation is only slight and at $H_a=2.4\text{Oe}$ domains are formed in the free layer, figure 3.10(b). The magnetisation vector in the “switched” magnetic domain lies to the *right* of H_a , although close to antiparallel alignment with H_b . Further small increases in H_a causes the domain walls to rapidly sweep through the free layer leaving once again a single domain state, figure 3.10(c). Further increases in H_a then cause the magnetisation vector to rotate clockwise, back towards the applied field direction. This is in the opposite sense to the rotation before the switch took place. Eventually alignment of the magnetisation vector with H_a is obtained and no further changes in the magnetic state are observed for further small increases in field strength.

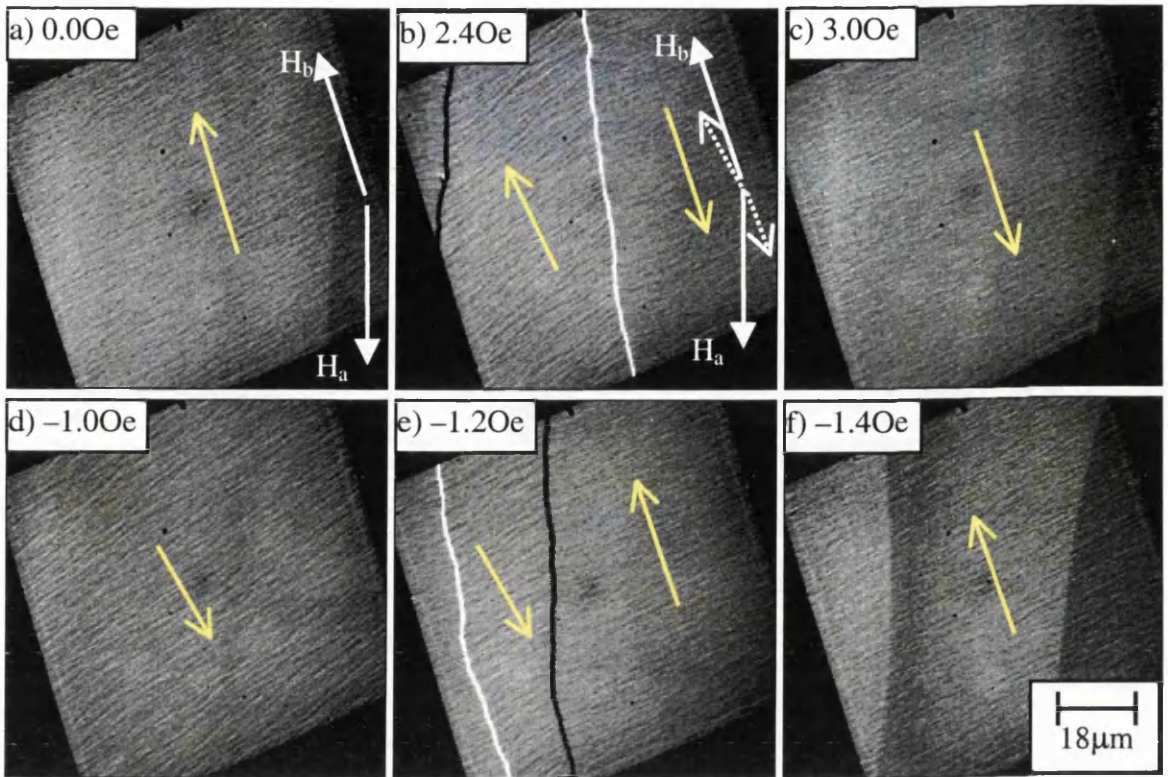


Figure 3.10(a-f): Free layer reversal mechanism for a $Ni_{80}Fe_{20}$ spin-valve with $h_J=0.15$.

The angle of applied field $\theta=163^\circ$.

This type of free layer reversal has been labelled a Mode A-type reversal^[13]. The important point to note is that the magnetisation vector overshoots H_a at the switching field and then rotation in the opposite sense is observed until alignment is achieved.

As H_a is decreased in strength back towards 0Oe, the free layer magnetisation reversal follows broadly the same processes in reverse. For example, the magnetisation vector is observed to rotate in an anti-clockwise sense back towards antiparallel alignment with H_b , and in fact continues slightly past it, figure 3.10(d). At $H_a=-1.2$ Oe the reverse “switch” in the magnetisation vector occurs with domains forming in the free layer. Within the accuracy of visual measurement ($\approx 5^\circ$), the direction of magnetisation in the “reversed” domains is approximately coincident with H_b (the easy axis), figure 3.10(e). Again, after a slight increase in the strength of H_a the domain walls sweep through the layer and a single domain state is obtained within the area of view, figure 3.10(f). Varying contrast broad “stripes” can be seen across some of the images in figure 3.10. These are not magnetic in origin, but are an artifact occasionally caused during drying of the micrographs following photographic development. In subsequent sections, contrast of this nature is ignored.

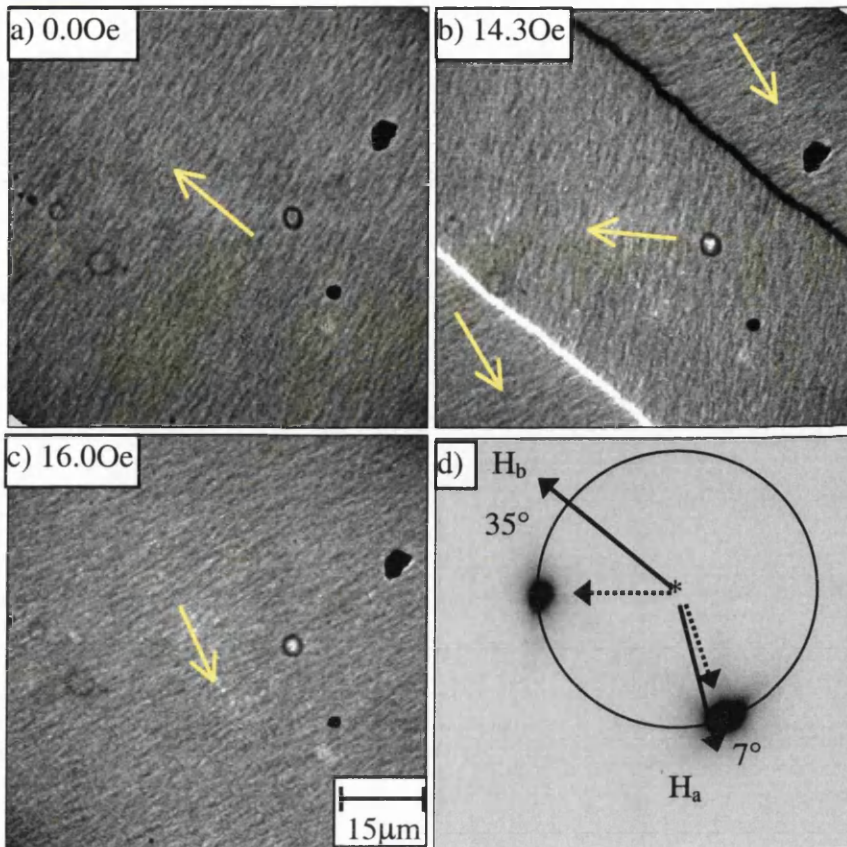


Figure 3.11(a-c): Free layer reversal mechanism for a $\text{Ni}_{66}\text{Fe}_{16}\text{Co}_{18}$ spin-valve with $h_J=0.49$ and **(d)** accompanying low angle diffraction (LAD) pattern. The angle of applied field $\theta=145^\circ$.

Figure 3.11 shows the free layer magnetisation reversal for a spin-valve with $h_J=0.49$ with the applied field at $\theta=145^\circ$. In zero field the free layer is in a single domain state and the magnetisation vector is coincident with the biasing direction. As the applied field H_a is increased the magnetisation begins to rotate towards the applied field direction in an anticlockwise sense. At 14.3Oe the magnetisation has rotated to $\sim 35^\circ$ from the biasing direction when domains are formed in the free layer, figure 3.11(b). The magnetisation vector in the “switched” magnetic domains is $\approx 7^\circ$ to the *right* of H_a . The LAD pattern for the magnetic state of figure 3.11(b) is shown in figure 3.11(d). It shows that as the reversal proceeds the magnetic vectors are well defined and that little dispersion of the magnetisation is present in the free layer. Note that for ease of interpretation the low angle diffraction patterns have been rotated by 90° so that the lines from the centre to the spots are parallel to their corresponding magnetisation directions. The domain walls rapidly sweep through the free layer upon very small field increase leaving once again a

single domain state. Further increases in H_a then cause the magnetisation vector to rotate clockwise, back towards the applied field direction. This is in the opposite sense to the rotation before the switch took place. Eventually alignment of the magnetisation vector with H_a is obtained and no further changes in the magnetic state are observed with continued increases in field strength. This also corresponds to a mode A-type reversal.

Figure 3.12 shows another example of a mode A-type reversal. In this case $h_j=0.38$ for a $Ni_{80}Fe_{20}$ based spin-valve with $\theta=165^\circ$. Once again, as H_a is increased in strength the free layer magnetisation rotates in an anticlockwise sense away from H_b , figure 3.12(a). At $H_a=3.4Oe$ the magnetisation has rotated to $\approx 32^\circ$ to the left of H_b when domains are formed in the free layer. The direction of magnetisation in the “switched” domains lying at $\approx 10^\circ$ to the right of H_a , figure 3.12(b). The low angle diffraction pattern, figure 3.12(d) confirms this result, also illustrating the well defined magnetisation vectors. In this case the LAD pattern increases the accuracy with which the angles of magnetisation can be determined. As H_a is increased in strength beyond 3.4Oe the domain walls are observed to rapidly sweep through the free layer leaving a single domain state. This is followed by the magnetisation rotating in a clockwise sense back towards the direction of H_a until alignment is achieved.

Upon decreasing the strength of H_a after saturation is achieved the magnetisation begins to rotate anticlockwise, towards antiparallel alignment with H_b , figure 3.12(e). At $H_a=-0.5Oe$ domains are formed with the magnetisation in the still reversed domains lying at $\approx 10^\circ$ clockwise from H_a and the regions of switched magnetisation returning to $\approx 10^\circ$ to the left of H_b . Figure 3.12(h) shows this schematically. As H_a is further decreased in strength (Note that the fields are negative indicating that H_a is actually increasing in strength along a direction antiparallel to the indicated direction of H_a) the magnetisation gradually rotates back towards H_b , and in this case slightly past it due to the orientation of H_a . Again, the reversal is mode A in nature, and can be seen to be accompanied by a low number of domain walls rapidly sweeping through the free layer. In this case the LAD pattern for the reverse part of the hysteresis loop was not recorded.

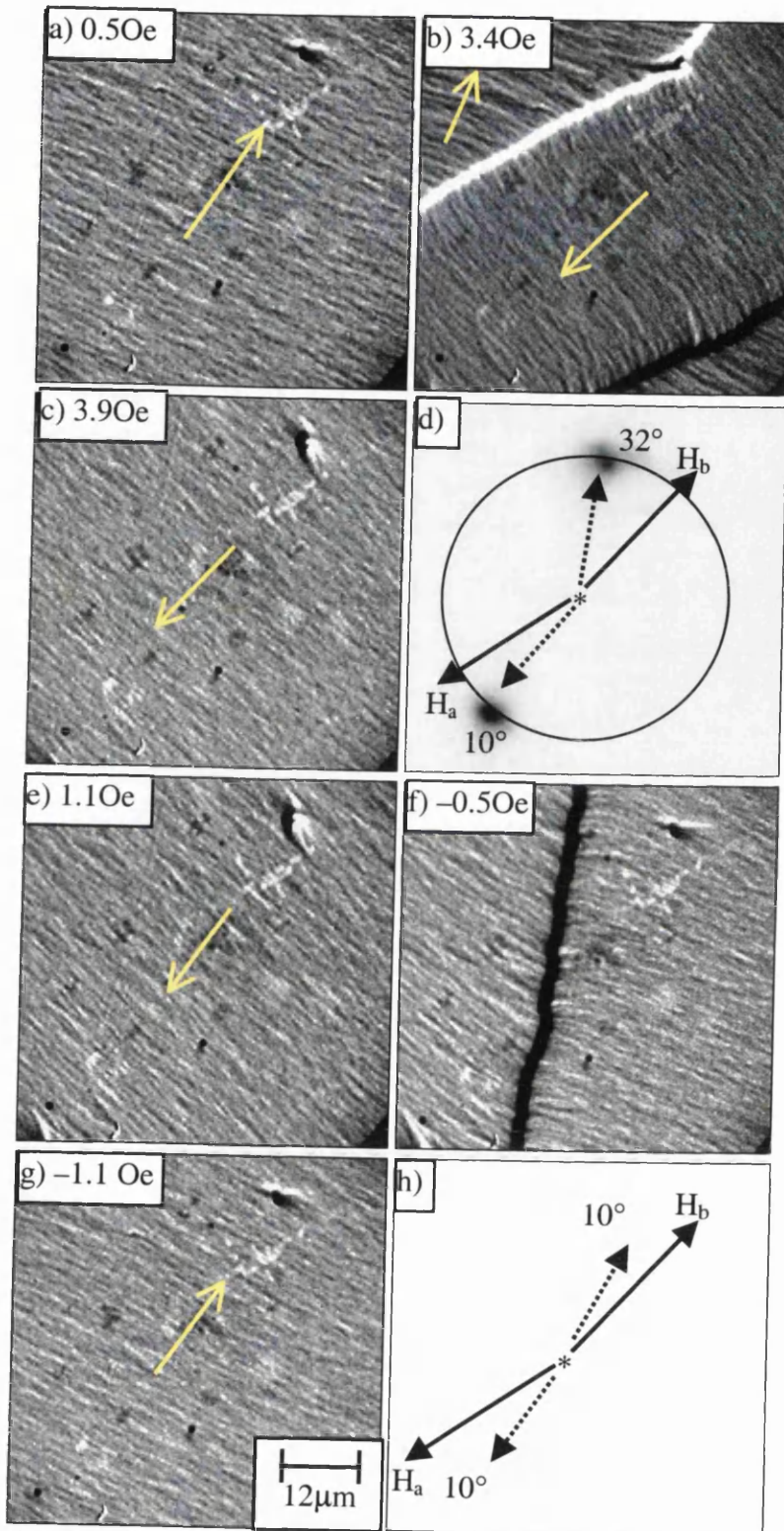


Figure 3.12(a-h): Free layer reversal mechanism for a $Ni_{80}Fe_{20}$ spin-valve with $h_J=0.38$ and an accompanying LAD pattern. The angle of applied field $\theta=165^\circ$.

As θ is decreased further, the following trends in the free layer reversal have been observed. The amount of magnetisation rotation increases during the free layer reversal.

Domains still form but there is a decrease in the domain wall angle and mobility. The number of domain walls also steadily decreases. Figure 3.13(a-h) shows these effects for the sample with $h_j=0.49$ discussed above but with $\theta=120^\circ$. The larger amount of magnetisation rotation that takes place can be seen in figure 3.13(a) which corresponds to the magnetic state just before domains are observed. Here the free layer magnetisation vector has rotated anti-clockwise by $\approx 55^\circ$ from H_b . At $H_a=19.1\text{Oe}$ many low angle domain walls have formed, figure 3.13(b). This image shows the state of maximum domain wall activity in the free layer. Domain processes can be observed over a relatively large field range ($\approx 2\text{Oe}$) and, as noted, have a much lower mobility compared with the previous examples. As the strength of H_a is increased further, low angle domain walls are formed in previously unswitched regions and annihilation of the walls in partly switched areas is observed. This process continues until the majority of the free layer has reversed, eventually approaching a single domain state, figure 3.13(c). The LAD pattern corresponding to the state shown in figure 3.13(b) is shown in figure 3.13(d). The large amount of magnetisation rotation that occurs before domain formation is depicted, (the angle between H_b and the first diffraction spot is now much larger at the switching field). The LAD pattern also shows that there are still two preferred orientations of magnetisation in the free layer during reversal, although there is now an almost continuous distribution of magnetisation angles about these two directions.

Broadly similar processes are observed in the free layer when H_a is decreased in strength back towards 0Oe for the reverse half of the hysteresis loop, see figures 3.13(e-h). The low angle diffraction patterns shown in figure 3.13 reveal that the magnetisation reversal is still mode A-type in nature. There is still a slight overshoot of the magnetisation vector to the right of H_a and the sense of magnetisation rotation is opposite to that before the reversal of the majority of the layer. However, it is now difficult to discern this from the Fresnel images alone, and the reversal mechanism involves a lot more magnetisation rotation incorporating domain assisted processes. The observed domains are smaller than for reversals at higher values of θ , and the domain walls now have low angle and mobility. The LAD patterns also reveal that there is now a larger range of directions of magnetisation present during the reversal of the free layer.

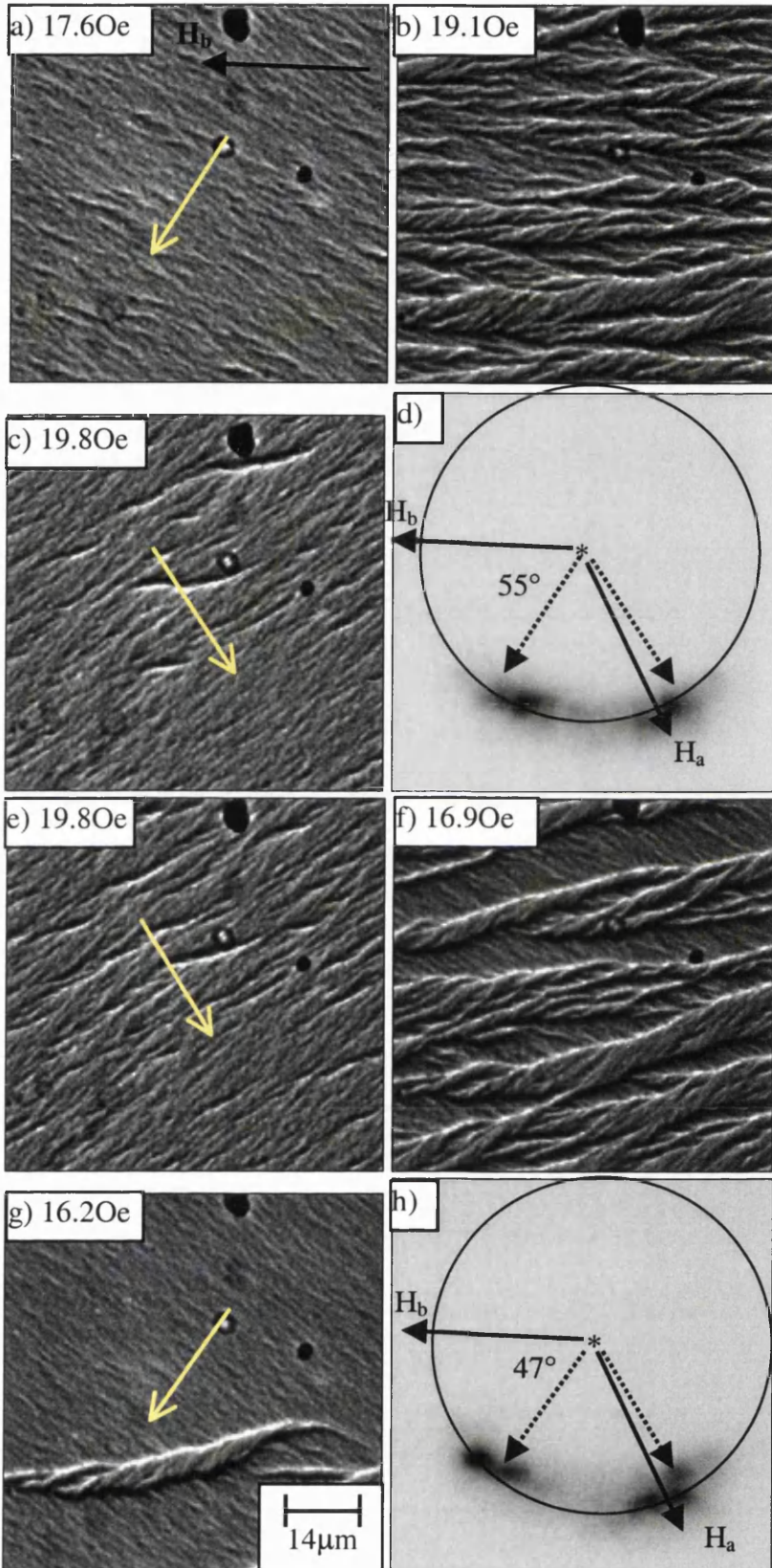


Figure 3.13(a-h): Free layer reversal and LAD data for spin-valve with $h_J=0.49$ and $\theta=120^\circ$.

The reversal mechanism of the free layer for the same sample after a 2° decrease in θ to 118° is shown in figure 3.14. In this example, the magnetisation in the free layer coherently rotates as H_a is increased from 0Oe, figure 3.14(a,b). The level of dispersion observed in the free layer passes through a maximum at $H_a \approx 16.5$ Oe, figure 3.14(c). The corresponding LAD pattern, figure 3.14(e) shows a large spread in the angles of magnetisation vector around the average direction of magnetisation. As H_a is increased further in strength the level of dispersion and amount of contrast in the Fresnel images decreases. The resulting direction of magnetisation being coincident with the direction of applied field H_a , figure 3.14(d). As H_a is decreased in strength, very little rotation of the free layer magnetisation is initially observed. However, when H_a was decreased to ≈ 17.7 Oe, figure 3.14(f), the level of dispersion started to increase. At $H_a = 16.5$ Oe, figure 3.14(g), the dispersion had reached a maximum. As H_a is reduced further the level of dispersion steadily decreases and the free layer eventually returns to a single domain state and the direction of magnetisation can be seen to rotate back towards the direction of H_b , figure 3.14(h,i). Note that in this reversal the point at which the maximum state of dispersion is observed is $H_a = 16.5$ Oe for both increasing and decreasing the strength of H_a . Thus the reversal mechanism is almost anhysteretic. This remains the case in several of the examples that follow.

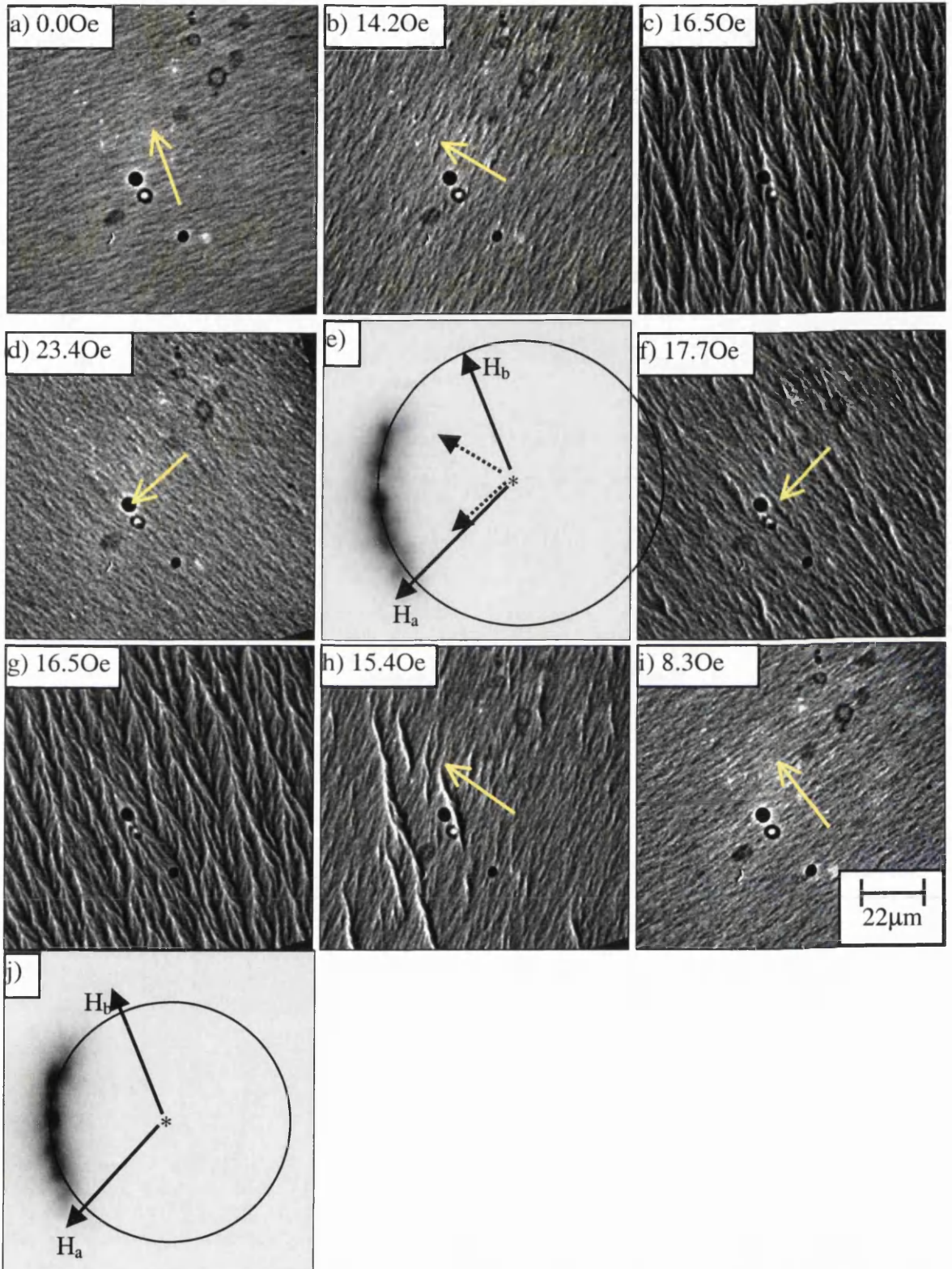


Figure 3.14(a-j): Free layer reversal mechanism for a spin-valve with $h_f=0.49$ and an accompanying LAD patterns. The angle of applied field $\theta=118^\circ$.

Figure 3.15 shows the free layer reversal for this sample at $\theta=116^\circ$. The Fresnel images shown in figures 3.15(a-c) and (e-g) shows the reversal as H_a is increased and decreased in strength respectively. Figures 3.15(d,h) are sequences of LAD patterns which were taken separately as H_a was varied. They do not correspond directly to the Fresnel images, but are shown here in order that the level of dispersion present during reversals may be discussed. It is assumed that the free layer reversal mechanism is the same regardless of the imaging mode employed. Note that the LAD patterns have not been superimposed into one image because there was some thermal drift present during collection of the patterns. This effectively moves the center of the circle that corresponds to the undeflected electron beam. Thus a circle has not been used to assist in the description of these sequences.

The Fresnel images shown in figure 3.15(a-c), (e-g) reveal that the free layer reversal now proceeds by a combination of coherent rotation of magnetisation including an increase in the level of dispersion part of the way through the reversal. This is true for both increasing and decreasing H_a . Sequences of LAD patterns showing the level of dispersion present in the free layer are shown in figure 3.15(d) for increasing the strength of H_a , and 3.15(h) for decreasing the strength of H_a . For the case of increasing field strength the low angle diffraction pattern can be seen to start as being a well defined spot, figure 3.15(d) at 0.0Oe. As H_a increases to 10.2Oe a slight broadening of the spot can be observed. At $H_a=12.0$ Oe a considerable broadening of the diffraction pattern can be seen. This corresponds to a state which will closely resemble that presented in the Fresnel image shown for $H_a=12.5$ Oe in figure 3.15(b). As H_a increases in strength beyond that corresponding to the maximum state of dispersion (12.5Oe) the extent of spreading in the LAD pattern decreases and eventually returns to a well defined spot at approximately $H_a=17.6$ Oe. This corresponds to the case where the free layer is in a single domain state with a small range of angles of magnetisation present.

Three LAD images are shown in the sequence figure 3.15(h) which relate to the level of dispersion observed while decreasing H_a back to 0Oe. As H_a passes through the field range where a large amount of dispersion was observed for the Fresnel images (12.5Oe), the diffraction spot broadens out corresponding to the increased state of dispersion part of the way through the reversal.

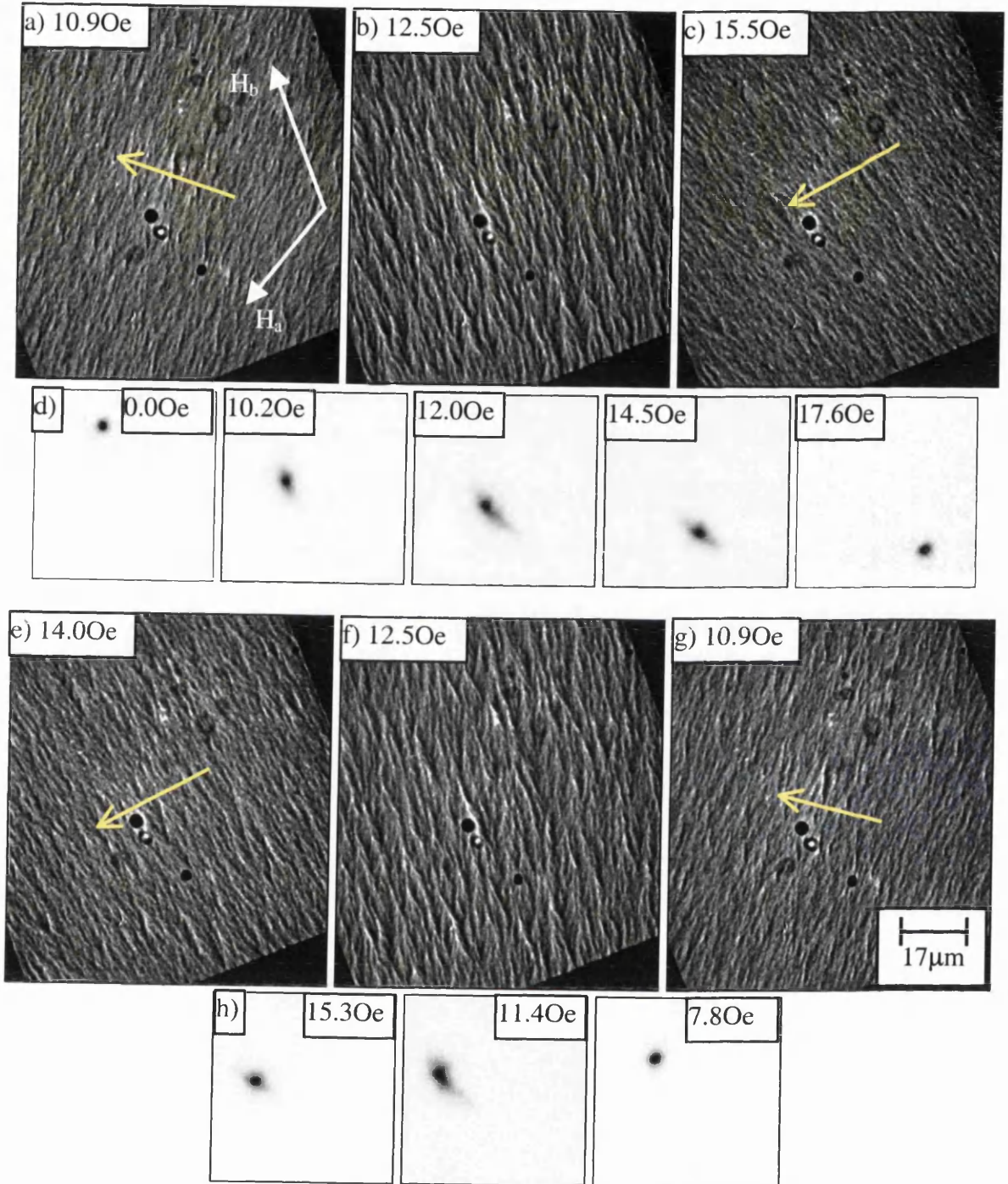


Figure 3.15(a-h): Free layer reversal mechanism for a $Ni_{66}Fe_{16}Co_{18}$ spin-valve with $h_j=0.49$ and an accompanying LAD sequences. The angle of applied field $\theta=116^\circ$.

Figure 3.16(a-h) shows a final free layer reversal mechanism for this sample with $h_j=0.49$ at $\theta=110^\circ$. In this example as H_a is increased from 0Oe the free layer magnetisation coherently rotates in an anticlockwise sense until alignment with H_a is achieved, figure 3.16(a-c). At no point during the reversal are domains formed, and only a slight increase in

the level of dispersion is perceived. The images contained within figure 3.16(d) show a LAD sequence which was recorded for increasing the strength of H_a . It can be seen from this figure that at no point during the reversal is there a significant increase in the level of dispersion which confirms the observations of the Fresnel images.

The reversal of the free layer when decreasing H_a back towards 0Oe is shown in figure 3.16(e-g). It can be seen that the free layer magnetisation coherently rotates clockwise from the direction of H_a to the direction of H_b as the strength of H_a is reduced. The sequence of LAD images to accompany this reversal is shown in figure 3.16(h). It shows that as H_a is reduced in strength that the diffraction spot remains well defined, corresponding to the free layer remaining single domain with little dispersion.

This type of reversal has been labeled a Mode C-type reversal. It corresponds to the case where the magnetisation coherently rotates from alignment with H_b to alignment with the direction of H_a . This reversal process is observed to be anhysteretic and no significant increase in the level of dispersion is observed as the reversal proceeds.

Figure 3.17 shows an example of a mode C-type reversal for a sample with $h_J=0.38$ at $\theta=112^\circ$. In this case the free layer magnetisation can be seen to coherently rotate from alignment with H_b to the direction of H_a as the strength of H_a increases. In this example the source of thermal drift in the LAD imaging mode was eliminated. This allowed LAD patterns to be recorded with the same centre of reference. Thus figure 3.17(d) shows the 3 LAD patterns corresponding to the Fresnel images shown in 3.17(a-c) superimposed onto the same image. It can be seen that the diffraction spot remains a small well defined spot and coherently rotates around the radius of a circle as the strength of H_a is increased and causes the free layer magnetisation to rotate towards the direction of H_a .

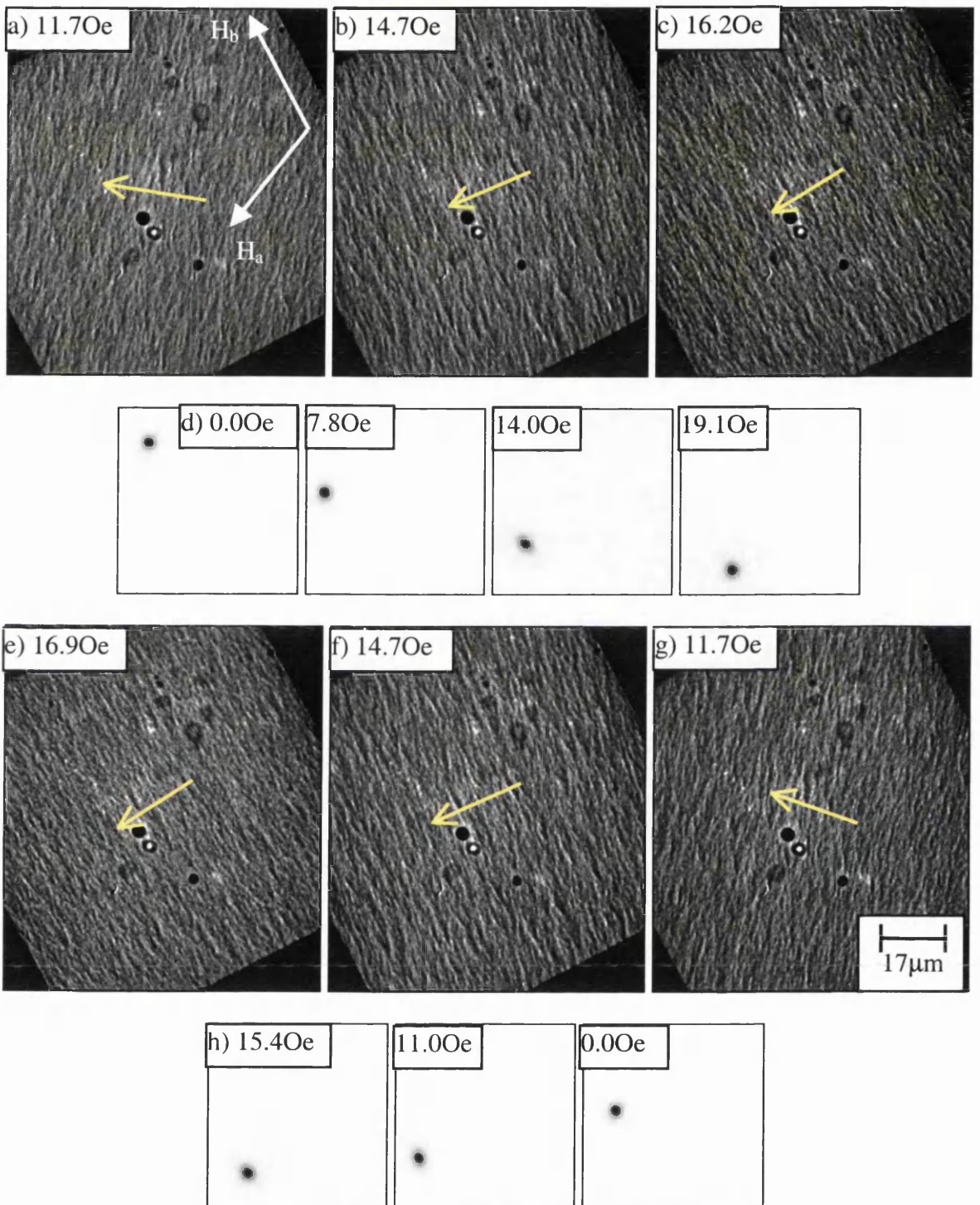


Figure 3.16(a-h): Free layer reversal mechanism for a $\text{Ni}_{66}\text{Fe}_{16}\text{Co}_{18}$ spin-valve with $h_J=0.49$ and an accompanying LAD sequences. The angle of applied field $\theta=110^\circ$.

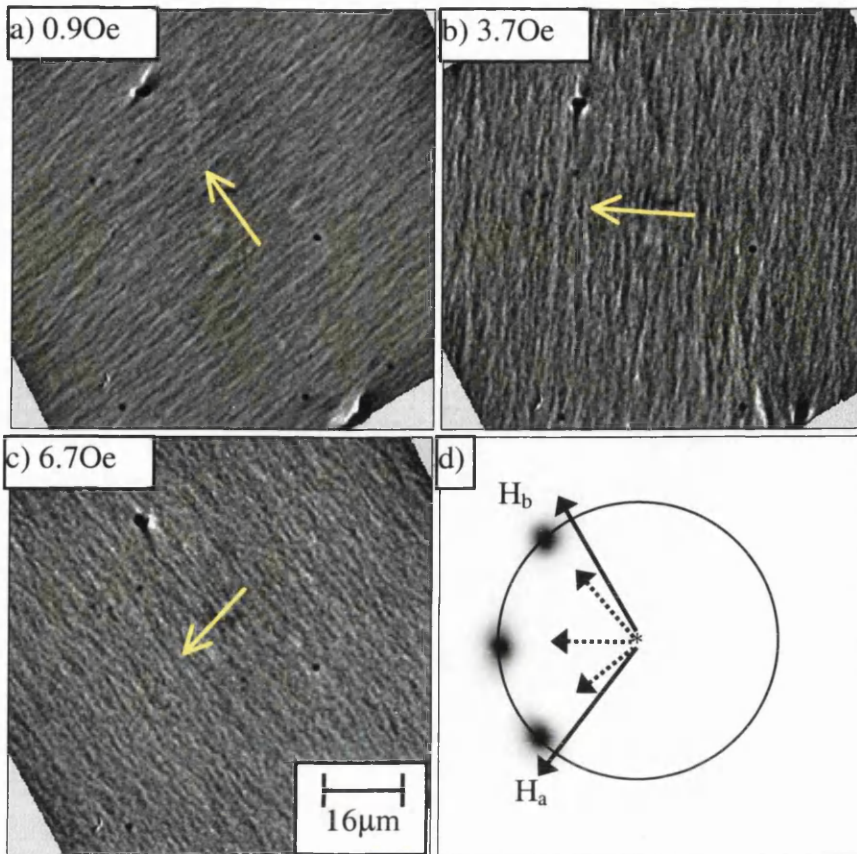


Figure 3.17(a-c): Mode C-type reversal for a spin-valve with $h_f=0.38$ at $\theta=112^\circ$ ($t_{Cu}=5.0nm$, $Ni_{80}Fe_{20}$) and (d) superimposed LAD patterns.

The examples discussed in this section illustrate the free layer reversals for a range of spin-valves with $h_f < 1$. At values of θ close to 180° mode A-type reversals were observed. However as θ was decreased the mode of reversal steadily approached mode C (coherent rotation of magnetisation). This was facilitated by an increasing number of low angle domain walls being present in the free layer at the switching fields. The domain wall angles and mobility both decreased as θ was reduced. Eventually the reversal was better described by a combination of magnetisation rotation incorporating a state of enhanced dispersion part of the way through the reversal process. LAD assisted in the determination of the level of dispersion present, and it was observed to decrease as θ was reduced. Eventually no discernable increase in the level of dispersion could be detected, and the reversal proceeded by coherent rotation of magnetisation alone.

3.7.2 SPIN-VALVES WITH $h_J > 1$.

This section describes the modes of reversal and trends in the magnetic properties observed for spin-valves with $h_J > 1$ as a function of applied field direction θ . Figure 3.18 shows a free layer reversal at $\theta = 155^\circ$ for the spin-valve introduced in section 3.6.2 with $t_{Cu} = 3.0\text{nm}$ and $h_J = 1.13$. Initially the free layer is in a single domain state with the magnetisation oriented along the biasing direction in zero field, figure 3.18(a). As H_a is increased the magnetisation rotates towards the applied field direction in an anticlockwise sense in a similar manner to that described in the previous section. Once H_a is increased to 6.2Oe the magnetisation has rotated to $\sim 24^\circ$ from the biasing direction. Domains are then formed with the magnetisation in the switched areas lying at $\sim 33^\circ$ to the *left* of H_a as shown in figure 3.18(b). Note that in this case the magnetisation does not overshoot the applied field direction but remains to the left of it. Further increases in H_a cause the domain walls to rapidly sweep through the free layer followed by rotation of magnetisation in the same anticlockwise sense (as before switching took place) until alignment with H_a is obtained, figure 3.18(c). The low angle diffraction pattern corresponding to the state shown in figure 3.18(b), figure 3.18(d), as well as confirming this result shows that little dispersion accompanies the free layer reversal. This type of free layer reversal has been labelled a mode B-type reversal corresponding to the case where the interlayer coupling between the two ferromagnetic layers is sufficiently strong to constrain the magnetisation to the half plane bounded by the applied field and biasing directions (H_a and H_b).

As θ is decreased, the following trends in the free layer reversal are observed. The amount of magnetisation rotation observed increases during the free layer reversal. However, domains still form but there is a decrease in domain wall angle and domain wall mobility. The number of low angle domain walls also steadily increases. Figure 3.19 shows these effects for the same sample as shown in figure 3.18 above but with θ reduced to 149° . It can be seen that a large number of low angle domain walls are formed during the reversal, figure 3.19(b). These exist over a relatively large field range (few Oe) and, as noted, have a lower mobility compared with the previous example.

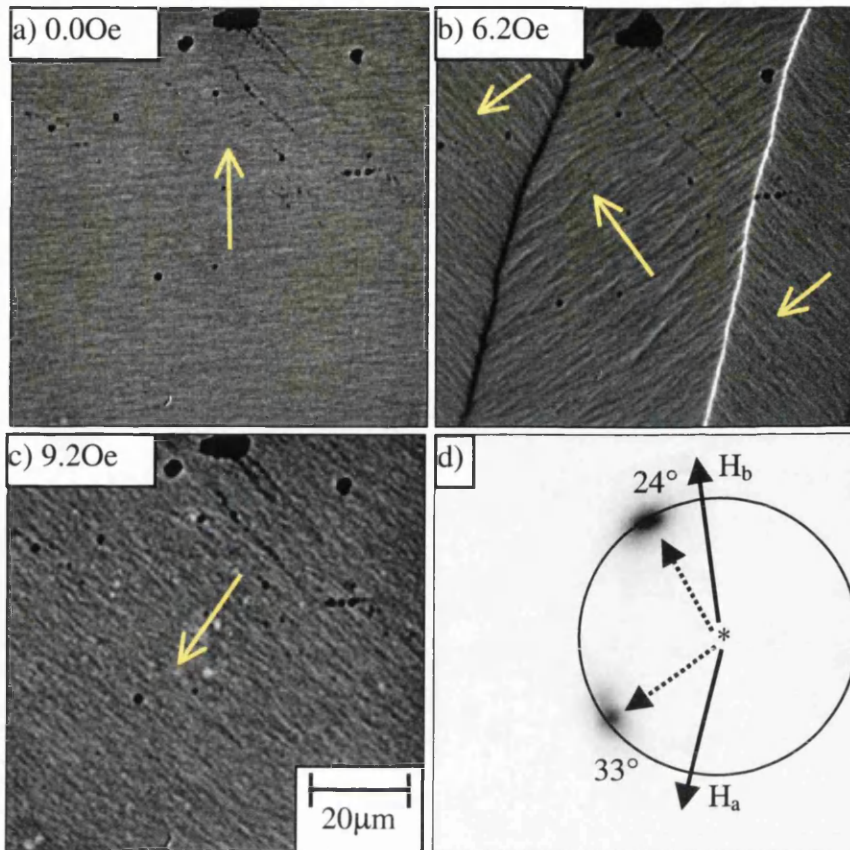


Figure 3.18(a-c): Mode B-type reversal for a spin-valve with $h_j=1.13$ at $\theta=155^\circ$ ($t_{Cu}=3.0\text{nm}$, $Ni_{80}Fe_{20}$) and (d) corresponding LAD pattern.

The corresponding low angle diffraction pattern for the Fresnel image shown in figure 3.19(b) is shown in figure 3.19(d). This reveals that there is a continuous range of magnetisation orientations present during switching. As the applied field strength is increased further, low angle domain walls are formed in previously unswitched regions and annihilation of the walls in the central area of the specimen is observed. The range of angles present gradually decreases as the reversal continues. The magnetisation in the switched domains lies to the *left* of the applied field direction and rotates in an anti-clockwise sense as H_a is increased until alignment with the field direction is obtained.

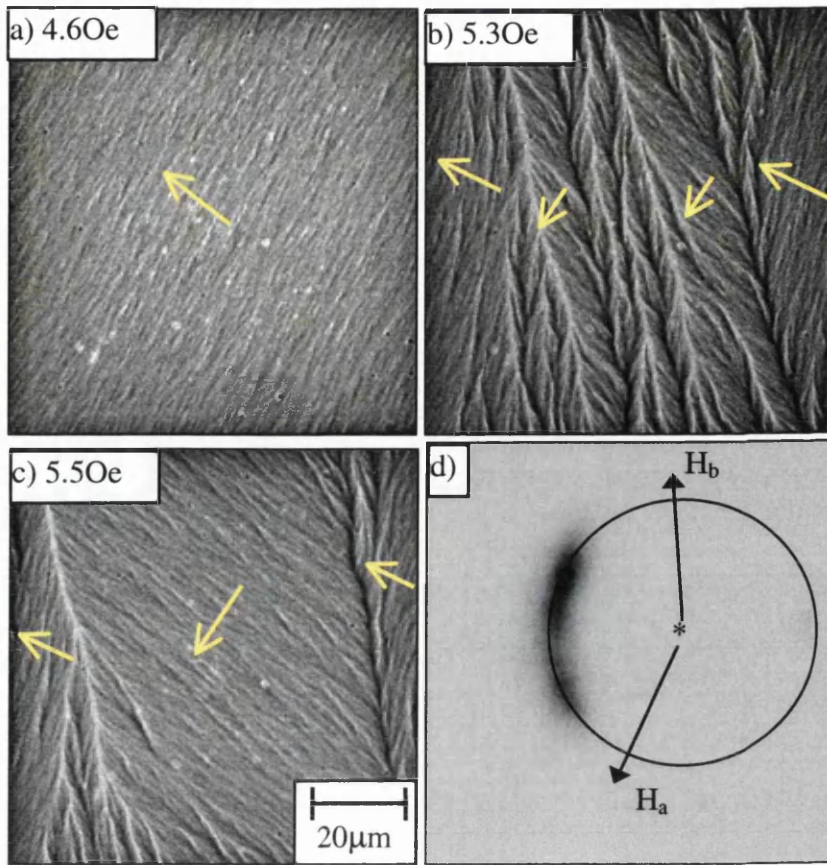


Figure 3.19(a-c): Mode B-type reversal for a spin-valve with $h_j=1.13$ at $\theta=149^\circ$ ($t_{Cu}=3.0\text{nm}$, $Ni_{80}Fe_{20}$) and (d) corresponding LAD pattern.

Figure 3.20 shows the free layer reversal for the above spin-valve with $\theta=144^\circ$. At $H_a=0.0\text{Oe}$ the free layer magnetisation is coincident with the biasing direction. As H_a increases in strength the magnetisation gradually rotates towards the direction of H_a , figure 3.20(a,b). $H_a=6.0\text{Oe}$, the level of dispersion present in the free layer starts to increase and passes through a maximum at around 6.2Oe as shown in figures 3.20(c,d). As H_a is increased in strength beyond 6.2Oe the free layer magnetisation returns to a well defined direction to the left of H_a , and gradually rotates towards it, figures 3.20(e,f). Eventually alignment between the direction of magnetisation and H_a is achieved. A sequence of LAD patterns was recorded for this example and are shown in figure 3.20(g). Although thermal drift prevents quantitative analysis it is possible to confirm that the level of dispersion increases during

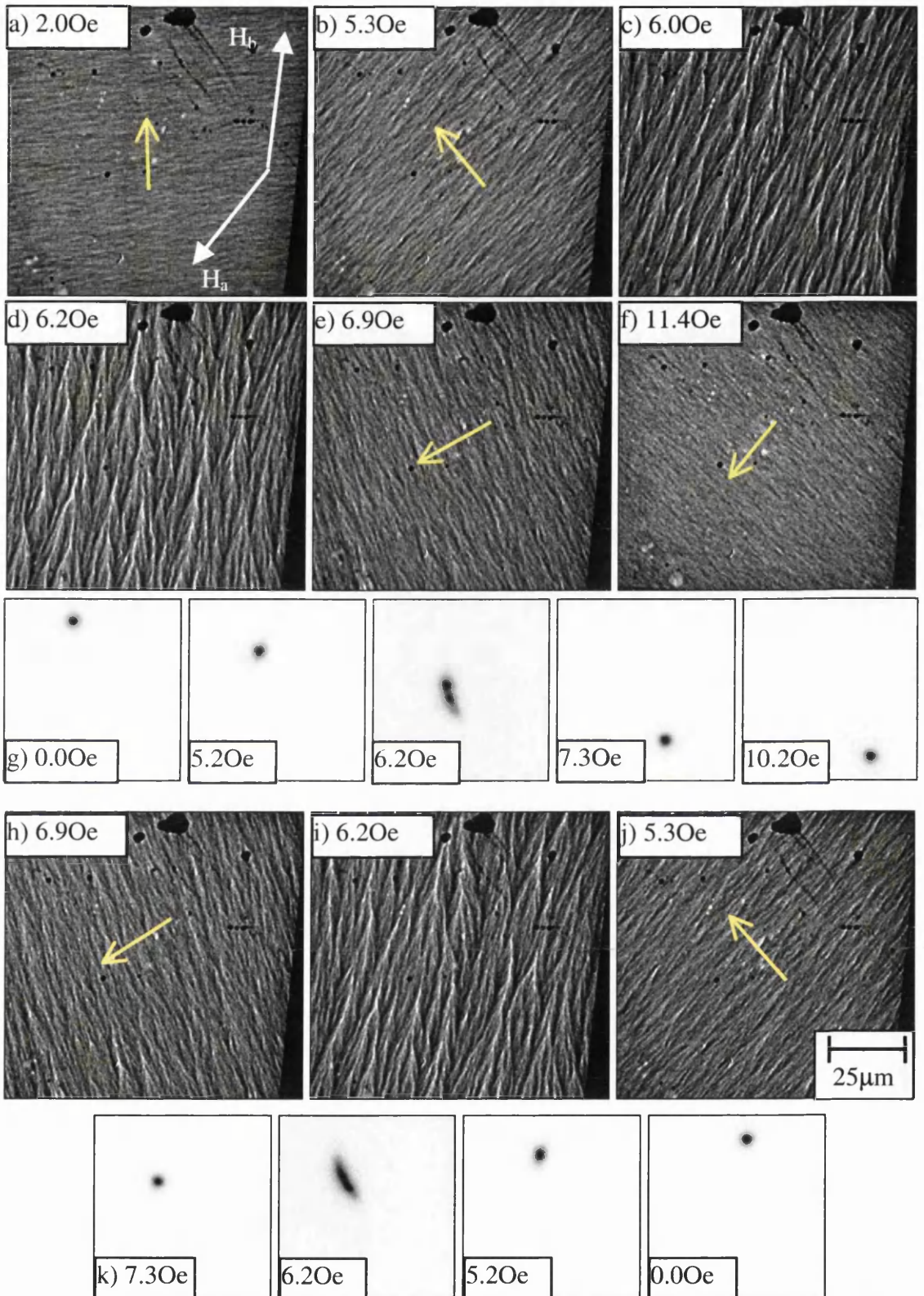


Figure 3.20(a-k): Free layer reversal mechanism for a $\text{Ni}_{80}\text{Fe}_{20}$ spin-valve with $h_j=1.13$ and an accompanying LAD sequences. The angle of applied field $\theta=144^\circ$.

part of the reversal close to $H_a=6.2\text{Oe}$. It can be seen that at fields well below and above that which dispersion was observed in the free layer that the diffraction spot is circular and well defined. However, at $H_a\approx 6.2\text{Oe}$, the diffraction spot splits into two main spots closely separated, with a broad range of contrast about them. This corresponds to a state similar to that shown in figure 3.20(d).

As H_a is decreased in strength following alignment between the magnetisation and H_a , broadly similar processes are observed in reverse. The magnetisation starts to rotate back towards H_b in a clockwise sense, figure 3.20(h), passing through a state of increased dispersion. The level of dispersion passes through a maximum at approximately 6.2Oe , figure 3.20(i) after which the free layer magnetisation returns to a well defined direction and continues to rotate in the same sense as before towards H_b , figure 3.20(j). As H_a decreases to 0.0Oe the free layer magnetisation returns to alignment with H_b , the biasing direction.

The sequence of LAD patterns recorded for decreasing the strength of H_a , figure 3.20(k) confirms that there is an increased level of dispersion around $H_a=6.2\text{Oe}$.

Thus at $\theta=144^\circ$ the free layer reversal mechanism involves coherent rotation of magnetisation followed by a state of increased dispersion part of the way through the reversal for both increasing and decreasing the strength of H_a . The sense of magnetisation rotation and the directions of free layer magnetisation during reversal confirm that this type of free layer reversal is therefore also mode B, however involving a state of increased dispersion rather than distinct domain processes as observed in examples 3.18 and 3.19.

With θ reduced to 141° as shown in figure 3.21 the reversal process is similar to that described above. The main difference in this example is the amount of dispersion encountered during the reversal has decreased. Accompanying this, an overall increase in the amount of magnetisation rotation that is observed during reversal increases. This is due to the lesser angular extent of the dispersed state. Figure 3.21 shows Fresnel images showing the reversal whilst varying the strength of H_a . Single LAD patterns are overlaid upon their corresponding Fresnel images. These show that there is now very little dispersion involved in the reversal as the level of splitting of the diffraction spots is very low.

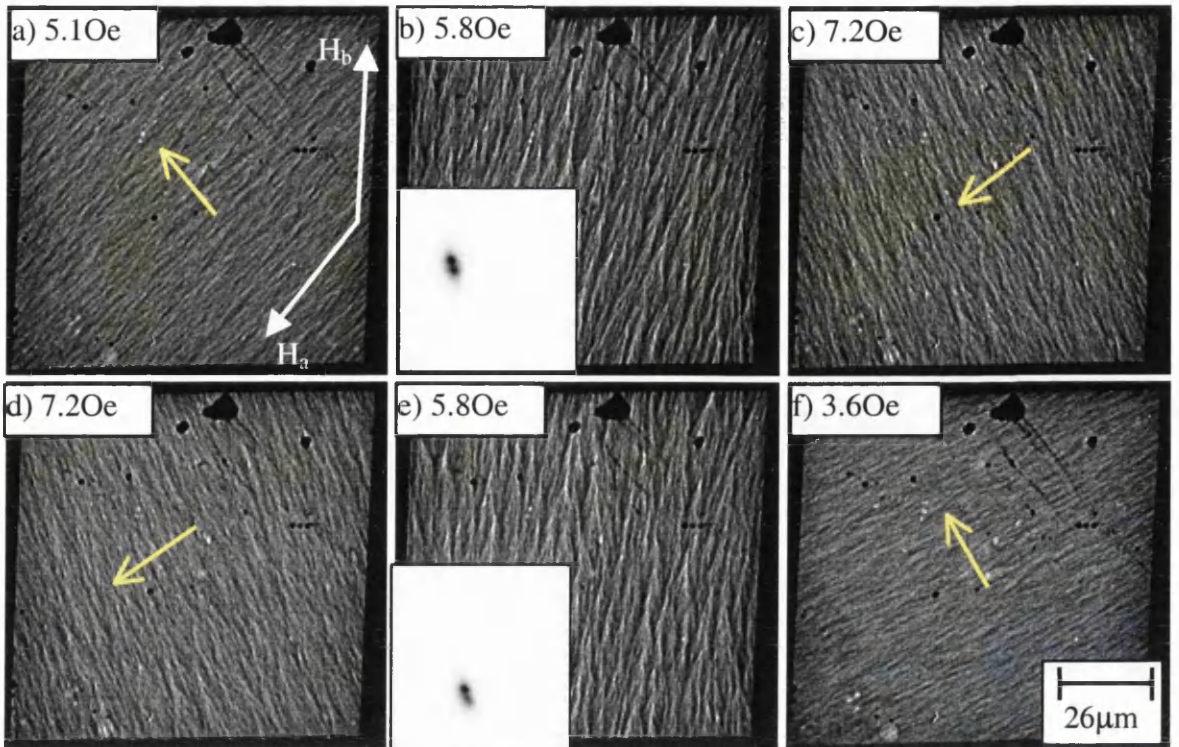


Figure 3.21(a-f): Free layer reversal mechanism for a $\text{Ni}_{80}\text{Fe}_{20}$ spin-valve with $h_J=1.13$ and an accompanying LAD patterns. The angle of applied field $\theta=141^\circ$.

As the angle of applied field is decreased further, the level of dispersion involved in the reversals decreases until it is indistinguishable from the magnetisation ripple that is normally present in the free layer. Figure 3.22 shows a final reversal for the sample with $h_J=1.13$ at $\theta=132^\circ$ in which the free layer magnetisation can be seen to coherently rotate from the direction of H_b at 0.0Oe to the direction of H_a and back again as the strength of H_a is varied. LAD data was observed for this case, and the diffraction spot remained well defined and circular. It traversed the circumference of a circle as the free layer reversal proceeded, similar to that shown in the example discussed previously for figure 3.17.

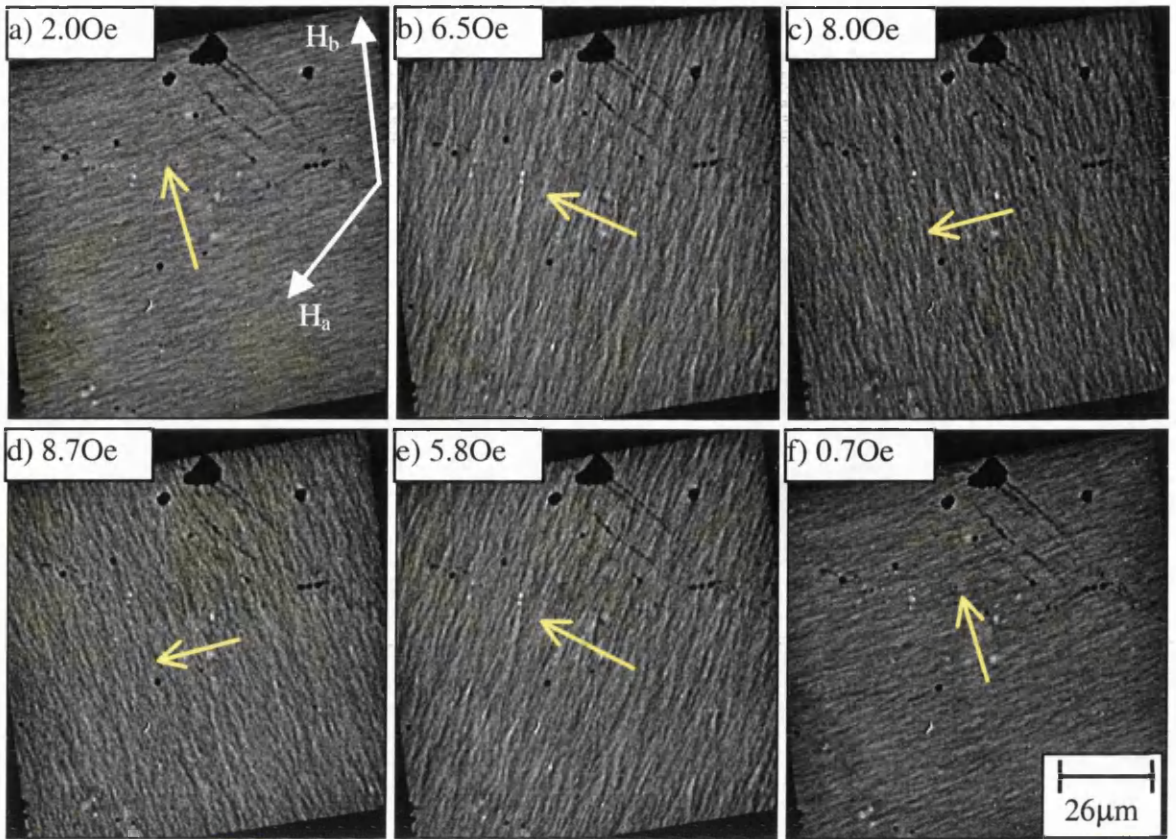


Figure 3.22(a-f): Free layer reversal mechanism for a $Ni_{80}Fe_{20}$ spin-valve with $h_J=1.13$.

The angle of applied field $\theta=132^\circ$.

For spin-valves with $h_J > 1$ mode B-type reversals were observed which were facilitated by the sweeping of a low number of domain walls through the free layer. A mode B-type reversal is characterised by a jump in the direction of magnetisation where the free layer magnetisation vectors do not overshoot the direction of applied field. That is, they are bounded by the half-plane containing the biasing direction and applied field direction. As θ was decreased, the reversal proceeded by increasing levels of rotation of magnetisation. Domain processes still assisted the reversals. However the domain walls that were observed had decreasing wall angles and mobility as θ was decreased.

Eventually, the reversal was better described as coherent rotation of magnetisation incorporating a state of increased dispersion. Although the directions of magnetisation indicated that the reversals were still of mode B in nature. The levels of dispersion decreased steadily as θ decreased, and eventually mode C-type reversals were observed, which was coherent rotation of magnetisation alone.

3.8 INTERPRETATION AND PHASE DIAGRAM

The examples discussed in the previous sections show that the free layer reversal can proceed by a number of mechanisms. Which one is observed depends on the interlayer coupling strength h_J and field orientation θ . Figure 3.23 shows a magnetic phase diagram showing the experimental data points and the predicted phase boundaries^[13]. For spin-valves with interlayer coupling strength $h_J > 1$ a mode B to mode C transition in the free layer reversal is both predicted and observed as the angle of applied field θ is decreased. For spin-valves with interlayer coupling strength $h_J < 1$ two phase transitions are predicted. Firstly a mode A to mode B transition is predicted. Further decrease in θ then results in a mode B to mode C transition. However, for the samples studied with $h_J < 1$ the range of θ over which mode B-type reversals are predicted is relatively small (2° in the maximum case) and were not observed experimentally. Indeed, depending on the strength of the interlayer coupling either a mode B to mode C or mode A to mode C transition was observed. The transition between modes was not as simple as predicted though, but occurred by the gradual increase in the amount of magnetisation rotation and introduction of a high density of low angle domain walls during the reversal. These walls steadily decreased in mobility and were present over a significant field range. The reversal eventually tended towards magnetisation rotation but before mode C reversals were found there was an intermediate region where discrete jumps between two orientations were replaced by rotation with much enhanced dispersion part way through the process. In other words a regime existed where it was difficult to know whether the better description was in terms of a high density of low angle walls or much enhanced magnetisation ripple. In all, the main discrepancy between the observed modes of reversal and the model predictions is the fact that the formation of domains is forbidden in the model but this is only infrequently the case experimentally. The angle θ at which mode C reversal could be ascribed to the free layer reversal was, however, in good agreement with the model as shown in figure 3.23.

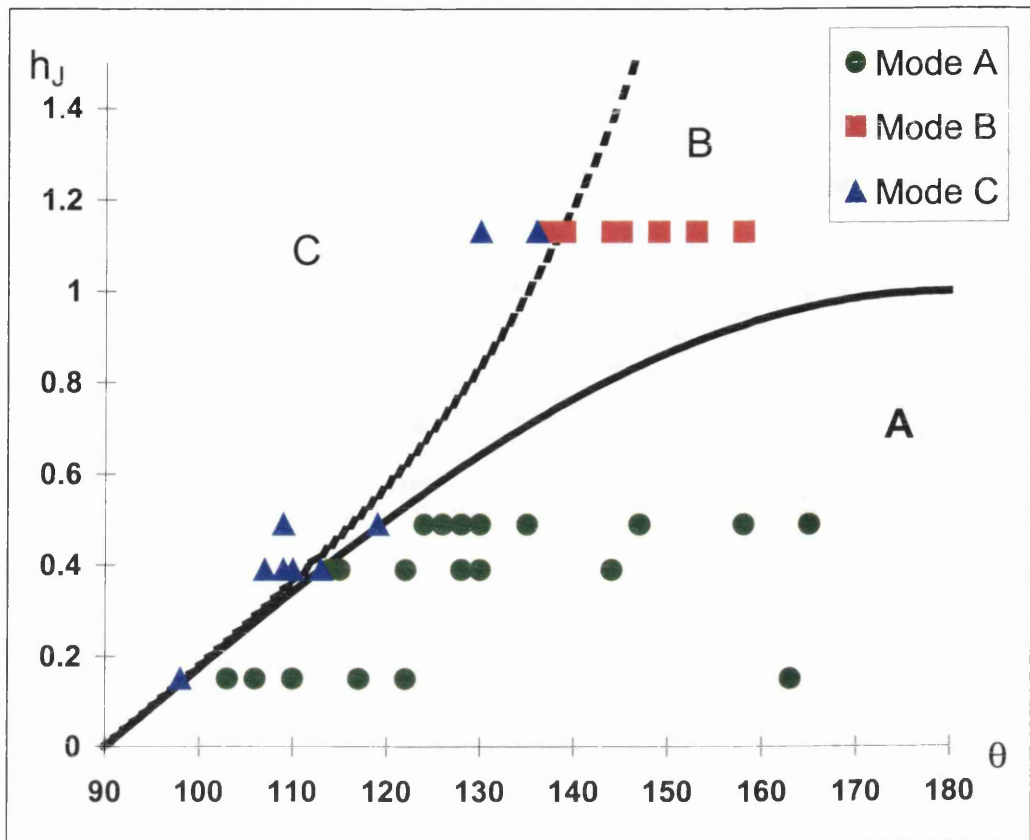


Figure 3.23: Magnetic phase diagram showing experimental data points and experimentally predicted boundaries between modes.

In order to understand more fully the discrepancies between the model and the experimental data it is necessary to look more closely at the way in which the predicted free layer energy varies during the reversal process. This is the topic of discussion in chapter 4.

3.9 CROSSED GEOMETRY

3.9.1 INTRODUCTION

The samples described this far have all been in the parallel anisotropy arrangement. It is also possible to obtain alternative anisotropy arrangements. One method is to rotate the sample (or magnets) between the deposition of successive magnetic layers of the spin-valve. Alternatively the spin-valve can be heated until the antiferromagnetic layer is raised above its Néel temperature and allowed to cool in the presence of a magnetic field. For

device applications a crossed anisotropy arrangement may be desirable in certain circumstances. This corresponds to the easy directions of the free and biased layers lying at 90° to each other.

This section briefly discusses the reversal mechanisms of spin-valves that have crossed anisotropy arrangements obtained by the latter method of cooling in the presence of a magnetic field. Due to the time constraints, only a limited period of study was available for the investigation of spin-valves with alternative anisotropy arrangements. The results in the following section are shown for illustrative purposes and are not intended to serve as a complete discussion on the subject.

3.9.2 CROSSED ANISOTROPY SPIN-VALVES WITH $h_j < 1$

The reversal mechanism of crossed anisotropy spin-valves with the structure 3.5nm Ta / 8.0nm $\text{Ni}_{80}\text{Fe}_{20}$ / 10.0nm Cu / 6.0nm $\text{Ni}_{80}\text{Fe}_{20}$ / 10.0nm FeMn / 5.0nm Ta with $h_j < 1$ were studied in the Philips CM20 electron microscope. Figures 3.24, 3.25 and 3.26 show reversal mechanisms for such a sample at $\theta = 180^\circ$, 150° and 90° respectively. θ is measured relative to the edge of the sample which is coincident with the biasing direction. It can be seen that at all angles of θ that the reversal involves complex domain processes. There is a very high occurrence of 360° wall structures during the reversals, particularly when θ is close to 180° .

At $\theta = 180^\circ$, figure 3.24, there is little magnetisation rotation involved in the reversal process, however erratic domain walls form readily and rapidly sweep through the free layer frequently forming 360° structures as H_a is varied. Alignment with H_a is readily achieved in regions that do not contain 360° walls and loops (which require a much higher field to annihilate them than what is typically required to reverse the rest of the film).

For the case of $\theta = 150^\circ$ more magnetisation rotation is observed than in the case of $\theta = 180^\circ$, however the reversal process is extremely complex involving a mixture of magnetisation rotation and domain assisted processes. The domain walls that form are less mobile than at higher values of θ , however unswitched regions tend to break up into chain-like structures containing many 360° walls, figures 3.25(b,c,d). Again, these are stable and are difficult to remove from the free layer with small applied fields.

At $\theta=90^\circ$, upon increasing the strength of H_a the free layer reversal proceeds by a combination of magnetisation rotation and a discontinuous jump in magnetisation towards the direction of H_a , figure 3.26(a,b). Low angle domain walls form, however these are of high density and low mobility. The direction of the free layer magnetisation after switching lies to the right of H_a , whereas before it was to the left. Following the jump in magnetisation, rotation of the magnetisation in a clockwise sense is observed until alignment is achieved. For the case of decreasing the strength of H_a after alignment is achieved, the magnetisation begins to rotate anticlockwise, back to the right, towards antiparallel alignment with H_b . At $H_a=1.4\text{Oe}$, it has rotated to $\approx 45^\circ$ to the right when reverse domains are nucleated, figure 3.26(d). Decreasing the strength of H_a then causes the magnetisation in these domains to rotate in opposite senses to each other until antiparallel alignment is achieved between the magnetisation in neighbouring domains, figure 3.26(e). This is an energetically unfavourable situation, and the free layer then rapidly breaks up into a complex domain arrangement, by domain wall nucleation and motion, figure 3.26(f).

For all angles of θ , the free layer response is very sensitive to the applied field, with $<50\text{Oe}$ normally required to reverse the majority of the free layer.

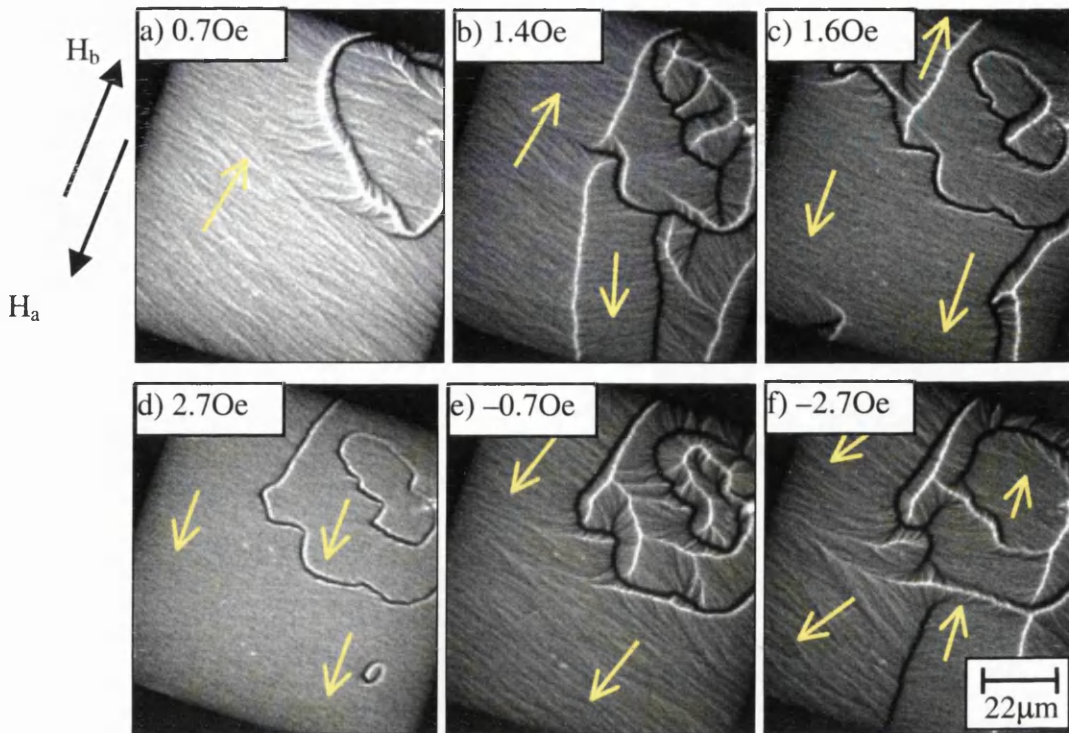


Figure 3.24(a-f): Free layer reversal mechanism for a $Ni_{80}Fe_{20}$ crossed spin-valve with $h_J < 1$. The angle of applied field $\theta = 180^\circ$.

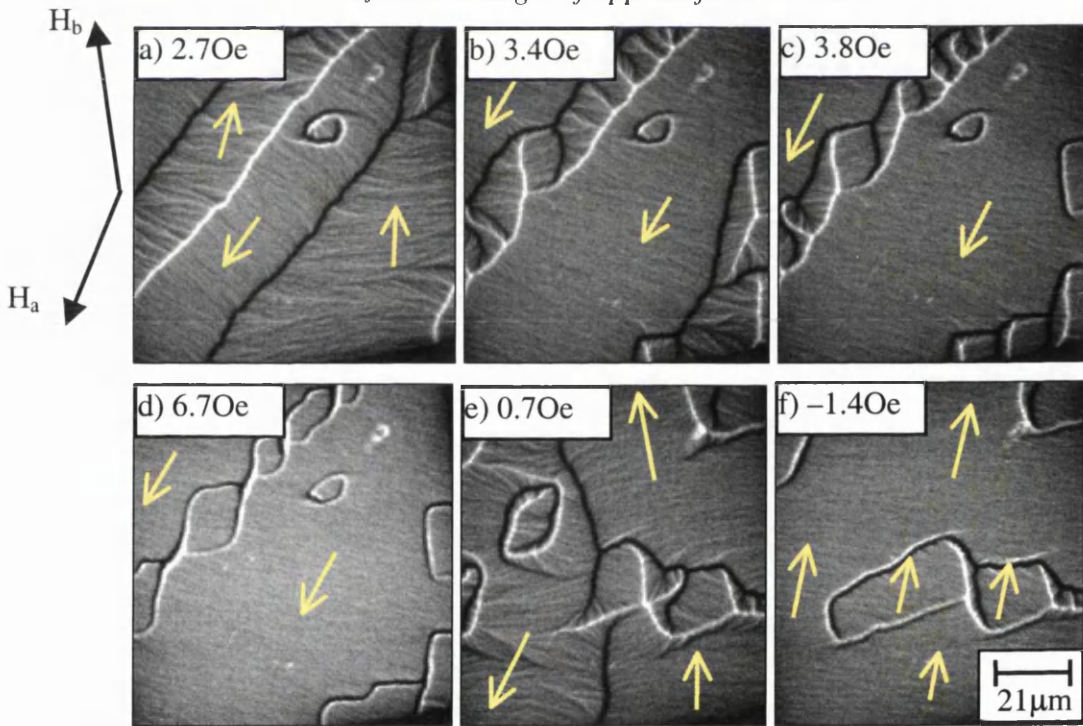


Figure 3.25(a-f): Free layer reversal mechanism for a $Ni_{80}Fe_{20}$ crossed spin-valve with $h_J < 1$. The angle of applied field $\theta = 150^\circ$.

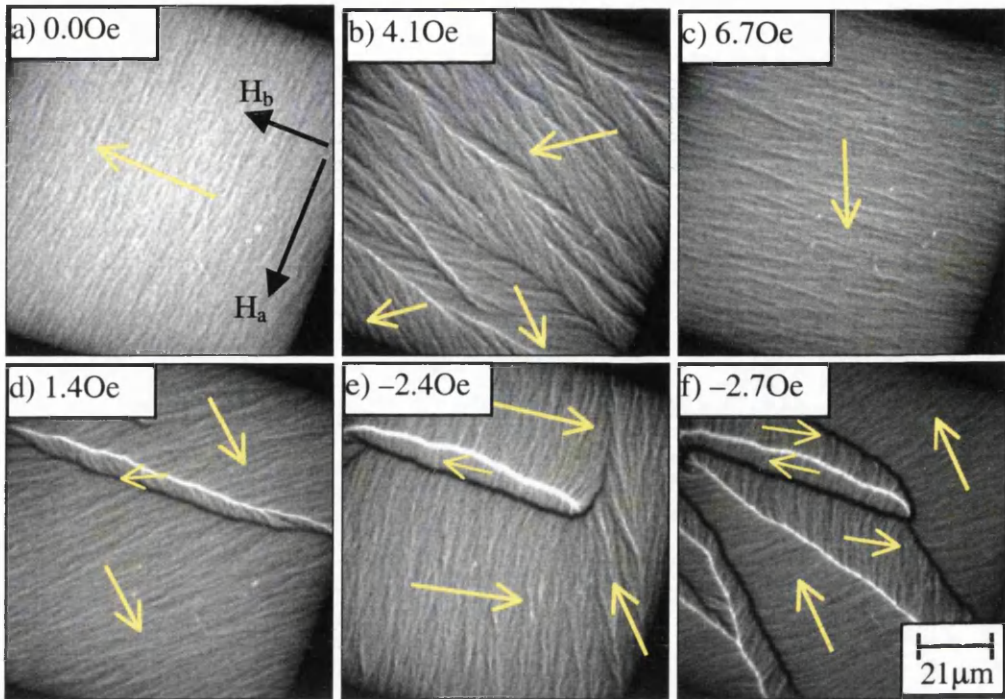


Figure 3.26(a-f): Free layer reversal mechanism for a $Ni_{80}Fe_{20}$ crossed spin-valve with $h_J < 1$. The angle of applied field $\theta = 90^\circ$.

We have seen that the free layer reversal in crossed anisotropy spin-valves with $h_J < 1$ is extremely complex compared to the parallel anisotropy case. The model^[13] predicts that as θ is reduced a mode A to mode B transition should be observed for the free layer reversal mechanism and that coherent rotation of magnetisation alone should never be achieved. In comparison with the model this is the only similarity that can be easily confirmed. It is noted that the thickness of the copper spacer layer in this case is 10nm, which results in a low interlayer coupling strength (recall $h_J = 0.15$ for a parallel anisotropy spin-valve with $t_{Cu} = 10\text{nm}$). Hence, it is impossible to make conclusive judgements from this sample alone, and a more detailed study of samples with a greater range of coupling strengths is required. For example, see section 7.3.1: future work.

3.10 DISCUSSIONS AND SUMMARY

In this chapter the structural and magnetic properties of FeMn-biased spin-valves was discussed. Investigations of the structural properties showed that the average grain size and distribution increased as the sample thickness increased. The smallest grain size that was observed was $3 \pm 1\text{nm}$, and grains of this size were observed in all of the investigated

films. In the thicker films larger sized grains were common (up to approximately 25nm diameter). Closer inspection revealed that these were in fact groups of smaller grains closely grouped together. The upper limit of average grain size was estimated to be of the order of 10-12nm in diameter.

Investigations of the diffraction patterns showed that considerable $\langle 111 \rangle$ texturing was present in all of the films. It also showed that the Ta layers were body centred cubic ($a=0.330\text{nm}$) and the ferromagnetic layers were face centred cubic ($a=0.352\text{nm}$).

The study of the magnetic properties of spin-valves concentrated on parallel anisotropy cases, however some data on crossed geometry was presented.

For parallel anisotropy spin-valves easy axis reversals showed that the free layer reversed by the magnetisation orientation changing from parallel to antiparallel alignment with the biasing direction and back again. The reversal was assisted by the rapid sweeping of domain walls through the free layer. These reversals also allowed the strength of the interlayer coupling strength to be measured, which was in the range 0.15 to 1.13 for the studied spin-valves.

The reversal mechanism of parallel anisotropy spin-valves was intensively investigated as a function of applied field direction θ . Three modes of reversal were identified depending on the strength of h_J and the value of θ .

For spin-valves with $h_J < 1$ mode A type reversals were observed as θ was decreased from 180° . This mode of reversal is shown schematically in figure 3.27(a) and corresponds to cases where the uniaxial anisotropy K of the sample dominates. Eventually the reversal proceeded by coherent rotation of magnetisation alone (mode C-type reversal). This is shown schematically in figure 3.27(c). The boundary between modes was shown to be indistinct, and involved the free layer reversal proceeding by an increasing amount of magnetisation rotation as θ was decreased. This was accompanied by the formation an increasing density of low angle domain walls which had low angle and mobility. Eventually the reversal could be best described as coherent rotation of magnetisation involving a state of increased dispersion part of the way through the process until coherent rotation of magnetisation alone was observed.

For spin-valves with $h_J > 1$ mode B type reversals were initially observed when θ was decreased from 180° . This mode is shown schematically in figure 3.27(b). It corresponds to the cases where the interlayer coupling strength is sufficiently strong to constrain the free layer magnetisation to the half plane containing H_b and H_a . In this case

similar trends in the reversal mechanism were observed as θ decreased until mode C-type reversals were eventually observed.

A phase diagram with the experimental data points and predicted phase boundaries was shown. Although the predicted boundaries between modes was distinct, and experimentally the change was gradual, the angle at which mode C type reversals were both observed and predicted were in general agreement.

A crossed anisotropy spin-valve with $h_j < 1$ was briefly investigated. The limited results shown show that the free layer reversal was extremely complex for all angles of applied field. Although an increasing amount of magnetisation rotation was observed as θ was decreased, complex domain processes were observed at all angles of θ . These type of reversals are not fully understood at present, and a more detailed investigation of alternate anisotropy arrangements is required before detailed conclusions can be made.

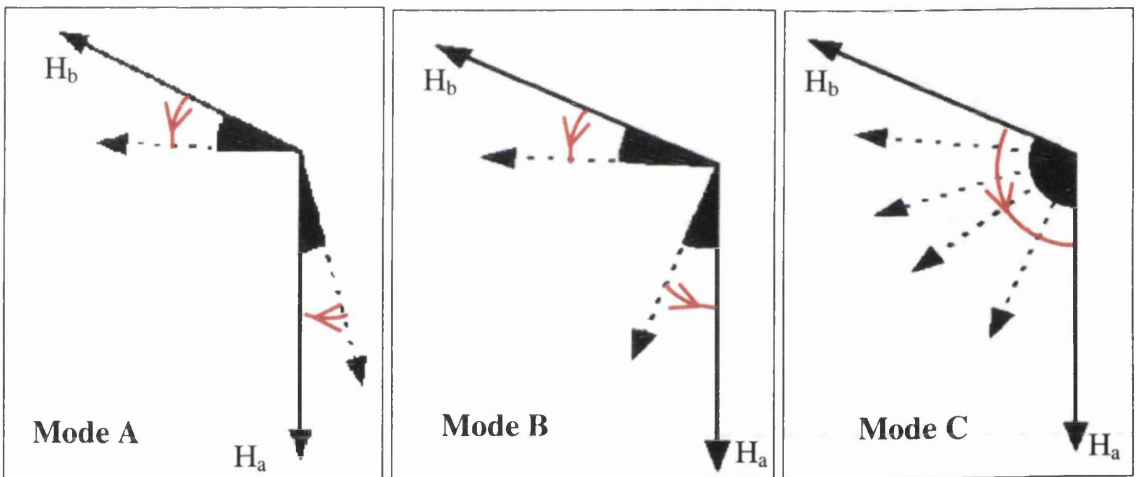


Figure 3.27(a-c): Schematic representations of free layer modes of reversal.

REFERENCES

- [1] Rijks Th-G S et al, (1994), *J. Appl. Phys.*, **76**, 1092.
- [2] Chikazumi S, (1964), in “*Physics of Magnetism*” ed. S.H. Charap, (J Wiley & Sons).
- [3] Gillies M F et al, (1995), *J. Appl. Phys.*, **78**, 5554.
- [4] Folkerts W et al, (1994), *IEEE Trans. Magn*, **MAG-30**, 3183.
- [5] Gillies M F, Chapman J N, Kools J C S, (1995), Presented MML conference. Cambridge, 1995
- [6] Gillies M F, (1996) Thesis, University of Glasgow.
- [7] Jacobs J W M, Verhoven J F C M, (1986), *J. of Microscopy*, **143**, 103.
- [8] Dieny B, Gurney B A, Lambert S, Mauri D, Parkin S S P, Speriosu V S, Wilhoit D R, US patent 5206590.
- [9] Wilts C H, Humphrey F B, (1968), *J. Appl. Phys.*, **69**, 1191.
- [10] Kitade Y et al, (1995), *IEEE Trans. Magn.*, **31**, 2000.
- [11] Mayazaki T et al, (1994), *J. Magn. Magn. Mat.*, **129**, pp L135.
- [12] Rijks Th. G S M et al, (1997), *J. Appl. Phys.* **82**, 7.
- [13] Labrune et al, *J. Magn. Magn. Mater.* **171** (1997) 1.

CHAPTER 4: MAGNETIC MODELLING OF THE FREE LAYER REVERSAL OF FeMn BIASED SPIN-VALVES.

4.1 INTRODUCTION

In order to gain a deeper understanding of the free layer reversals discussed in the previous chapter, magnetic modelling of the free layer energy of the spin-valve is now presented. A modified Stoner-Wohlfarth coherent rotation model developed by Labrune^[1] is introduced. It is then used to model the free layer energy variation as a function of magnetisation orientation for the spin-valves discussed in chapter 3. The discrepancies between the model and experimental observations are also discussed. Finally, a qualitative description of the observed domain processes is given in relation to the free layer energy for the corresponding experimental conditions.

4.2 MODELLING OF THE FREE LAYER REVERSAL PROCESS

The model makes 3 approximations:

- i) Homogeneous magnetisation in the plane of the film:
This forbids the presence of domains and domain processes in the spin-valve.
- ii) Homogeneous magnetisation along the film normal within a layer:
Thus there can be no “twist” of the magnetisation vector within a ferromagnetic film.
- iii) The biased layer magnetisation remains fixed:
i.e the pinned layer remains fixed in direction over the field interval of interest for the free layer reversal.

Under these assumptions the energy function per unit area is:

$$E = KD \sin^2 \varphi - \mu_0 D \underline{M} \cdot \underline{H}_{eff} \quad 4.1$$

Here K is the anisotropy (assumed to be uniaxial) of the free layer and D is its thickness; φ is the angle of free layer magnetisation with respect to the biasing direction, \underline{M} is the magnetisation vector and $\underline{H}_{\text{eff}}$ is the effective field - the vector sum of the applied field \underline{H}_a and interlayer coupling field \underline{H}_j . Normalising E by KD gives

$$\Gamma = \frac{E}{KD} = \sin^2 \varphi - 2\underline{h}_{\text{eff}} \cdot \underline{m} \quad 4.2$$

Γ is the reduced energy per unit area for the parallel anisotropy case and $\underline{m} = \underline{M}/M$ a unit vector along the direction of magnetisation. H_K is the anisotropy field.

$$\underline{h}_{\text{eff}} = \underline{h}_a + \underline{h}_j \quad 4.3$$

where

$$\underline{h}_{\text{eff}} = \frac{H_{\text{eff}}}{H_K} \quad H_K = \frac{2K}{\mu_0 M} \quad \text{and} \quad \underline{h}_j = \frac{H_o}{H_K}$$

The anisotropy axis and biasing field, H_b , are both oriented along the negative x-axis, figure 3.2 (repeated again in figure 4.1 below). Thus in the xy-plane one gets:

$$\Gamma = \sin^2 \varphi - 2h_x \cos \varphi - 2h_y \sin \varphi \quad 4.4$$

where

$$h_x = -h_a \cos \theta - h_j$$

$$h_y = h_a \sin \theta$$

are the x and y components of $\underline{h}_{\text{eff}}$ respectively.

It is important to note that the interlayer coupling is equivalent to an additional constant field component along the negative x-axis. By using equation 4.4 it is possible to calculate how the free layer energy varies for a given spin-valve as a function of applied field strength along the direction θ .

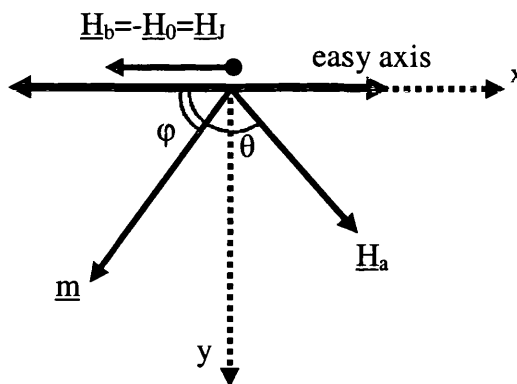


Figure 4.1: Orientation of in-plane magnetisation vectors.

To use the model and to compare its predictions with what is observed experimentally, values must be assigned to various parameters. Experimentally we determine H_1 and H_2 , the fields at which the free layer switches and also the orientation of the magnetisation φ before and after the switch. From the values of H_1 and H_2 when $\theta=180^\circ$, the easy axis offset H_0 is determined and this, normalised by H_K (see section 4.2) allows the reduced interlayer coupling strength h_j to be calculated.

4.3 MODELLING OF THE FREE LAYER EASY AXIS REVERSAL

The reduced energy density curves for an easy axis reversal ($\theta=180^\circ$, $H_0=5.25\text{Oe}$ ($h_j=1.13$)) have been calculated using equation 4.4 and are shown in figure 4.2(a) for various applied field strengths. At $H_a=0.6\text{Oe}$ there is an energy minimum at $\varphi=0^\circ$ and a maximum at $\varphi=180^\circ$. This means that the equilibrium free layer magnetisation lies at $\varphi=0^\circ$, along the biasing direction, and the most energetically unfavourable orientation of the free layer magnetisation is antiparallel to the bias direction. As H_a is increased to 3.4Oe the minimum still lies at $\varphi=0^\circ$, albeit at a higher value whilst around $\varphi=180^\circ$ a local energy minimum forms. At $H_a=H_0=5.25\text{Oe}$ the energy of the $\varphi=0^\circ$ and $\varphi=180^\circ$ states is equal. Large energy barriers separate the two minima with their maxima at $\varphi=90^\circ$ and 270° . Increases in H_a above 5.25Oe result in $\varphi=180^\circ$ becoming the global minimum and there is a continuing reduction in the energy barriers; however, it is not until $H_a=9.9\text{Oe}$ that the energy barrier vanishes. A discontinuous jump in magnetisation from $\varphi=0^\circ$ to $\varphi=180^\circ$ is then predicted. In the opposite case of decreasing H_a the description is reversed whereby

the magnetisation lies at $\varphi=180^\circ$ until the corresponding energy barrier vanishes at $H_a=0.6\text{Oe}$. The above therefore predicts a free layer magnetisation reversal in which the magnetisation discontinuously jumps from $\varphi=0^\circ$ to $\varphi=180^\circ$ at $H_a=9.9\text{Oe}$ and vice versa when $H_a=0.6\text{Oe}$.

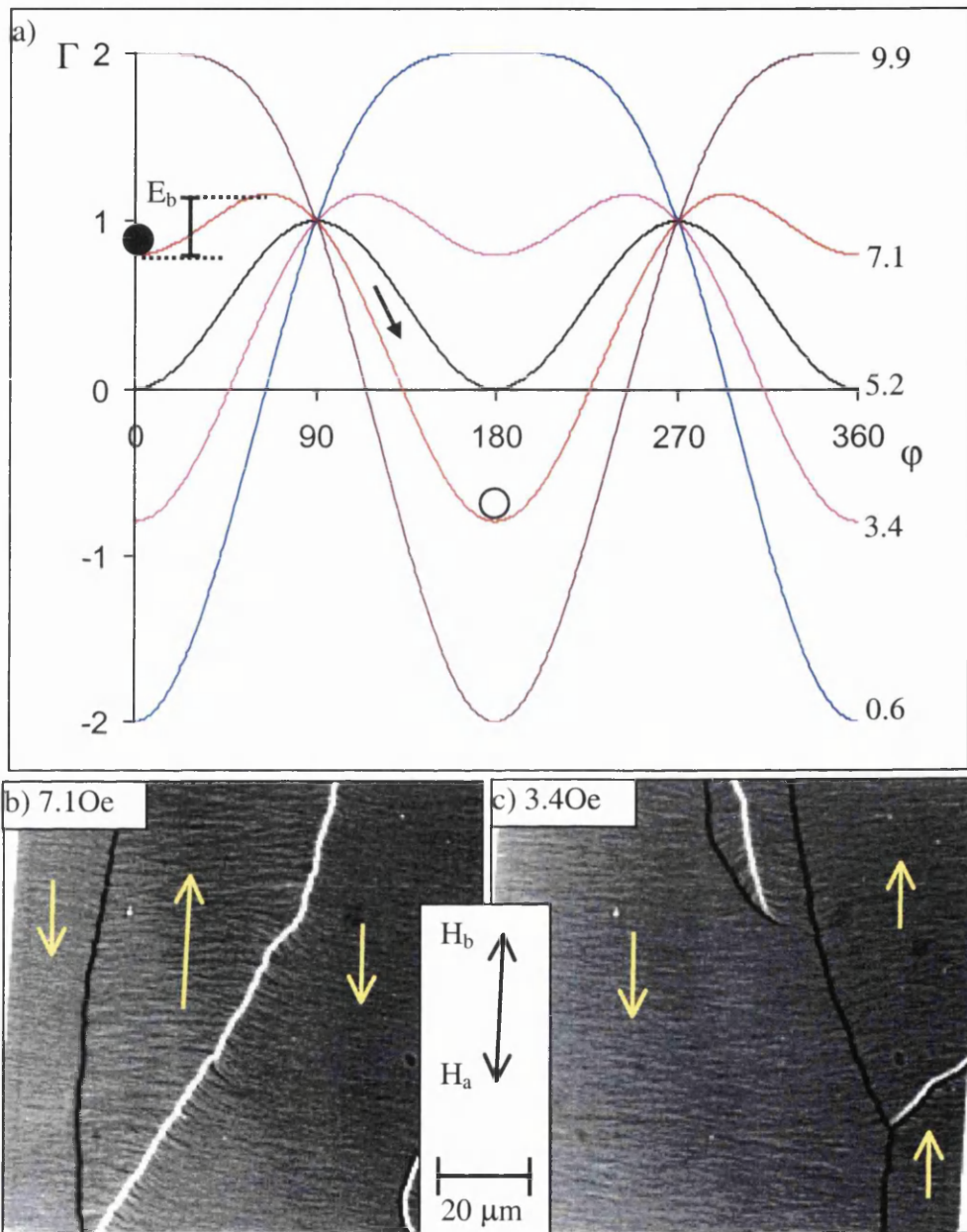


Figure 4.2: (a) Energy versus φ curves for a spin-valve with $H_0=5.25\text{Oe}$ ($h_J=1.13$) for various applied strengths at $\theta=180^\circ$, (b) and (c) Fresnel images at the switching fields.

Figures 4.2(b,c) show the experimental free layer reversal for the above case. It is found that at $\theta=180^\circ$ the free layer magnetisation lies at $\varphi=0^\circ$ until $H_a=7.1\text{Oe}$. A low number of

domain walls then rapidly sweep through the free layer facilitating reversal of the magnetisation to $\varphi=180^\circ$. Upon decreasing H_a the magnetisation in the free layer lies at $\varphi=180^\circ$ until $H_a=3.4\text{Oe}$ when domains assist in the reversal of the magnetisation to $\varphi=0^\circ$. By considering figure 4.2a it can be seen that the free layer reversal has occurred at an applied field $H_a=H_1$ which is less than the switching field predicted by the model, denoted H_{s1} . The respective values are 7.1Oe compared to 9.9Oe . Also, for the decreasing field case the experimental switching field H_2 is reached before the theoretical switching field which is denoted by H_{s2} (3.4Oe compared to 0.6Oe). The energy barrier is overcome during the free layer reversals by the formation of domains, which are forbidden in the model. Growth of domains whose magnetisation is favourably oriented is obtained by rapid motion of a low number of domain walls through the free layer.

4.4 MODELLING OF MODES OF REVERSAL

Figure 4.3 shows Γ vs φ curves for the mode A reversal discussed for the spin-valve with $h_j=0.49$ at $\theta=145^\circ$ (figure 3.11). As the strength of H_a is increased the energy minimum shifts to the right from its initial position at $\varphi=0^\circ$ (solid marker) - corresponding to magnetisation rotation in an anticlockwise sense. At 17.0Oe the energy barrier vanishes and a discontinuous jump in the magnetisation vector to $\varphi=159^\circ$ (14° overshoot from H_a) is predicted. As H_a is increased further the energy minimum shifts towards the applied field direction (open marker) corresponding to magnetisation rotation in the clockwise sense. This is characteristic of a mode A reversal. However, experimentally we have observed magnetisation rotation followed by domain processes at 14.3Oe, with the resultant magnetisation vector overshooting H_a by $\approx 7^\circ$ after which the magnetisation vector rotates back towards H_a until alignment is obtained. It can be seen from figure 4.3 that an energy barrier was overcome at the switching field of 14.3Oe which is where domains were observed to be formed, figure 3.11.

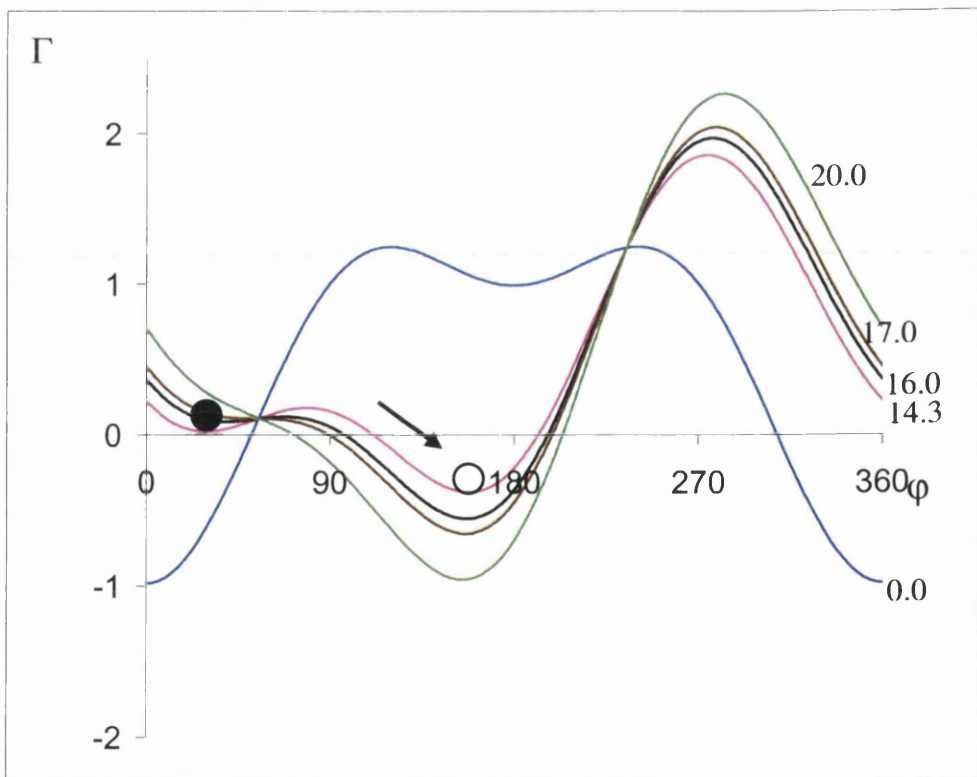


Figure 4.3: Energy versus φ curves for a spin-valve with $H_0=9.55\text{Oe}$ ($h_j=0.49$) for various applied field strengths expressed in Oe at $\theta=145^\circ$.

Figure 4.4 shows how Γ varies for a mode B reversal for the spin-valve with $h_J=1.13$ at $\theta=155^\circ$ (figure 3.18). In this case the energy minimum also shifts to higher values of φ upon initial increase of H_a . At 6.6Oe the energy barrier vanishes with the magnetisation predicted to jump to the energy minimum at $\varphi=149^\circ$. Further increase in H_a causes the energy minimum to continue to shift in the same sense towards H_a at $\varphi=155^\circ$, characteristic of a mode B reversal.

Experimentally however, the free layer reversal proceeds by a mode B reversal but involves domain processes at $H_a=6.2\text{Oe}$. Again an energy barrier is overcome, as can be seen in figure 4.4. Also note that the model predicts a larger amount of magnetisation rotation than is observed experimentally.

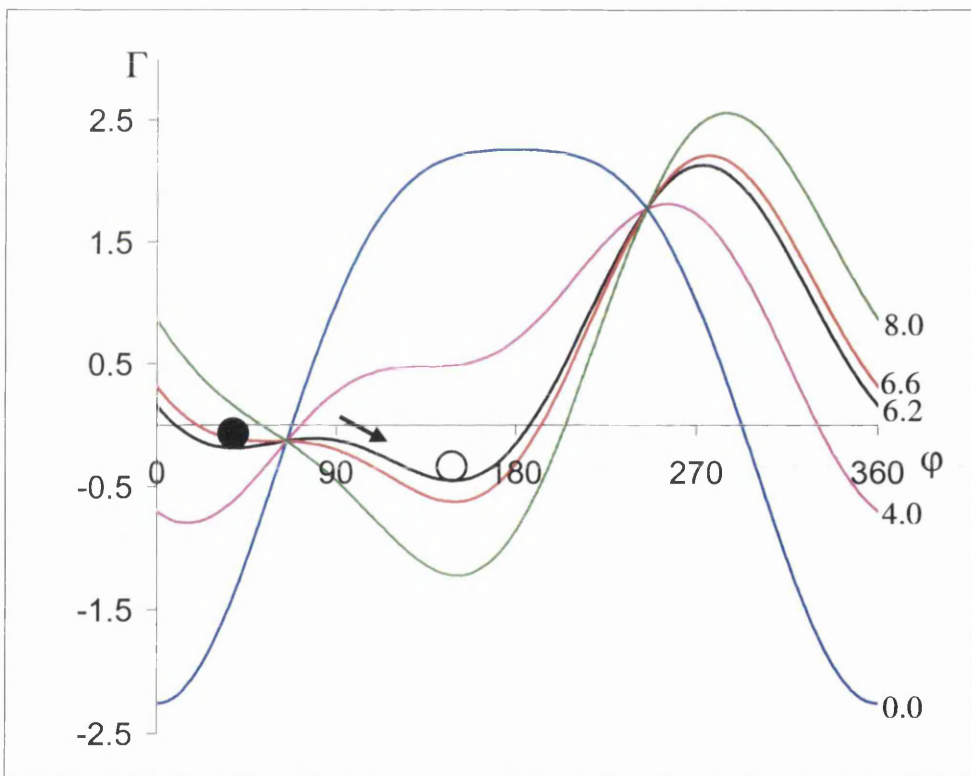


Figure 4.4: Energy versus φ curves for a spin-valve with $H_0=5.25\text{Oe}$ ($h_J=1.13$) for various applied field strengths expressed in Oe at $\theta=155^\circ$.

Figure 4.5 shows Γ vs φ curves for a spin-valve with $h_j=0.38$ at $\theta=112^\circ$ for which a mode C reversal was observed (figure 3.17). In this case there is only a single global energy minimum as the applied field is increased from zero. The magnetisation vector lies in the minimum and steadily shifts to increasing angle as indicated, corresponding to coherent rotation of magnetisation.

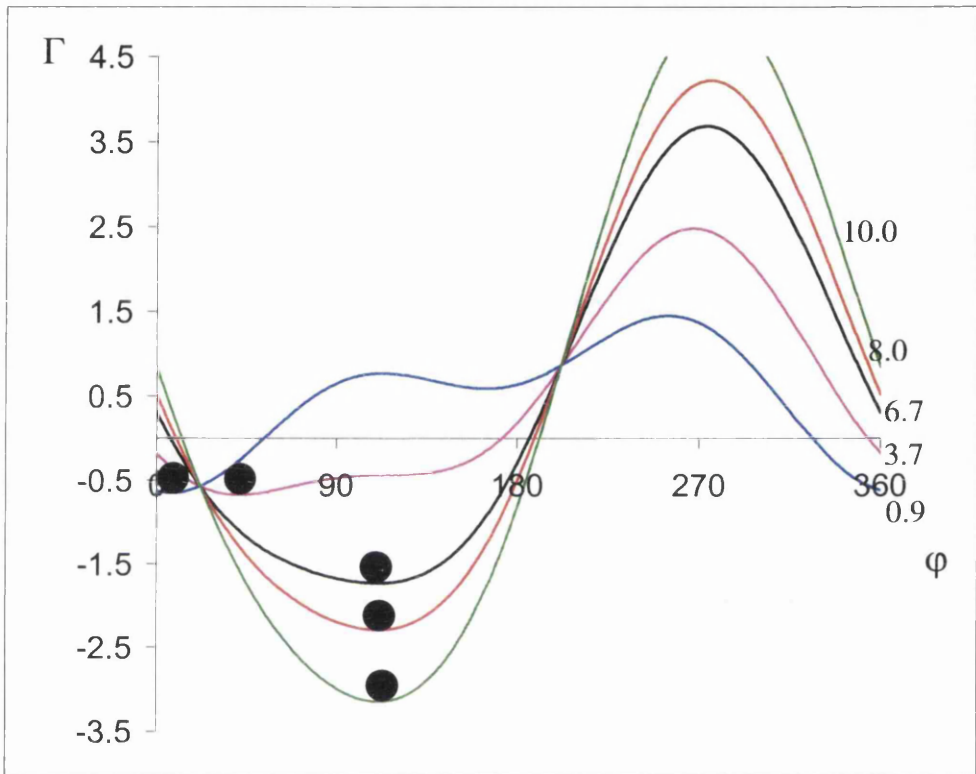


Figure 4.5 Energy versus φ curves for a spin-valve with $H_0=1.8\text{Oe}$ ($h_j=0.38$) for various applied field strengths expressed in Oe at $\theta=112^\circ$.

We have seen that 3 modes of reversal are both predicted and observed. However for mode A and mode B reversals, domain processes in the free layer facilitate the overcoming of an energy barrier and switching is observed at a field that is less than predicted. The applied field strength H_{s1} (or H_{s2}) at which the discontinuous jump in magnetisation vector is predicted occurs when the energy barrier to the global energy minimum vanishes. The theoretically predicted and experimentally observed switching fields are plotted in figure 4.6 for the spin-valve with $h_j=1.13$ as a function of θ .

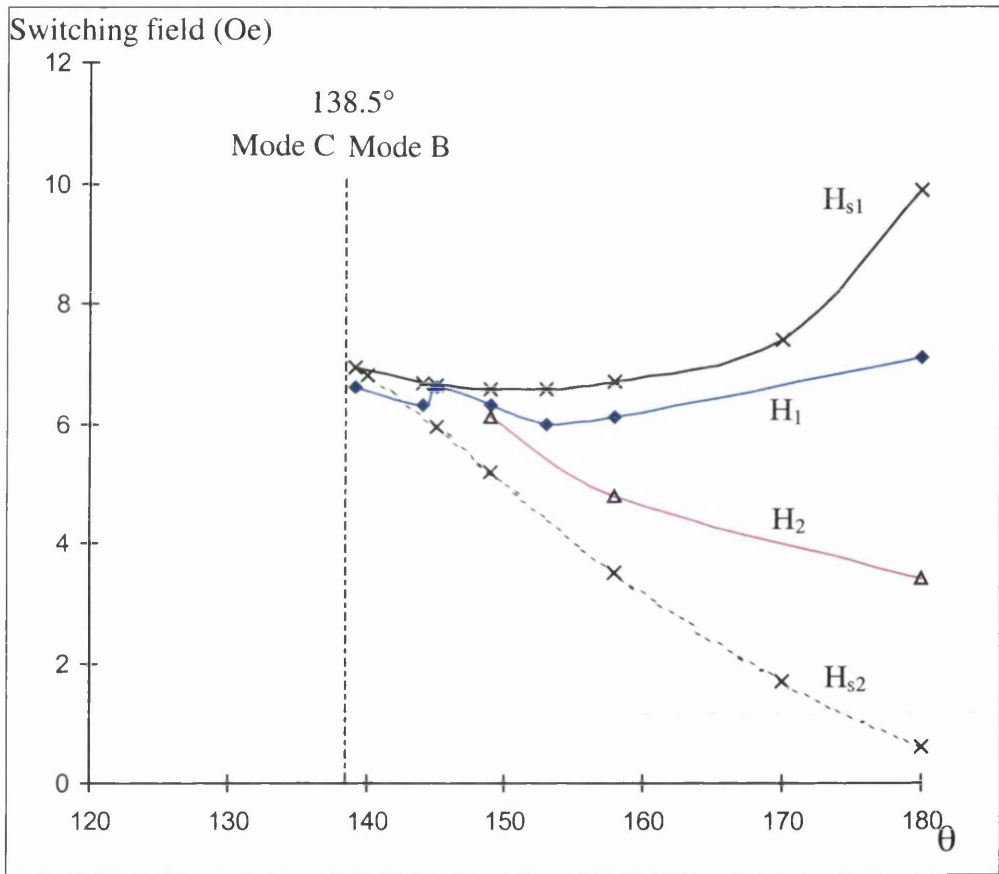


Figure 4.6: Experimental and theoretical switching fields as a function of θ ($h_j=1.13$).

On this figure and in discussions below, the theoretically predicted switching field for increasing field strength is labelled H_{s1} and the corresponding experimental field labelled H_1 . For the decreasing field case, the theoretical and experimental switching fields are labelled H_{s2} and H_2 respectively. Mode B reversals are predicted for the range $138.5^\circ < \theta < 180^\circ$ and mode C reversals for $\theta < 138.5^\circ$. A large decrease in H_{s1} is observed upon initial decrease of θ from 180° . Thereafter a slight increase is observed as the

boundary with mode C is approached. For the decreasing field case, H_{s2} steadily increases as θ is decreased. At the phase boundary between modes B and C, the two switching fields converge and H_s curves vanish as coherent rotation of magnetisation is then predicted. The experimental results are also shown on the curve, and similar trends are observed. However, H_1 is observed at a field which is less than the predicted value H_{s1} and H_2 is observed at a field which is greater than the predicted value H_{s2} . The difference between the predicted and observed curves decreases, and is less than 1.5Oe for $\theta < 165^\circ$. This is due to the fact that as θ is decreased the field at which the two energy minima become equal is much closer to H_s and only a low energy barrier results once it becomes favourable to switch to the global minimum.

As the experimentally observed switching fields lie within the predicted curves for the range of θ studied, an energy barrier must have been overcome in order for the magnetisation reversal to proceed. The reduced energy barrier density $\Delta E/KD$ which was overcome during the reversals is plotted as a function of θ in figure 4.7. This is a maximum at $\theta = 180^\circ$ and decreases rapidly as θ decreases towards the boundary with mode C.

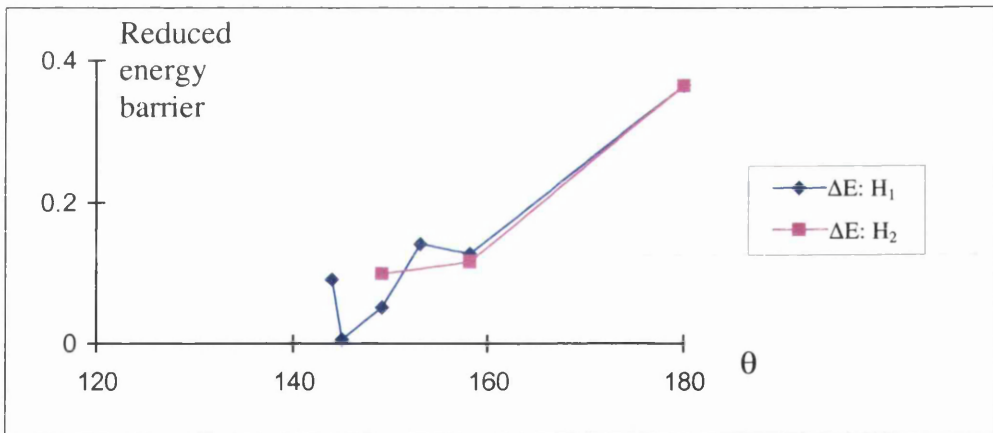


Figure 4.7: Energy barrier as a function of θ at experimental switching field ($h_J = 1.13$).

For the case of a spin-valve with $h_J = 0.38$ (< 1), mode A reversals are predicted from $112.8^\circ < \theta < 180^\circ$ and mode B from $111.2^\circ < \theta < 112.8^\circ$. Thereafter mode C is predicted. Note that mode B is only predicted to be observed over a small angular range ($< 2^\circ$) and was not observed. The switching field against θ curves are shown in figure 4.8. In this case the two theoretical curves H_{s1} and H_{s2} do not converge as θ is decreased. There is a large difference

in the predicted switching fields for all angles of applied fields, right down to the boundary with mode B.

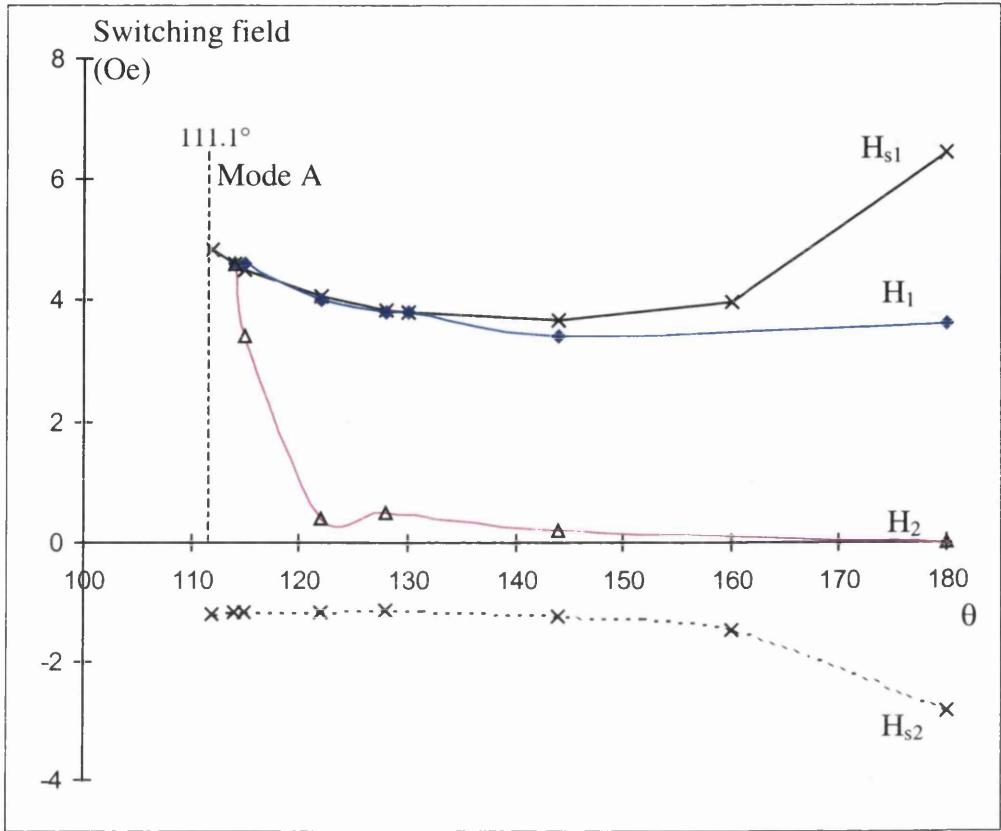


Figure 4.8: Experimental and theoretical switching fields as a function of θ ($h_J=0.38$).

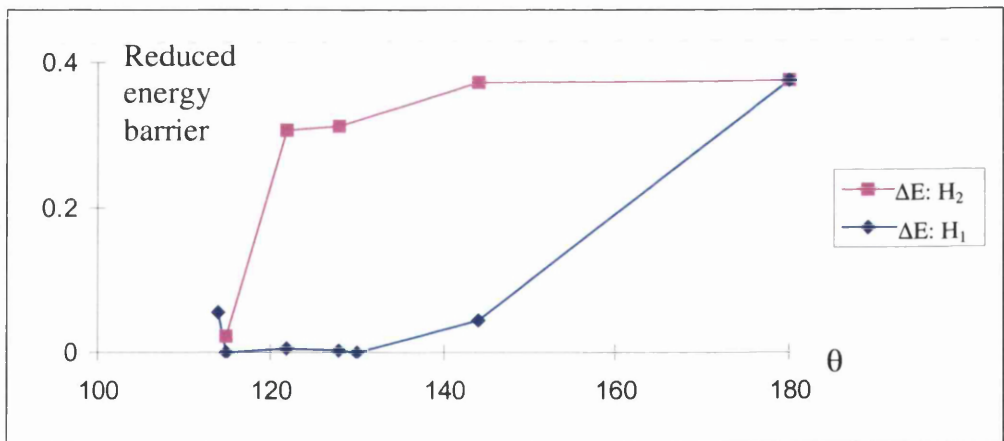


Figure 4.9: Energy barrier as a function of θ at experimental switching field ($h_J=0.38$).

The H_1 curve shows a significant discrepancy from H_{s1} at $\theta=180^\circ$ but this rapidly decreases as θ decreases and close agreement between the two curves is obtained. The

energy barrier which is overcome decreases as θ is decreased, figure 4.9. H_2 does not converge with its theoretical counterpart H_{s2} . There is a difference of approximately 1.5Oe until θ is decreased below 122° . A large increase in H_2 is then observed, the values rapidly approaching that of H_{s1} , figure 4.8. The reduced energy barrier which is overcome in this case stays approximately constant at ≈ 0.3 until $\theta < 122^\circ$. It then falls rapidly to almost zero. Upon investigation of the energy curves, two cases are observed for decreasing applied field strengths depending upon the angle of applied field θ .

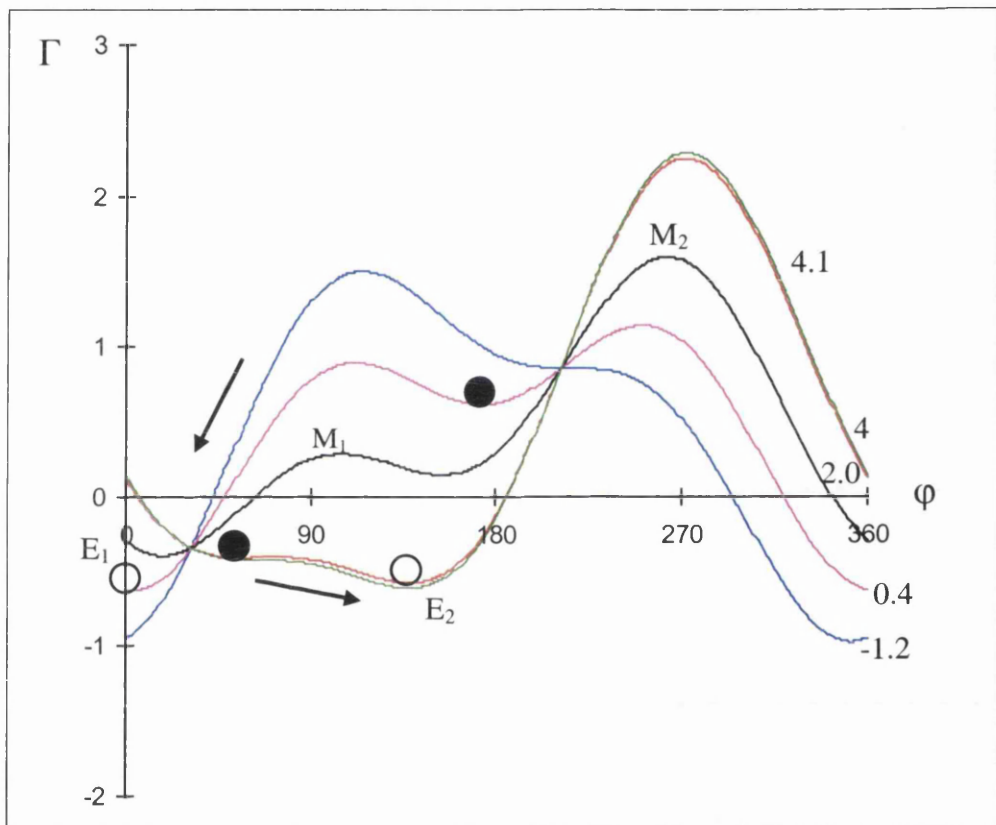


Figure 4.10: Energy versus ϕ curves for a spin-valve with $H_0=1.8\text{Oe}$ ($h_j=0.38$) for variable applied field strengths (Oe) at $\theta=122^\circ$.

As the applied field strength is decreased towards H_{s2} for a given θ the energy minimum E_2 within which the magnetisation lies steadily increases, figure 4.10, so that the minimum E_1 quickly becomes the global minimum. However, there is a small energy maximum M_1 which must be overcome before a transition can proceed. As the applied field is decreased further the rate of increase of M_1 is more rapid than the rate of increase of E_2 . The energy barrier M_1-E_2 therefore increases. It is in fact the energy maximum M_2 which decreases in

energy and vanishes at H_{s2} . In practice domains form at 0.4Oe. The energy barrier M_1-E_2 (which is approximately equal to 0.3 in reduced units) is overcome at this field. This barrier is not the one which vanishes at H_{s2} .

In the second regime $111.2^\circ < \theta < 122^\circ$, the experimentally observed switching field, H_2 , increases rapidly and approaches H_{s1} . Similar behaviour in the energy curves is observed as in the above case, but now the free layer reversal proceeds when the energy barrier M_1-E_2 is low and the applied field strength is still close to H_{s1} .

We now summarise the results for the other two spin-valves with $h_j=0.49$ and $h_j=0.15$. For the spin-valve with $h_j=0.49$ the form of the theoretical switching curves is similar to that for $h_j=0.38$ but experimentally the same trends as displayed by the strongly coupled spin-valve with $h_j=1.13$ are observed. However, the difference in switching fields is larger than for the $h_j=0.38$ spin-valve. This is because $Ni_{66}Fe_{16}Co_{18}$ is used for the ferromagnetic layers and has a higher anisotropy than $Ni_{80}Fe_{20}$. For the weakly coupled spin-valve with $h_j=0.15$ the experimentally observed switching field curves approach the predicted ones as θ is decreased. Furthermore during free layer reversal the energy barrier which is overcome by domain processes is the one that vanishes at the theoretically predicted switching field as was the case for the spin-valve with $h_j=1.13$.

4.5 DOMAINS AND DOMAIN WALL CONSIDERATIONS

The mode A and mode B free layer reversals that have been observed involve the formation of domain walls and these play a key role in the switching process. In the case of mode C where coherent rotation of magnetisation was observed the free layer remains single domain throughout. The properties of domains observed during the first two modes of reversal are now the subject of discussion. Three cases in particular are highlighted with relation to the appropriate Γ vs φ curves.

4.5.1 CASE 1

Figure 4.11 shows Fresnel images corresponding to the reversal of the free layer in a spin-valve with $h_j=0.15$ at $\theta=163^\circ$. The values of applied field at which switching occurs and the directions of magnetisation are indicated. For both increasing and decreasing H_a the free layer reversal is assisted by a small number of domain walls which rapidly sweep

through the free layer facilitating growth of domains with favourably oriented magnetisation. Inspection of the Γ vs φ curves for these experimental conditions, figure 4.11(c), shows that once the associated energy barrier has been overcome a large saving in energy is obtained by magnetisation switching to the deeper energy minimum. The wall angles observed are large: close to 180° and the walls are approximately parallel to the applied field direction.

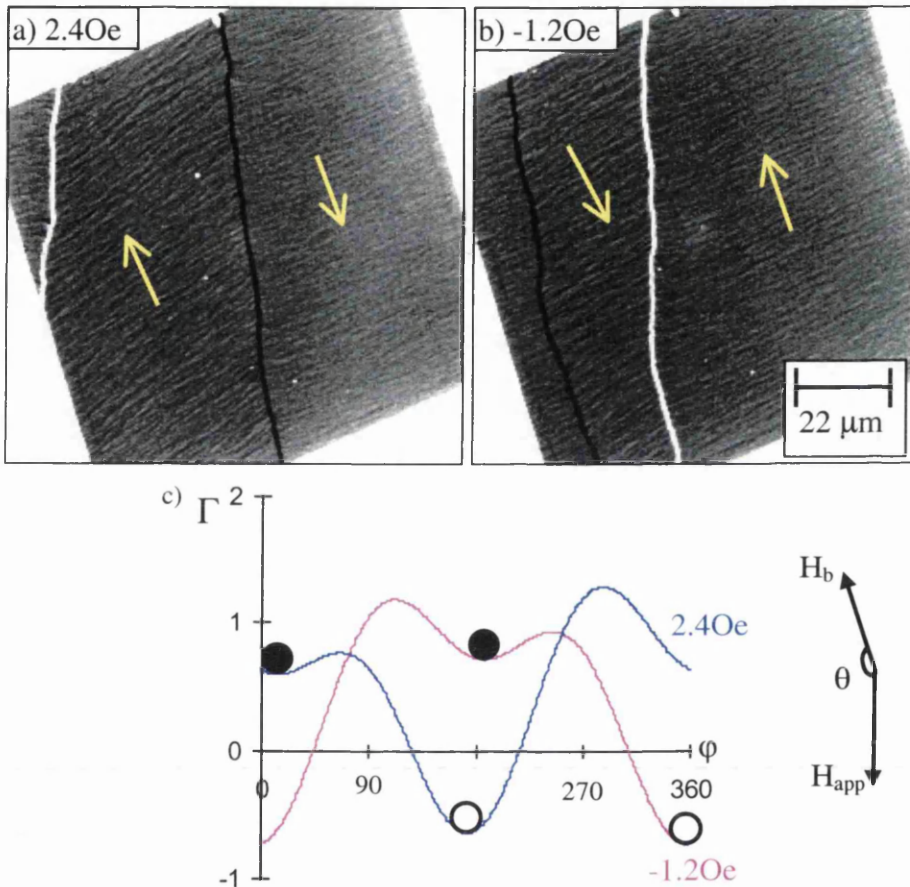


Figure 4.11: Free layer reversals for a spin-valve with $h_j=0.15$ at $\theta=163^\circ$ and associated energy curves.

This results in a large force upon the wall therefore giving it high mobility. The low number of observed domain walls is accounted for by considering the probability of domain wall formation. Within a given energy range a low range of magnetisation angles are permitted - corresponding to deep energy minima. As the energy barriers are relatively large and the magnetisation lies within a small range of angles around the minimum there

will be relatively few sites available for domain wall nucleation. However, once a wall does form, it propagates rapidly through the free layer, resulting in a large energy saving.

Figure 4.12 shows another example of this type of behaviour for a spin valve with $h_J=0.49$ at $\theta=165^\circ$, and confirms the above result.

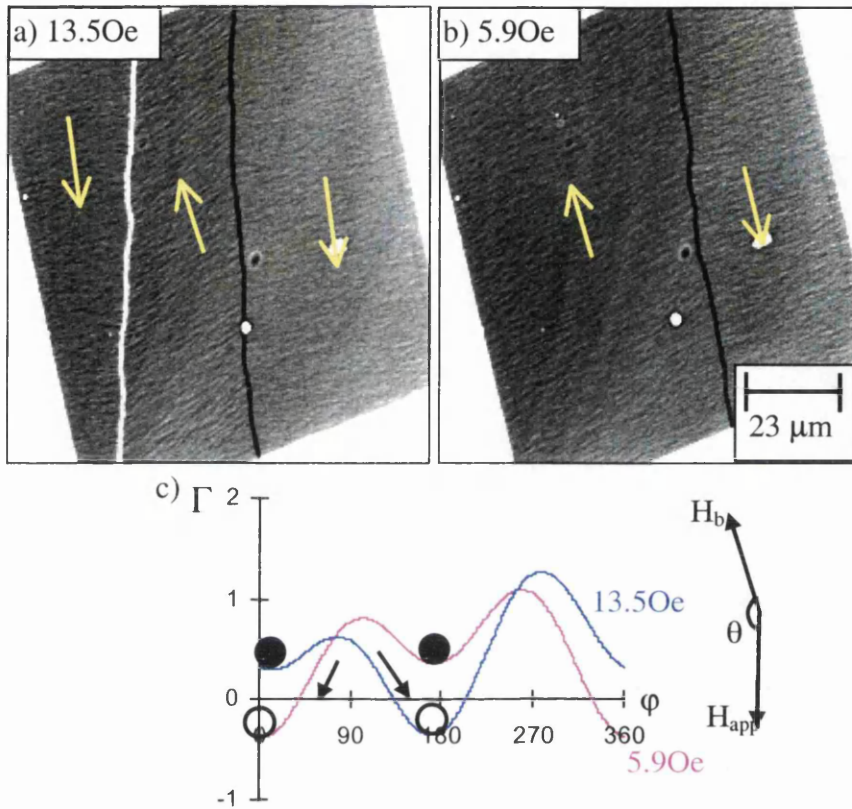


Figure 4.12: Free layer reversals for a spin-valve with $h_J=0.49$ at $\theta=165^\circ$ and associated energy curves.

4.5.2 CASE 2

Figure 4.13 shows Fresnel images corresponding to the reversal of the free layer in a spin-valve with $h_j=0.49$ at $\theta=126^\circ$. The values of applied field and angles of magnetisation are indicated. In this case it can be seen that a much larger number of domain walls are formed during the reversals. These have lower wall angles and their orientation is such that they exhibit low mobility and are present over a larger field range ($\approx 0.50\text{Oe}$). Figure 4.13(c) shows the Γ vs ϕ curves for these conditions. The energy saving obtained and the energy barrier which is overcome during these reversals are considerably lower than in the previous case. Further, the change in magnetisation angle predicted at the switching field decreases markedly. This is always the case as mode C is approached. The lower wall angle and the wall orientation results in a lower wall mobility and the decreased energy barrier facilitates the nucleation of more domains. At the appropriate fields the energy function varies little over a larger range of magnetisation directions.

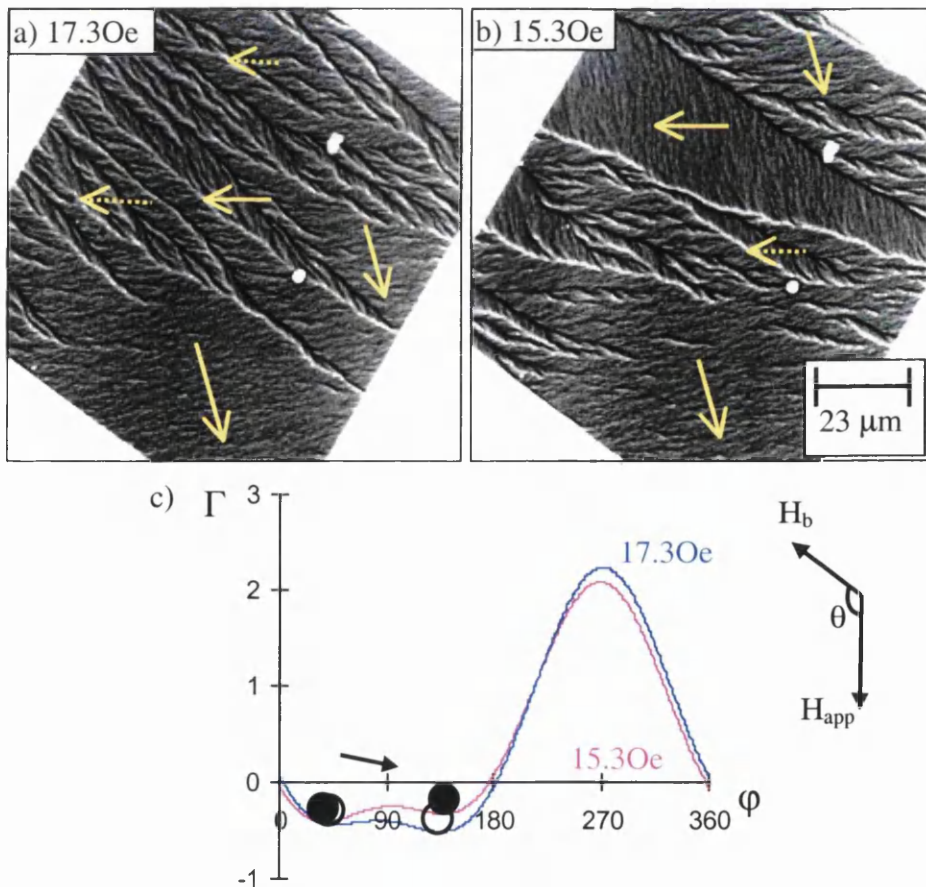


Figure 4.13: Free layer reversals for a spin-valve with $h_j=0.49$ at $\theta=126^\circ$ and associated energy curves.

4.5.3 CASE 3

The above two cases describe similar behaviour for both increasing and decreasing H_a . Figure 4.14 shows the free layer reversal of a spin-valve with $h_j=0.38$ at $\theta=122^\circ$. In this case different domain processes are observed for the increasing field and decreasing field sections of the hysteresis loop. Upon increasing the applied field a large number of low angle domain walls are observed. These exhibit low mobility and are present over a relatively large field range. Correspondingly the Γ vs ϕ curve (figure 4.14(c), 3.9Oe) reveals a low energy barrier and a relatively small energy saving. Here the switching fields are very close to the predicted values. Upon decreasing the applied field strength, at 0.4Oe, the free layer reversal proceeds by a small number of domain walls rapidly sweeping through the layer. A large energy saving is obtained during reversal as can be seen from the energy curve.

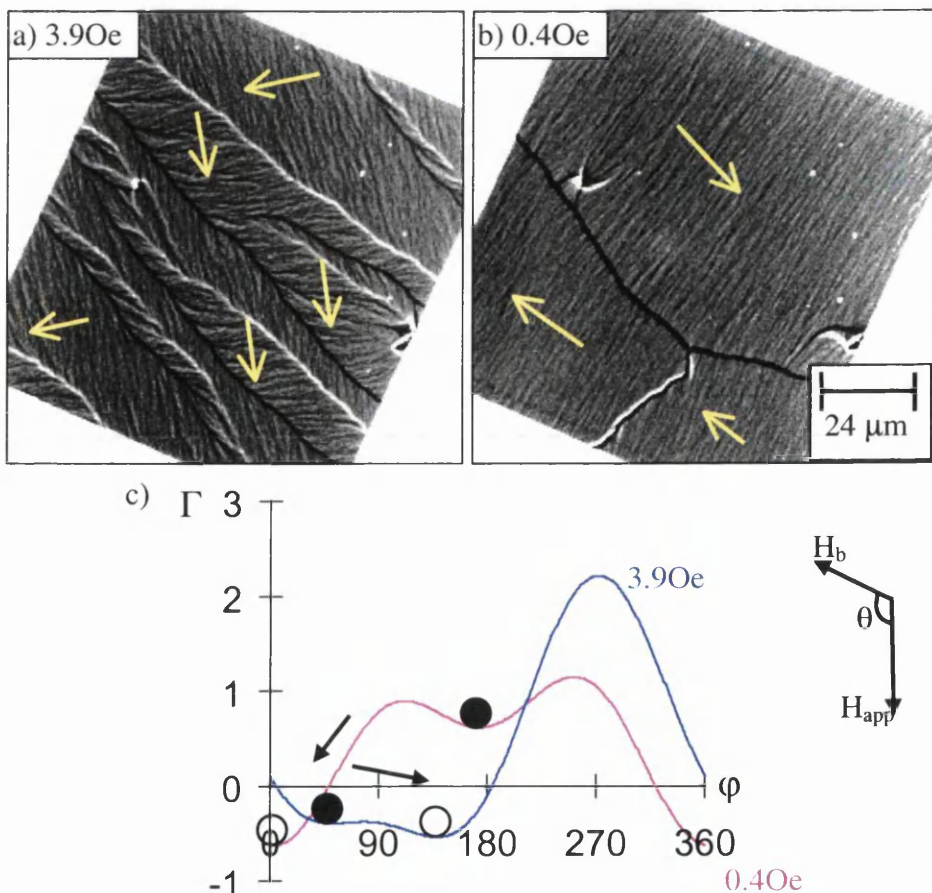


Figure 4.14: Free layer reversals for a spin-valve with $h_j=0.38$ at $\theta=122^\circ$ and associated energy curves.

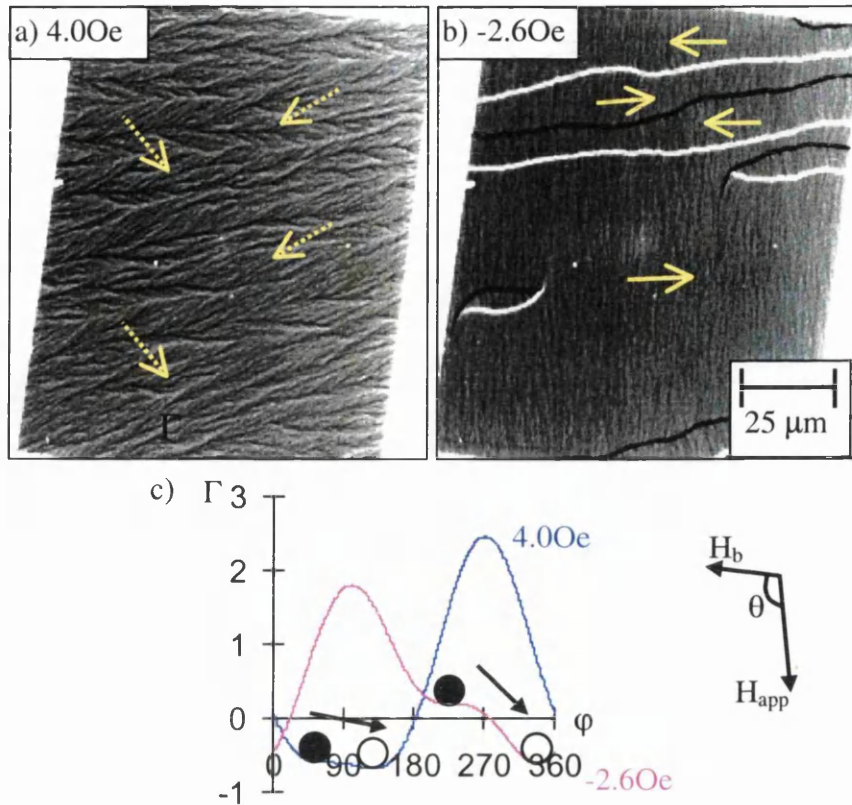


Figure 4.15: Free layer reversals for a spin-valve with $h_j=0.15$ at $\theta=103^\circ$ and associated energy curves.

Figure 4.15 shows a free layer reversal for a spin-valve with $h_j=0.15$ at $\theta=103^\circ$. In this case a larger number of low angle domain walls are formed upon increasing the applied field strength (almost tending to a dispersion like effect), figure 4.15(a). Upon decreasing the applied field strength however, it can be seen that well defined domains are formed, figure 4.15(b). These walls are of higher angle and are of high mobility. It was fortunate to capture these walls in the image. Inspection of the energy curves for this case confirms this result. For example, for the case of increasing the applied field strength, there a small energy barrier separating the two energy minima which are of similar energy themselves. However, for the decreasing field case, there is a small energy barrier when the reversal is observed to take place, with a correspondingly large saving in energy being observed to the energy minimum. The low energy barrier accounts for the relatively large number of domain walls observed, and the high mobility can be understood by the large energy saving obtained.

4.6 DISCUSSIONS AND SUMMARY

By using a modified Stoner-Wohlfarth coherent rotation model^[1] it was shown that the 3 observed modes of free layer reversal can be predicted. For example mode A-type reversals were both predicted and observed for spin-valves with $h_j < 1$, and mode B-type reversals for spin-valves with $h_j > 1$ (as shown on the magnetic phase diagram 3.23). However domain wall formation did enable an energy barrier to be overcome during these 2 modes of reversal. This accounted for differences, sometimes significant, between the predicted and observed switching fields. The form of the energy curves allowed the nature of the domain processes involved in different regimes to be predicted. Well away from the phase boundary with mode C, substantial energy barriers were frequently overcome by the formation and propagation of walls, leading to considerable energy savings. Here highly-mobile high angle walls, few in number, were usually involved. However, as the phase boundary with mode C was approached (see figure 3.23) typical energy curves displayed wide shallow minima, separated by only small energy barriers. A much higher density of comparatively low mobility walls could be predicted to form in such instances. The observation that the transition between modes was not distinct is again due to the fact that energy barriers can be overcome by the formation of domains. Overall, the model has provided an invaluable guide to establishing where rotational processes exist and has allowed us to infer the nature of the domains processes that can take place in these type of spin-valves.

REFERENCES

[1] M. Labrune et al, (1997) *J. Mag. Mag. Mat.*, **171** 1

CHAPTER 5: EXCHANGE BIASING OF $Ni_{80}Fe_{20}$ BY $FeMn$ AND $IrMn$ ANTIFERROMAGNETIC LAYERS

5.1 INTRODUCTION

In order to achieve successful operation of a spin-valve multilayer, it is necessary that the direction of magnetisation in one of the ferromagnetic layers remains fixed as the other changes orientation under the influence of magnetic flux from a passing magnetic tape or disk. One method of achieving this is by direct exchange coupling at the interface between one of the ferromagnetic (F) layers and an antiferromagnetic (AF) pinning layer. The exchange coupling can be represented by an exchange biasing field, H_{eb} . This corresponds to a shift in the hysteresis loop of the ferromagnetic layer along the field axis, as shown schematically in figure 5.1.

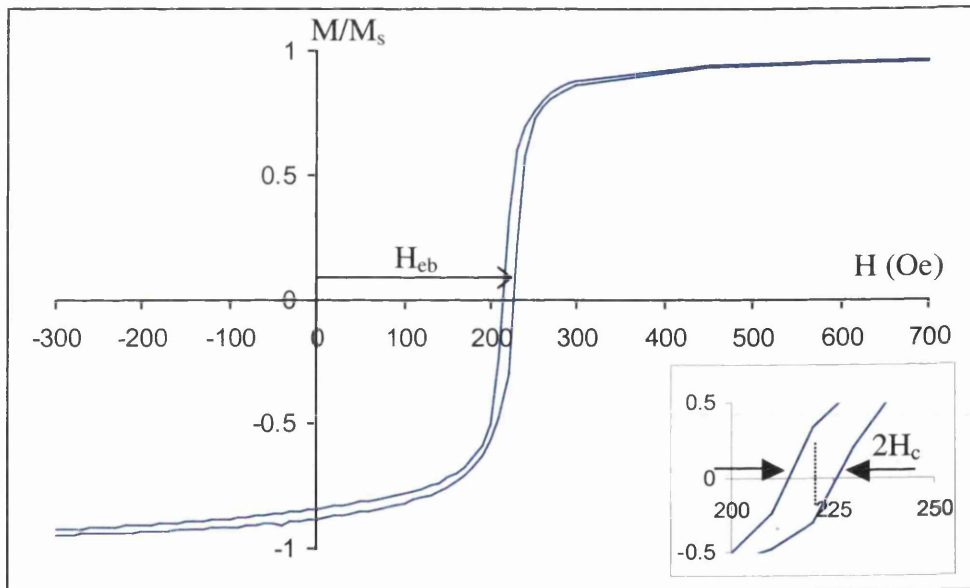


Figure 5.1: Magnetisation loop of 6.0nm $Ni_{80}Fe_{20}$ / 25.0nm $Ir_{20}Mn_{80}$ layer showing H_{eb} and H_c (inset).

For a single pinned layer the exchange biasing field H_{eb} is given by

$$H_{eb} = \frac{J_{eb}}{\mu_0 M_s t_p} \quad 5.1$$

where J_{eb} is the exchange bias energy, and M_s and t_p are the saturation magnetisation and thickness of the pinned layer respectively. Note the inverse thickness dependence of the exchange biasing field on the ferromagnetic layer thickness.

Another important quantity which is useful in the description of the temperature dependence of biasing is the blocking temperature, T_b . For an antiferromagnet this coincides with the Néel temperature, and is the point at which antiferromagnetic order, and thus any exchange biasing is lost. The temperature dependence of the biasing generally follows the form^[1]

$$J_{eb}(T) = \frac{(T_b - T)}{T_b} J_{eb}(T = 0) \quad 5.2$$

Although values of J_{eb} are normally quoted at room temperature, from a fundamental point of view it is better to compare values at $T=0K$.

A minimum AF layer thickness is required to observe exchange coupling at room temperature. This is related to the fact that the blocking temperature of thin films increases with thickness. For example T_b for a 5nm FeMn film is 50degreesC, whereas it has increased to 155degreesC for a 15nm thick FeMn film. Thus at room temperature a minimum AF layer thickness is required to obtain antiferromagnetic order, and hence exchange coupling with an adjacent ferromagnetic layer. Increasing the thickness of the AF layer indefinitely, however, has a detrimental effect on device performance. This is because of shunting of the sense current in the AF layer which lowers the overall GMR of the system. For this reason one would ideally use an insulator for the biasing material. Normally one must optimise the AF layer such as to provide sufficient biasing while maintaining maximal GMR amplitude. It is, however, imperative that the biasing field be sufficiently greater than the switching field of the free layer over the required range of operating temperatures. It is also desirable to have the coercivity H_c of the pinned layer small compared to H_{eb} , figure 5.1 inset.

Several examples of biasing materials are shown in table 5.1 with a comparison of their important parameters and associated references. The values quoted are often for optimised films. The following section discusses various advantages and disadvantages attributable to the various biasing systems.

Material	$J_{eb}(300)$ mJ/m ²	$H_{eb}(300)$ Oe	T_b °C	R_{sh} Ω	Comments	References
FeMn	0.09	150-200	150	140	Poor corrosion resistance, Low T_b	2-5
TbCo	0.26	500	160	200-500	Bias degrades irreversibly	7-9
NiO	0.05	100	200	10^8	Surface important, unstable mechanism	2,5,10-13
NiMn	0.14	270	>400	175	Requires anneal, otherwise good	2,14
IrMn	0.11	213	287	200	Anneal improves properties, good corrosion resistance	15-17

Table 5.1: Comparison of various exchange biasing materials and parameters.

FeMn^[2-5] has been studied extensively for use as a biasing material since it was first used to successfully bias a barber pole head structure^[6]. The γ -phase of $Fe_{50}Mn_{50}$ deposited in the presence of a magnetic field with $\langle 111 \rangle$ texture results in an exchange biasing field of 150-200Oe at room temperature. The exchange biasing degrades in the range 100-150°C, and is irreversible above $\approx 150^\circ\text{C}$ which makes use in modern device applications problematic due to the need for operation at temperatures in excess of 100°C. Thus we say that the blocking temperature T_b is $\approx 150^\circ\text{C}$ for biasing by FeMn. The material also possesses a sheet resistance R_{sh} of $\approx 140\Omega$ which is usually measured by a conventional 4 probe setup. When high currents are used this contributes to the heating effect as a significant proportion of the sense current is shunted through the AF layer. Another disadvantage of using FeMn as a biasing material is that it is particularly susceptible to corrosion^[4], which could cause device performance deterioration with time, or severely lower the process yield during manufacturing.

Another material which has been proposed is TbCo^[7-9], which is actually a compensated ferrimagnet. It has been found that maximum exchange biasing can be obtained for a composition of 27.5 at. % Tb^[8]. In optimised films one can obtain an H_{eb} of $\approx 500\text{Oe}$ at room temperature. Also, a high sheet resistance of 200-500 Ω makes TbCo a

viable candidate as a biasing material. However, the main disadvantage is that the biasing degrades irreversibly for $T \geq 130^\circ\text{C}$ with $T_b \approx 160^\circ\text{C}$. Cooling through the blocking temperature in the presence of a field does not cause exchange biasing to return.

NiO is also a material which has been shown to exhibit exchange biasing. Its principal advantages are that it has a T_b of $\approx 200^\circ\text{C}$ and is an insulator with a high resistance of $10^8 \Omega$. However, it has a lower H_{eb} than FeMn and TbCo, being approximately 100 Oe at room temperature. Successful biasing with NiO requires the properties of the AF/F interface to be carefully controlled^[10,11]. Original studies required that the NiO layer be deposited at elevated substrate temperature^[11,12]. To avoid interface mixing this meant that the NiO layer had to be deposited first, at the bottom of the multilayer stack, leading to an inverted spin-valve structure. The problem requiring deposition at elevated temperature was overcome^[13] though, enabling conventional structures to be deposited. Another requirement when considering device application is long term and thermal stability of exchange biasing. Unfortunately it has been found that exchange biasing by NiO is unstable^[5].

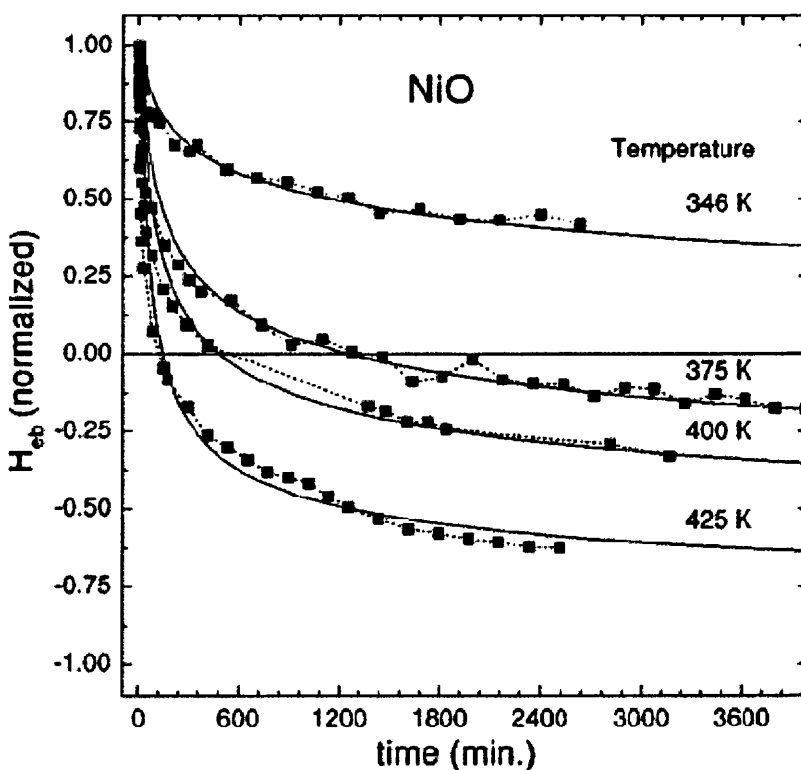


Figure 5.2: Time dependence of the exchange bias field H_{eb} during a forced antiparallel alignment of the magnetisation in the ferromagnetic layer^[5]. Several temperatures are shown for the sample configuration 60nm NiO / 5nm $Ni_{66}Fe_{16}Co_{18}$.

When the pinned ferromagnetic layer is forced antiparallel to the biasing direction by an external field the strength of H_{eb} decreases, and can in fact change sign. This problem is particularly bad for NiO and the effect is extenuated at elevated temperatures, as demonstrated in figure 5.2^[5].

NiMn has also been shown to exhibit exchange biasing when in contact with a ferromagnet^[2,14]. A relatively high $H_{eb}(300) \approx 270$ Oe can be observed. Other factors are a T_b of $>400^\circ\text{C}$, excellent corrosion resistance, and a higher resistance than FeMn of $\approx 175\Omega$. This makes NiMn a promising candidate for device applications. The principal disadvantage, however, is that in order to obtain the strong exchange biasing the material requires a high temperature anneal^[2].

More recently^[15-17] $Ir_{20}Mn_{80}$ has become interesting as an exchange biasing material. The reasons are that IrMn has an improved level of exchange biasing over FeMn, ($H_{eb}(300) \approx 220$ Oe, although values as high as 640Oe have been reported^[16]). T_b is $\approx 287^\circ\text{C}$, the resistance is $\approx 200\Omega$ and excellent corrosion resistance have been reported^[15,16]. It is also noteworthy that upon initial annealing the MR of devices based upon IrMn improves^[15,16] which is thought to be due to the relaxation of strain. Annealing experiments using CoFe alloys as the ferromagnets found an improvement in T_b and a slight weakening of H_{eb} ^[16].

5.2 $Ni_{80}Fe_{20}$ LAYERS BIASED BY $Fe_{50}Mn_{50}$ and $Ir_{20}Mn_{80}$.

This section describes the structural and magnetic properties of layers of permalloy biased by $Fe_{50}Mn_{50}$ and $Ir_{20}Mn_{80}$. The structural work was carried out on the JEOL 2000 FX electron microscope and, due to the high fields required, the CM20 objective lens field was used to reverse the pinned layers in the magnetic investigations.

5.2.1 STRUCTURAL PROPERTIES

Figure 5.3(a,b) shows bright and dark field images of a 6.0nm $Ni_{80}Fe_{20}$ layer biased by 10.0nm of FeMn. The average grain size was 7.5 ± 2.5 nm and calculated by randomly measuring a large number of crystallites (>40) from the dark field image.

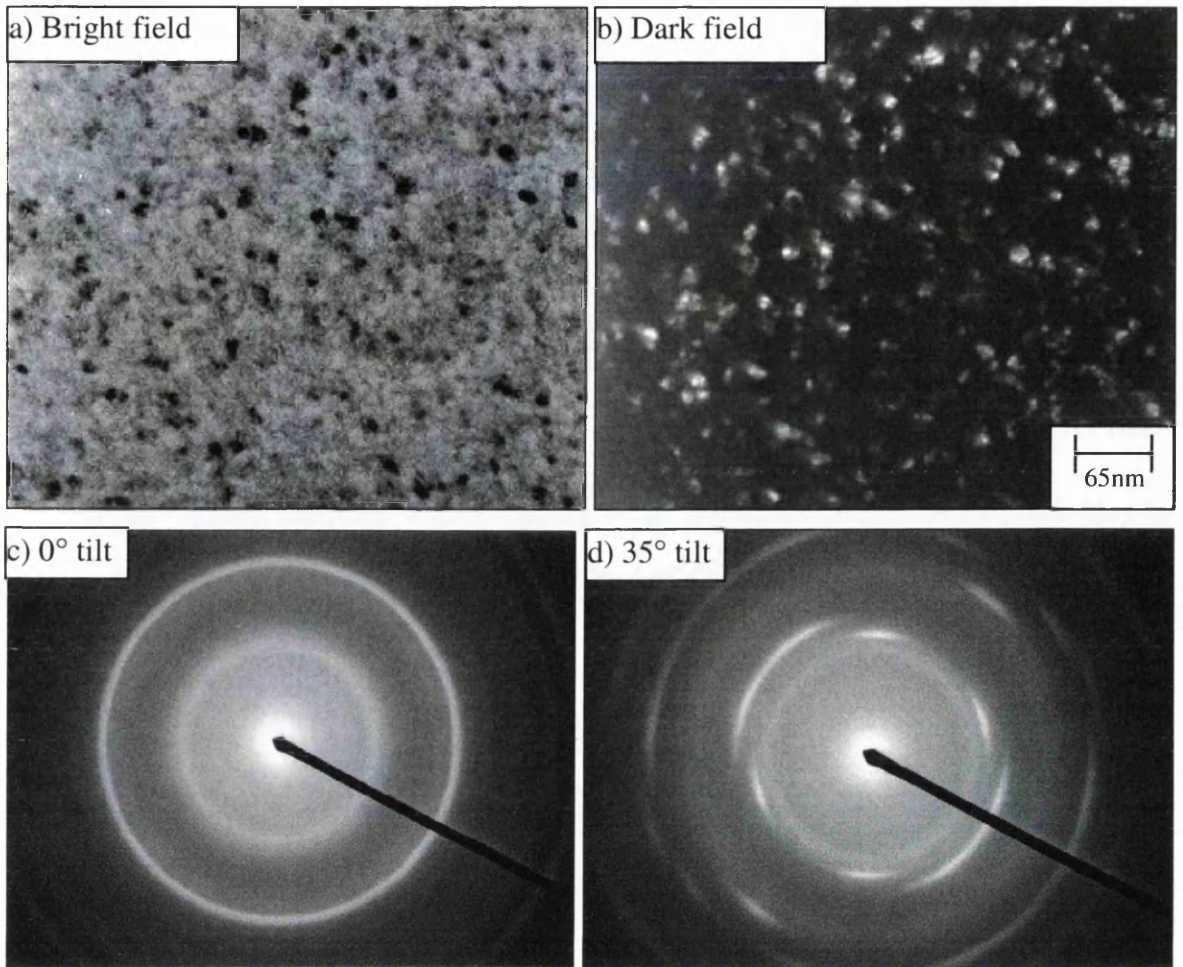


Figure 5.3: Sample 3.5nm Ta / 6.0nm $Ni_{80}Fe_{20}$ / 10.0nm $Fe_{50}Mn_{50}$ / 3.5 nm Ta. **a)** Bright and **b)** dark field images, average grain size 7.5 ± 2.5 nm. **c,d)** Electron diffraction patterns at **c)** 0° tilt **d)** 35° tilt.

Figures 5.3(c,d) show electron diffraction patterns for the same sample. These confirm the presence of ‘bcc’ rings from the Ta layers which are poorly crystalline and contribute diffuse untextured rings. The ‘fcc’ contributions are from the permalloy and FeMn layers. The tilted specimen diffraction pattern, figure 5.3(d), shows additional reflections and considerable texturing can be seen. It is the FeMn and permalloy layers that are highly textured, and this corresponds to $\langle 111 \rangle$ growth. The individual FeMn and permalloy contributions are not resolved in the images, but a broadening of the higher order reflections can be seen due to the slight lattice mismatch between the two alloys.

Figure 5.4(a,b) shows bright and dark field images of a 6.0nm layer of $Ni_{80}Fe_{20}$ biased by 10.0nm of $Ir_{20}Mn_{80}$.

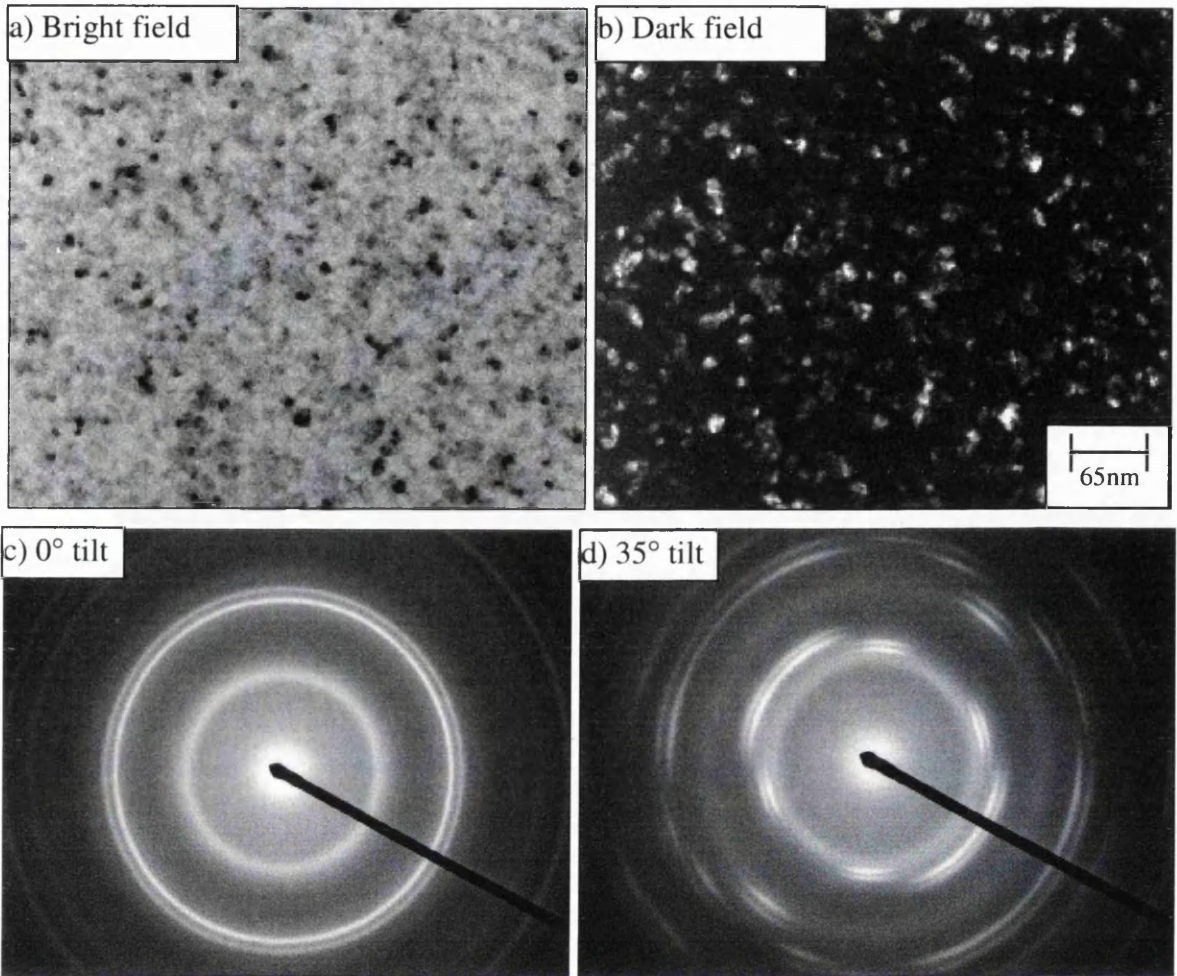


Figure 5.4: Sample 3.5nm Ta / 6.0nm $Ni_{80}Fe_{20}$ / 10.0nm $Ir_{20}Mn_{80}$ / 3.5 nm Ta. **a)** Bright and **b)** dark field images, average grain size 7.0 ± 3.0 nm. **(c,d)** Electron diffraction patterns at **c)** 0° tilt **d)** 35° tilt.

The crystallite size was measured in the same way as for the FeMn sample and an average size of 7.0 ± 3.0 nm was obtained. One would expect a similar value for the IrMn sample due to the 2 samples being the same thickness and similar growth conditions used in the depositions.

Figures 5.4(c,d) show untilted and tilted specimen electron diffraction patterns. Additional reflections can be seen in both patterns when compared to that for FeMn which are due to the presence of the IrMn layer. Analysis of the diffraction pattern 5.4(d) is shown below in figure 5.5. This clearly shows the presence of two ‘fcc’ layers. Using the ratio of the gradients of the two lines and measuring that the upper line is resultant from the $Ni_{80}Fe_{20}$ layer it is possible to calculate the lattice parameter of the lower line. The resultant value is $3.77 \pm 0.03 \text{ \AA}$. This is in close agreement with reference [16] in which the lattice parameter

of $Ir_{20}Mn_{80}$ is reported to be 3.79\AA , measured by x-ray diffraction. Several other samples were studied which had $IrMn$ thicknesses of 20, 25 and 30 nm. Analysis of the diffraction patterns yielded similar results, with an average lattice parameter for $Ir_{20}Mn_{80}$ of 3.78\AA .

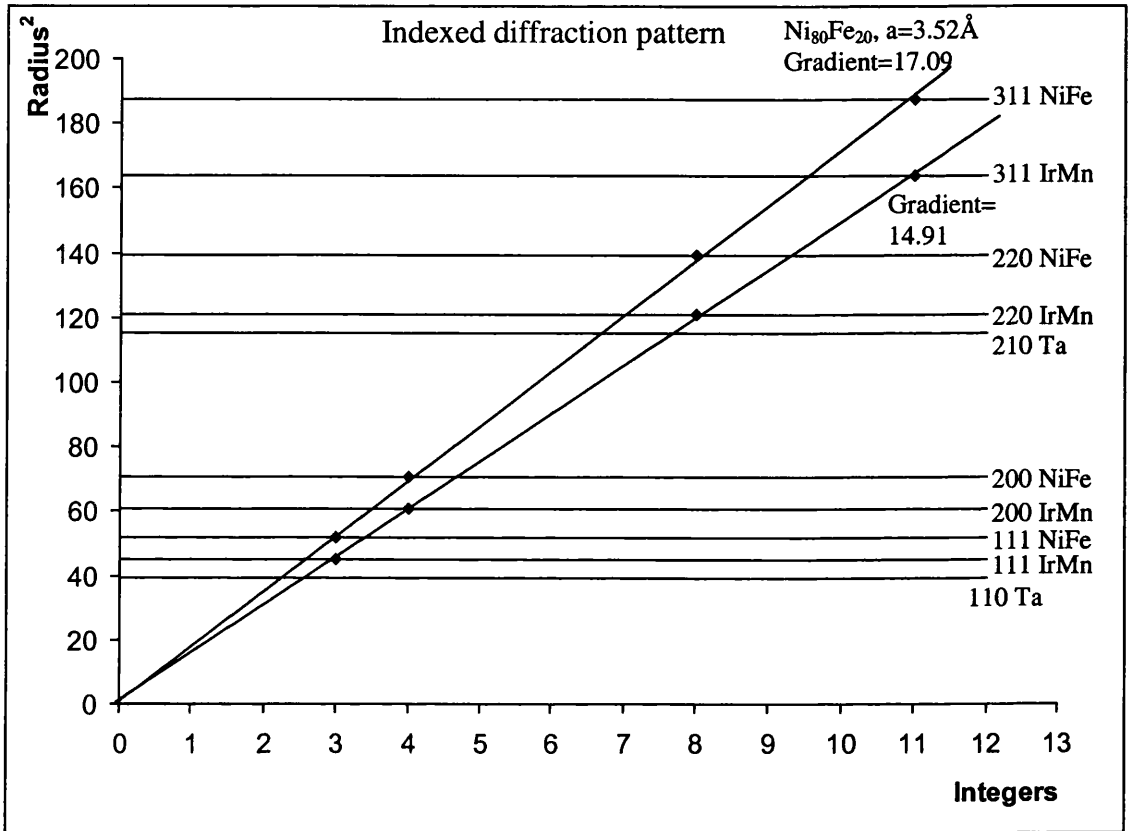


Figure 5.5: Indexed diffraction pattern for the sample with configuration 3.5nm Ta / 6.0nm $Ni_{80}Fe_{20}$ / 10.0nm $Ir_{20}Mn_{80}$ / 3.5nm Ta.

The similarities that exist between the two diffraction patterns 5.3d and 5.4d are worth mentioning here. There are additional reflections that are observed upon tilting of the specimen, indicative of $\langle 111 \rangle$ texture, and the presence of the diffuse rings from the tantalum seed and capping layers. From these results we can conclude that the growth of the $IrMn$ layer is very similar to the growth of the $FeMn$ layer with both layers exhibiting $\langle 111 \rangle$ texture. Also, a similar grain size of approximately 7 nm is observed for both of the examined samples.

5.2.2 MAGNETIC PROPERTIES

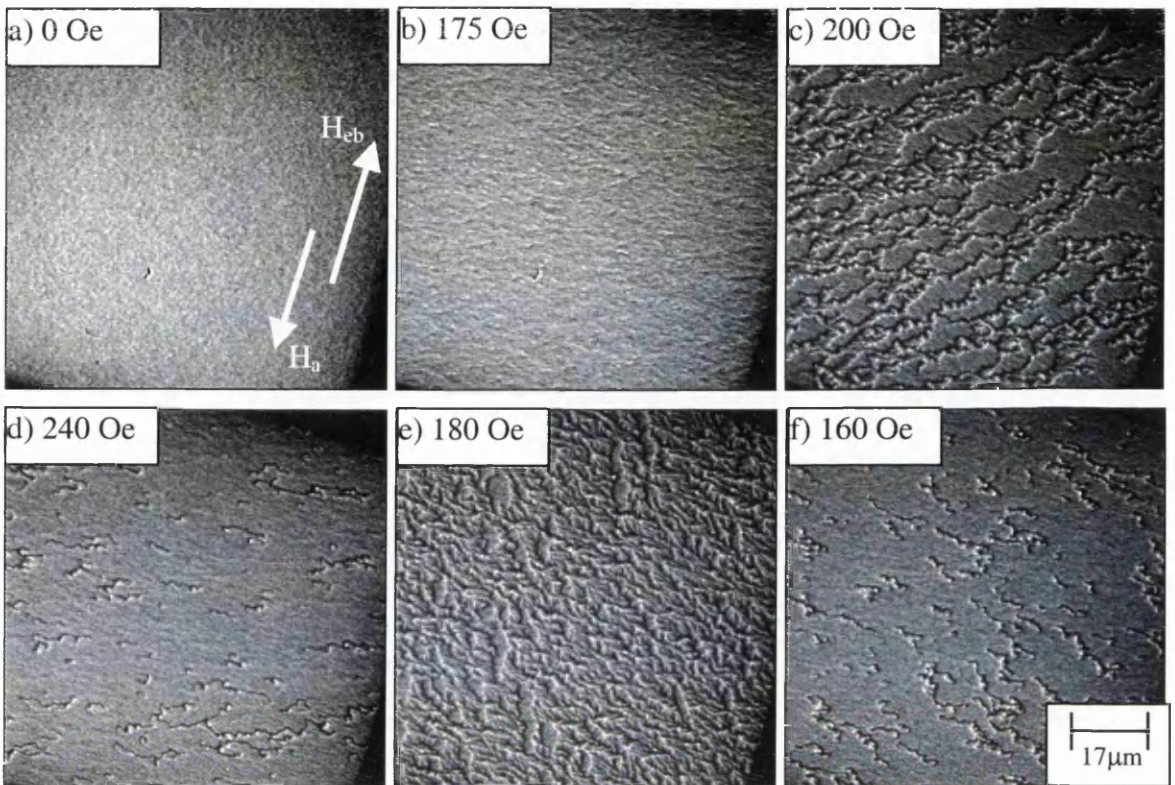


Figure 5.6: Magnetisation reversal of a 6.0nm $Ni_{80}Fe_{20}$ layer biased by 10.0nm of $FeMn$.

Figure 5.6(a-f) shows Fresnel images of the magnetisation reversal of a 6.0nm thick layer of $Ni_{80}Fe_{20}$ biased by 10.0nm of $FeMn$. Upon application of a magnetic field antiparallel to the biasing direction no changes in the magnetic structure of the pinned layer were observed until the value of the in-plane field exceeded ≈ 150 Oe. As the field increased in strength beyond this value an increase in the ripple contrast is observed, figure 5.6(b). Following this the pinned layer magnetisation breaks into many small irregular domains, figure 5.6(c). During this part of the reversal many directions of magnetisation are present, and the domain walls are erratic in shape and length, the domain walls are typically 1-2 μ m in separation. The domain wall density was very high and extremely low wall mobility was observed. As the applied field strength was increased further, the areas of switched magnetisation grew in size at the expense of the unswitched regions. After the majority of the film had reversed, many small 360° wall segments remained present in the pinned layer, figure 5.6(d). These were stable and required a much higher applied field (>300 Oe) to annihilate them. Directionality can be seen in the orientation of the wall segments, for

example in figure 5.6(d) there is a greater proportion of the walls oriented approximately horizontally across the image than vertically. Upon reduction of the applied field strength, similar processes were observed with the bulk of the film returning to the original direction by an applied field of ≈ 160 Oe, figures 5.6(e,f). Again, many 360° wall segments remained in the film until the applied field strength approached 0Oe. This type of reversal mechanism is markedly different from both the reversals of isolated permalloy layers^[18] and the free layer reversals of spin-valves as reported in chapter 3. It is however similar to that reported for 8.0nm $Ni_{80}Fe_{20}$ layers biased by 8.0nm of FeMn^[18]. For example the switching field required to reverse the pinned layer is enhanced due to the exchange biasing effect of the FeMn layer. Strong local pinning of domain walls is observed and 360° structures are stabilised in both cases. However, notable differences between the reported reversal mechanism^[18] and that observed do exist. For example, the field strength required for reversals to occur is greater in this case than that reported, this can be accounted for by noting the inverse thickness dependence of H_{eb} on t_p , equation 5.1. Also the amount of magnetisation rotation observed is less than reported. The amount of magnetisation rotation and the effect of local pinning sites was observed to be highly dependent on the exact orientation of H_a with respect to H_b . For example a $\approx 3^\circ$ misalignment caused a significant amount of magnetisation rotation and less homogeneous domain structure to be observed as the pinned layer reversal proceeded. The likely cause for there being such an erratic domain structure during reversal is that there are many fluctuations in the strength of the local pinning between the $Ni_{80}Fe_{20}$ and FeMn layer across the specimen. This causes different areas to start to reverse at slightly different fields. The large number of strongly pinned regions then inhibits domain wall motion and an erratic strongly pinned domain structure is what results. The directionality in the stabilised domain 360° wall structures is thought to be due to domain walls forming along strongly pinned regions which are orthogonal to the direction of magnetisation in the pinned layer just before it breaks up into domains.

Figure 5.7(a-i) shows the magnetisation reversal for a 6.0nm $Ni_{80}Fe_{20}$ / 10.0nm IrMn sample which is the same as that discussed above, except that the FeMn layer has now been replaced by IrMn. The overall reversal mechanism can be seen to be similar to that for the FeMn biased layer. The magnetisation ripple contrast increases with field before the majority of the film reverses, figure 5.7(b,c). This is followed by areas of the pinned layer breaking up into small irregular domains with an erratic domain structure

separating switched regions, figure 5.7(d). Again, once the majority of the film has reversed there are still 360° walls present and high values of applied field (>300 Oe) are required to annihilate them. Upon decrease of the applied field strength a similar reversal mechanism is observed, and the film returns to its original configuration with the pinned layer magnetisation realigning with the biasing direction. 360° wall structures are stabilised down to zero applied field, figure 5.7(h,i).

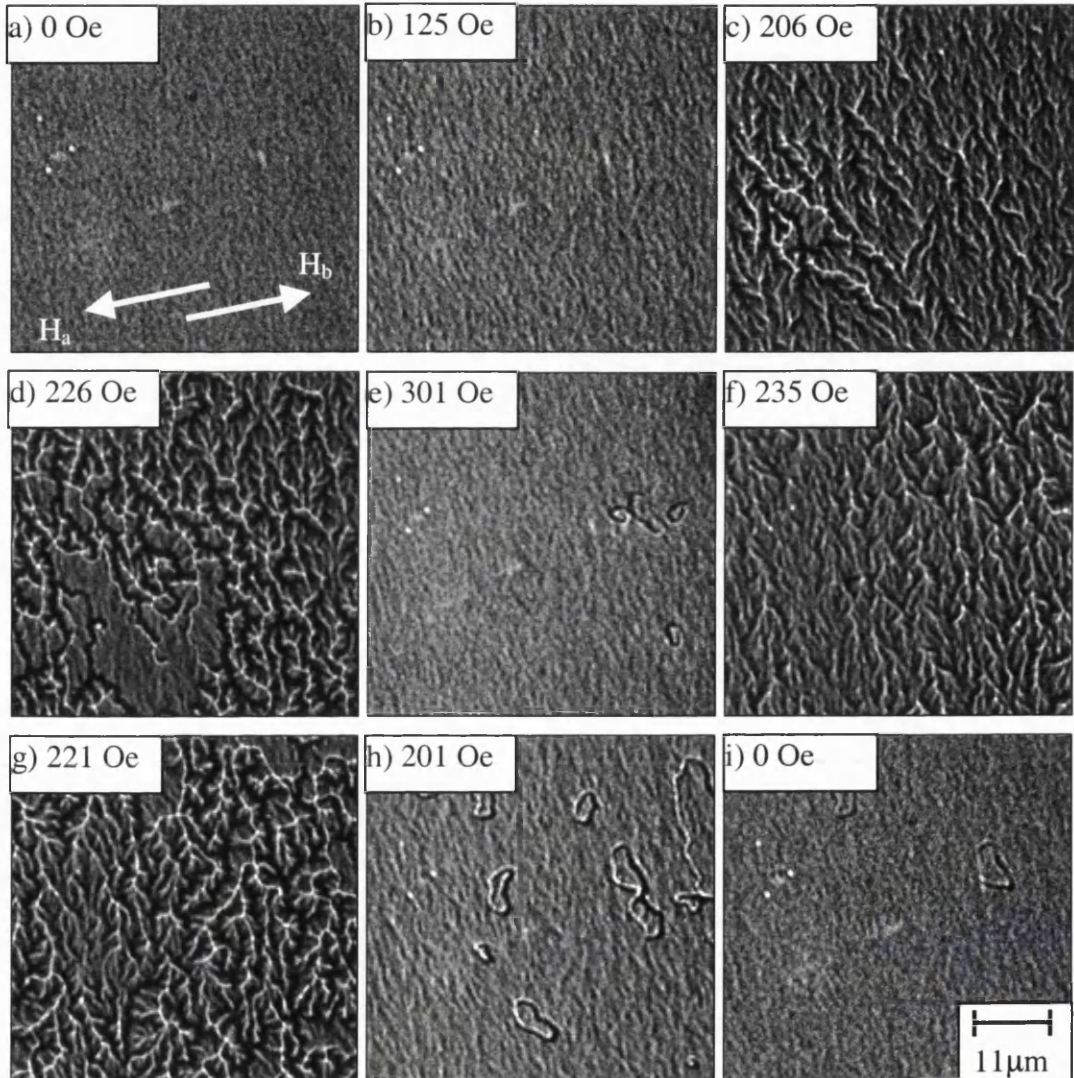


Figure 5.7: Magnetisation reversal of a 6.0nm $Ni_{80}Fe_{20}$ layer biased by 10.0nm of IrMn.

The reversal of FeMn and IrMn layers are not, however, identical. In the case of IrMn some regions start to reverse sooner than others, figure 5.7(d), and the 360° wall segments resemble 360° loops in a lot of cases. This could be due to a greater variation in the strength of pinning across the sample, but slight changes to the direction of H_a revealed

that the homogeneity of the reversal and amount of magnetisation rotation observed were strongly affected by the accuracy of alignment of H_{eb} with respect to H_a . It can also be seen that the switching fields for the layer biased by IrMn are higher than that for FeMn and also that IrMn biased layer has a smaller coercivity H_c . Table 5.2 summarises the two results and shows that the corresponding exchange bias energies are $\approx 0.098 \text{ mJ/m}^2$ for FeMn and $\approx 0.115 \text{ mJ/m}^2$ for IrMn.

	FeMn	IrMn
H_{eb} (300)	190 Oe	223 Oe
H_c	10 Oe	2.5 Oe
J_{eb} (300)	0.098 mJ/m^2	0.115 mJ/m^2

Table 5.2: Summary of pinned layer properties at room temperature. The sample configuration was 6.0nm $Ni_{80}Fe_{20}$ / 10.0nm AF.

Two other samples with IrMn as the biasing material have been investigated at room temperature. These also have 6.0nm $Ni_{80}Fe_{20}$ layers, but the thickness of the IrMn is varied. Reversal of the pinned layers at room temperature revealed a similar reversal mechanism as for the 10.0nm sample, but there was a variation in H_{eb} . The results are plotted in figure 5.8.

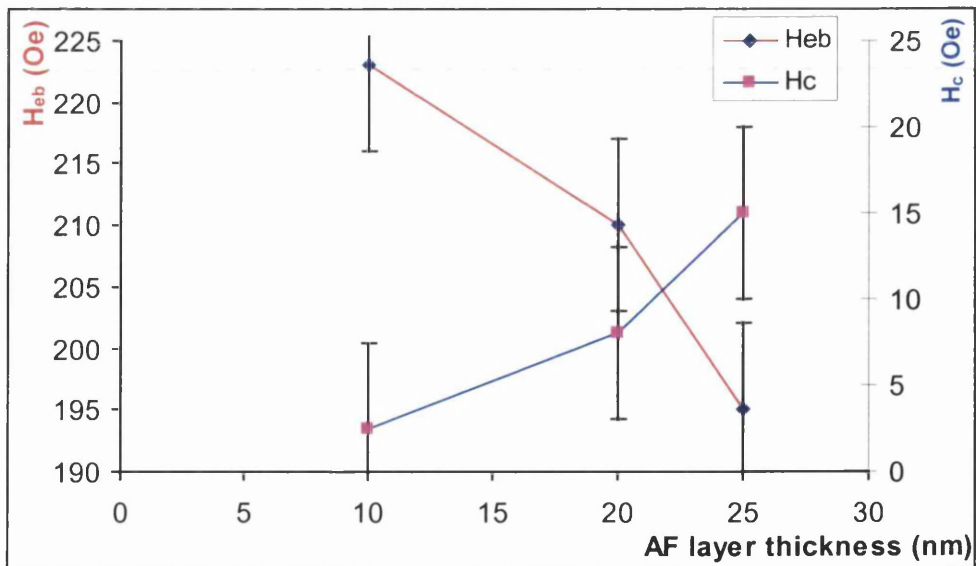


Figure 5.8: Variation of H_{eb} and H_c as a function of AF layer thickness.

These results show that as the thickness of the antiferromagnetic (AF) layer increases there is a decrease in H_{eb} . The decrease in H_{eb} with thickness is not a new result^[2]. This has been observed for the cases of FeMn, NiO, and annealed NiMn in this thickness range. Although reference [2] does not provide a description of the reasons for the decrease in H_{eb} with thickness, for all cases a large increase in H_{eb} is observed at the onset of biasing at some minimal AF layer thickness ($\approx 4\text{nm}$ for FeMn) before a maximum is passed through ($\approx 7\text{nm}$ for FeMn). Thereafter a decrease in H_{eb} is observed with increasing the AF layer thickness. Due to the errors involved in determining H_c it is not possible to provide a description of its behaviour as a function of AF layer thickness at room temperature.

5.3 TEMPERATURE DEPENDENCE OF BIASING

This section presents results on the variation of the pinned layer reversal mechanism as a function of temperature. Results are primarily discussed for layers biased by IrMn and FeMn. Variations in temperature are achieved by utilising specialised sample holders for use in the CM20 electron microscope. These enable either cooling of the sample to $\approx -150^\circ\text{C}$ or heating to temperatures in excess of 400°C enabling study of the magnetisation reversal for a range of temperatures up to and above the blocking temperature of the AF layers. Figures 5.9 and 5.10 show the results of such experiments on layers of $Ni_{80}Fe_{20}$ biased by both IrMn and FeMn.

Figure 5.9 shows variation in H_{eb} and figure 5.10 shows variation in H_c as a function of temperature for the two samples discussed in previous sections. The experimental procedure is as follows. Firstly the magnetisation reversal of the pinned layer is recorded at room temperature, section 5.2.2. Following this the sample is cooled by liquid N_2 whereby the minimum temperature reached at the sample was $\approx -150^\circ\text{C}$. The temperature was then increased by means of small heating coils built into the specimen holder and the reversal mechanism was measured at a range of temperatures up to the blocking temperature. H_{eb} and H_c were then estimated from the images of the magnetisation reversal.

Figure 5.9 shows the variation in H_{eb} to be approximately linear for both of the samples, the best fit lines are fitted using equation 5.2 and data from table 5.2. As the temperature increases a decrease in the exchange coupling is observed which is consistent with the behaviour predicted by equation 5.2. These results are in agreement with results

which have been presented elsewhere^[14,16,17]. These show that the effect of heating $Ni_{80}Fe_{20}$ layers biased by $FeMn$ and $IrMn$ from room temperature causes H_{cb} to decrease to 0 at the blocking temperature and that the decrease is approximately linear with temperature.

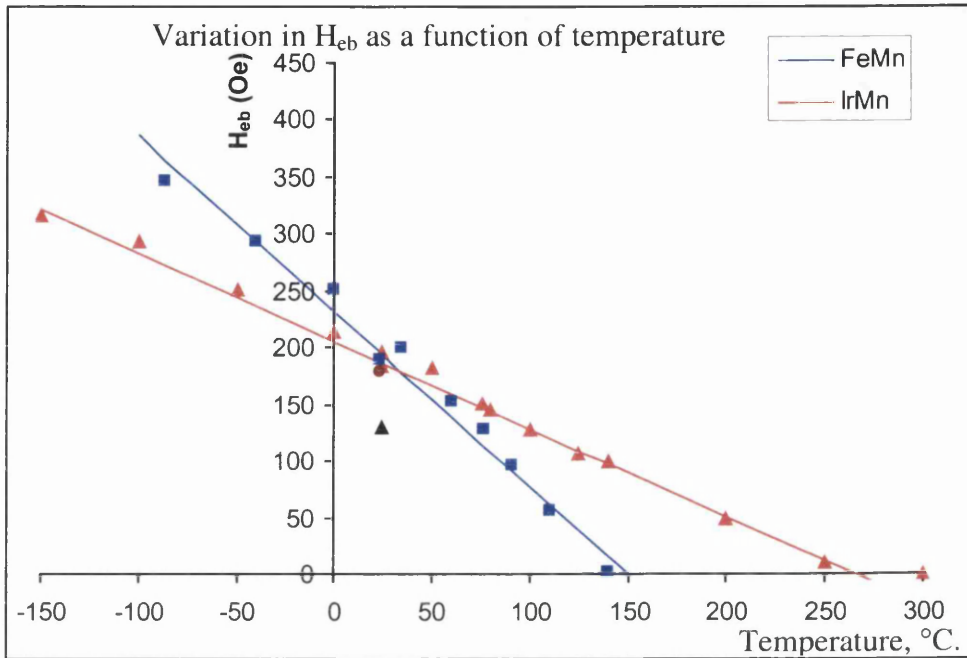


Figure 5.9: Variation in H_{cb} as a function of temperature for 6.0nm $Ni_{80}Fe_{20}$ layers biased by 10.0nm $FeMn$ (blue data) and 10.0nm $IrMn$ (red data) layers.

The variation of coercivity with temperature is shown in figure 5.10. In both of the cases investigated it can be seen that there is a large increase in the coercivity upon decreasing the temperature. Heating causes H_c to fall rapidly and small values (<10Oe) are obtained for temperatures above $\approx 75^\circ C$. The lines shown are as a guide to the eye.

At temperatures above room temperature we have observed that the values of H_c are small, and a significant error does exist ($\pm 7Oe$) in the values presented. This makes discussion of the properties of H_c vs T difficult when measurements are made from interpretation of electron micrographs. Fortunately there is a large increase in H_c as T is decreased below room temperature. In [2] H_c can be seen to decrease with increasing temperature for samples biased by $FeMn$ and NiO . However, the values for samples biased by $FeMn$ are small (<10Oe), and the data presented are all for increasing temperatures above room temperature measured in a vibrating sample magnetometer (VSM).

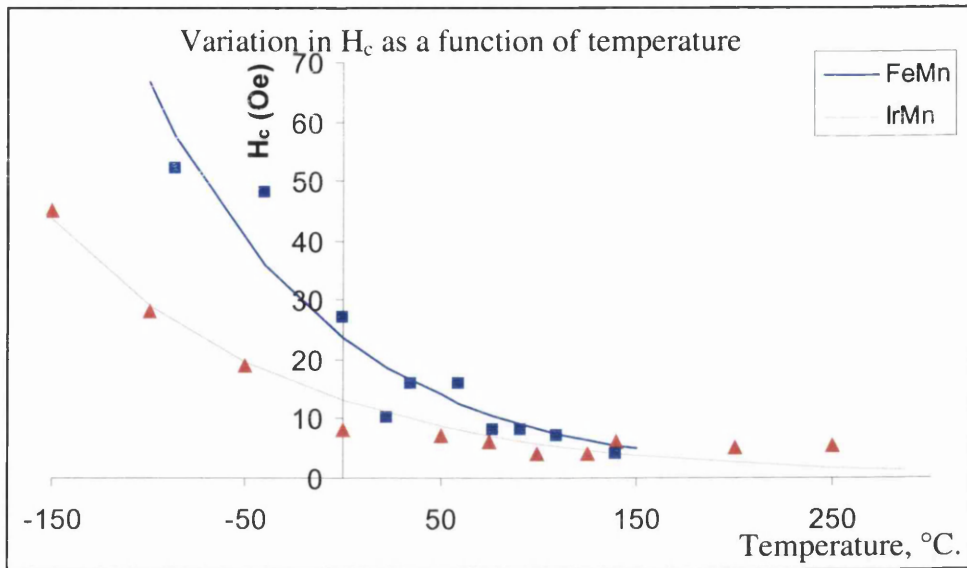


Figure 5.10: Variation in H_c as a function of temperature for 6.0nm $Ni_{80}Fe_{20}$ layers biased by 10.0nm $FeMn$ (blue data) and 10.0nm $IrMn$ (red data) layers.

After the samples had been heated to above their blocking temperatures they were allowed to cool in the presence of a magnetic field. This should cause exchange biasing to return along the direction of applied field. Once the samples had returned to room temperature further investigations were made of the pinned layer reversal (see section 5.3.3). A decrease in the strength of the pinning was found in both cases. For $FeMn$ the value of H_{eb} returned to ≈ 0.9 of the original value before heating and for $IrMn$ the decrease was more severe with the post anneal H_{eb} returning to only ≈ 0.66 of the original value. Decreases have also been observed elsewhere^[17] although the decrease was to ≈ 0.4 of the original value for an $IrMn$ biased layer. Differences in experimental set-up between this and the reported work^[17] include a thicker $Ni_{80}Fe_{20}$ layer and the rates of heating and cooling were different. Also, the field geometry was different as in the CM20 electron microscope a large vertical field is used with the sample tilted in order that an in-plane component of field be introduced a the sample. For tilt angles $< 90^\circ$ a component out of the plane of the sample still exists. This makes a quantitative comparison impossible. Nevertheless, a decrease in the strength of H_{eb} has been observed for both cases.

5.3.1 EFFECT OF COOLING ON MAGNETIC MICROSTRUCTURE

This section discusses differences in the magnetic microstructure of the pinned layer reversal mechanism as a result of cooling of the samples pinned by IrMn and FeMn.

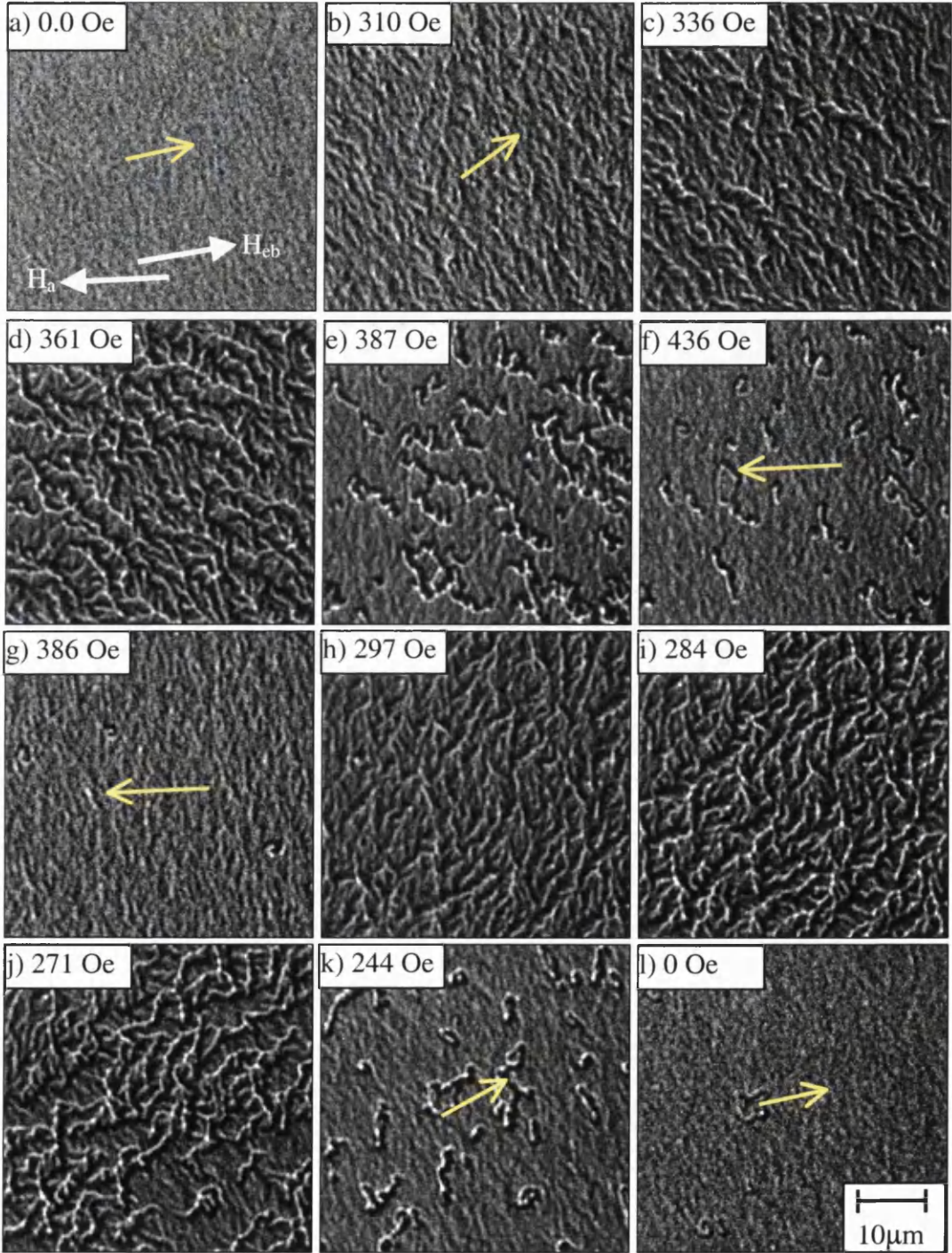


Figure 5.11(a-l): Pinned layer magnetisation reversal for a 6.0nm $Ni_{80}Fe_{20}$ / 10.0nm IrMn sample at $-150^{\circ}C$.

Figure 5.11(a-l) shows the magnetisation reversal of a 6.0nm layer of $Ni_{80}Fe_{20}$ exchange biased by 10.0nm of IrMn at $-150^{\circ}C$. As the applied field H_a is increased in strength from 0Oe no changes in the state of the magnetisation are initially observed and the pinned layer magnetisation remains oriented along the direction of exchange biasing as indicated in figure 5.11(a). However, as H_a is increased above ≈ 250 Oe a slight rotation of the magnetisation followed by an increase in the magnetisation ripple contrast is observed, figure 5.11(b). Further increases in the amount of ripple contrast are observed as H_a is increased further and eventually domains start to form, figure 5.11(c). The domains that form are relatively small in size ($\approx 2-3\mu m$) and the domain walls are observed to be erratic in shape and highly immobile, figure 5.11(d). During switching the direction of magnetisation changes from being closely aligned with the exchange biasing direction to being almost coincident with the direction of H_a . The majority of the reversal takes place over a relatively large field range of ≈ 50 Oe, figure 5.11(c-e) and domain processes are observed to take place throughout this applied field range. As H_a is increased, the reversal proceeds by mainly nucleation and annihilation of domain walls. A small amount of magnetisation rotation is again observed after the majority of the film reverses as alignment with H_a is achieved. This is due to a slight misalignment between the direction of H_a and H_{eb} . Following switching of the majority of the pinned layer, there is a large number of 360° wall segments remaining in the film, figure 5.11(e,f). These are stable and remain as H_a is increased in strength beyond that required to reverse the majority of the film. Before decreasing H_a , the in-plane component of magnetic field was increased to 700Oe to remove as many of the remaining 360° structures present in the film as possible. The strength of H_a was then decreased. Figure 3.11(g) shows the state of magnetisation in the free layer at $H_a=386$ Oe in which it can be seen that a few small 360° structures still remain and the approximate direction of magnetisation in the pinned layer is coincident with the direction of H_a as indicated. Now, as H_a is reduced, the magnetisation initially remains along the direction of H_a , then rotates slightly before an increase in the amount of magnetisation ripple is observed and the pinned layer eventually starts to break up into domains again, figure 5.11(h,i). The domain processes observed for decreasing H_a are remarkably similar to the increasing field case, with a large number of domain walls forming which are highly erratic in shape and have low mobility. Again, after the majority of the pinned layer has reversed back towards the exchange biasing direction, a lot of 360°

wall segments remain in the pinned layer, figure 3.11(k). A low number of these are observed to remain in the down to zero applied field, figure 3.11(l).

This reversal mechanism is similar to that discussed for the pinned layer reversals shown in figure 5.7 at room temperature. However, in this case the applied field strengths required to reverse the pinned layer are increased compared to that required at room temperature. These results give $H_{eb} \approx 3160\text{e}$ and $H_c \approx 460\text{e}$ at $T = -150\text{ }^\circ\text{C}$. The small amount of magnetisation rotation observed during the reversal is due to a slight misalignment between the directions of H_a and H_b .

Figures 5.12 and 5.13 show the pinned layer reversal at $-100\text{ }^\circ\text{C}$ and $-50\text{ }^\circ\text{C}$ respectively. The imaging conditions and sample orientation is the same as for the observations made at $-150\text{ }^\circ\text{C}$, however the following differences in the reversal mechanism are noted. As H_a is increased in strength there is a greater amount of magnetisation rotation observed before the pinned layer breaks up into domains, for example compare figures 3.11(b), 3.12(a) and 3.13(a) which show the state of the pinned layer magnetisation just before it breaks up into domains. Further, the density of 360° domain structures present in the layer just after the domain assisted part of the reversal decreases as the temperature is increased. This is thought to be a consequence of 2 factors. The first is that as the temperature increases, the number of strongly pinned regions will be diminished due to thermal excitation, leading to a lower number of strongly pinned domain walls in the sample. The other factor is due to the slight misalignment between H_a and H_b , which leads to an increased level of magnetisation rotation. These result in the angle subtended during the domain assisted part of the reversal being decreased, and a lower probability of 360° wall structures being formed. However, quantitatively the most notable result obtained from these sets of images is that the strength of the exchange biasing decreases with increasing temperature. The results are plotted on figure 5.9 discussed previously.

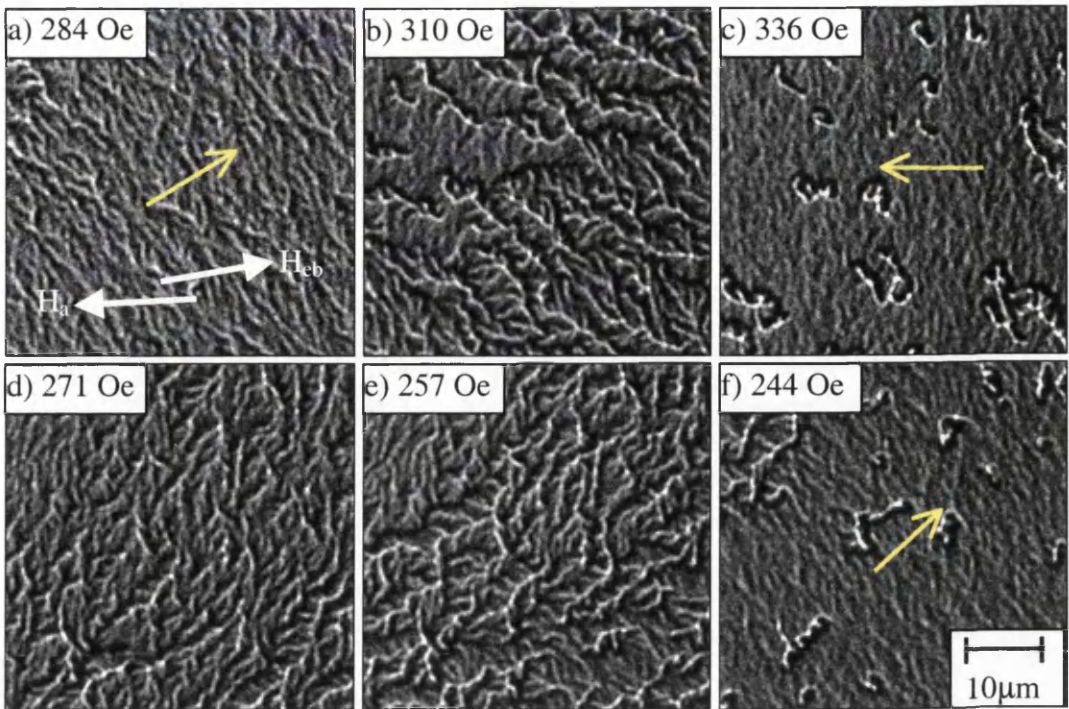


Figure 5.12(a-f): Pinned layer magnetisation reversal for a 6.0nm $Ni_{80}Fe_{20}$ / 10.0nm IrMn sample at $-100^{\circ}C$.

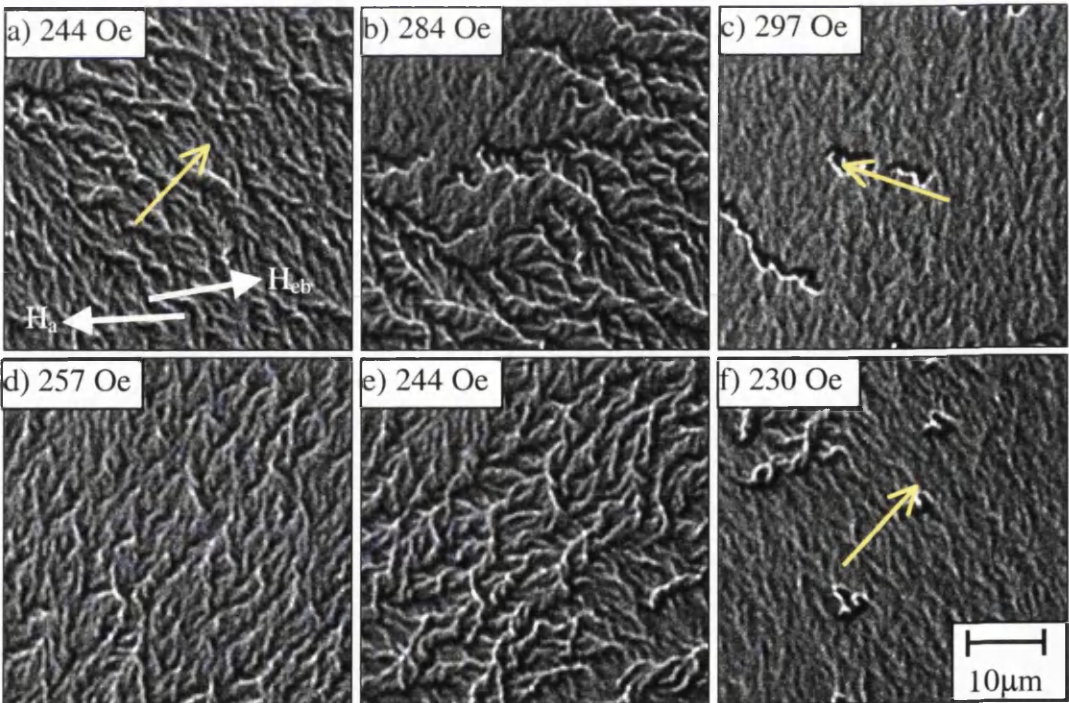


Figure 5.13(a-f): Pinned layer magnetisation reversal for a 6.0nm $Ni_{80}Fe_{20}$ / 10.0nm IrMn sample at $-50^{\circ}C$.

Figure 5.14 shows 3 portions of the magnetisation reversal at various temperatures for the FeMn-biased sample. They are sequences which were recorded just after reversal of the majority of the pinned layer at -86 (a-c), -40 (d-f) and $0^{\circ}C$ (g-i) while increasing the strength of H_a . It can be seen from the 1st image for each temperature (a,d,g) that the field at which the reversal is taking place is decreasing with increasing temperature. This is expected as H_{eb} decreases with increases in T . Further, after the majority of the reversal is complete there are less 360° structures stabilised in the film the higher the temperature, figure 5.14(b,e,h). Then, as the applied field is increased to $465Oe$ at all temperatures, the number of 360° structures that remain decreases the higher the temperature.

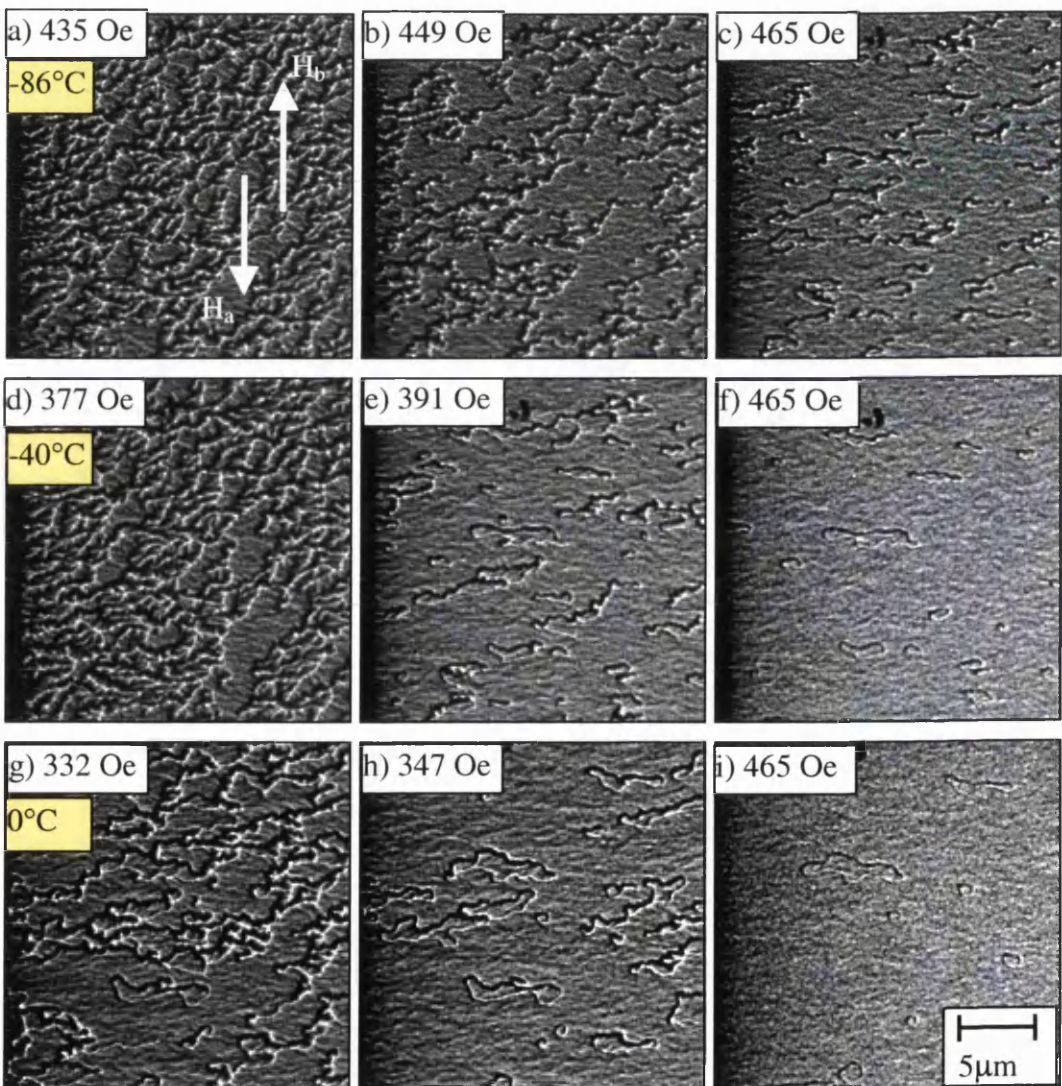


Figure 5.14: State of the pinned layer just after reversal at temperatures $-86^{\circ}C$ (a-c), $-40^{\circ}C$ (d-f), $0^{\circ}C$ (g-I). Sample $6.0nm Ni_{80}Fe_{20} / 10.0nm FeMn$.

These, and the results for the $IrMn$ samples indicate that the strength of the exchange biasing, H_{eb} , increases with decreasing the temperature. However, the amount of 360° structures that are stabilised in the films are also influenced by the temperature: The lower the temperature, the greater number of 360° structures will be formed as the pinned layer reverses. Also, they can exist to higher applied fields when the temperature is reduced. This suggests that the influence of local pinning sites plays an important role in the reversal mechanism, and in determining the overall strength of the exchange biasing field.

5.3.2 EFFECT OF HEATING ON MAGNETIC MICROSTRUCTURE

The previous discussions are informative from a fundamental point of view, but it is rare that any device incorporating an exchange biased layer would operate at temperatures below $0^\circ C$. The aim of this section is to provide a discussion of the magnetic microstructure during reversal at elevated temperatures.

Figure 5.13(a-l) shows 4 series of reversals for increasing the applied field strength at $50^\circ C$ (a-c), $100^\circ C$ (d-f), $140^\circ C$ (g-i), and $200^\circ C$ (j-l) for a $6.0nm Ni_{80}Fe_{20} / 10.0nm IrMn$ sample. Each set of data is shown in order that the differences in the reversal at varying temperature may be observed. The pinned layer reversal mechanism for all temperatures studied comprises of an initial increase in magnetisation ripple. This is followed by magnetisation rotation which is probably due to a slight misalignment between the exchange biasing direction and the applied field directions, figure 5.15(a,d,g,j). Following the rotation, the greatest variation in micromagnetic behaviour is observed as a function of temperature as the reversal continues.

At $50^\circ C$ the pinned layer can be seen to still break up into a complicated domain pattern, figure 5.15(b). However, a large portion in the centre of the image can be seen to have already fully switched with the resultant direction of magnetisation being close to that of H_a . The remaining viewable area follows with small increases in H_a , however the domain walls that are formed are of lower angle than in the previous studies, and are readily annihilated, figure 5.15(b,c). In this case few 360° domain wall structures are stabilised, and those that do are easily removed from the pinned layer by further small increases in the strength of H_a . Rotation and alignment of the direction of pinned layer

magnetisation with the direction of H_a is eventually observed following further increases in the strength of H_a .

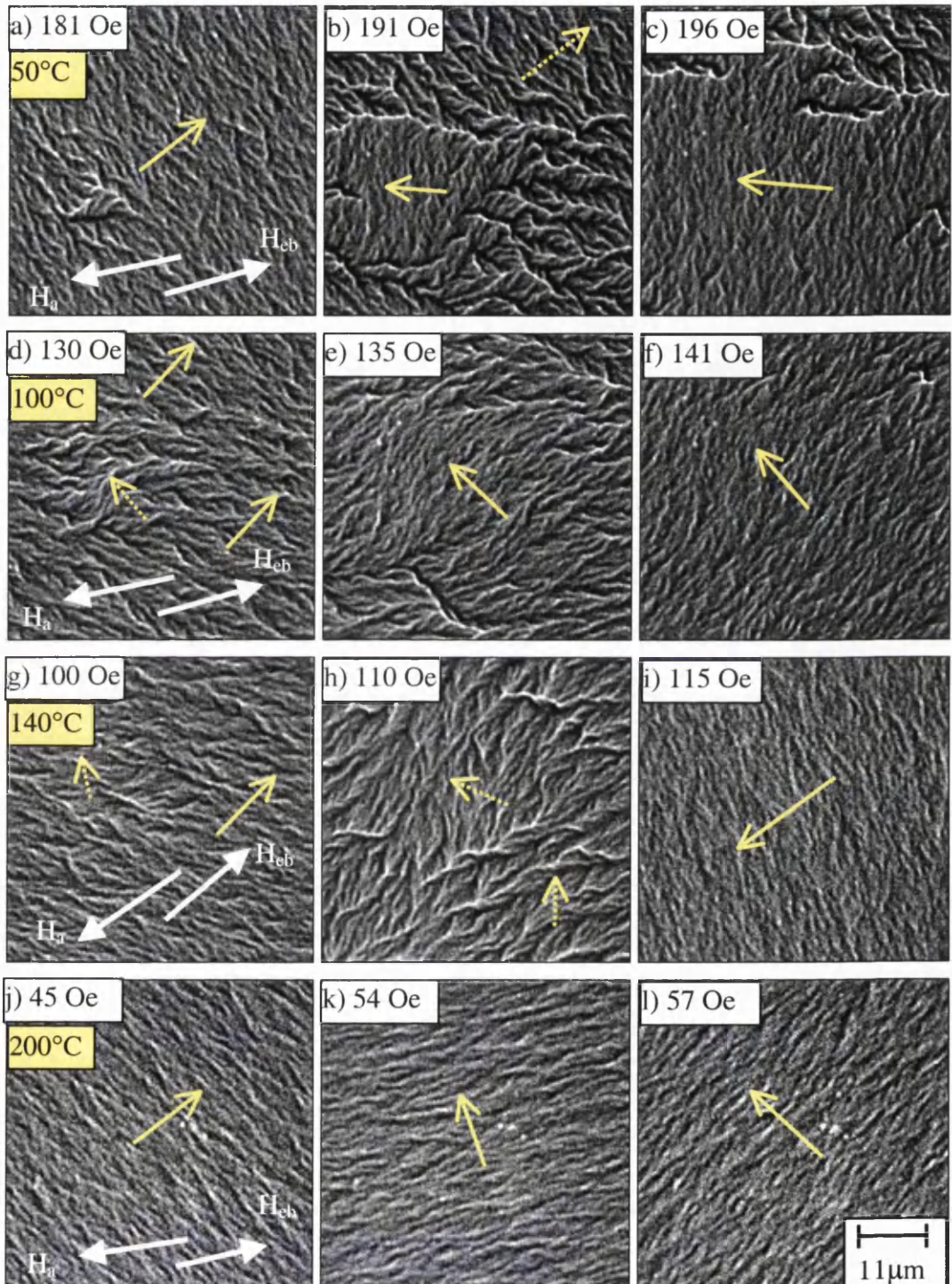


Figure 5.15: Effect of heating upon the pinned layer reversal mechanism at 50 °C (a-c), 100 °C (d-f), 140 °C (g-i) and , 200 °C (j-l). Sample 6nm $Ni_{80}Fe_{20}$ / 10nm $IrMn$.

At $100^{\circ}C$, the strength of applied field required to cause the pinned layer to reverse is lower than that required for $50^{\circ}C$. Figure 5.15(e) shows that as the reversal proceeds, the film does not break up into a complicated domain pattern, but that a much more homogeneous transition of the magnetisation takes place. It can be seen that domain wall density is low, those that do form are of low angle and readily annihilated. Inspection of the magnetisation ripple reveals that there is a “waviness” in the direction of magnetisation across the field of view, but that the variation is not large enough to allow many domain walls to form. Figure 5.15(f) shows that the angle subtended by the pinned layer magnetisation during the reversal is less than that for the 50° case (compare figure 5.15(c) and (f)). Finally, as H_a is increased in strength, the pinned layer magnetisation again rotates towards the direction of H_a until alignment is achieved.

At $140^{\circ}C$, a large amount of magnetisation rotation is observed as the reversal proceeds. At $H_a=110Oe$, the pinned layer passes through a state which is best described by enhanced dispersion. A few low angle domain walls exist over a small applied field range before coherent rotation of the pinned layer magnetisation towards H_a is observed as the strength of H_a is increased. Note that an applied field of $115Oe$ is still required to cause alignment of the pinned layer magnetisation with H_a , indicating that the effect of exchange biasing is still present, however the mechanism by which the reversal proceeds has changed markedly from the room temperature case.

The temperature of the sample was then increased to $200^{\circ}C$, and the pinned layer magnetisation reversal is shown in figure 5.15(j-l). In this case the pinned layer magnetisation can be seen to coherently rotate towards the direction of H_a as the strength of H_a is increased. Note that the applied field strengths required to cause reversal are still significantly greater than that required to reverse either a single layer of $Ni_{80}Fe_{20}$ or the free layer of a spin-valve.

As the temperature is increased above $200^{\circ}C$ the reversal mechanism is very similar to that shown in figure 5.15(j-l). The main effect of small increases in temperature is to reduce the strength of H_a required to cause magnetisation rotation and hence alignment of the pinned layer magnetisation with the direction of H_a .

The blocking temperature of $IrMn$ is around $287^{\circ}C$, so increasing the temperature above this should result in a change in the reversal mechanism.

Figure 5.16 shows the reversal for the above sample at $\approx 300^\circ\text{C}$. The reversal mechanism above the blocking temperature is now markedly different from temperatures below the blocking temperature. There is now a larger amount of dispersion in the film, and this increases with very small changes in applied field antiparallel to the original biasing direction. A small amount of magnetisation rotation is observed before a single domain wall rapidly sweeps through the ferromagnetic layer at $H_a=1.8\text{Oe}$, figure 5.16(c). The magnetisation in the reversed regions lies close to the applied field direction, and further small increases cause the magnetisation to rotate towards the field direction and a decrease in the magnetisation ripple contrast is observed.

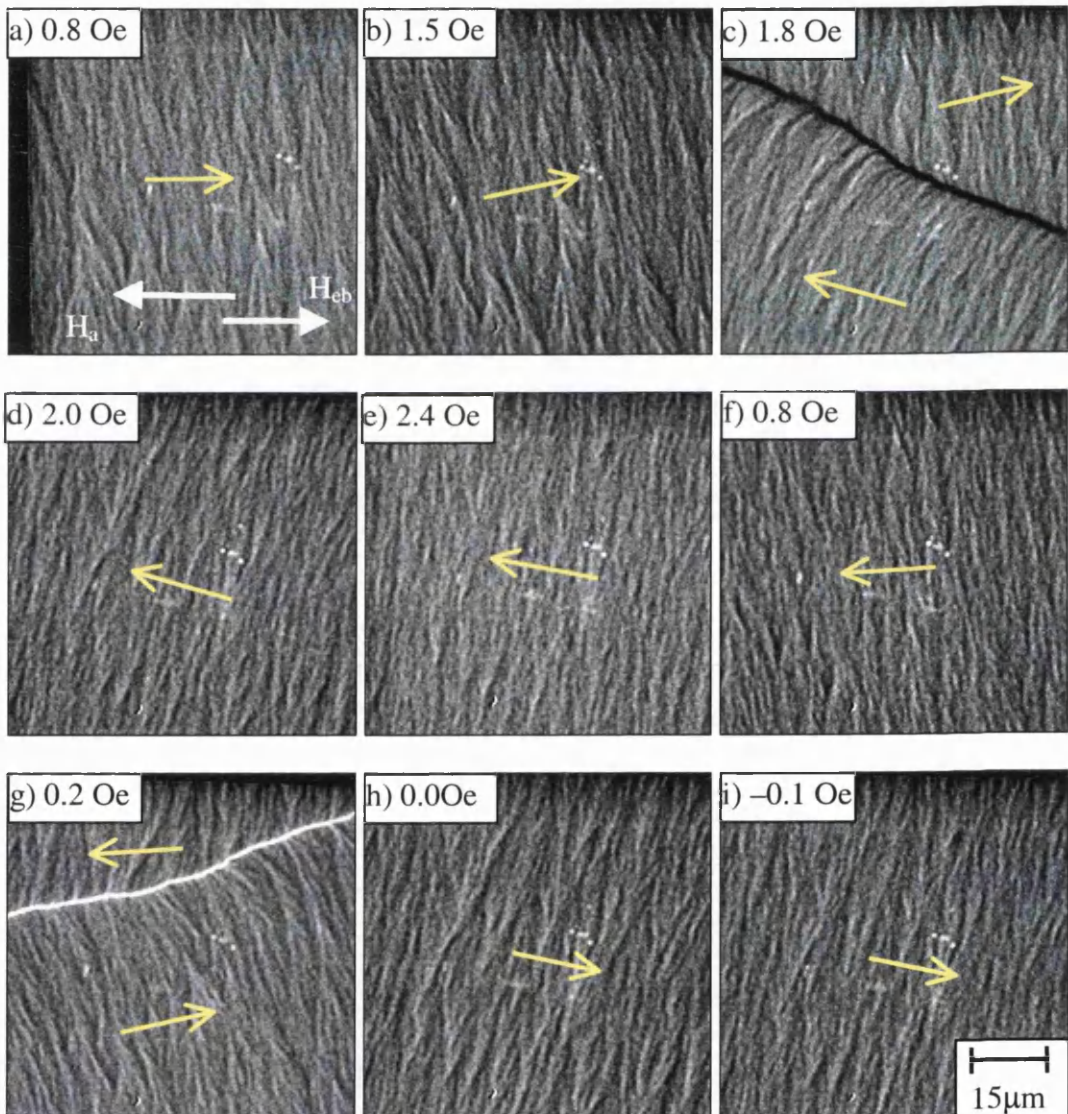


Figure 5.16: Reversal mechanism at 300°C for 6.0nm $Ni_{80}Fe_{20}$ / 10.0nm IrMn.

Upon decreasing the applied field strength the opposite processes occur. An increase in the dispersion is followed by another single domain wall sweeping through the layer facilitating the reversal. Some magnetisation rotation is observed before the magnetisation approaches its original direction once more. This type of reversal is very similar to that observed for isolated permalloy layers^[18].

5.3.3 COOLING FROM ABOVE THE BLOCKING TEMPERATURE

Once study of the pinned layer reversal at temperatures above the blocking temperature was complete the sample was cooled back to room temperature. The process of cooling was achieved simply by turning off the power to the heating coils and allowing the sample to return to room temperature. The sample was tilted in the presence of a vertical field which saturated the ferromagnetic layer. Once the antiferromagnet cooled below its blocking temperature exchange biasing should return along the direction of the in-plane magnetic field.

Figure 5.17 shows the pinned layer reversal for the sample once it has returned to room temperature. At zero applied field the magnetisation ripple contrast is low making it difficult to infer the direction of magnetisation in the pinned layer, figure 5.17(a). It is likely that the magnetisation at zero field is close to the direction of H_a during cooling, which is antiparallel to H_a as indicated. As the applied field strength is increased, the magnetisation reversal proceeds by an increase in magnetisation ripple and also magnetisation rotation, figure 5.17(b). A state then forms whereby many small, locally pinned low angle domain walls form facilitating the reversal. The direction of magnetisation in switched regions lies towards the direction of H_a , figure 5.17(c,d). The domain walls are high in density but have a low mobility. They are readily annihilated with small increases in field strength which causes unswitched areas in the pinned layer to reverse. The net result is that the percentage of the pinned layer magnetisation in the switched direction grows at the expense of unswitched regions. The direction of magnetisation is not immediately coincident with H_a after switching, figure 5.15e. Further increases in H_a are required to cause continued rotation of the magnetisation towards H_a and any remaining locally pinned domain walls to annihilate, figure 5.17(e,f). Eventually alignment is achieved between the pinned layer magnetisation and H_a . Upon decreasing the

applied field strength broadly similar processes can be seen to take place in reverse, figure 5.17(g-l).

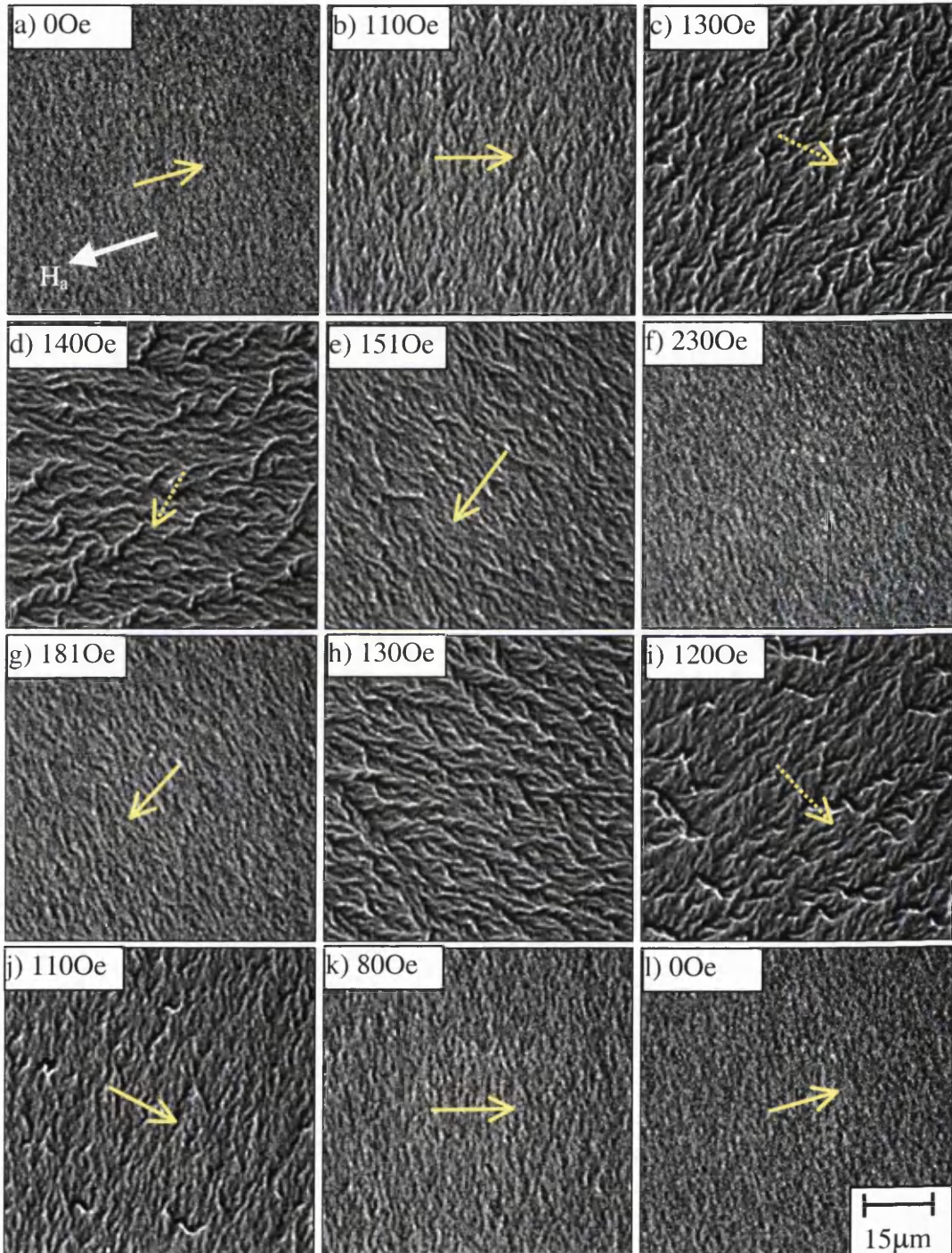


Figure 5.17(a-l): Pinned layer reversal for 6.0nm $Ni_{80}Fe_{20}$ / 10.0nm IrMn sample. Cooled from 300 °C to room temperature.

It can be seen from the figure that once the sample has returned to room temperature that the exchange biasing returns with $H_{eb} \approx 130\text{Oe}$. This is approximately 0.66 of the original value of 197Oe. Initially the coercivity H_c was $\approx 2.5\text{Oe}$, from these results it is not possible to measure any significant change in value. The way in which the reversal proceeds involves more magnetisation rotation than before annealing, which is a surprising result. One would expect the direction of H_{eb} to be perfectly aligned with the applied field in the microscope after cooling, as it is the direction along which H_{eb} should return. This effect is not fully understood at present but may be a consequence of the fact that the sample was cooled in the presence of a vertical field where there was still a significant component out of the plane of the film.

Diffraction patterns and high magnification bright and dark field images of the samples were taken after annealing. None of these showed structural variations in either the amount of texturing or the grain size when compared with the as deposited state of the samples. This is in agreement with earlier work^[17].

5.4 DISCUSSIONS AND SUMMARY

The exchange biasing effect in layers of Ni₈₀Fe₂₀ biased by FeMn and IrMn has been investigated as a function of temperature. At room temperature where it was possible to achieve very good alignment of H_{eb} with the applied field direction, exchange biasing energies of 0.098mJ/m^2 and 0.115mJ/m^2 were obtained for FeMn and IrMn respectively. The reversal proceeded by an initial increase in the magnetisation ripple followed by complex domain assisted processes. Large numbers of small 360° domain wall structures were formed which were stable and required high field strengths to annihilate them. As the temperature was decreased H_{eb} increased in agreement with theory. Much larger numbers of 360° domain walls were formed at decreasing temperature, indicative of increasing local pinning of the ferromagnetic layer by the antiferromagnet. An increase in H_c was also observed at decreasing temperatures.

At elevated temperatures both H_{eb} and H_c decreased and lesser numbers of 360° walls were observed as the temperature increased. Also, an increasing amount of magnetisation rotation was observed. Eventually the pinned layer reversal proceeded by coherent rotation of the pinned layer magnetisation, but at increased applied fields than required for either isolated layer or spin-valve free layer reversals. The rotation is thought

to be due to the slight misalignment between H_{eb} and H_a in the variable temperature rods. This misalignment is caused because the biasing direction of the sample must be aligned with the tilt axis of the sample rod by the naked eye. There is no facility to rotate the sample in-situ, so one must achieve the best alignment before beginning observations. Unfortunately due to design limitations it is not possible to correct for this. However, the technique used in this work was to initially orient the sample accurately in a rod with rotate facility then to carefully transfer the sample to the variable temperature rod.

Once the temperature was increased above the blocking temperature of the AF layer a marked change in the reversal mechanism was observed. It proceeded at small applied field strengths by an increase in the magnetisation ripple contrast followed by a slight rotation of the magnetisation. As the applied field was increased further the reversal was facilitated by the sweeping of a single domain wall through the layer. This is very similar to the reversal of an isolated ferromagnetic layer.

Cooling of the pinned layer in the presence of a magnetic field caused exchange biasing to return for both the FeMn and IrMn samples. However, H_{eb} was somewhat diminished from its original value, especially in the case of IrMn. The reversal mechanism was somewhat different after cooling, it proceeded by much more magnetisation rotation during the reversal process. This suggests that the direction of H_{eb} did not return exactly along the intended direction of applied field, which may be indicative of the cooling procedure which involved a component of magnetisation out of the plane of the sample.

Investigations of the structural properties before and after annealing indicated that no detectable changes were taking place, for instance the grain structure and level of texturing were unaffected.

The results presented in this chapter are valid for both the FeMn and IrMn biasing systems, however notable advantages of biasing by IrMn are observed, for instance the slightly higher value of H_{eb} at room temperature for IrMn, but more significantly the significantly higher blocking temperature T_b .

REFERENCES

- [1] Tsang C, Lee K, (1982), J. Appl. Phys. **53**, 2605.
- [2] Lin T et al, (1995), IEEE Trans. Mag. **31**, 2585.
- [3] Jungblut R et al, (1995) J. Magn. Magn. Mat. **148**, 300.
- [4] Imagawa T, (1993), Digests of international conference, (invited), CA-01.
- [5] Van der Heidjen P A et al, (1998), Appl. Phys. Lett. **65**, 1183.
- [6] Hempstead R D et al, (1978), IEEE Trans. Mag. **MAG-14**, 521.
- [7] Freitas P P et al, (1994), J. Appl. Phys. **75**, 6480.
- [8] Cain C W et al, (1988), IEEE Trans. Mag. **24**, 2609.
- [9] Folkerts W et al, (1994), J. Appl. Phys. **76**, 6391.
- [10] Shen J X, Kief M T, (1996), J. Appl. Phys. **79**, 5008.
- [11] Soeya S et al, (1996), J. Appl. Phys. **79**, 1604.
- [12] Carey M J et al, (1992), Appl. Phys. Lett. **24**, 60.
- [13] Egelhoff W F et al (1995) J. Appl. Phys. **78**, 1.
- [14] Lin T et al, (1994), Appl. Phys. Lett. **65**, 1183.
- [15] Fuke H et al, (1995), European Patent Application EP0717422A1
- [16] Fuke H et al, (1997), J. Appl. Phys. **81**, 4004.
- [17] Van Driel J et al, (1998), submitted to J. Magn. Magn. Mat.
- [18] Gillies M F, Chapman J N, (1995), J. Appl. Phys. **78**, 5554.

CHAPTER 6: THE EFFECT OF MOLYBDENUM IMPURITY ON PERMALLOY

6.1 INTRODUCTION

The work carried out in this chapter was carried out over a 10 week period of study at the Philips “NatLab” research laboratories in Eindhoven. At that time Philips manufactured heads, and this aspect of the project addressed a specific technological problem. Namely that the anisotropic magnetoresistance (AMR) ratio in magnetic recording read heads was $\approx 1\%$ less than the value of 2.7% that can be achieved for $\text{Ni}_{80}\text{Fe}_{20}$ ^[1]. In order to improve process yield and device performance it was desirable to maximise the AMR ratio in the final working sensor. An improvement in the final AMR ratio may have allowed the lifetime of AMR based sensors to be extended. This would reduce the costs associated with changing to new manufacturing techniques required for deposition of GMR based sensors, for example UHV multi-target sputtering equipment.

It was suggested that a possible cause of performance deterioration could be due to molybdenum (Mo) impurity in the active permalloy ($\text{Ni}_{80}\text{Fe}_{20}$) layer of the sensor. During manufacture, Molybdenum was deposited on top of the $\text{Ni}_{80}\text{Fe}_{20}$ and acted as an adhesion layer for gold contact pads in the head assembly. Excess Mo was then removed by wet chemical etching before a sealing SiO_2 layer is deposited at 300°C. The highest temperature that the sensor was exposed to is 300°C for 15 minutes at this stage. It is possible that diffusion of the Mo was occurring and contributing a detrimental effect to the AMR ratio.

It has been shown that the AMR ratio of permalloy can be substantially reduced by the introduction of only 1-3 wt % of 3d transition metal impurities^[2]. Figure 1 shows that only 2 wt % addition of $M=\text{Mn}, \text{Cu}$ or Cr to $\text{Ni}_{82}\text{Fe}_{18}$ reduces the AMR ratio to below 1%. Although Mo was not included in this work, Mo is below and next to Cr and Mn in the periodic table. A similar effect upon $\text{Ni}_{80}\text{Fe}_{20}$ might be expected by Mo impurity. It is noted that in [2] electrolytic iron, nickel and the 3d transition metals are arc-melted in an argon gas atmosphere before evaporation onto a glass substrate. In this thesis, the samples were deposited by RF-diode sputtering, and the impurity atoms were possibly incorporated

into the magnetoresistive $\text{Ni}_{80}\text{Fe}_{20}$ after deposition by a thermally assisted diffusion process.

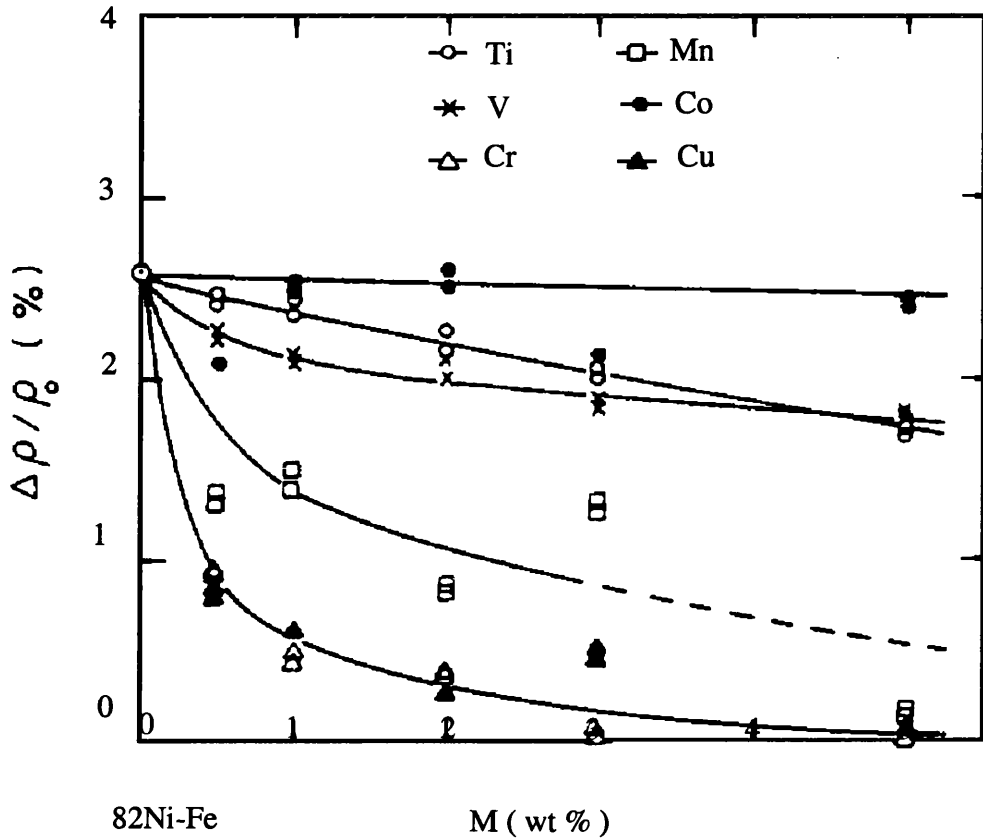


Figure 6.1: Anisotropic magnetoresistivity ratio of $82\text{Ni-Fe}+M$ film as a function of the content of M .

6.2 EXPERIMENTAL CONDITIONS

The configuration of the samples were as follows: $\text{Si} / 4\text{nm TiO} / 32\text{nm Ni}_{80}\text{Fe}_{20} / 6\text{nm Mo}$. They were deposited on a silicon wafer by RF-diode sputtering at a power of 300W, 450V target bias and a growth rate of $\sim 0.35\text{nm s}^{-1}$. An easy axis was defined during deposition by application of a constant 600Oe field in the plane of the sample. The planar dimensions of each sample were $4 \times 12\text{mm}$.

Initial magnetoresistance measurements were made using a fixed 4-point probe method, and a correction taken into account for the dimensions of the sample. The specimens were then thermally processed by annealing in a vacuum oven in the presence of a magnetic field along the easy axis supplied by a magnetic yoke. The temperature profile

and annealing time were varied, as discussed below. Following annealing treatment, magnetoresistance measurements were repeated. These were obtained by positioning 4 needle probes onto the surface of the sample. Voltage and current readings were taken and an external field was applied and controlled by computer. The data were then converted into magnetoresistance data ($R(\Omega)$ as a function of $H(\text{Oe})$). It is also possible to measure the saturation magnetisation of the $\text{Ni}_{80}\text{Fe}_{20}$ by employing a vibrating sample magnetometer (VSM).

Selected samples were then examined by Rutherford Backscattering Spectrometry (RBS) which can give depth profile of atom concentrations in the sample; when compared to the original samples it is then possible to observe the level of diffusion that has taken place in thermally processed samples.

6.3 ELECTRICAL AND MAGNETORESISTIVE PROPERTIES

6.3.1 INITIAL EXPERIMENTS

Initially a set of measurements was made for the as deposited state of the sample. Table 1 shows results from measurements made on several samples thus enabling average values to be obtained.

QUANTITY	VALUE	ERROR
R (Ω)	6.00	0.20
AMR (%)	1.44	0.03
H_k (Oe)	4.5	0.5
M_s (T)	1.04	0.15

Table 6.1: Data for as deposited 4nm TiO / 32nm $\text{Ni}_{80}\text{Fe}_{20}$ / 6nm Mo samples.

It can be seen that for the as-deposited samples, the AMR ratio is considerably less than can be achieved in optimised films. It is well known that the AMR ratio depends on many factors such as film thickness, grain size, and film surface conditions. Also, vacuum quality, substrate temperature and deposition rate have also to be considered^[1]. These are

complicated processes, but the purpose of this work is not to provide an in depth discussion of these factors, but to investigate the effect of annealing upon a single type of sample used in manufacturing.

6.3.2 ANNEALING EXPERIMENTS

The samples were annealed at variable temperatures in the range 200-350°C. For each temperature, the anneal time was kept constant in order that the temperature at which the onset of diffusion began could be established. Figure 6.2 shows the temperature and resistance profile for an anneal at 200°C. The experiment consists of 3 phases:

1. **HEATING:** This is done over a period of 20 minutes so that any overshoot in temperature is minimised. This was necessary because the heating element was either 'ON' or 'OFF'. The temperature had to be slowly increased to ensure that the temperature increased in small increments in between measurements which were at 30 second intervals.
2. **ANNEALING:** This was done for 30 minutes in each case. The temperature is set at a constant value, but it can be seen that there are fluctuations in the measurement of approximately $\pm 15^\circ$. This is likely to be a combination of the temperature rising and falling around the set value between measurements and variations in the readings with time.
3. **COOLING:** As the sample is under vacuum, cooling follows the form of an exponential decay. It can be seen that it takes ≈ 250 minutes to cool the sample back to room temperature. It would be impossible to allow air to enter the chamber at high temperatures as the sample would oxidise immediately.

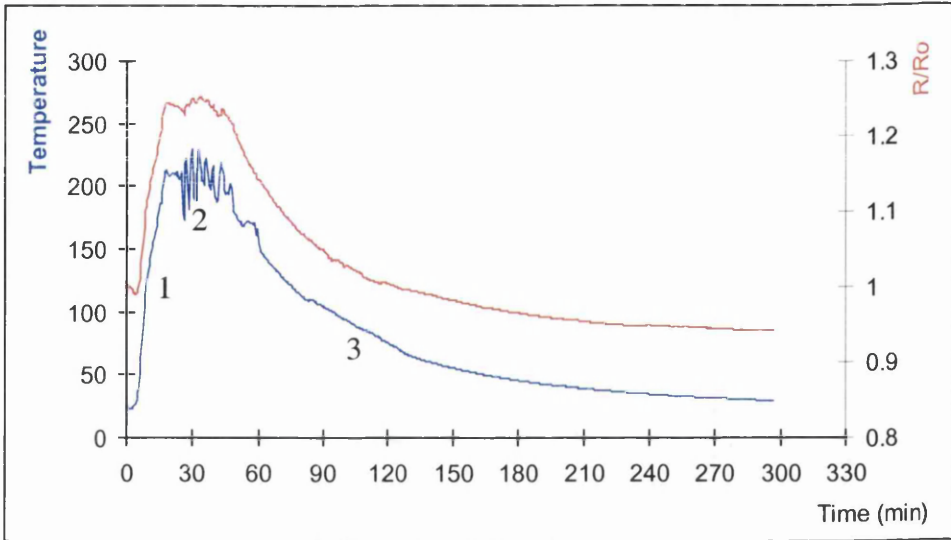


Figure 6.2: Resistance and temperature profile as a function of time.

Figure 3 shows a typical magnetoresistance (MR) curve measured by the 4-point method introduced above. The MR is calculated by using equation 6.1.

$$MR = \frac{\Delta R}{R} = \frac{(R_p - R_{ap})}{R_{ap}} \tag{6.1}$$

R_p is the resistance when the magnetisation is parallel to the current direction (high state), and R_{ap} is the resistance when the magnetisation is perpendicular to the current direction (low state). The method for calculating the anisotropy field H_k is shown on figure 6.3.

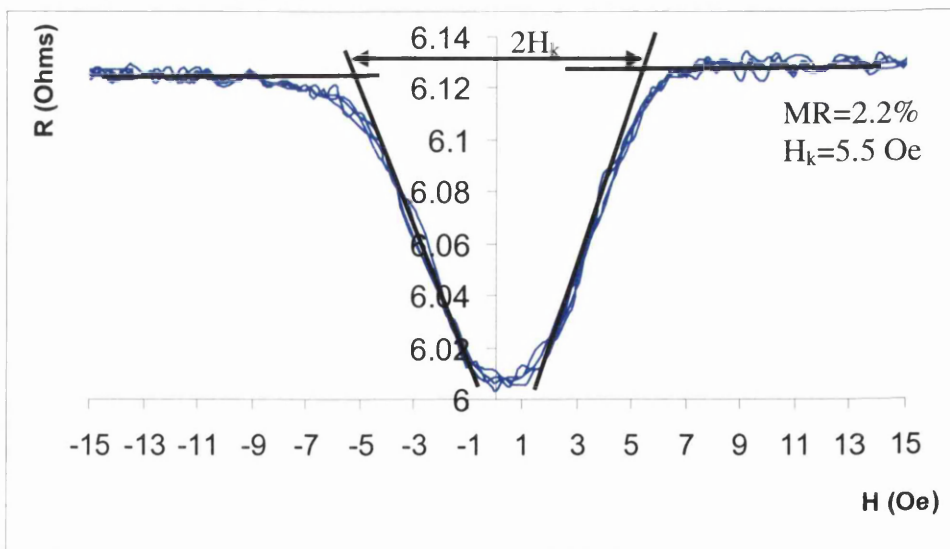


Figure 6.3: MR curve for 200°C anneal along the easy axis.

Annealing experiments of the profile discussed above (figure 6.2) were carried out at temperatures of 200, 225, 250, 275, 300, 325 and 350°C. Measurements of MR, R, and H_k were then made. The results are shown graphically in figures 6.4, 6.5 and 6.6.

For anneals at temperatures below 275°C there is a decrease in the sheet resistance upon annealing, figure 6.4. A corresponding increase in the AMR ratio is observed, figure 6.5. This effect has been reported before^[1], where $Ni_{70}Co_{30}$ and $Ni_{80}Fe_{20}$ samples were annealed at 400°C for an hour. High resolution TEM investigations revealed that the grain size had grown after the heat treatment had been performed which had the effect of lowering the resistance.

At 275°C a sharp increase in the sheet resistance is observed upon annealing and the MR decreases. This change is also observed for annealing above 275°C and indicates that an irreversible change is taking place around this temperature. H_k is observed to stay constant at ≈ 5.0 Oe within the experimental errors for the range of annealing temperatures studied.

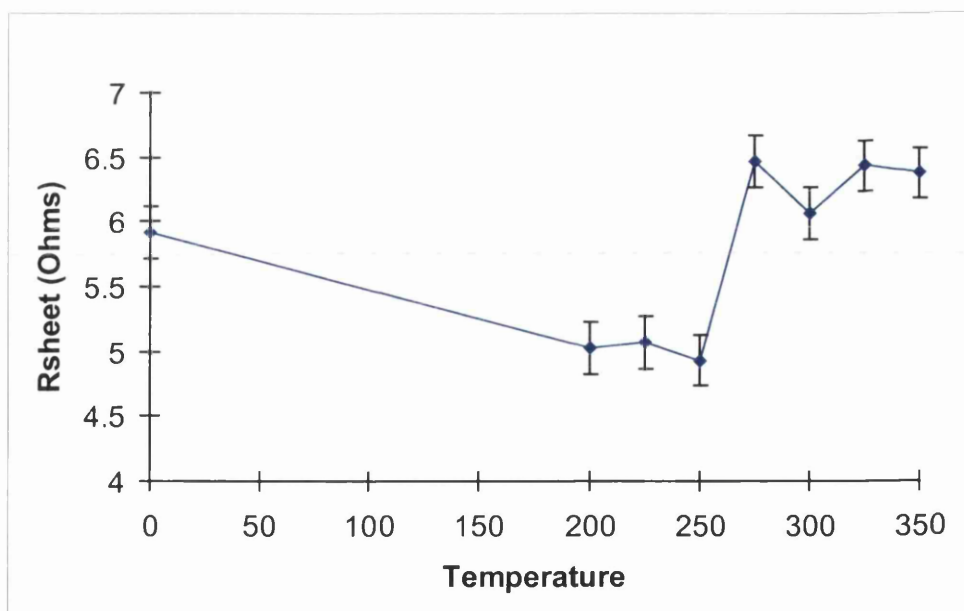


Figure 6.4: Sheet resistance as a function of annealing temperature.

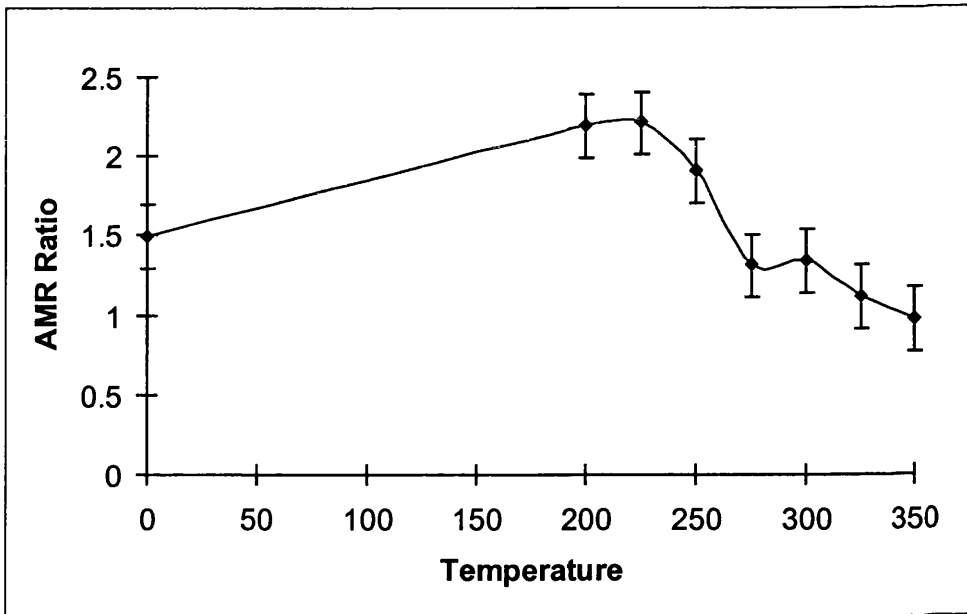


Figure 6.5: AMR ratio as a function of annealing temperature

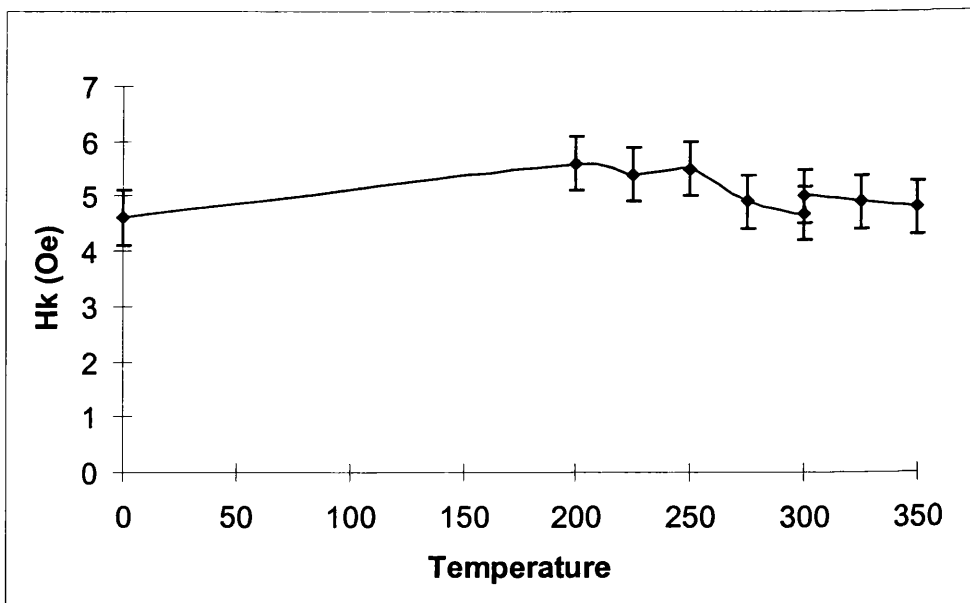


Figure 6.6: Anisotropy field as a function of annealing temperature

One possible reason for the change in resistance upon annealing above 275°C is that Mo diffusion into the Ni₈₀Fe₂₀ layer may have taken place. In order to ascertain whether this is true, compositional analysis is necessary. The technique employed in this case is Rutherford backscattering spectrometry (RBS).

6.4 RUTHERFORD BACKSCATTERING SPECTROMETRY

Figure 6.7 shows the results from Rutherford Backscattering Spectrometry (RBS) on an unannealed sample (dashed line) and a sample annealed at 350°C (solid line). The main discrepancy between the two curves is at the interface region between the Mo and NiFe layers. In the unannealed sample the Mo concentration falls off before the NiFe peak begins. However in the case of the annealed sample the concentration does not fall off completely but levels out and to an approximately constant level into the NiFe layer. This indicates that diffusion of Molybdenum has taken place in a sample which has been annealed at 350°C. Another point worth noting is that the curves do not exactly overlap in the remainder of the spectrum, this is probably due to inhomogeneity in the deposition system producing layers with slightly different thickness from sample to sample.

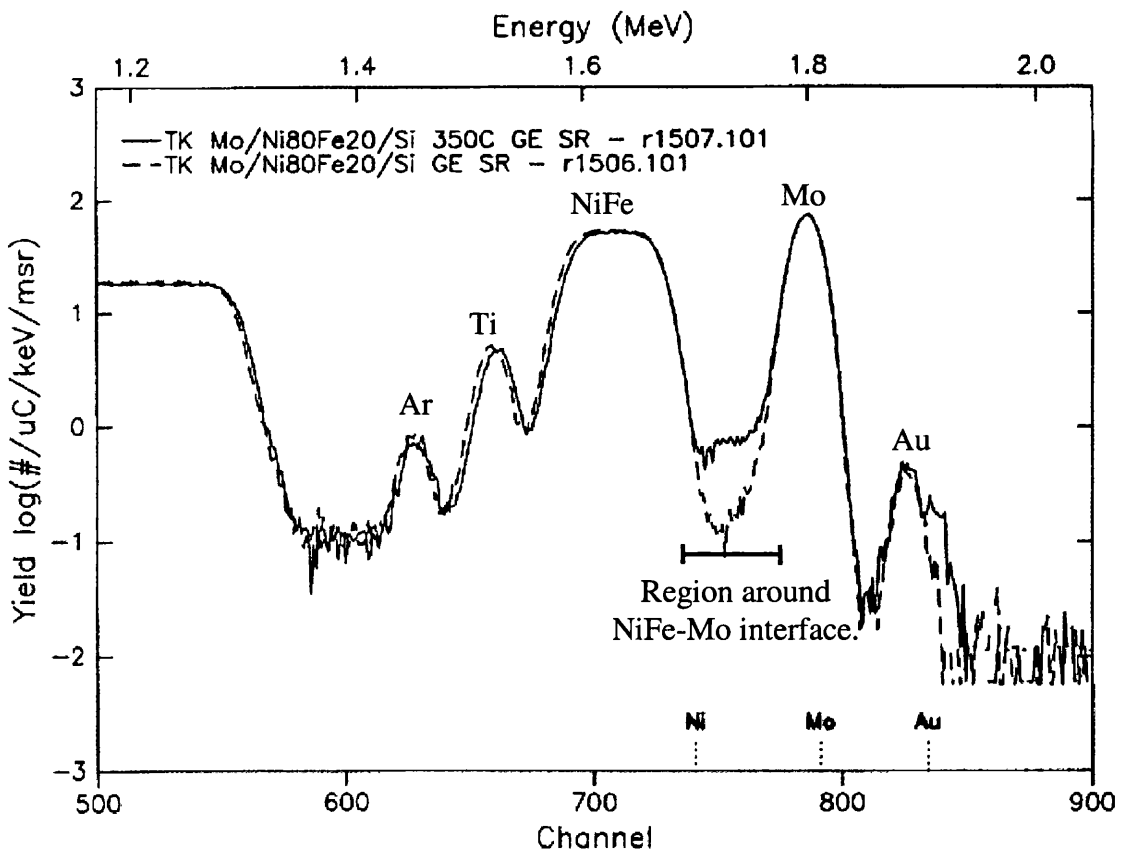


Figure 6.7: RBS spectrum for sample with no anneal (dashed line) and an anneal at 350°C (solid line).

Figure 6.8 shows a close up of the interface region between the Mo and NiFe layers. Results are shown for 5 annealing temperatures up to 350°C plus the original sample. Two regimes are evident:

- i. For annealing temperatures less than 275°C the Mo concentration falls off to the level of the as deposited sample, indicating that no Molybdenum diffusion has taken place.
- ii. For annealing temperatures at and above 275°C the Mo concentration level is enhanced as the NiFe layer is approached, indicative that Mo diffusion has taken place. Simulation and fitting revealed that the amount of diffusion was less than or of the order of 1% Mo diffusion into the NiFe layer.

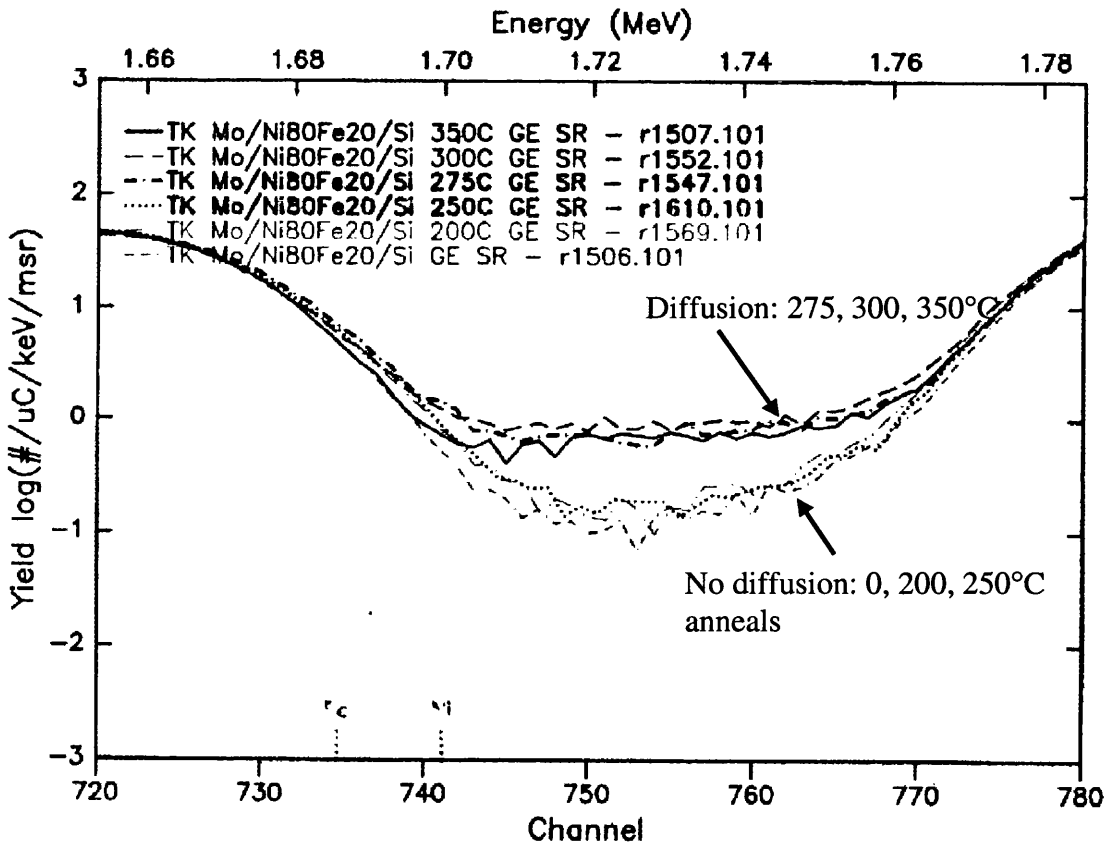


Figure 6.8: RBS spectrum in the region between the Mo and Ni₈₀Fe₂₀ layers.

Diffusion of Mo during the manufacturing process would be during the deposition of the SiO₂ layer by PECVD process. Initially some as deposited samples were placed into the PECVD deposition chamber and exposed to a temperature of 300°C for 15 minutes. No process gases were introduced in the first case. Secondly, samples were treated in the same way but this time process gases were introduced. 0.2µm of SiO₂ was deposited. Although MR measurements could not be made after the deposition was done, RBS analysis was performed and revealed that no molybdenum diffusion had taken place in either of these cases.

6.5 DISCUSSIONS AND SUMMARY

The AMR ratio in permalloy with a Molybdenum layer deposited on the top surface can be slightly improved by annealing at temperatures less than 275°C for 30 minutes. This is attributed to grain growth during the annealing process which lowers the density of defects in the sample, and hence the sample resistance. No diffusion of Mo into the Ni₈₀Fe₂₀ layer is detected by Rutherford backscattering spectrometry (RBS) for anneals at these temperatures. However for annealing treatment at and above 275°C a sharp increase in the sheet resistance is observed and a corresponding decrease in the AMR ratio is observed. RBS revealed that the order of 1% Mo was diffusing into the permalloy layer. The level of diffusion observed was not related to the temperature (for T≥275°C), and this suggests that the diffusion process is more likely to be due to Mo diffusion down the grain boundaries in the Ni₈₀Fe₂₀ layer rather than an interdiffusion process whereby a NiFeMo alloy phase is formed at the boundary between the two layers. It would be necessary to perform more detailed analysis such as TEM cross sectional, X-ray or electron diffraction analysis to provide a conclusive result.

RBS measurements performed on samples which had been subjected to 300°C for 15 minutes in the PECVD deposition chamber (with and without process gases to simulate the manufacturing process) revealed that no molybdenum diffusion was taking place. It is likely that the time of exposure of the samples to high temperature was not long enough for the diffusion to take place. With reference to figure 6.2, the annealing experiments caused

the sample to be at a higher temperature for a longer period of time than in the PECVD chamber.

From the point of view of the manufacturing process, these results show that it is unlikely that Mo diffusion is playing a significant detrimental effect in AMR device performance. However, as long as the annealing temperature is less than the deposition temperature, prolonged annealing does not detrimentally affect the AMR^[3] (as long as the applied field is along the easy axis during anneal). Perhaps the solution is to achieve optimum AMR in as-deposited samples in the first place in order to prolong the life of existing manufacturing processes.

REFERENCES

- [1] McGuire T R, Potter R I, (1975), IEEE Trans. Mag, **11**, 1018.
- [2] T. Miyazaki and T. Ajima, Impurity effect an the anisotropic magnetoresistivity of 82Ni-Fe alloy film, JMMM 81(1989) 91-95.
- [3] Wilts C H, Humphrey F B, J Appl. Phys, **39**, 1191.

CHAPTER 7: CONCLUSIONS AND FUTURE WORK

7.1 INTRODUCTION

The work presented in this thesis has shown various possible magnetic reversal mechanisms of spin-valves and related films by utilising Lorentz imaging modes of transmission electron microscopy. Reversals of the free layer in a range of spin-valves were extensively studied, and 3 possible modes of reversal were described and modelled using a coherent rotation model. The reversal mechanism of layers of $\text{Ni}_{80}\text{Fe}_{20}$ biased by FeMn and IrMn were also studied as a function of temperature. An interesting range of reversals were observed depending on the sample temperature. This has an important role in the thermal stability of spin-valves in commercial devices.

7.2 CONCLUSIONS

The reversal mechanisms of the free layer of a range of parallel anisotropy spin-valves were investigated in chapter 3. Fresnel imaging and low angle diffraction revealed that there were 3 possible modes of reversal that could take place depending on the strength of the interlayer coupling, h_J , and field orientation, θ . For spin-valves with $h_J < 1$ mode A-type reversals were initially observed. This corresponded to a combination of magnetisation rotation and a distinct jump in the direction of magnetisation part of the way through the reversal. The switched magnetisation was observed to have overshoot the applied field direction at the switching field. This mode corresponded to cases where the uniaxial anisotropy K of the sample dominates. As θ was decreased, mode C-type reversals were eventually observed. This corresponded to the case where coherent rotation of magnetisation alone was observed. This would be the preferred mode of operation for sensor applications.

For spin-valves with $h_J > 1$ the free layer reversal mechanism initially observed was mode B, in that magnetisation rotation was observed initially, followed by a jump in the direction of magnetisation part of the way through the reversal. However, in this case the interlayer coupling strength was sufficiently strong to constrain the magnetisation to the

half-plane containing the biasing direction and applied field direction. As θ was decreased mode C type reversals were also eventually observed.

The boundary between the modes of reversal was shown to be indistinct, and involved the free layer reversal proceeding by an increasing amount of magnetisation rotation as θ was decreased. This was accompanied by the formation of an increasing density of low angle domain walls which had low angle and mobility.

A phase diagram with the experimental data points and predicted phase boundaries was shown. Although the predicted boundaries between modes was distinct, and experimentally the change was gradual, the angles at which the mode C type reversals were both predicted and observed were in general agreement.

In chapter 4, a modified Stoner-Wohlfarth coherent rotation model was shown to predict 3 modes of reversal. These corresponded to the reversal mechanisms that were observed experimentally, however 2 of the observed modes ('A' and 'B') involved domain processes which were forbidden in the model. Investigation of the energy curves revealed that an energy barrier was overcome at the experimentally observed switching field. This was facilitated by the formation of domains and frequently led to the observed switching field being less than the predicted value. The form of the energy curves allowed the nature of the domain processes to be inferred. In particular, deep energy minima and large energy barriers led to a low density of rapidly sweeping domain walls facilitating the free layer reversal. On the other hand, for cases where there were shallow energy minima with low energy barriers, a free layer reversal which exhibited a large number of low angle domain walls with low mobility was observed.

The exchange biasing effect in layers of $\text{Ni}_{80}\text{Fe}_{20}$ biased by FeMn and IrMn as a function of temperature was investigated in chapter 5. Room temperature exchange biasing energies of 0.098mJ/m^2 and 0.115mJ/m^2 were obtained for FeMn and IrMn respectively. The room temperature reversals proceeded by an initial increase in the magnetisation ripple followed by complex domain assisted processes. Large numbers of 360° domain wall structures were formed which were stable and required high fields to annihilate them.

Cooling of the samples caused the strength of H_{eb} and H_{c} to increase, and an increase in the number of 360° domain wall structures formed in the pinned layers increased. As the samples were heated, the strength of H_{eb} and H_{c} decreased as the

temperature increased. Correspondingly, the number of 360° walls formed was observed to decrease and a greater amount of magnetisation rotation was observed during the reversals. This was thought to be due to a slight misalignment between the direction of in-plane magnetic field and the biasing direction. The decrease in the strength of H_{eb} was shown to be linear with increasing temperature, decreasing to zero at the blocking temperature of the antiferromagnetic biasing layer.

Once the pinned layer temperature was increased above the blocking temperature of the antiferromagnetic pinning layer, ($\approx 140\text{-}150^\circ\text{C}$ for FeMn and $\approx 285^\circ\text{C}$ for IrMn), the pinned layer reversal changed markedly. It now proceeded by an initial increase in the magnetisation ripple followed by a single domain wall rapidly sweeping through the ferromagnetic layer. This occurred at low applied fields, and the reversal mechanism was now similar to that of an isolated ferromagnetic layer. At temperatures above the blocking temperature, antiferromagnetic order, and hence the effect of exchange biasing, is lost.

After heating to temperatures above the blocking temperature, the samples were allowed to cool to room temperature in the presence of an applied field along the initial direction of biasing. Exchange biasing was observed to return, but it was significantly reduced from its initial room temperature value. No differences in the structural properties such as the average grain size and level of texture were observed when comparing the as-deposited and heated samples.

The effect of annealing $\text{Ni}_{80}\text{Fe}_{20}$ samples with a Mo layer deposited on top was investigated in Chapter 6. This was a brief study and was conducted to address a particular technological problem at the time. The results show that the AMR ratio can be slightly improved for annealing for temperatures $<275^\circ\text{C}$ for 30 minutes. This is due to an improvement in the sheet resistance probably due to grain growth which lowers the defect density associated with grain boundaries. For annealing at temperatures $\geq 275^\circ\text{C}$ for 30 minutes, a sharp increase in the sheet resistance is observed. This has the effect of lowering the AMR ratio. RBS analysis revealed that $\approx 1\%$ Mo had diffused into the $\text{Ni}_{80}\text{Fe}_{20}$ layers, but this concentration was independent of annealing temperature after the onset of diffusion was observed. It is thought that this was due to Mo diffusion down the grain boundaries at temperatures $\geq 275^\circ\text{C}$ rather than an interdiffusion process.

7.3 FUTURE WORK ON CONTINUOUS FILMS

7.3.1 ALTERNATE ANISOTROPY ARRANGEMENTS

The work presented on the free layer reversals of spin-valves in this thesis concentrated on films in a parallel anisotropy arrangement. Only a small section was given over to discussion of a crossed-anisotropy spin-valve. The coherent rotation model used in the modelling work can easily be extended to alternative anisotropy arrangements. Equation 7.1 shows the energy functional for the general case. ϵ is the angle between the easy axis of the free layer and the biasing direction ($\epsilon=0^\circ$ for the parallel anisotropy case).

$$\Gamma = \sin^2(\varphi - \epsilon) - 2h_{eff} \cdot m \quad 7.1$$

The predicted phase diagram from the crossed anisotropy arrangement is shown in figure 7.1.

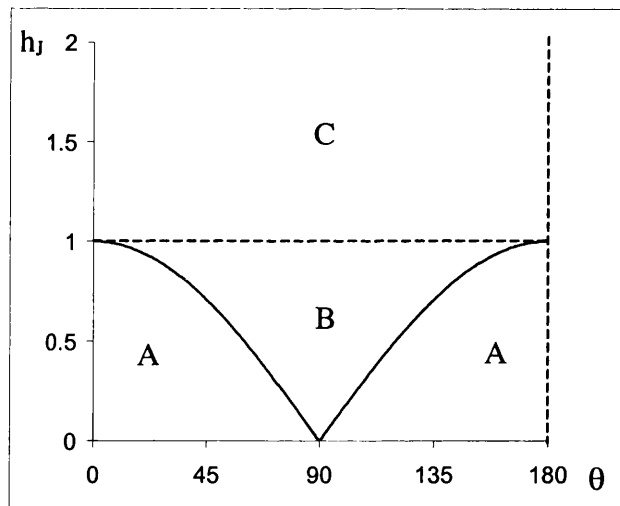


Figure 7.1: Phase diagram for the free layer reversal mechanism in spin-valves in a crossed anisotropy arrangement ($\epsilon=0^\circ$). Predicted modes of reversal shown.

This figure shows that for crossed anisotropy spin-valves with $h_J > 1$, mode C-type reversals alone are predicted which corresponds to coherent rotation of magnetisation alone. For $h_J < 1$, the figure shows that a mode A to mode B transition in the mode of reversal should be observed as θ is reduced from 180° . Investigations of the parallel anisotropy case showed that the range of θ over which mode B-type reversals were predicted was small

($\approx 2^\circ$) and there were not observed experimentally when $h_J < 1$. Thus a mode A to mode B transition has not yet been observed experimentally. The crossed anisotropy case therefore provides several interesting cases for study, as well as investigating samples whose coupling strength $h_J \approx 1$.

7.3.2 INFLUENCE OF TEMPERATURE ON SPIN-VALVE SAMPLES

The work carried out on the temperature dependence of biasing showed that the strength of exchange biasing decreased as the temperature was increased. These studies were, however, carried out on isolated pinned layers of $\text{Ni}_{80}\text{Fe}_{20}$. It would be instructive to repeat the experiments on complete spin-valve structures. Of particular interest would be studies at temperatures where the switching field of the pinned layer was only slightly greater than that of the free layer. One would expect an increase in the level of dispersion and some magnetisation rotation in the pinned layer as the switching field was approached. It has been observed that there is an increase in the level of dispersion and slight magnetisation rotation in the pinned layer just before switching, this would be expected to affect both the switching field and switching mechanism of the free layer reversal.

7.3.3 INFLUENCE OF COOLING

After the samples were cooled back to room temperature following heating to above the blocking temperature, exchange biasing was observed to have returned, but at a diminished value from the initial room temperature result. Additional experiments are necessary to understand this effect more fully. For example in the experiments presented in this thesis, the sample was heated in the Philips CM20 TEM. Magnetic fields are applied via the objective lens, and are therefore perpendicular to the sample at 0° tilt. It is normal to then tilt the sample to induce a component of this field in the plane of the sample. Thus in the experiments previously described, while the sample was cooled there was still a component of the field out of the plane of the sample.

Investigation of the effect of the component of field out of the plane of the sample would be beneficial. For example, cooling at variable tilt angle, or constant tilt angle and variable vertical field strengths. Ideally a magnetising stage should be fitted to

this microscope which would allow magnetic fields to be applied in the plane of the sample without tilting.

7.4 PATTERNED SAMPLES

7.4.1 INTRODUCTION

While the experiments in this thesis have provided considerable understanding into the possible reversal mechanisms of continuous spin-valve films, it is also necessary to consider the effects of patterning on the magnetic state. These effects will be strongly influenced by demagnetising fields and are important as any application of spin-valves in devices will involve patterning.

One patterned structure is the ‘picture frame’ which was used in the prototype magnetic tape head assemblies by Philips in the DCC tape system. Any mechanisms of formation of domains need to be understood as they can be a source of noise in the final device. This section shows several image sequences that were an initial study of the effect of patterning.

7.4.2 ‘L-SHAPED’ SAMPLES

A proposed ‘picture frame’ structure is shown schematically in figure 7.2. Also, the configuration of a patterned sample used to investigate domain structures that may form is shown.

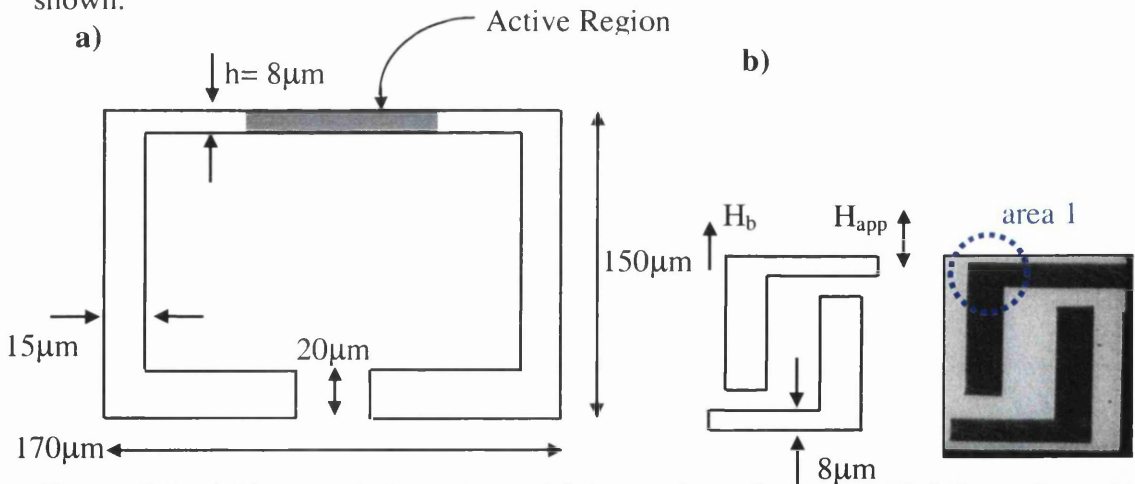


Figure 7.2: a) Shape and dimensions of “picture-frame” element, b) Schematic and image of L-shaped spin-valve sample used to study magnetic properties.

The magnetic properties of the area which is close to the corner where the active region meets the wider section, labelled 'area 1' on figure 7.2(b) is of interest. It is on top of this corner and along the length of the wider strip that contact pads are deposited so that the sense current passes through the active area of a sensor. If a domain wall is nucleated in this region, and propagates down the length into the active area, performance deterioration may result.

Figure 7.3 shows the reversal mechanism of the corner area around 'area 1' of the sample described above in figure 7.2(a). The sample configuration is 3.5nm Ta / 8.0nm Ni₈₀Fe₂₀ / 2.8nm Cu / 6.0nm Ni₈₀Fe₂₀ / 10.0nm Fe₅₀Mn₅₀ / 3.5nm Ta.

The applied field has been cycled from 10.5Oe to -15.5Oe and back to 9.4Oe (positive fields indicate along the biasing direction). Initially, the majority of the sample magnetisation is parallel to the applied field direction, along the biasing direction. However close to the edges of the thinner 8µm strip the magnetisation does not align with the applied field. Two domain walls can be seen down the length of the sample, emanating from the corners where the strip meets the top section. This is due to the magnetostatic interaction between the 'free' and 'pinned' magnetic layers at the edges of the specimen. When the 2 layers are oriented parallel to each other the magnetostatic energy is high, figure 7.3(a,h) due to similar charges at the specimen edges, shown schematically in figure 7.4(a). The magnetisation close to the edges therefore lies at an angle to the bias direction in order to minimise the magnetostatic energy. In contrast, when the magnetisation is approaching antiparallel alignment as shown in figure 7.3(d) the state is energetically favoured, as shown schematically in figure 7.4(b).

An interesting part of the magnetisation reversal is observed when the applied field strength is increased from -4.2Oe up to 9.4Oe, figures 7.3(e-h). At -4.2Oe, the magnetisation in the thin strip has rotated to approximately orthogonal alignment with the biasing direction. At 0.0Oe, domains in the central portion of the thin strip start to form. The magnetisation here resembles an "S" shape, as indicated on figure 7.3(f). However, with a small field increase a central domain is formed, figure 7.3(g), with the magnetisation directions indicated; the two domain walls are again observed. As the applied field is increased further the domain walls move towards the edges and some magnetisation rotation towards the applied field direction is observed, figure 7.3(h). Complete saturation does not occur due to the magnetostatic energy consideration at the edges discussed previously.

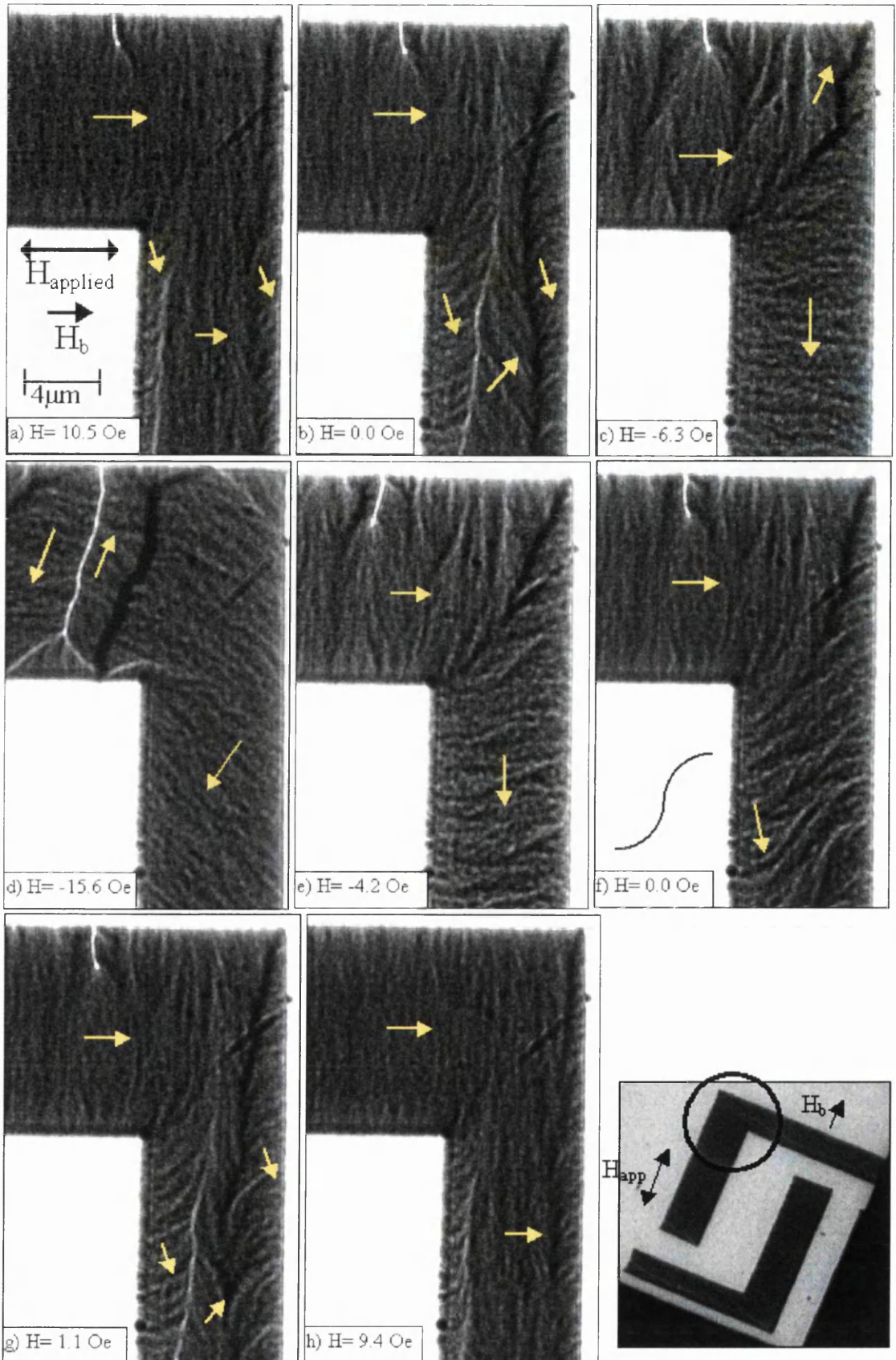


Figure 7.3: Magnetisation reversal of patterned spin-valve element

This type of reversal mechanism is complicated, as there is an interplay between the magnetostatic energy at the edges of the sample, the interlayer coupling, and applied field. Investigation of samples with different strip widths and interlayer coupling strengths is of interest. Also, investigation of samples with different shapes may be beneficial, as this may determine, in part, the mobility and nucleation of domain walls.

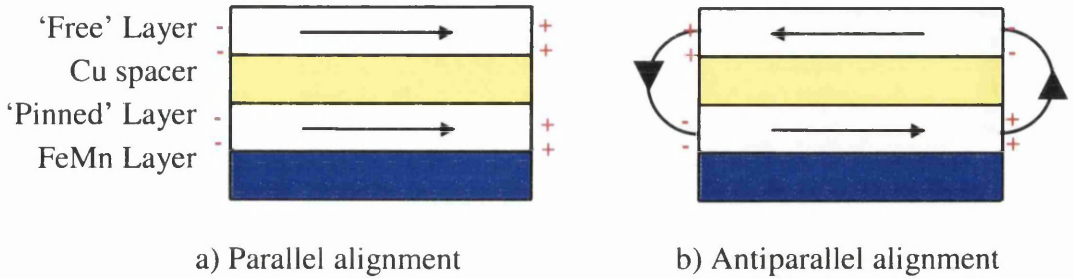


Figure 7.4: Schematic cross-section of spin-valve element. *a) Ferromagnetic layers are parallel: like charges repel at sample edges. b) Ferromagnetic layers are antiparallel: opposite charges at edges result in flux closure across Cu spacer layer.*

7.4.3 OTHER SHAPES AND SIZES OF ELEMENTS

This section shows several examples of images of domain structures that form in spin-valve elements with different shapes and sizes. These can be deposited on the same substrate, allowing images to be efficiently collected for all of the different shapes on the sample for the same experimental setup using the microscope CCD camera. Note that in the following examples that the applied field direction is either parallel or antiparallel to the biasing direction throughout.

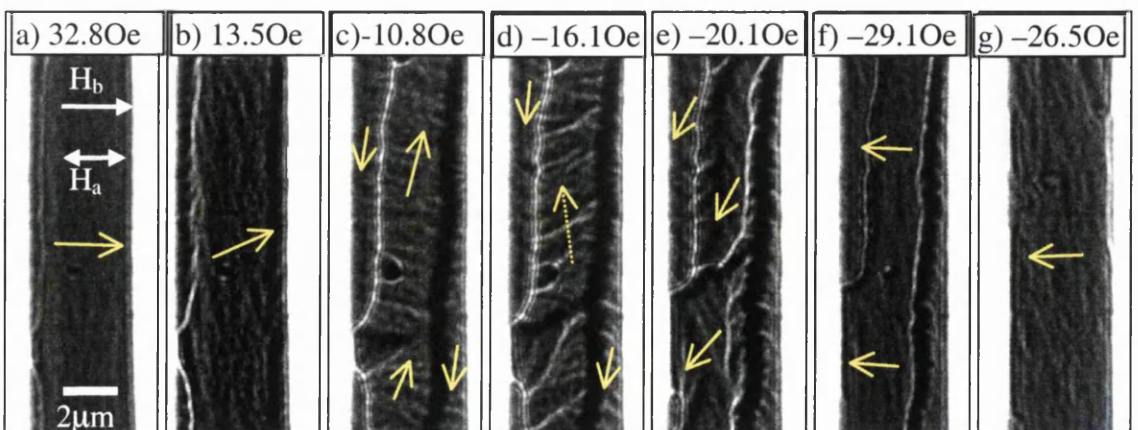


Figure 7.5: Examples of domain structures formed in a long patterned spin-valve strip.

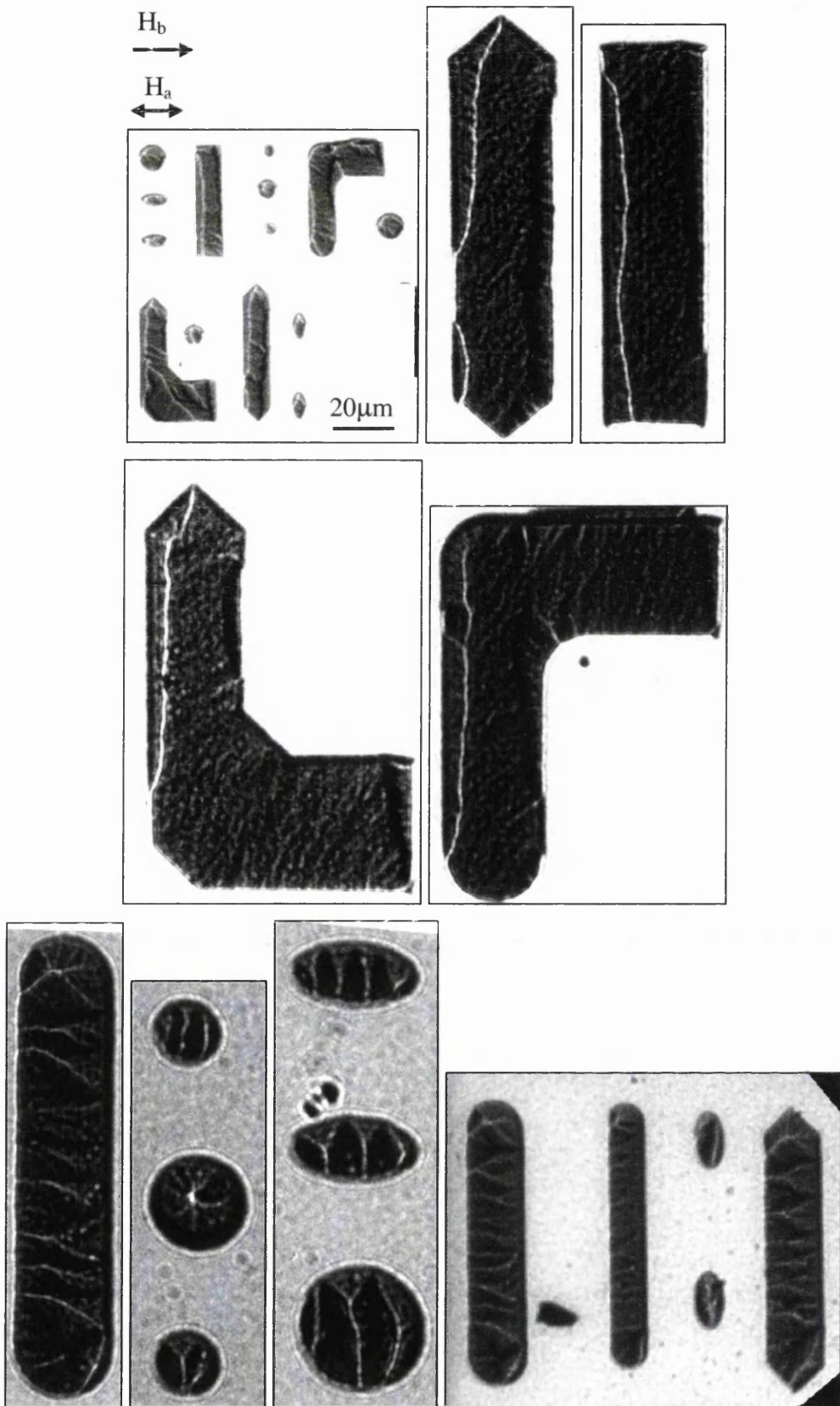


Figure 7.6: Fresnel images showing domain structures in various shapes of patterned spin-valve material.

It is clear from the images shown in this section that there are many possible permutations of sample configuration and experimental conditions which are still worth investigation by TEM. This is interesting from both a fundamental point of view and as for assisting in developing new applications as sensors and memory materials. It would be a worthwhile study which is a body of work in its own right.